UTS UNIVERSITY OF TECHNOLOGY SYDNEY

Bimetallic Nanoporous Sponges

Sanaa Abdullah M Alzahrani

Thesis submitted in fulfilment of the requirements for the degree of

Doctor of Philosophy in Science

under the supervision of
Dr. Annette Dowd (principal supervisor)
Prof. Michael Cortie (co-supervisor)
Dr. Sujeewa De Silva (co-supervisor)

University of Technology Sydney
Faculty of Science

August 2024

Certificate of original authorship

I, Sanaa Abdullah M Alzahrani declare that this thesis, is submitted in fulfilment of the requirements for the award of Doctor of Philosophy in Science, in the School of Mathematical and Physical Sciences, Faculty of Science at the University of Technology Sydney.

This thesis is wholly my own work unless otherwise referenced or acknowledged. In addition, I certify that all information sources and literature used are indicated in the thesis.

This document has not been submitted for qualifications at any other academic institution.

This research is supported by the Australian Government Research Training Program.

Signature: Sanaa

Date: 11/02/2025

Dedication

To my family,

You have been my source of inspiration and support. Without your beautiful prayers, unconditional love, and encouragement over the past few years, it would have been impossible for me to complete this dissertation. I am genuinely thankful to have you in my life.

Acknowledgements

First of all, I would like to express my sincere appreciation to my principal supervisor, Dr Annette Dowd, for giving me the opportunity to work under her supervision and for her unlimited support and mentorship during the lab work and thesis writing. Her understanding and assistance during the most challenging tasks and times have been a source of strength for me. Without her insightful feedback and encouragement, I would not have been able to accomplish this work. Words are powerless to express my gratitude.

I also want to extend my gratitude to my co-supervisor, Professor Michael Cortie, for all the guidance, support and outstanding feedback, also for his assistance with electrochemical capacitance measurements and data analysis. His insightful suggestions and knowledge have taken this research far beyond its initial scope.

I am also grateful to my co-supervisor, Dr Sujeewa De Silva, for her unwavering support and guidance throughout my PhD journey, as well as for her assistance with XRD and EDX analyses.

Many thanks also go to Associate Professor Matthew Arnold for his help in setting up ellipsometry measurements and for sharing his knowledge regarding the fitting of ellipsometry models. I would like to thank Dr Danica Solina for her assistance in producing the samples analyzed for electrochemical capacitance, and Dr Mahnaz Maddahfar for her help in preparing the probe molecule (R6G) solution for the SERS experiment.

I would like to express my deepest gratitude to Associate Professor Cindy Gunawan for her supervision and support in the biology-related sections of my work. I also thank Dr Riti Mann and Dr. Oliver McNeilly for patiently training and assisting me for many hours in the biology lab. A special thanks to Dr Oliver McNeilly for his help with the fluorescence microscope as well.

I want to thank all the academic, professional, and laboratory technician staff at the School of Mathematical and Physical Sciences and the School of Life Sciences who assisted me over the past few years and provided me with training.

This research was conducted under a PhD scholarship, and I would like to take this opportunity to thank Umm Al-Qura University, Makkah, Saudi Arabia, for their financial support. Their contribution has been crucial in ensuring the successful completion of this work.

Last but not least, I am greatly grateful to all of my colleagues, especially Raja, Fatima, Manal, Salma, and Eman, who made this journey more enjoyable.

Publications and Conference Presentations Arising from This Work

- **Published paper**

Alzahrani, S. A., De Silva, K. S. B., Dowd, A., Arnold, M. D., & Cortie, M. B. (2024). Effect of precursor composition and heat-treatment on the morphology and physical properties of Ag nanosponges. *Results in surfaces and interfaces*, *15*, 100217. https://doi.org/10.1016/j.rsurfi.2024.100217

- **Conference poster**

Sanaa A. Alzahrani, R. M., Cindy Gunawan, Sujeewa S.B. De silva, Annette Dowd, and Michael B. Cortie. (2023). *Exploring the antibacterial power of nanoporous silver coatings* [Conference poster]. IBMD 2023 Research Week, University of Technology Sydney.

Abstract

Silver has been successfully tailored at the nanoscale to demonstrate significant variations in its properties when compared to its bulk form, such as electrical conductivity, thermal conductivity, optical response, mechanical property and antibacterial performance. A relatively unexplored nanostructural form is that of silver containing nanopore structures, or so-called nanoporous silver (*np-S*). This material has many of the features common to other forms of silver nanostructures including high surface area to volume ratio, enhanced chemical sensing potential, thermal stability, and so forth, but combines them in a self-supporting rigid framework. These unusual properties open the door for use nanoporous silver in a wide range of applications, such as in biosensors and plasmonic photocatalysis, energy storage, chemical and biological sensing. There are still important outstanding questions about how to control the morphology of *np-S* and the resulting effect on the physical properties, which must be answered for *np-S* to become a viable platform for such applications.

Nanoporous silver was fabricated by dealloying $Ag_{100-x}Al_x$ alloys. The precursor alloys were made in the form of thin films using magnetron co-sputtering with a range of compositions 24.6 and 72.6 at. % Al. The removal of Al and the formation of *np-S* was achieved by dealloying in NaOH at room temperature. The resulting *np-S* had a ligament-pore structure. The size of the *np-S* ligaments decreased from 32 to 13 nm as the Al content increased. Decreasing the ligament sizes of the sponges increases electron scattering, thereby increasing its electrical resistivity. There was a systematic alteration in the optical properties of the *np-S* thin films. As the ligament size decreased and pore density increased, the np-S thin films exhibited less metallic behaviour. These changes culminated in the sponge prepared from the 72.6 at. % Al precursor having non-metallic characteristics about light with a wavelength shorter than about 1110 nm (1.12 eV). Due to the localized surface plasmon resonance and irregular nanostructures, which led to anomalous dispersion and inhomogeneity of light, *np-S* thin films demonstrated anomalous refractive index and decreased light reflectance with decreasing ligament sizes.

The antibacterial performance of the three-dimensional *np-S* thin films with an interconnected, bi-continuous ligament/pore nanostructure was studied against two gram-negative bacteria strains, specifically Pseudomonas aeruginosa (P. aeruginosa) strain of PAO1 and Escherichia coli (*E. Coli*) strain of DH5α. The high *OD* values measured using the microplate reader indicate that the growth of Pseudomonas aeruginosa continued, even with increasing *np-S* thin film coupons to 5, due to the forming of strong biofilms. On the other

hand, a small reduction in the growth rate of Escherichia coli was observed with increasing *np-S* thin films with the smallest ligament size (13.1 nm) with increasing the thin films coupons in the suspension to 5, due to increasing surface area of the thin films which produces more active sites for interaction. Two bacterial growth phases were detected during the 8-h measurement: the lag and exponential phases. Fluorescence images collected after 6 hours of incubation confirmed these findings, showing similar results. The bacterial cells viability decreased from 97±7 % for untreated cells to 87±6% after treatment with *np-S* thin film (ligament size is 13.1 nm).

Gradient composition AgAl alloy thin film has been effectively produced by altering the deposition procedure by applying fixed current to the two deposition guns without sample rotation. Gradient nanoporous thin film (*G-np-S*) was generated using dealloying approaches for the NaOH solution. A broad range of Al compositions between 38 and 81 at. % was obtained, producing gradient nanopore structures with pore and ligament diameters ranging from 12 to 28 nm and 10 to 30 nm, respectively, and increasing pore density with Al content. The thin film racks were observed at positions with Al content between 48 to 81 at.%. The cracks increased in number and width with increased Al content due to volume shrinking during dealloying or residual stress. Increasing the Al content, thereby decreasing ligament and pore size, led to varying the optical response of the material. There was a systematic shift in the optical properties of the sponges towards less metallic behaviour with decreasing pore and ligament sizes. It was observed that the nanoporous Ag film, characterised by a smaller pore size diameter of 12 nm, demonstrated a significantly higher SERS activity compared to the np-S film with a larger pore diameter of 28 nm, with the enhancement factor increase from 3.43×10^6 (ligament size 30 nm) to 3.93×10^7 (ligament size 10 nm). Materials with these properties can be used in many applications, such as waveguides or optical filters.

Heat treatment is the other way to adjust the composition of the alloys and hence the morphology of the nano-sponges. In this section, three-dimensional bulk silver sponges with an interconnected, bi-continuous ligament/pore nanostructure were obtained by chemical dealloying of heat-treated bulk Al_xAg_{100-x} precursors with $x \approx 82$ at. % in 2 M HCl aqueous solution at room temperature. The impact of heat treatment on the nanostructure of the bulk sponges was investigated. It found that increasing the temperature from 350°C to 500°C with the step of 50°C led to an increase in the average pore size from 36 nm to 51 nm and the average ligament size from 31 nm to 59 nm. These pore and ligament sizes are higher than those produced by dealloying the thin film alloy. Testing these bulk ag sponges against *E. coli* DH5α

showed that bulk Ag sponges with large pores 51 and 50 nm and ligament sizes 46 and 59 nm exhibited the highest antibacterial activity compared with sponges with small pore and ligament sizes. The antibacterial performance of the Ag sponges against *E. coli* DH5α showed a direct relationship between bacterial growth inhibition and the concentration of remaining Al-Ag sponges with 9 at. % residual Al inhibited the growth of *E. coli* by 28% after 8-h of treatment, whereas Ag sponges with 20 at. % residual Al inhibited the growth of *E. coli* by only 2.6%.

Generally, nanopore silver sponges with different morphologies, varying pores, and ligament sizes were fabricated. These materials demonstrated unique physical properties compared to their bulk counterparts.

List of tables

List of figures

Table of Contents

Chapter 1 Introduction and aim

1.1 Introduction

The synthesis and control of nanoporous materials have attracted significant attention in materials science due to their remarkable structural properties, including high surface area, tunable pore sizes, and range of applications. Nanoporous silver (*np-S*) is particularly significant among these advanced materials because of its high electrical conductivity, plasmonic properties, and inherent antimicrobial activity. These properties make *np-S* a candidate for diverse applications including catalysis, sensing, energy storage and biomedical devices. However, achieving precise control over the morphology of mesoporous silver remains a significant challenge. This control is important because the material performance is linked to its morphological characteristics.

The ability to control the morphology of mesoporous silver is essential for optimising its properties. The optical properties, which are characterized by the refractive index (*n*) and extinction coefficient (*k*), are influenced by the material's nanostructural features, and in turn affect its performance in applications such as Surface-Enhanced Raman Spectroscopy (*SERS*). *SERS* is an analytical technique that enhances Raman scattering signals and relies on the morphology of silver nanostructures to create "hot spots" where the electromagnetic field is intensified. The capacitance of *np-S*, relevant to energy storage applications, is also dependent on the morphology via the surface area and porosity. Finally, the antibacterial effects of *np-S*, which are of great interest for biomedical and public health applications, are also closely related to the material's surface morphology. Variations in pore size, surface roughness and overall structure can influence the interaction between silver and bacterial cells and alter the material's antimicrobial efficacy.

1.2 Thesis motivation

The overarching motivation of this thesis is to understand how different synthesis conditions can be used to control the morphology of *np-S*, and how these morphological variations impact the material's properties. This aim is systematically addressed through the objectives of each chapter as described below, which contribute to achieve the broader research goal.

Chapter 4 of this thesis focuses on controlling the morphology of *np-S* thin films, including pore size, ligament size, and porosity, by varying the primary alloy compositions during the deposition process. This chapter probes how precursor compositions influence the

morphology of the produced sponges and examines their impacts on optical and electrical properties. The outcomes of this chapter highlight the role of controlling the morphology of the sponges in optimizing *np-S* properties for use in advanced sensing and electrical applications.

Chapter 5 of the thesis investigates the antibacterial performance of *np-S* thin films with controlled structural features. It studies the relationship between the morphology of the nanoporous thin films and their antibacterial properties, showing the importance of using nanoporous materials in biological applications.

Chapter 6 of this thesis introduces a novel deposition technique to create composition gradients, enabling a systematic study of how morphology changes across the substrate under uniform preparation conditions. This chapter also highlights how controlled morphological gradients enhance the ability to link structural variations with SERS activity and optical properties.

Chapter 7 of the thesis provides additional correlations by studying the effect of heat treatment and bulk morphology on the antibacterial performance of the *np-S* sponges.

Addressing these objectives allows us to fill gaps in the current understanding of *np-S* synthesis for the development of more effective and versatile nanomaterials.

The significance of this research extends beyond materials science because it enables potential advancements in the development of high-performance sensors, energy storage devices and antimicrobial surfaces. This research aims ultimately to enhance the utility of *np-S* in these applications by studying how to optimise the morphology.

1.3 Thesis structure

This thesis is structured as follows:

Chapter 2 provides a detailed review of the literature on nanoporous materials with an emphasis on dealloyed silver nanostructures. This chapter discusses the synthesis techniques, characterization methods and applications of *np-S*.

Chapter 3 outlines the experimental methodologies used in this study. It details the synthesis processes used to create thin films and bulk samples of *np-S*, as well as the various characterization techniques used to investigate their structural, optical, electrical, and antimicrobial properties.

Chapter 4 concerns the optical and electrical properties of thin film *np-S*. This chapter explores how different morphologies influence the refractive index, extinction coefficient, and conductivity of the films.

Chapter 5 focuses on the antimicrobial effects of thin film *np-S* with a particular emphasis on the relationship between morphology and antibacterial efficacy.

Chapter 6 presents a systematic study of the composition-morphology relationship in *np-S*, using a gradient composition thin film precursor alloy. This chapter also investigates the *np-S* performance in Surface-Enhanced Raman Spectroscopy (*SERS*).

Chapter 7 explores the properties of mesoporous silver derived from an ingot of precursor alloy after heat treating at different temperatures. The chapter examines the resulting morphologies and their impact on antibacterial activity of the mesoporous silver.

Finally, Chapter 8 concludes the thesis with a summary of the key findings, implications for future research and potential applications of tailored *np-S*. The contribution of this research to the field of materials science, particularly in the areas of nanotechnology and antimicrobial surfaces is also discussed.

Chapter 2 Literature review

2. Overview

Due to the unique combination of silver's (Ag) inherent properties, such as high electrical conductivity, chemical stability, malleability, and antibacterial efficacy; along with its nanoscale sponge-like structures, nanoporous silver (*np-S*), a type of plasmonic nanoporous metal, has gained considerable attention in recent years (Güzel, 2018; Seehra, 2018). The current review of the literature focuses on providing an in-depth overview of the existing knowledge of research on *np-S* prepared by dealloying, with a particular emphasis on the key features that affect its performance, the understanding of its properties, and the applications that rely on its distinctive properties.

2.1 Nanoporous materials (NPMs)

The concept of porous materials (*PMs*) refers to solid materials with porosity ranging from 0.2 to 0.95, representing the proportion of pore volume (V_{pore}) compared to the total volume of the material ($V_{material}$). These materials can be described as nano-sized fluid (gas or liquid) pockets, also known as pores, embedded within a solid matrix called ligaments (Goodall, 2013; Jibowu, 2016). The top-view image in Figure 2.1 illustrates a bicontinuous nanoporous structure of np-S, highlighting nanoscale pores and ligaments with a random size distribution.

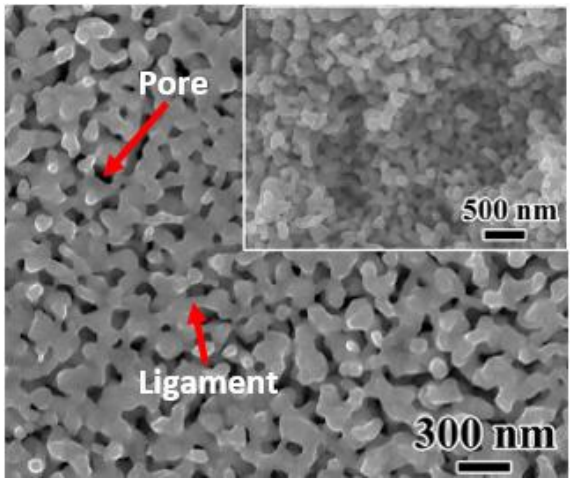

Figure 2. 1 Top-view SEM image of np-S prepared by dealloying $Ag_{45}Mg_{35}Ca_{20}$ metallic glass in 0.05 mol/L HCl. Red arrows indicate the pore and ligament structures produced after leaching out Mg and Ca from the initial alloy (a) acquired at high magnification (300 nm), and (b) at low magnification (500 nm) (Li et al., 2016).

PMs can be grouped into three types according to their pore size: microporous (with pore diameters not exceeding 2 nm), mesoporous (with 2- 50 nm pore diameters), and macroporous (with pore diameters exceeding 50 nm) (Sing, 1985). However, many scientists

do not strictly adhere to these classifications, and the term “nanoporous” has been widely applied in scientific literature with various definitions. Considering this, this thesis will use the nanoporous term synonymous with mesoporous.

Numerous naturally occurring porous structures exist, such as those present in wood, leaves, bones, cotton, and so forth. The presence of pore structures serves specific functions; for instance, it facilitates fluid flow, gas adsorption, heat conductivity and contributes to mechanical stability such as in wood (Plötze & Niemz, 2011). Furthermore, porous materials can be produced artificially, creating structures with tunable pore sizes and distributions that enhance the properties of the materials to meet specific application requirements. These materials include metallic, ceramic, polymeric, and composite types (Beg et al., 2017; Biener et al., 2009; Cousins & Zhang, 2019; Okon et al., 2018). Among all these types of nanoporous materials, metallic nanoporous sponges, especially coinage metals such as gold (Au), silver (Ag) and copper (Cu), have received more attention due to their exceptional electrical conductivity, enhanced catalytic activity, high mechanical strength, and biocompatibility, which makes these material essential in advanced energy, sensor technologies and antimicrobial applications (Zhang & Li, 2012b). Ag has been extensively used in research and industrial applications to fabricate porous material nanostructures because it exhibits superior resistance to corrosion in air and aqueous solutions under atmospheric conditions compared to Cu, and it is more cost-effective than Au (Aromaa et al., 2021; Tang & Zheng, 2018; Zhang et al., 2015; Zhou et al., 2018).

2.2 Fabrication techniques for NPMs and np-S

The production of nanoporous materials with controllable features and architectures is an essential requirement for many applications to maximize their functional potential, such as adsorption, molecular selectivity, sensing, contaminant removal, storage, and release, which rely on their structural properties, particularly the enhanced surface area afforded by their porous architecture (Ariga et al., 2012). Many techniques have been used to prepare NPMs, each tailored to achieve specific structural and functional properties. Generally, two primary approaches dominate the fabrication area of nanomaterials: the top-down and the bottom-up approaches (Abid et al., 2022; Ron et al., 2018). The subsections below will further investigate these approaches, providing an explanation of their theory, benefits, and challenges while emphasizing their usage in preparing nanoporous silver and their applications.

2.2.1 Bottom-up approach

Bottom-up approaches focus on creating sponge-like structures at the nanoscopic scale by reacting or organizing their fundamental components, such as atoms, molecules, or nanoparticles. Techniques such as templating, sol-gel synthesis, surfactant-mediated synthesis, electrodeposition, and self-assembly have been successfully applied to produce NPMs with remarkable versatility and precision (Abid et al., 2022; Biswas et al., 2012; Hemanth et al., 2022; Liu et al., 2011). These methods are promising for fabricating nanoporous materials with unique properties. Among these bottom-up nanofabrication techniques, the templating and self-assembly methods stand out as the most prominent.

2.2.1.1 Template-based method

The template-based method is one of the most common approaches for producing micro to macro-porous materials with high pore uniformity and organization. It involves three main processes, including designing, preparing and filling an organic or inorganic template with well-defined porous structures to enable the creation of the desired nanoporous material. The prepared template is filled with the target materials using an appropriate technique such as physical vapor deposition (PVD), electrochemical deposition, or other comparable methods. Subsequently, the template is removed through chemical etching, calcination, or solvent extraction, resulting in the formation of the nanoporous structure (Ariga et al., 2012; Zhang & Li, 2012b); these processes are outlined in Figure 2.2.

The template-based method has been organized into three guiding frameworks or templates: hard, soft, and multiple. Rigid and pre-designed moulds, such as anodic aluminium oxide (AAO) and mesoporous silica templates, are usually used as hard templates. In contrast, flexible and self-assembled templates, like surfactants, polymers, or micelles, are usually used as soft templates. (Biener et al., 2008; Hemanth et al., 2022; Rebbecchi Jr & Chen, 2018; Zhang & Li, 2012b).

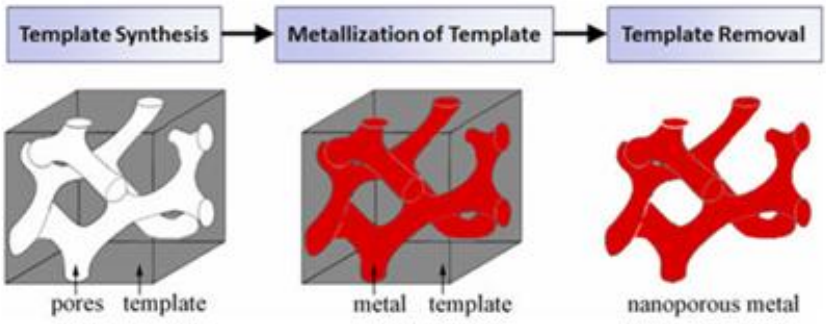

Figure 2. 2 The three main processes that describe the templating- based method to prepare nanoporous materials; these procedures include template preparation, metallization and removal (Rebbecchi Jr & Chen, 2018).

Arrayed *np-S* thin films with well-defined and uniform nanopores have been produced successfully on polymethylmethacrylate (PMMA) and polydimethylsiloxane (PDMS) substrates using AAO templates with pore sizes of 50 nm, 70 nm, and 90 nm were used to create the nanoporous structure. The produced *np-S* thin films exhibited high Surface-Enhanced Raman Scattering (SERS) sensitivity for detecting biomolecules as Rhodamine 6G (R6G) (Zhang et al., 2020). Furthermore, a highly ordered mesoporous silver with a large surface area was prepared using 3D cubic mesoporous silica (KIT-6) with controlled surface hydrophobicity as a hard template (KukáShon et al., 2009).

Despite the remarkable success of this method for preparing nanoporous materials, several challenges limiting its usage have been reported. One major challenge is that it is time-consuming and energy-intensive due to the complexity of the procedure (Chen et al., 2013; Sang et al., 2022). Another challenge lies in the difficulty of removing the template material, which can potentially damage the nanoporous structure or affect the performance of the materials due to residual template material (Wu et al., 2020).

2.2.1.2 Self-assembly method

Self-assembly is a template-free, efficient, and straightforward route for synthesizing porous nanostructures from metal nanoparticles (NPs). This process leverages interactions such as electrostatic forces, van der Waals forces, or specific chemical bonds, as illustrated in Figure 2.3. The method involves controlling various parameters, including the concentration of capping agents, solution pH, and reducing agent concentration, to produce sponge-like structures (Kudernac et al., 2009; Zhu et al., 2015).

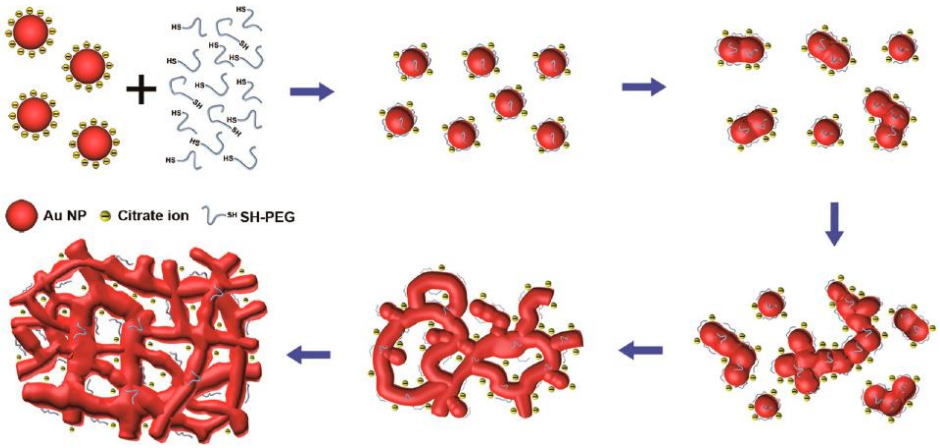

Figure 2. 3 self-assembly method to prepare mesoporous gold sponge from gold nanoparticles (Au NPs); citrate ions are utilized to stabilize the Au NPs during synthesis. At the same time, thiolated polyethylene glycol (SH-PEG) acts as a destabilizing agent that allows the Au NPs to aggregate and self-assemble into sponge-like structures (M.-J. Lee et al., 2016).

The capping agents act as stability agents, anchored to the *NPs'* surface and producing electrostatic repulsion through an electric double layer around each *NP*. This repulsion prevents the particles from aggregating under normal conditions. The force of the electric double layer depends on the ionic strength of the solution. To reduce this repulsive force, excess salts such as halide ions Cl^- or Br^- , which replace the capping agent on the surface of *NPs*, are recommended to be added to increase the ionic strength, hence facilitating coalescence and fusion of particles into sponge-like nanostructures (M.-J. Lee et al., 2016; Zhu et al., 2015).

Liu and co-workers prepared *np-S* structures with high surface area and interconnected networks using the self-assembly of noble metallic spherical aggregates from monodisperse nanoparticles. Citrate ions were used as capping agents to stabilize the silver nanoparticles (Ag NPs), while the evaporation of the organic phase destabilized the colloidal system, promoting nanoparticle aggregation and self-assembly. The *np-S* structures exhibited high SERS activity for sensing and superior catalytic efficiency for chemical reactions (Liu et al., 2013).

Using the self-assembly method for creating sponge-like nanostructures offers significant advantages in simplicity and scalability. However, this method faces many challenges that limit its applicability for preparing nanoporous materials, including the high cost of precursors, difficulty controlling ligament and pore sizes, residual contaminants from capping agents and stabilizers, and requirement for precise optimization and monitoring (Kim et al., 2008; M.-J. Lee et al., 2016; Liu et al., 2013).

2.2.2 Top-down approach

In nanotechnology, the top-down strategy -also known as the destructive approach- describes creating nanostructures by breaking down bulk materials into nanoscale building blocks using physical or chemical methods (Abid et al., 2022). Unlike the bottom-up approach, which builds nanopore structures atom by atom or molecule by molecule, top-down methods use existing materials and reshape them into the desired architecture by removing atoms or introducing porosity. Due to the drawbacks of bottom-up approaches, such as requiring highly controlled environments, complexity in achieving uniform and reproducible results and higher costs in terms of materials and setup, up-down approaches introduce themselves as cost-effective, easy to set up, widely available and high degree of control over the size and shape of the nanostructures (Wang et al., 2022).

The top-down approach can be divided into physical and chemical methods. In the physical methods, physical forces or energy, such as light or ions, are applied to modify the bulk material and generate a nanoporous structure. Laser ablation and ion beam irradiation are

both examples of physical methods (Białous et al., 2016; Miyaji & Nitta, 2017). In contrast, chemical methods employ reactions or selective etching of elements or compounds from bulk materials to generate nanoporous structures such as dealloying (Erlebacher et al., 2001a; Wang et al., 2022; Zou et al., 2018). The following section will delve into the dealloying route, exploring its history, underlying mechanisms, and the factors influencing the dealloying process.

2.2.2.1 Dealloying method

Dealloying is a controllable method for producing 3D nanoporous structures. Among all the methods utilized to produce NPMs, dealloying has proven to be a highly effective method for fabricating nanoporous structures with a randomly porous architecture. This technique offers several advantages, including simplicity, speed, ease of control, cost-effectiveness, and eliminating the need for complex chemical synthesis processes (Liu et al., 2018; Qiu et al., 2011b). It is the method of extracting one component from an alloy system, leaving behind a sponge-like structure formed by the remaining element. It works by leaching out the less stable element in the aqueous solution while the more stable one reorganizes into porous nanostructures (Ding & Zhang, 2016; Liu et al., 2018; Wang et al., 2009b).

As can be seen in Figure 2.4, this method dates back to ancient times when pre-Columbian South American civilizations used depletion gilding to enrich the gold surface of tumbaga, a gold-copper (Au-Cu) alloy. The process involved removing copper (Cu) through a corrosive solution or dissolving oxidized copper formed by heating the alloy in air, giving tumbaga the appearance and shine of pure gold (Au) (Ding & Zhang, 2016; Newman et al., 1999; Sparavigna, 2016). During that period, the formation of porous nanostructures via alloy corrosion was largely speculative due to the limitations of observational techniques. Although Raney nickel was produced from aluminium–nickel (Al-Ni) alloys in the 1920s (Raney, 1940), its microstructure and performance remained insufficiently studied until 1963 when Pickering and Swann employed transmission electron microscopy (TEM) for first time to examine the structure of dealloyed copper-gold (Cu-Au), copper-aluminium (Cu-Al), copper-zinc (Cu-Zn) and magnesium-aluminium (Mg-Al) alloys, thereby revealing the development of nanoporous structures began at grain boundaries (Pickering & Swann, 1963). In 1980, Keir and Pryor used scanning electron microscopy (SEM) to investigate the porous nature of the binary copper-manganese (Cu-Mn) alloys after dealloying in 0.5 M NaCl solution (Keir & Pryor, 1980). The dealloying mechanism of binary alloys, especially silver-gold (Ag-Au) alloys, was clarified

experimentally and by simulation in the 2000s by Erlebacher and co-workers (Erlebacher et al., 2001a).

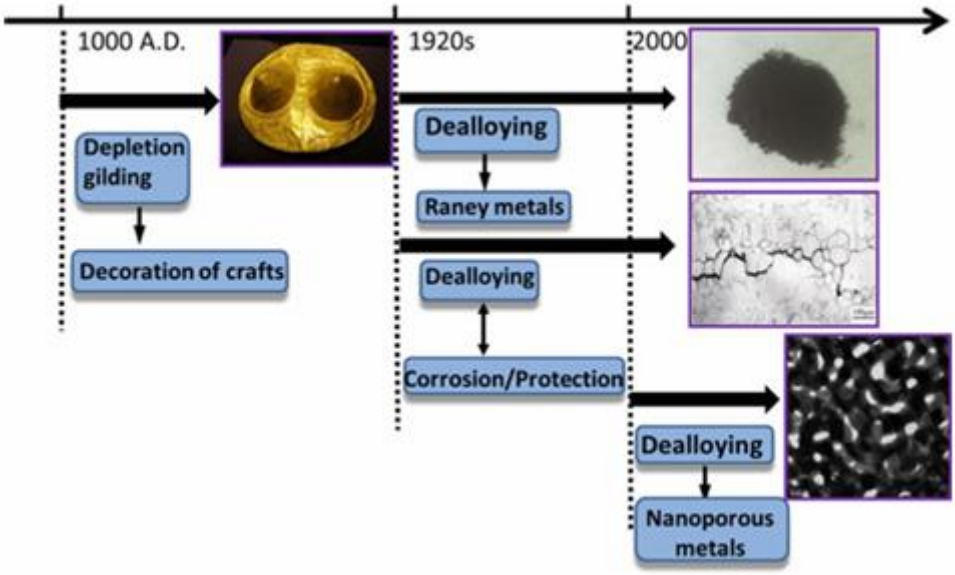

Figure 2. 4 A diagram illustrates the history of dealloying technique and their advancements (Ding & Zhang, 2016).

Designing binary alloys as precursors for effective dealloying

Alloy systems are fundamental components in dealloying processes to form nanoporous materials. *NPMs* can be derived from various binary or ternary alloy systems (Cheng & Hodge, 2014; Xu et al., 2010). In the case of binary alloys, which are the focus of this study, the system typically consists of two elements, and the alloy should possess four essential characteristics (Ding & Zhang, 2016; Erlebacher, 2004; Erlebacher et al., 2001a; Vajtai, 2013):

- ***Difference in galvanic series positions of alloy components***

The galvanic series is a way of listing alloys and metals based on how likely they tend to corrode in a given electrolyte (Gadag & R. V. Gadag, 2010). Table 2.1 below lists the metals in order of their galvanic series, where the metals at the top are the cathodes (positive electrodes), and those at the bottom are the anodes (negative electrodes). Metals with high potential values, located near the top of the series, are typically more noble, passive, and less likely to corrode in the presence of electrolytes. However, for an effective dealloying process, alloys must contain metals with differences in their positions on the galvanic series to drive selective dissolution and hence create the nanoporous structures, as no significant reactions occur between metals close to each other in the series (Campbell, 2008; Chen et al., 2013). When the alloy (built of two different metals) is immersed in the electrolyte, these metals are in electrical contact. Thus, a potential difference will be naturally established, which leads to a

current flow, causing the less noble or more active metal to corrode. In contrast, the more noble or passive metal remains unaffected (Campbell, 2008).

Table 2. 1 Galvanic series of metals relative to hydrogen which has zero potential (Carvill, 2014).

Metal		Potential difference (v)	
Gold	NOBLE	+1.70	CATHODIC
Platinum	↑	+0.86	↑
Silver		+0.80	
Copper		+0.34	
Hydrogen		0	
Lead		−0.13	
Tin		−0.14	
Nickel		−0.25	
Cadmium		−0.40	
Iron		−0.44	
Chromium		−0.74	
Zinc		−0.76	
Aluminium		−1.67	
Magnesium		−2.34	
Sodium		−2.71	
Calcium	BASE	−2.87	ANODIC

Np-S has been fabricated via selective leaching of one or more active elements such as Zn, Cu and Al out of binary Ag-Zn (Li et al., 2013), Ag-Cu (Wang et al., 2019) and Ag-Al (Detsi et al., 2012; Liu et al., 2018; Qiu et al., 2011b; Song, Gao, Zhang, & Zhai, 2011; Wang et al., 2009b), or ternary Ag-Mg-Ca (Li et al., 2016) solid solution alloys which are eventually leading to the formation of three dimensional, bi-continuous and open pore morphologies percolating through ligament structures. Among these alloy systems, the selective etching of Al from Ag-Al alloy has been identified as the most effective rout for producing *np-S*. This may be attributed to the rapid and direct dissolution of Al in acidic and alkaline aqueous solutions which leads to the discharge of proton in acidic solution (1) while the reduction of water to hydrogen is observed in alkaline solution (2) as the following chemical reactions demonstrate (Boukerche et al., 2014; Emregül & Aksüt, 2000).

$$Al_{(s)} + 3\,H^{+}{}_{(aq)} \rightarrow Al^{3+}{}_{(aq)} + 3/2H_{2(g)}\uparrow \quad \text{..... (1)}$$

$$Al_{(s)} + 3H_2O_{(aq)} + OH^{-}{}_{(aq)} \rightarrow Al(OH)^{-}_{4\,(aq)} + 3/2H_{2(g)}\uparrow \quad \text{..... (2)}$$

On the other hand, Ag exhibits high corrosion resistance in both alkaline solutions and acidic solutions at low concentrations (Groysman, 2009). Moreover, the significant potential difference of 2.47 V between Ag (+0.80 V) and Al (-1.67 V), which drives the dissolution process (Qiu et al., 2011b).

- ***High atomic ratio of less noble component of the alloy***

The concentration of alloy components plays a crucial role in regulating the dealloying process. This critical concentration range of the noble metal in the alloy within which dealloying can occur is known as the parting limit. For most binary alloy systems that exhibit nanoporous structure evolution, the parting limit usually ranges between 20 and 60 at.% (Schwarz et al., 2004). When the concentration of the noble metal is excessively high, dealloying is inhibited due to the passivation of the alloy's surface, which is caused by the stability of the noble metal. On the other hand, if the concentration of the noble metal is too low, the remaining noble metal tends to form nanoparticles rather than porous structures, thereby preventing the formation of a nanoporous material. Therefore, the less noble metals component should be the dominant component in the alloy composition (Chen et al., 2013; Ding & Zhang, 2016). In regarding to Ag-Al alloy system, it is found that a critical alloy composition or parting limit of Al-Ag system is approximately 60 at.% Ag (Wang et al., 2009b).

- ***Homogeneous single phase***

Structurally, alloy systems can be classified as single-phase and multi-phase alloys. The single-phase alloys are critical for producing uniform nanoporous structures during dealloying. In single-phase (homogeneous) alloys, the atoms of the added element dissolve together with the host lattice uniformly to form a solid solution, resulting in a predictable and stable structure similar to the parent components' structure as Figure 5.2 (a) illustrates. Therefore, the selective dissolution of the less noble component occurs evenly, forming the connected nanoporous structures. On the contrary, multi-phase alloy systems consist of two or more distinct phases, creating phase boundaries or separation within the alloys, as shown in Figure 5.2 (b). This separation may lead to non-uniform dissolution and inducing cracking during dealloying. Because of this, the preparation of single-phase precursor alloys is essential for an effective dealloying process (Chen et al., 2013; Ding & Zhang, 2016; Schwartz, 2016).

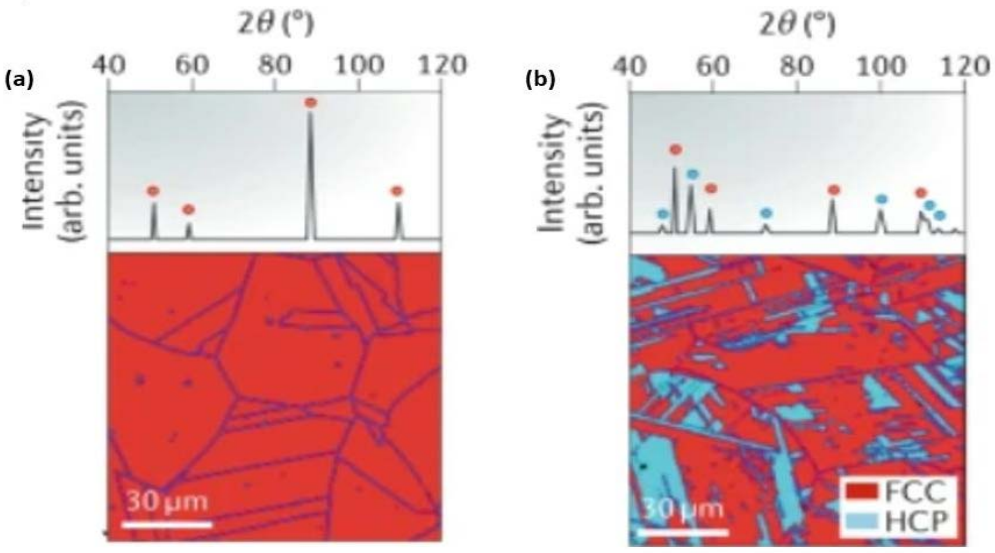

Figure 2. 5 XRD patterns and SEM images of (a) single-phase $Fe_{80-x}Mn_xCo_{10}Cr_{10}$ alloy and (b) multi-phase $Fe_{80-x}Mn_xCo_{10}Cr_{10}$ alloy (George et al., 2019)

- ***High surface diffusion of noble component of the alloy***

Surface diffusion can be described as the migration of atoms, molecules, or clusters along the surface of a solid material. During the dealloying process, the less noble atoms on the surface dissolve and are removed, which creates vacancies as Figure 6.2 shows. Particles of noble component on the surface gain enough energy to overcome potential energy barriers, such as those that arise from atomic bonding, coordination, and interatomic interactions, and move by "hopping" to neighbouring sites, then reorganize into islands. The surface diffusion rate affected by many factors such as crystallographic orientation of the surface, direction of the diffusion, temperature, and interatomic forces. The diffusion rate of the more noble component at the alloy/electrolyte interface must be sufficiently high to avoid the accumulation of that component at the interface, passivate the surfaces, and also to support the formation of nanoscale pores and ligaments (Baboian, 2005; Chen et al., 2013; Laskar et al., 2012).

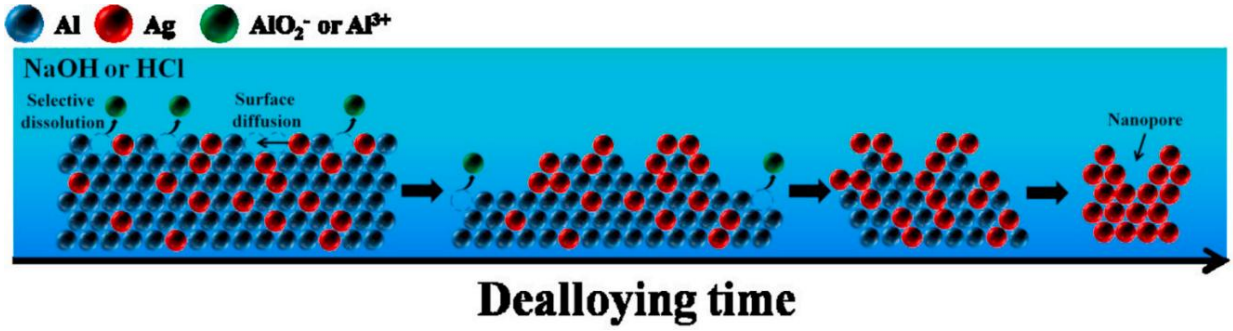

Figure 2. 6 Dissolution of Al atoms and surface diffusion of Ag atoms in an Ag-Al alloy during dealloying in NaOH and HCl solutions. The continued dissolution of the less noble Al atoms leads to the formation of AlO_2 or Al^{+3} in the solution, while the diffusion of the more noble Ag atoms along the surface ultimately results in the formation of nanoporous structures (Luo et al., 2020).

Mechanism of nanoporous formation during dealloying process

The exact physical mechanism behind the nanoporosity evolution during the dealloying process has not yet been entirely understood and clarified. However, many simulation models and numerical solutions have been proposed to explain the formation of nanoporous networks. The most widely used model is a kinetic Monte Carlo model that illustrates the suggested mechanism of dealloying processes of Ag-Au alloy and nanoporosity formation. The model was presented by Erlebacher et al. (Erlebacher et al., 2001a). This model can be applied to most other alloy systems. The dealloying mechanism involves the selective dissolution of less noble atoms (the active component in the alloy) when exposed to acidic or alkaline electrolyte

solutions. These atoms are more reactive and readily dissolve, leaving behind a framework of more noble atoms (the non-active component in the alloy). The remaining noble atoms diffuse along the alloy surface and tend to cluster into islands, rather than remaining as isolated adatoms, which passivates the surface and regulates the dealloying process.

As dealloying progresses, porosity evolves dynamically due to the interplay between the dissolution of less noble atoms and the diffusion and reorganization of more noble atoms. This results in the formation of a three-dimensional bicontinuous nanostructure. Over time, thermodynamic forces drive surface coarsening, where smaller ligaments merge into larger ones to reduce surface energy, increasing the pore and ligament size and stabilizing the porous structure (Erlebacher, 2004; McCue, Benn, et al., 2016). These processes are illustrated in Figure 2.7. The surface diffusivity (*2D*) of the non-active element in the nanoporous is given by (Jing et al., 2024; Qian & Chen, 2007; Zhang et al., 2012; R. Zhang et al., 2019):

$$D_s = \frac{[d(t)]^4 kT}{32\,\gamma t a^4} \quad \text{..... (2.1)}$$

Where *d(t)* is the average ligaments size at the de-alloying time *t* in nm, *k* is the Boltzmann constant (1.3086×10^{-23} J K^{-1}), *T* is the temperature during the de-alloying process in *K*, γ is the surface energy in J m^{-2}, *t* is de-alloying time in *s*, and *a* is the lattice parameter in nm (Y. Yang et al., 2019).

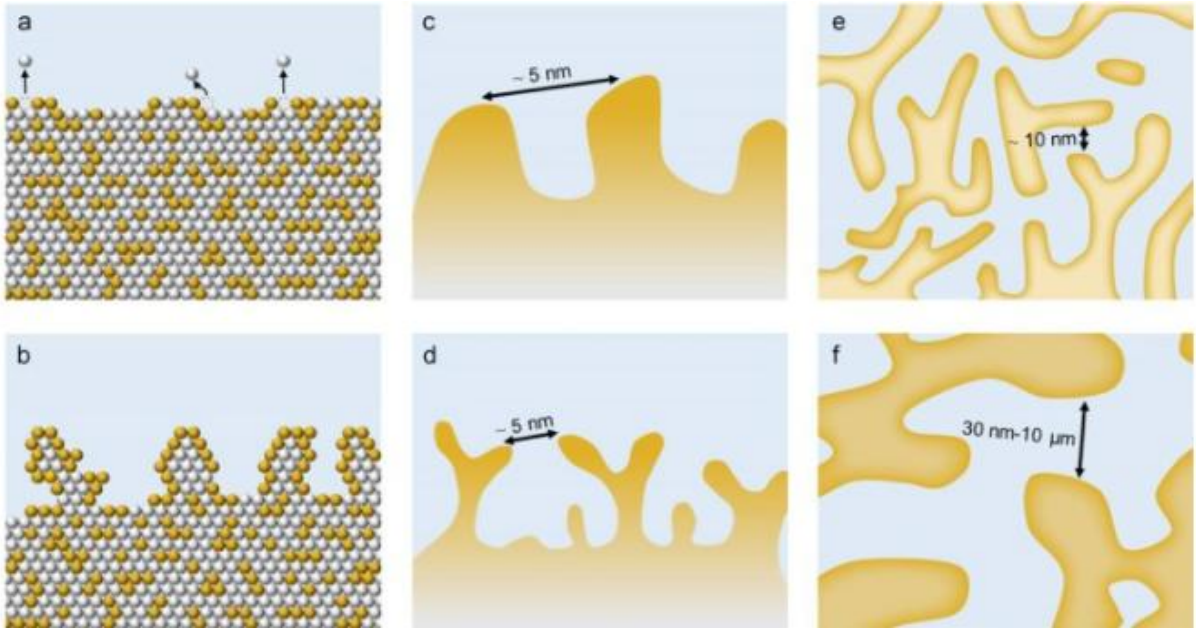

Figure 2. 7 A model illustrates the porosity evolution of an Ag-Au alloy during the dealloying process (orange circles represent Au atoms, while grey circles represent Ag atoms), a) The process begins with the selective dissolution of Ag atoms, creating terrace vacancies on the surface, b) Au atoms diffuse along the surface and cluster, forming stable islands that passivate the exposed regions, c) and d) As dissolution continues, insufficient Au atoms are available to fully passivate the increasing surface area, leading to undercutting and bifurcation of ligaments, e) A nanoporous structure emerges,

characterized by Au-rich ligaments. Initially, some Ag may remain within the ligament interiors, but it is progressively removed during extended dealloying, f) The dealloying process continues with the exposure of ligament interiors to the electrolyte, leading to the dissolution of residual Ag. Over time, this results in coarsening, with an increase in ligament and pore size due to the reduction of surface energy and prolonged dealloying duration (McCue, Benn, et al., 2016).

Factors affecting the dynamics of dealloying process

Many processing parameters affect the dynamics of the dealloying process and the formation of nanoporous structures; the parameters include alloy compositions, electrolyte type, electrolyte concentration, immersion time and temperature (Kurowska-Tabor et al., 2016; G. Li et al., 2021; R. Li et al., 2014; Lim et al., 2020b; Qiu et al., 2011b; Zhang et al., 2012; R. Zhang et al., 2019; R. Zhang et al., 2018).

- ***Alloy composition***

As mentioned previously, the primary alloy systems that form nanoporosity upon dealloying must possess certain properties. For example, these alloys are typically rich in the active component (Zhang & Ying, 2017). It has been observed that a critical alloy composition, or parting limit, for the Al-Ag system is approximately 60 at.% Ag (Wang et al., 2009b).

In this context, increasing the Ag content can result in the diffusion of Ag atoms along the alloy surface during the dealloying process. This may lead to surface passivation, which impedes the movement of the electrolyte solution into the bulk of the alloy. As a result, the Al atoms are protected from corrosion, thereby hindering the evolution of nanoporosity (Chauvin et al., 2016).

A recent study by Chauvin et al. (Chauvin et al., 2016) provides clear evidence supporting this phenomenon. Their findings indicate that a highly porous film was formed after dealloying an Al-Ag alloy with an initial Ag content of 23 at.% in 2 wt.% HCl for 20 min. Similarly, when the initial Ag content was 40 at.%, the resulting dealloyed film exhibited a fully porous Ag structure. In contrast, at a higher initial Ag content (50 at.% Ag), no significant porosity was observed. These results are illustrated in Figure 2.8.

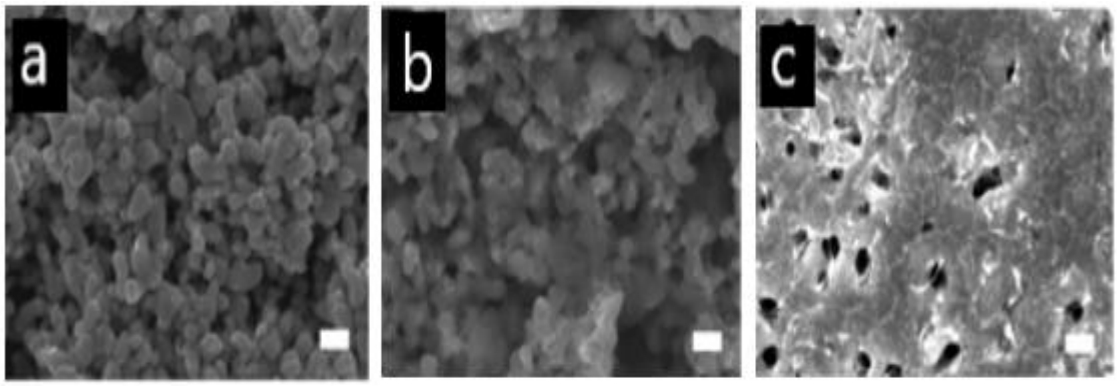

Figure 2. 8 top-view SEM images for np-S prepared by de-alloying of a) Al- 23 at.% Ag, b) Al- 40 at.% Ag, and c) Al- 50 at.% Ag in 2 wt.% HCl for 20min. Scale bar:100nm (Chauvin et al., 2016).

However, within the appropriate composition range, alloy composition significantly influences the size of pores and ligaments (Mokhtari et al., 2018). Experimentally, dealloying AgAl alloys with varying Ag content, ranging from 15 to 50 at.%, in 20 wt.% NaOH at room temperature (Wang et al., 2009b), and AgAl alloy thin films with Ag concentration from 30 to 56 at.% in 1 M HCl (Zeng et al., 2023) showed the same trend. The ligament sizes of the resulting *np-S* structures increased progressively with higher Ag content, as demonstrated in Table 2.2 (Wang et al., 2009b). This correlation highlights how the precise control of alloy composition can be leveraged to tune the structural characteristics of dealloyed materials.

Table 2. 2 Impact of changing the AgAl starting alloys compositions on the ligament size after de-alloying into 20 wt% NaOH at room temperature (Wang et al., 2009b)

Alloy composition (Al- at.% Ag)	**15**	**20**	**25**	**30**	**35**	**40**	**45**	**50**
Ligament size (nm)	94±5	109±5	111±5	230±10	207±11	258±15	228±16	448±25

- ***Type of the electrolyte solution***

Beyond the initial alloy composition, the type of electrolyte used during the dealloying process plays a significant role in tuning nanoporous structures. The interactions between alloy atoms, and electrolyte ions influence the dissolution and diffusion of alloy components, which are critical for porosity evolution. Therefore, selecting an appropriate electrolyte is a key parameter for the success of the dealloying process (Vajtai, 2013).

In the case of Ag-Al precursors, dealloying has been conducted in acid-based electrolytes such as oxalic acid ($H_2C_2O_4$) (Liu et al., 2018; Song, Gao, Zhang, & Zhai, 2011), phosphoric acid (H_3PO_4) (Song, Gao, Zhang, & Zhai, 2011), sulfuric acid (H_2SO_4) (Song, Gao, Zhang, & Zhai, 2011), and hydrochloric acid (HCl) (Cheng & Hodge, 2014; Detsi et al., 2012; Liu et al., 2018; Qiu et al., 2011b; Song, Gao, Zhang, & Zhai, 2011; Wang et al., 2009b; Xu et al., 2010), as well as in alkaline aqueous solutions like sodium hydroxide (NaOH) (Cheng & Hodge, 2014; Liu et al., 2018; Qiu et al., 2011b; Wang et al., 2009b; Xu et al., 2010). It is found that dealloying in alkaline treatments often results in a narrower pore size distribution compared to acidic treatments (Lin et al., 2014).

For example, previous research demonstrated that a uniform *np-S* structure with a small ligament size of 30 nm could be formed using a 1 M NaOH solution to dealloy an $Ag_{23}Al_{77}$ (at.%) alloy at 30°C for 72 h (Xu et al., 2010). This uniformity may be attributed to the formation of Ag(OH) or Ag_2O layers at the alloy/electrolyte interface, which can inhibit both

the diffusion of Ag atoms and the dissolution of Al atoms (Xu et al., 2010; Zhang et al., 2009). On the contrary, using a 1 M HCl solution produced a much less uniform *np-S* structure with a wider ligament size distribution ranging from 200 nm to 300 nm (Xu et al., 2010). This divergence may result from the adsorption of chloride anions (Cl^-), which accelerates the diffusion of Ag along the interface and enhances the corrosion of Al, leading to a coarser nanoporous structure with larger ligament and pore sizes (Qiu et al., 2014; Xu et al., 2010; Zhang et al., 2009). Additionally, Cheng and Hodge reported that *np-S* prepared by chemical dealloying of $Ag_{25}Al_{75}$ in 1 M NaOH exhibited greater thermal stability compared to *np-S* dealloyed in 5 wt% HCl (Cheng & Hodge, 2014). Even when using two acid electrolytes, different nanopore structures can be produced. Yang et al. (Yang et al., 2022) reported that *np-S* with coral-like ligaments 55.6 nm in size formed when the $Mg_{82.43}Ag_{17.57}$ alloy was dealloyed in tartaric acid due to slower dissolution and extended diffusion. In contrast, granular ligaments with the size of 16.8 nm were observed when the alloy was dealloyed in citric acid due to aggressive etching and limited diffusion.

- ***Concentration of the electrolyte solution***

To selectively remove the more active component, dealloying must be conducted at an appropriate electrolyte concentration. Studies have shown that dealloying in lower electrolyte concentrations slows the process, preventing the complete formation of a nanoporous structure (Qiu et al., 2014; Stuckner et al., 2020). On the other hand, higher electrolyte concentrations can reduce the uniformity of the nanoporous structure (Bekana et al., 2019) and induce significant coarsening of ligaments (Jin et al., 2017).

For example, Xu et al. (Xu et al., 2010) reported that chemical dealloying of an $Ag_{23}Al_{77}$ (at.%) alloy in a 1 M NaOH solution for 72 h produced ligaments with an average size of approximately 30 nm. When the NaOH concentration was increased to 2 M and dealloying was conducted for 48 hours, the resulting *np-S* exhibited a characteristic ligament length scale of 40 nm. A similar trend was observed during the dealloying of an $Ag_{60.5}Ca_{39.5}$ (at.%) alloy in HCl solutions of varying concentrations, as shown in Table 2.3 (Jin et al., 2017).

Table 2. 3 Impact of changing the HCl concentration on the ligament diameters of np-S formed by de-alloying $Ag_{60.5}Ca_{39.5}$ (at.%) alloy at room temperature (Jin et al., 2017).

HCl concentration (M)	$\mathbf{1 \times 10^{-3}}$	$\mathbf{1 \times 10^{-5}}$	**0.01**	**0.05**	**0.1**	**0.2**
Ligament size (nm)	37±6.5	38.3±6.6	61.1±9.2	74.9±9.2	81.5±8.5	89.6±8.9

- ***Immersion time***

Leaching time plays a significant role in tuning and controlling ligament size and specific surface area. As immersion time increases, the distribution of ligaments and pores

becomes larger and more uniform. This effect is attributed to the high diffusivity of the non-active component at the electrolyte/alloy interface, which remains significant even at room temperature (Chen et al., 2013). This allows the formation of complete and uniform nanoporous structures.

The relationship between immersion time and ligament size can be described using equation below. With extended dealloying duration, coarsening behavior is observed due to the continued surface diffusion of the non-active component (Chen et al., 2013). However, long immersion may result in nanoporous structures with surface irregularities (Bekana et al., 2019).

$$d^n = KtD_s \ldots\ldots\ldots\ldots\ldots\ldots (2.2).$$

Here, *d* represents the ligament size, *n* is the coarsening exponent, *K* is a constant, *t* is the dealloying duration, and *Ds* is the surface diffusivity of the non-active component (Jin et al., 2017).

For example, dealloying an $Ag_{23}Al_{77}$ (at.%) alloy in a 2 M NaOH solution at 30°C for varying durations (12, 24, and 48 h) resulted in a porous Ag morphology with increasing ligament sizes of approximately 15, 30, and 40 nm, respectively, as illustrated in Figure 2.9 (a and b) (Xu et al., 2010). Additionally, the influence of immersion time on pore diameters was investigated by Chauvin et al. (Chauvin et al., 2016). Their results revealed a significant increase in pore size in np-Ag films formed from Al-23 at.% Ag, Al-40 at.% Ag, and Al-50 at.% Ag alloys after dealloying in 2 wt.% HCl for 5, 10, and 20 min. However, in the case of Al-50 at.% Ag, the pore size became constant after 10 min of leaching time due to surface passivation.

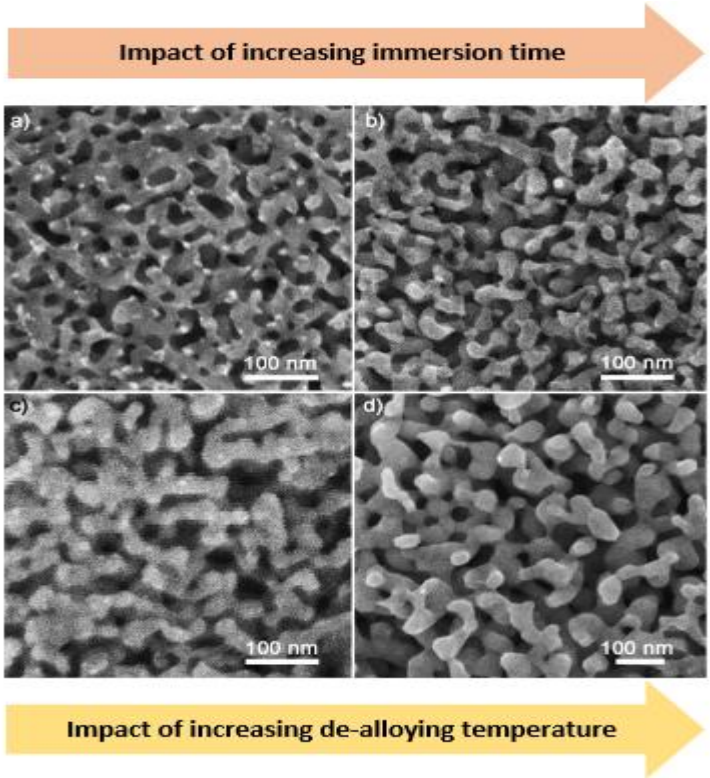

Figure 2. 9 Top-view SEM images demonstrating the impact of increasing dealloying time and temperature on the formation of np-S during the dealloying of $Ag_{23}Al_{77}$ (at.%) alloy in 2 M NaOH solution at 30°C. The images correspond to (a) 12 h, (b) 24 h, (c) 48 h, and (d) 40°C for 48 h (Xu et al., 2010).

- ***Temperature***

The evolution of nanoporous structures is strongly influenced by the dealloying temperature. Smaller pore sizes are typically formed at lower dealloying temperatures due to the reduced diffusion rates of noble metals during the process (Chen et al., 2013).

For instance, Xi et al. (Xu et al., 2010) experimentally demonstrated that dealloying an $Ag_{23}Al_{77}$ (at.%) alloy with a thickness of 50 µm in NaOH solution at 30°C for 48 h produced *np-S* with a ligament size of 40 nm. However, increasing the dealloying temperature to 40°C for the same duration resulted in *np-S* with an average ligament size of 70 nm, as illustrated in Figure 2.9 (c and d). A similar trend was observed by Jin et al. (Jin et al., 2017) for the $Ag_{23}Al_{77}$ (at.%) alloy system dealloyed in water. Their results showed that the ligament diameters increased from 29.8 ± 6.2 nm to 52.0 ± 8.6 nm when the temperature was raised from 303 K to 353 K, respectively. Sun et al. (Sun et al., 2024) observed that the ligament morphology of *np-S* prepared by dealloying $Mg_{82.43}Ag_{17.57}$ alloy at different temperatures of 298 K, 333 K, and 363 K for 10 h developed gradually from granular to coral-like structures as the temperature increased. Additionally, the ligament size increased from 16.8 nm, 45.7 nm, to 55.63 nm, while pore size decreased from 0.36 µm, 0.27 µm, to 0.21 µm.

Although there are many studies that have focused on preparing *np-S* through the dealloying of Ag-Al alloys and investigating the effects of preparing and dealloying conditions on its microstructure, research on the impact of alloy composition on the structure and properties of *np-S* remains limited. A closer look at the literature reveals that most of these studies have examined *np-S* derived from Ag-Al alloys with Ag concentrations of 50 at.% or less, leaving the influence of higher Ag content largely unexplored. It is expected that increasing the Ag content will alter the microstructure of the sponge, thereby affecting pore/ ligament sizes and its surface area, which leads to produce coarser surface or more interconnected structures as a result of differences in dealloying kinetics and Ag diffusion. These structural changes can improve properties such as electrical conductivity and mechanical stability, which make this kind of *np-S* highly promising for functional and structural applications like energy storage, catalysis, filtration and sensing. Therefore, considering a wider range of Ag compositions in the parent alloys is essential for unlocking new possibilities.

2.3 Applications of *np-S*

Owing to their unique characteristics such as corrosion resistance, enhanced chemical reactivity, improved thermal conductivity, low density, high adsorption capacity, biocompatibility and so on. which are attributed to their high surface area to volume ratio, bi-continuous interconnected ligament-void architecture and nano-size structures, nanoporous metals have been employed widely in many applications ranging from energy storage and generation, catalysis, sensing, advanced material design to medical devices, among others (Barsuk et al., 2016; Chaloupka et al., 2010; Jing et al., 2024; R. Li et al., 2015). The following section will focus on providing information about the use of *np-S* as surface enhanced Raman substrates, supercapacitors, catalysis, and biomedicine.

2.3.1 Np-S as a surface enhanced Raman scattering substrate

The first Raman scattering was observed in the 1920s by Indian scholar C. V. Raman. Raman scattering occurs when monochromatic light of a fixed photon energy interacts with molecules in a material, two scattering processes can be observed as a result of the interaction. One of these scattering is Rayleigh scattering (also known as elastic scattering), which results from elastic collisions between light photons and particles. In this scattering, the scattered light has the same wavelength as the incident light. The other scattering is Raman scattering, undergoes inelastic scattering, which is due to energy differences that occur when light photons interact with particles, leading to a change in the molecules' vibrational or rotational energy levels. There are two types of Raman scattering; Stokes scattering is observed when the scattered light has lower wavelength, whereas anti-Stokes scattering is detected when the scattered light has higher wavelength (Liu et al., 2022). The two scattering processes are shown in Figure 2.10 a. The Raman shift can be determined as the difference between the energy of the incidence rays to the energy of scattered rays, as shown in Figure 2.10 b. Figure 2. 10 b shows that the stronger intensity Raman scattering signal is the Stokes-Raman. Therefore, the presented Raman spectra usually are Stokes bands. Nevertheless, the signal of this scattering is very weak compared to the fluorescence signal by a factor of 10^6 to 10^{10}. To enormously amplify the Raman signal, molecules should be placed near the surface of suitably nanostructured substrates, thereby the enhanced Raman scattering is known as surface-enhanced Raman scattering (SERS) (Pilot et al., 2019)

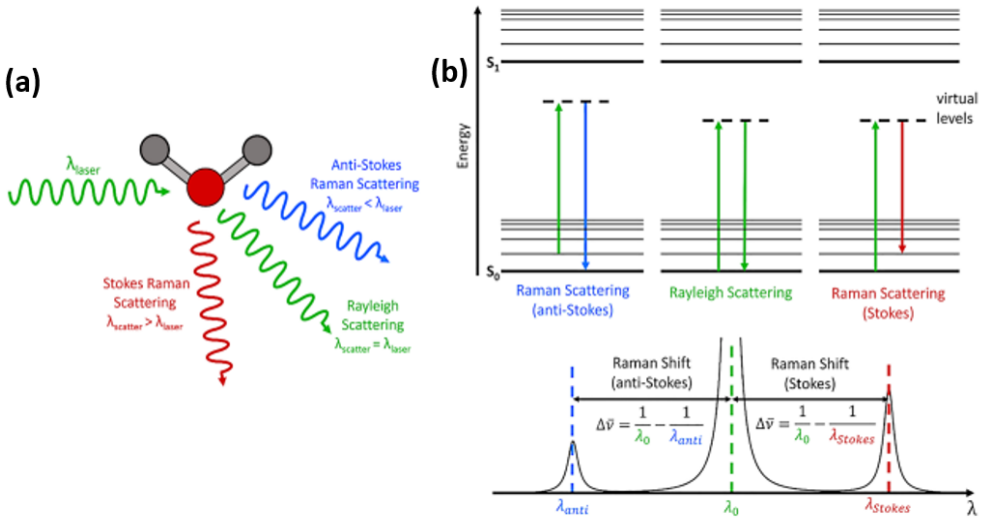

Figure 2. 10 (a) elastic and inelastic scattering occur during the interaction between incidence rays and molecules, (b) Raman shift between two levels with different energy (Dey, 2023).

Surface-Enhanced Raman Scattering (SERS) is a very sensitive and sophisticated spectroscopic technique that enhances molecules' Raman signals by adsorbing them on metallic nanostructures. It permits the detection of small quantities of substances. The SERS technique is widely used in biosensing, chemical warfare agent detection, food safety, pollution monitoring, and other fields (Li et al., 2019) (Jayram et al., 2015) (Chi et al., 2020; Nowak et al., 2019). One of the fundamental concepts behind this sensor is using localized surface plasmon resonance (LSPR), which enhances the intensity of a local electromagnetic field (or hot spots). The LSPR is produced when electromagnetic radiation is confined within metallic nanostructures smaller than the wavelength of light. The occurrence is a consequence of the interactions between the incident rays and the surface electrons located in a conduction band (Asane et al., 2018; Capaccio et al., 2021; Chen et al., 2011; Detsi et al., 2014; Ruffato et al., 2011; Sardana et al., 2014). This interaction results in coherent localized plasmon oscillations, which have a resonant frequency highly dependent on the dimensions, morphology of nanostructures, and the dielectric function of the medium. The nanoscale surface of the metal must be rough/fractal to achieve the local field EM (Barbillon et al., 2007; Bryche et al., 2016; Faure et al., 2008). The second concept behind the enhanced SERS is related to a charge transfer process that occurs when probe molecular and metallic orbitals combine, which lowers the energy of the resonant molecular Raman compared to the energy of the free molecule, which in turn causes a chemical effect (Le Ru et al., 2007; Sur & Chowdhury, 2013; Tian et al., 2002). These two enhancement mechanisms are demonstrated in Figure 2.11.

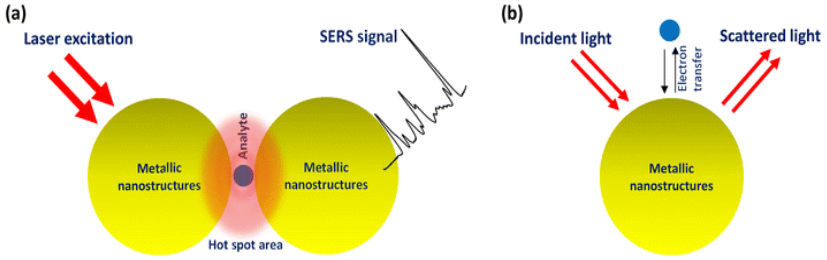

Figure 2. 11 Diagram depicting the two mechanisms for enhancing Raman signals, (a) the electromagnetic field enhancement mechanism, and (b) the chemical enhancement mechanism (Hassanain et al., 2022).

Np-S prepared by template-based method and lithography process exhibited intense Raman enhancement with EF around 10^6; the intensity of the Raman signal diminished as the width of the pores increased, possibly because the electric field was reduced (Capaccio et al., 2021; Zhang et al., 2020). *Np-S* made by dealloying a precursor alloy is one promising material for high-potential SERS substrates. A two-step dealloying process carried out by Qiu et al. (Qiu et al., 2011b) using melt-spun $Ag_{30}Al_{70}$ alloys resulted in np-S substrates with small pore sizes between 80 and 190 nm and less Al residues, leading to enhanced SERS performance with EF about ~7.5×10^5. The dealloying process was carried out at room temperature and 85 °C. Nevertheless, By electrochemically dealloying Ag-Mg-Ca ribbons, Li et al. (R. Li et al., 2014) created nanoporous Ag with pores ranging from 25 to 61 nm in size, and they studied the process and evolution of porosity. Compared to nanoporous gold and copper, the enhancement factors of nanoporous Ag for SERS substrates are higher, suggesting that these glasses benefit SERS substrates (Table 2.4 provides more instances of previous work).

Table 2. 4 Previous research on np-S films as a substrate for SERS

R	Year	Preparation method	Probe molecule	Concentration	Laser wavelength, nm	Laser power	Pore size, nm	Raman band, cm^{-1}	EF
(Qiu et al., 2011b)	2011	Dealloying of $Ag_{30}Al_{70}$ at RT and then aging at 85°C	R6G	10^{-5} M	633	changeable	80-190	1366	~7.5×10^5
(R. Li et al., 2014)	2014	Electrochemical dealloying of $Ag_{40}Mg_{40}Ca_{20}$ $Ag_{50}Mg_{35}Ca_{20}$ $Ag_{40}Mg_{30}Ca_{20}$ $Ag_{55}Mg_{25}Ca_{20}$ $Ag_{60}Mg_{20}Ca_{20}$	R6G	10^{-3} mol L^{-1}	532		 33 49 61 39 25	1650	 ~7.6×10^8
(Vantasin et al., 2016)	2016	In-place galvanic reduction of a AgCl template	PATP	10^{-3} M	532	0.01 mW	60	1075	~2.5×10^6
(Ma et al., 2016)	2016	O_2 plasma treatment	4-MBA	10 mM	633	0.56 mW	100	1590	~6×10^6
(Lawanstiend et al., 2018)	2018	Reduce the AgCl template into np-AgMSs by chemical reduction	PATP	10^{-6} M	532	1 mW	38-133 33-134 40-65	2117	
(Bekana et al., 2019)	2019	Dealloying of Ag/α-Fe_2O_3 nanocomposite In 0.01 M HCl 0.01 M H_2SO_4	R6G	10^{-9} M	532	5μW	 73 51	1650	 ~7.5×10^6

(Zhang et al., 2020)	2020	Template-assisted sol–gel inverse-imprinting of Ag on polydimethylsiloxane (PDMS) substrates	R6G	10^{-6} mol L^{-1}	532		90	614	~10^6
		Template-assisted sol–gel inverse-imprinting of Ag on nanoporous anodic aluminum oxide (AAO	R6G	10^{-6} mol L^{-1}	532		90	614	~10^5
(Lim et al., 2020a)	2020	Self-assembled polymeric micelles	R6G	10^{-5} M	785	22 mW	11.1 26.7	1361	~10^4 to 10^5
(Cao et al., 2020)	2020	Self-assembly of AgNTs onto a GNP tip	MBN	0.1 M	633	1.7 mW	30- 50	2230	~4.8×10^5
(Capaccio et al., 2021)	2021	Inductively Coupled Plasma (ICP)	4-MBA	10^{-6} M	532	10 µW	30	1575	~6.5×10^7
(Zeng et al., 2023)	2023	Dealloying of $Ag_{30}Al_{70}$ $Ag_{46}Al_{54}$ $Ag_{56}Al_{44}$	R6G	10^{-6} M	532		85 51 246	615.8	~1.58×10^5

Despite these many studies that have focused on employing np-S as Raman substrates, most have relied mainly on conventional sample preparation methods that involve separate processing steps, leading to inconsistencies. Those methods neglect the advantages of a continuous gradient structure of the sponge, as pore and ligament sizes vary systematically. Investigating SERS performance on such a sponge-like structure enables a more accurate and comprehensive understanding of the relationship between microstructure and Raman signal enhancement, leading to more reliable and comparable results.

2.3.2 Np-S as a supercapacitor

A supercapacitor (SC) is one of the electrochemical energy storage devices with a distinctive integration of high power density which reaches up to 10 kW/kg for short time, fast reversibility and long cycle life as compared to batteries and conventional capacitors (Crawley, 2017; R. Li et al., 2015; Qiu et al., 2015). Supercapacitor typically consists of three main internal components as Figure 2.12 shows: two electrodes, a separator, and an electrolyte. The two electrodes in the supercapacitor are made of a material with a high surface area, high electrical conductivity and high electrochemical stability (Sang et al., 2022). The separator plays a significant role in preventing direct contact between the two electrodes and enables the transit of ions through the separator to the electrodes. The electrolyte is used as an ionic conductor, facilitating ion diffusion during charge and discharge cycles (Gulzar et al., 2016). The capacitance range of supercapacitors is between 100- 1000 F higher than that for the conventional capacitors, which is between micro to millifarads (Forouzandeh et al., 2020).

The performance of the supercapacitors can be evaluated by testing the two main parameters: energy density and power density. The energy density E refers to how long an energy storage device can provide power, and it can be written as following expression:

$$E = \frac{1}{2}CV^2 \ldots\ldots\ldots\ldots\ldots\ldots (2.3)$$

Whereas the power density P implies how quickly the device can deliver energy, it can be given as.

$$P = \frac{1}{4}\frac{V^2}{R_S} \ldots\ldots\ldots\ldots\ldots\ldots (2.4)$$

Where C is the capacitance, V is the applied voltage and R_s is the capacitor resistance (Gulzar et al., 2016).

Based on the energy storage mechanisms in supercapacitors, SCs can be classified into two types: electric double-layer capacitors (EDLCs) and pseudocapacitors. In the EDLCs, and under the influence of an applied voltage to the supercapacitor electrodes, the charges are accumulated on the electrode surface, and the positive and negative ions in the electrolyte spontaneously move towards the opposite-charged electrodes, as shown in Figure 2.12 b. This leads to a double charge layer at the electrode/electrolyte interface, which stores the charges electrostatically without a faradaic reaction. The charge storage and transfer mechanism in the EDLCs is identical to that of conventional electrostatic capacitors. However, the EDLCs exhibit exceptionally high capacitance due to the narrow separation between the double layers and the large contact area at the electrode/electrolyte interface compared to conventional electrostatic capacitors (Ates, 2016; Qiu et al., 2015; Yue & Liang, 2015). The capacitance of EDLCs is affected by the surface area of the electrodes available for reversible ions adsorption and the conductivity of the electrodes, which influence the transport of electrons and ions (Gulzar et al., 2016).

On the other hand, applying an electric potential to the cathode (negative electrode) and anode (positive electrode) of pseudocapacitors leads to oxidizing the positive electrode, which means it loses electrons, and reducing the negative electrode, which means it gains electrons. To balance the differences in the charges at the electrodes, positive ions in the electrolyte move towards the cathode to neutralize the gained electrons, whereas negative ions migrate towards the anode to balance the loss of electrons, as demonstrates in Figure 2.12 c. Therefore, the charge storage and high capacitance in pseudocapacitors are achieved through fast, reversible (reduction/oxidation) redox reactions at the surface or near-surface of the electrodes (Crawley, 2017)

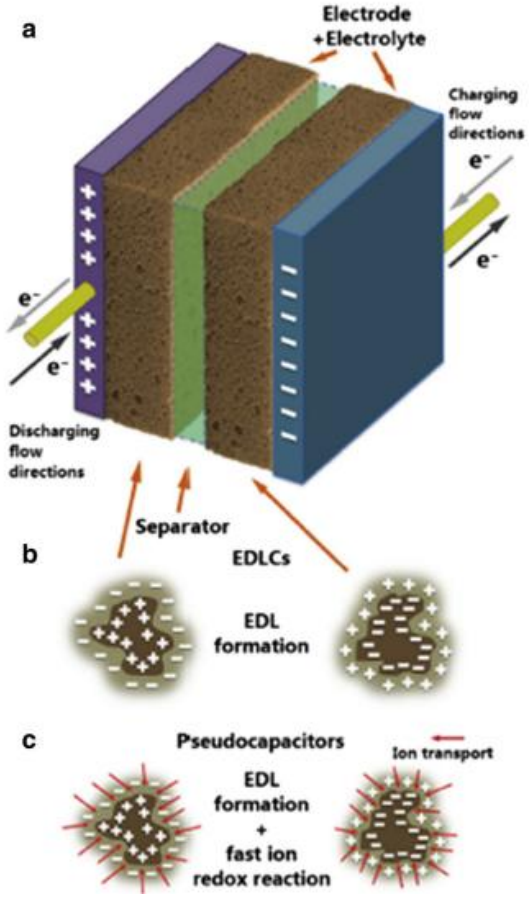

Figure 2. 12 Schematic sketches showing (a) the typical components of a supercapacitor, including the electrodes, separator, and electrolyte; (b) the charge storage mechanism in a double-layer capacitor; and (c) the charge storage mechanism in a pseudocapacitor (Yue & Liang, 2015).

The third type of supercapacitor is the hybrid supercapacitor, which combines both energy storage mechanisms: non-faradaic and faradaic reactions. The energy density of this type of supercapacitor is enhanced without a significant loss in rate stability or cycling capability (Crawley, 2017).

Nanoporous silver (np-S), with high surface area, porosity, and electrical conductivity, has become an ideal candidate for use as a supercapacitor electrode. Numerous studies have been conducted to evaluate the performance of np-S as an electrode in supercapacitors. Most of these studies investigate the influence of depositing metal oxides on the np-S electrode to produce metal oxide-based pseudocapacitors with improving capacitance, increasing energy density, and enhancing cycle life stability. For example, Np-Ag@Fe_2O_3 with ligaments and pore sizes ranging from 50 to 300 nm, which was prepared by electrochemical reduction of AgX to produce Np-Ag followed by the deposition of Fe_2O_3 onto the silver framework, demonstrated a capacitance of 608 F/g, with a retention of 84.9% after 6000 charge/discharge cycles (Seok et al., 2018). On the other hand, NPS@MnO_2 composites, which were prepared via the electrochemical dealloying of $Ag_{45}Mg_{35}Ca_{20}$ followed by electroless plating of

nanocrystalline MnO_2 onto the silver structure, exhibited a significantly high capacitance 1088 F/g (R. Li et al., 2015).

2.3.3 Catalysis

A catalyst is a material that accelerates and enhances the rate at which a chemical reaction reaches equilibrium while retaining its original composition and quantity, without undergoing any permanent chemical change. Due to their large surface-to-volume ratio, controlled feature sizes, high active sites, high thermal and electrical conductivity, and low density, nanoporous metals as green and environmentally friendly catalysts (Bao et al., 2024; Chaturvedi et al., 2012; Zhang & Li, 2012a). Generally, the catalysis cycle can be summarized in three main steps. In the first step, gas or liquid molecules adsorb onto the active sites on the surface of a catalyst. The adsorbed reactant molecules interact at the surface, generating products. Finally, the produced products desorb at the catalyst's surface, regenerating the active sites for further reactions (Scandura et al., 2023).

Np-S has been used as a versatile and highly efficient catalyst for various applications, such as CO oxidation, anodic catalysts in fuel cells, organosilane oxidation, and CO_2 reduction (Barsuk et al., 2016; Dong et al., 2015; Kou et al., 2014; Z. Li et al., 2014; Qian et al., 2020). Kou et al (Kou et al., 2014). studied the catalytic activity of unsupported np-S prepared by dealloying $Mg_{77}Ag_{23}$ alloy for CO oxidation. The nanoporous structures support gas-phase reactions, contributing to high catalytic activity. However, catalytic performance is influenced by factors such as pore/ligament sizes and dealloying parameters. *Np-S* foils prepared by dealloying ternary $Ag_{38.75}Cu_{38.75}Si_{22.5}$ alloy have been tested as an anodic catalyst in direct ammonia-borane fuel cells. The results indicated that the prepared *np-S* foils show excellent stability over long-term operation, with no significant structural degradation observed, which displays the suitability of *np-S* for alkaline fuel cells (Barsuk et al., 2016). Li et al. (Z. Li et al., 2014) have utilized *np-S* for the selective oxidation of organosilanes ($R_{(4-n)}SiH_n$) by water or alcohols to produce the corresponding organosilanols ($R_{(4-n)}Si(OH)_n$) and organosilyl ($R_{(4-n)}Si(OR^4)_n$) ethers as the following chemical reactions show, respectively. The *np-S* catalyst demonstrated high efficiency and reusability, with H_2 as the only by-product, which emphasizes the potential of *np-S* for green chemistry applications.

$$R_{(4-n)}SiH_n + nH_2O \xrightarrow{np-S} R_{(4-n)}Si(OH)_n + nH_2$$

$$R_{(4-n)}SiH_n + nR^4OH \xrightarrow{np-S} R_{(4-n)}Si(OR^4)_n + nH_2$$

The electrocatalytic reduction of CO_2 to CO has been a key area of research for *np-S*. Zhang et al. (Y. Zhang et al., 2019)investigated the effect of halide ions such as F^-, Cl^-, Br^- and I^- on the catalytic performance of *np-S*; their results confirmed that the presence of halide ions can enhance the binding energy of intermediates, lowering the overpotential required for CO_2 reduction and improving Faradaic efficiency. On the other hand, Shi and his co-workers studied the impact of using the surfactant sodium dodecyl sulfate (SDS) to modify the properties of *np-S*; they found that the SDS-modified np-S electrode (C-AgNPs-SDS) showed superior performance in the selectively electrocatalytic reduction of CO_2 to CO with a Faradaic efficiency of 92.2% better than the Ag foil and the nanoporous Ag electrode (C-AgNPs) (Shi et al., 2019).

2.3.4 Biomedicine

Biocompatibility, which describes the ability of a material to meet its designated purpose without triggering any harmful effects on biological systems, as well as low toxicity to mammalian cells, are essential properties for materials used in biomedical applications (Suhag et al., 2024). Nanoporous metals, especially nanoporous gold (*np-G*) and *np-S*, which exhibit large surface-to-volume ratios, controllable nanopore structures, and excellent chemical stability, are the most suitable materials for use in medical applications. Research has shown that, when properly engineered, these metals in their sponge-like structures generally do not cause immune reactions, inflammation, or cytotoxic effects on mammalian cells, which makes them promise for use in many biomedical applications, like drug delivery, biosensing, and wound healing, careful design should be considered to reduce potential issues such as silver ion (Ag^+) release (Hu et al., 2012; Pawley et al., 2017; Sondhi et al., 2023; Wang et al., 2023; H. Zhang et al., 2018).

Regarding the drug delivery application, Pawley et al. (Pawley et al., 2017) synthesised a *np-S* matrix by crosslinking silver nitrate ($AgNO_3$) with ethylene diamine in an alkaline solution. The produced np-S matrix exhibited high surface area and large nano-scale pores, which enhanced the loading capacity of aspirin and enabled controlled drug release. They found that the *np-S* matrix demonstrated a rapid initial release of aspirin in phosphate buffered saline (PBS) solution at pH 7.4 and 37°C within the first two hours, followed by stabilization of the release. The study concluded that achieving sustained and gradual drug release over an extended period required some matrix modification. The use of *np-S* -containing dressings, which is commercially known as Medifoam®Silver, for wound healing exhibited strong antibacterial activity against Staphylococcus aureus and Pseudomonas aeruginosa, which achieved a 99.9%

bacterial inhibition growth. The small, uniform pore size enhances capillary absorption and retention of wound exudates, which creates a moist environment optimal for healing (S. M. Lee et al., 2016). Hu and co-workers found that utilising nanoporous bioglass with a high surface area of 467 m^2/g and uniform nanopores of 6 nm loaded with Ag showed enhancing hemostatic performance due to the presence of Ag^+ and nanopore structures of the nanoporous bioglass. The release of Ag^+ inhibited the growth of Escherichia coli, achieving a 99% bacterial inhibition rate. Meanwhile, the high surface area and nanoporous structure of the nanoporous bioglass contribute to absorbing water from the blood, concentrating clotting factors, and reducing clotting time (Hu et al., 2012).

2.4 Nanostructural Characteristics

A variety of nanostructural features influence the effectiveness and efficiency of employing *np-S* in many applications. Understanding and controlling these factors is essential for optimizing *np-S* for its numerous applications in sensing, catalysis, environmental, and biomedical fields. The main feature is the interconnected ligament structure.

2.4.1 Interconnected Ligaments

The term "interconnected" in nanoporous materials is defined as the continuous pathways provided by the solid fraction frameworks, allowing for effective transportation of electrons. According to the ball and stick model, the structure of nanoporous metals can be described as a building block of four-coordinated spherical node interconnected by cylindrical ligaments as Figure 2.13 shows, with the nodes volume V_N of $4/3\,\pi R^3$, ligament volume V_L $\pi R^2(1-2R)$ and the ligament radius to node radius ratio $\sqrt{2/3}$. Each node is connected to four cylindrical ligaments, forming a robust and interconnected network (Huber et al., 2014). This simple model describes a regular and uniform nanoporous structures. The interconnected nature of the porosity in this nanostructure system guarantees a consistent distribution of reactants and products, which is necessary for catalytic processes and electrochemical reactions (Griffiths et al., 2020; Sang et al., 2022). The degree of interconnectivity in nanoporous structures have a significant impact on their physical properties, as will be shown in the following sections.

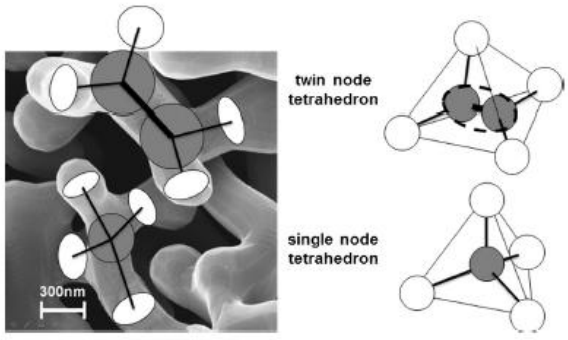

Figure 2. 13 ball and stick model of nanoporous structure consist of a network of interconnected (a) twin node and (b) single node and cylindrical ligaments (Huber et al., 2014).

Any prototypical network consists of structural elements with varying degrees of connectivity, as shown in Figure 2.14. There are highly connected 'octopus-like' fragments, which are connected to the whole network structure by at least seven nodes (Figure 2.14a), and single connected ligaments, which are connected to the rest of the network only at their bottom (Figure 2.14b) (Ron et al., 2020). This model demonstrates irregular and complex nanoporous materials.

Figure 2. 14 schematic figure illustrate (a) high connected ligament to the network and (b) single connected ligament to the structure of the nanoporous network (Ron et al., 2020).

The high connectivity of the *np-S* network was demonstrated using the cathodoluminescence (CL) microoscopic technique, as shown in Figure 2.15. The high connectivity of the produced silver ligaments permits charge flow through the network, resulting in different optical behaviour. The intense hotspots in the CL maps indicate the highly connected regions within the network, and vice versa (Ron et al., 2020). Due to the high-penetration depth of the X-ray beam, different X-ray based techniques have been employed to visualize the 3D nanoporous structure and provide quantitative analysis of the size distribution and interconnectivity of the pores across the whole sponge. These include X-ray ptychographic tomography, in situ synchrotron X-ray nano-tomography, transmission X-ray microscopy (TXM), and focus ion beam scanning electron microscopy (FIB-SEM) (Górecki et al., 2023; Liu et al., 2021; Zhao et al., 2018).

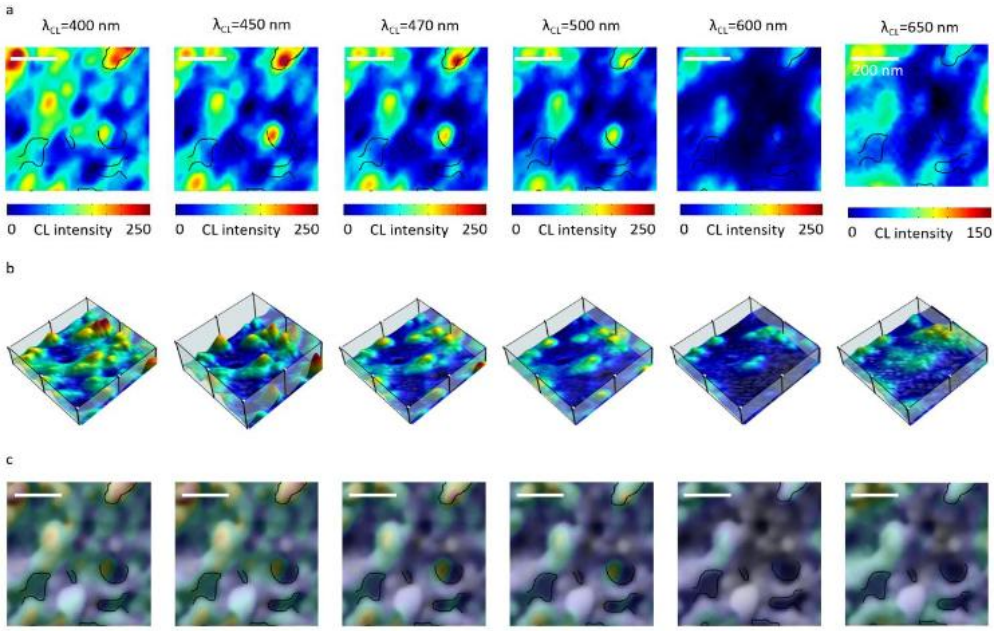

Figure 2. 15 high connectivity ligaments of np-S network (a) 2D CL emission patterns obtained at different wavelengths λ = 400, 450, 470, 500, 600 and 650 nm, (b) 3D CL patterns generated from (a), and (c) Overlaid SEM-CL images collected at the same magnification (scale bar 200 nm). A black contour line indicates the ligament structure location as detected from the SEM image (Ron et al., 2020).

2.5 Properties of *np-S*

Like other types of the nanostructures, plasmonic nanoporous metals exhibit fascinating properties which are significantly different from the same materials at larger dimensions, mainly due to three main effects; resonance conduction electron movement, quantum confinement effect and surface effects (Joudeh & Linke, 2022).

In nanoscale systems, the quantum confinement effect primarily stems from the constraint of the motion of electrons and holes inside a narrow space comparable to their de Broglie wavelengths, leading to modifications in the electronic band structure and hence indirectly changing the associated atomic structure. Furthermore, shrinking the dimensions of the materials to nanosized can influence the energies of the electronic states and the spacing between them. According to the free electron model, the electronic state energies depend on the inverse square of the dimension of the system in a specific direction ($1/L^2$) (Kelsall et al., 2005).

2.5.1 Large surface area

Reducing the size of a large cube to 8 cubes, 64 cubes, and then 512 cubes, as Figure 2.16 illustrates, leads to an increase in the number of surface atoms compared to the number of inside atoms. Similarly, if the dimensions of the bulk metal have been shrunk to nanoscale size, its surface area relative to volume will increase dramatically due to the increase in the number of its atoms exposed at the outer surface. Consequently, surface atoms significantly influence

the behaviour of these materials, enhancing their interaction with the environment (Han et al., 2021).

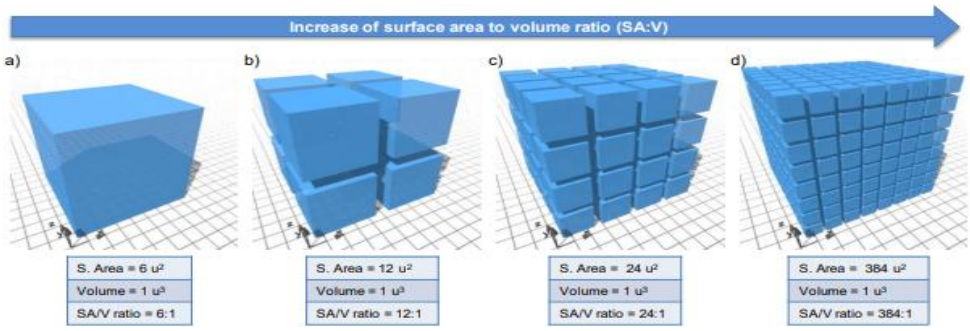

Figure 2. 16 schematic figure showing the increase in the surface area to volume ratio when the dimensions of the cubic representing the bulk material are lowered by cutting it into 8 cubes, then 64 cubes, and finally 512 cubes (Portilla, 2017).

Incorporating nanopore structures into these materials leads to a considerable improvement in the surface area-to-volume ratio, thereby achieving significant enhancements in their properties and behaviour (Barsuk et al., 2016; Khan et al., 2019; G. Li et al., 2021; Sang et al., 2022). Researchers have developed two methods to characterise the surface area of nanoporous materials [51]. The Brunauer, Emmett, and Teller (BET) method is a common and fundamental technique employed to quantify the specific surface area of materials with nanopore structures by measuring the amount of adsorbed nonreactive gases, typically nitrogen or argon, at a temperature of 77 K or 87 K by gravimetric, volumetric, or dynamic flow-through techniques. This approach involves utilising the BET isotherm model, which is dependent on the binding energy between the adsorbate and the surface, to determine the adsorption behaviour (Sinha et al., 2019; Y. H. Tan et al., 2012). The specific BET surface area can be determined by:

$$a_{BET} = n_m N_A \sigma_m \ldots\ldots\ldots\ldots\ldots\ldots (2.5)$$

Where N_A is Avogadro's number, σ_m is the cross-sectional area of the molecule, and n_m is the saturation capacity of the monolayer (Shi et al., 2021).

Measuring the specific surface area using the BET method is simple; however, it requires specific sample masses between 10 mg and 50 mg or more to measure surface area effectively. For sample masses lower than 10 mg, alternative approaches have been suggested, such as using Krypton-85 adsorption (Kulkarni et al., 2011).

Besides the BET method, electrochemical techniques provide complementary methods for characterising the surface area of nanoporous metals. It gives dynamic information about the electrochemical surface area, surface reactivity, and charge transfer kinetics of metals with nanopores. Various electrochemical methods have been used to determine the electrochemical

active surface area (ECSA). For instance, researchers estimated the ECSAs for as-deposited Ag thin film and as-de-alloyed *np-S* with pore dimensions ranging from 50 to 200 nm using the Pb under-potential deposition (UPD) method. They concluded that the surface area of the *np-S* is approximately 1.9 times larger than that of the as-deposited Ag thin film (Kurowska-Tabor et al., 2016), while the surface area of the *np-S* with a pore diameter of 80 nm, measured using the charge associated with the reduction of adsorbed oxygen (surface oxide reduction (SOR) method), increases by a factor of about 62 compared to dense Ag (Z. Li et al., 2015).

When Ag is in its nanoporous form, it has a larger specific surface area than its nanoparticles. This is because the nanoporous structure makes the surface rougher and the surface-to-volume ratio higher. Aggregation of Ag is also prevented by the presence of the network structure. The presence of nanoporous structures provides numerous active sites for surface reactions and interactions. Experimentally, Tastekova et al. (Tastekova et al., 2018) found that the specific surface area of *np-S* with pores ranging from 10 to 60 nm was 42 ± 5 m^2/g, while, Ag nanoparticles with particles ranging from 50 to 150 nm and 5 to 65 nm had a specific surface area of 26.7 m^2/g and 23.81 m^2/g, respectively (Ahmad et al., 2020; El-Kalliny et al., 2023; Shpigel et al., 2019; Zhou et al., 2009).

The surface area of metallic nanoporous sponges is affected by many factors such as pore sizes and annealing temperatures. Many investigations have demonstrated a correlation between the specific surface area of metallic nanoporous sponges and their pore size. Typically, nanoporous metals have a greater specific surface area when their pore size is smaller. The specific surface area value measured by Tastekova et al. (Tastekova et al., 2018) for *np-S* was higher (42 m^2/g, pore size 10 – 60 nm) compared to the value obtained by Krishna et al. (Krishna et al., 2010) with large pores (50 - 100 nm), which was 16 m^2/g. A notable reduction in the specific surface area of metallic nanoporous materials was observed with increasing annealing temperatures after dealloying. As listed in Table 2.5, annealing caused a decrease in specific surface area from 6.4 to 1.79 m^2/g and electrochemical active surface area from 5.34 to 1.65 m^2/g as the annealing temperature of *np-G* increased from room temperature to 400°C and pore size from 82 to 167 nm. This effect can be explained by the fact that increasing annealing temperature will enhance the surface self-diffusion of metal atoms, which leads to coarsened ligaments, increasing pore sizes, and decreasing both surface area and surface energy (Y. H. Tan et al., 2012).

Table 2. 5 The relationship between the annealing temperature and pore size, BET surface area, electrochemical active surface area and pore volume of nanoporous gold (np-G) (Y. H. Tan et al., 2012).

Nanoporous gold annealing T/°C	Pore Size, nm	Surface Area (S_{BET}), m^2g^{-1}	Electrochemical active surface area, m^2g^{-1}	Pore Volume, cm^3g^{-1}
Room temperature	82	6.4	5.34	0.044
100	102	6.35	4.85	0.034
200	129	5.37	4.34	0.021
300	148	4.57	3.92	0.015
400	167	1.79	1.65	0.0076

2.5.2 Optical properties of np-S

Metallic thin films containing embedded nanopore structures demonstrate optical properties that are remarkably different from those of their metallic counterparts. When a material with a range of nanopore and metallic material sizes and shapes interacts with electromagnetic waves, its optical response can be broad due to the support of multiple plasmonic modes. This results in a broadband optical response and the excitation of various plasmonic resonances that can be interpreted by using various approximation techniques to model its response, such as the finite element method (FEM) or effective medium Theory (EMT). (Koya et al., 2021; Michael et al., 2006; Ron et al., 2018). In this section, the review will focus on the effective medium approximation, especially Bruggeman (BG) theory which will be used in the results chapters to estimate the optical properties of the np-S thin films.

2.5.2.1 Effective medium theory and optical behaviour of nanoporous materials

An effective medium is a conceptual model that describes the average properties of complex nanostructure materials whose feature sizes are much smaller than the smallest interacting wavelength. Effective parameters such as a complex dielectric function ε_{eff} or an effective refractive index n_{eff} can be deduced by applying an effective medium theory (EMT) (also known effective medium approximation) when investigating the material's behaviour. The following equation relates the complex permittivity and the effective refractive index of the material:

$$\varepsilon_{eff} = (n + ik)^2 = \varepsilon_i + i\varepsilon_{ii} \quad \text{(2.6)}$$

If the real component ε_i and the imaginary component ε_{ii} of the permittivity are known, the refractive index n and extension coefficient k can be calculated (Detsi et al., 2014; Jalas et al., 2014).

The Maxwell-Garnett (MG) and Bruggeman (BG) models are the most widely used approximations for predicting the effective dielectric properties of composite materials. The MG theory is particularly effective for systems where isolated spherical particles are embedded

in a continuous host medium as Figure 2.17 a demonstrates. In the MG model, the resulting effective dielectric constant is asymmetric, as it depends on which material is designated as the host and which is the embedded phase. In contrast, the BG model produces a symmetric effective dielectric constant, reflecting the equal contribution and interaction from both materials as shown in Figure 2.17 b. This review will focus on the BG approximation within the Effective Medium Theory (EMT), as it is preferred for modelling the optical response of nanoporous materials due to their complex, highly interconnected structure, where both the metal and voids significantly influence the overall properties (Garoli et al., 2018; Zhou et al., 2023).

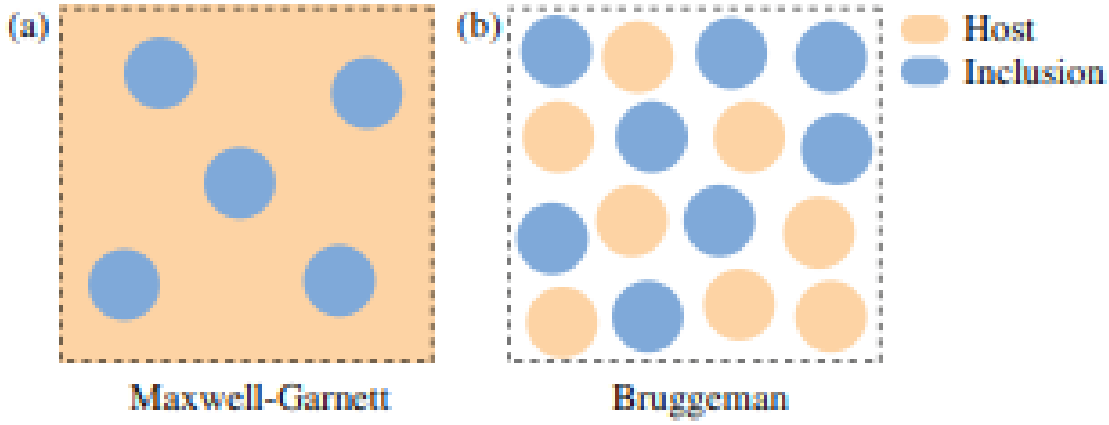

Figure 2. 17 Schematic diagram represents (a) an asymmetrical phase in Maxwell-Garnett theory and (b) symmetrical phases in Bruggeman approximation (Zhou et al., 2023)

- ***Bruggeman approximating of effective medium theory***

For a system with an interwoven matrix and inclusions to the degree of indistinguishable, extending to miss a clear line between matrix and inclusions, the Bruggeman model treats both components symmetrically and equivalently without assigning a dominant role to either the matrix or the inclusions. The electrodynamic treatment for the binary system is carried out twice: first, for the inclusion (with permittivity ε_i and volume fraction η_i) embedded within the effective medium, and then for the matrix (with permittivity ε_m and volume fraction η_m) embedded within the same effective medium. The combination of these two cases should result in the determination of the effective medium.

In the case of inclusion with radius a subjected to a uniform external electric field E_o aligned along the z-axis, situated at a distance from the inclusion. The system is described as a spherical coordinate system (r, θ) as depicted in Figure 2.18.

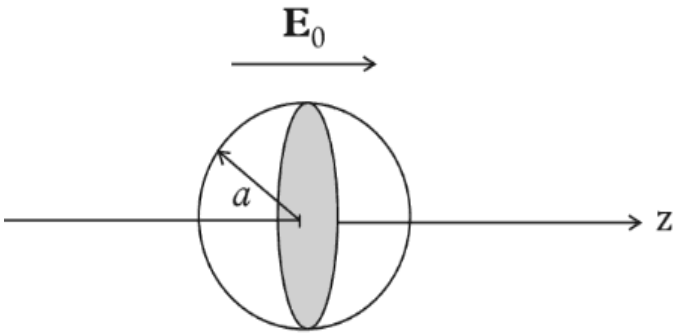

Figure 2. 18 Bruggeman approach to flux deviation through spherical inclusion (Choy, 2015)

The generated electrical field inside E_{inside} the inclusion and the electrical field $E_{outside}$ in the surrounding matrix outside the inclusion is given by

$$E_{inside} = -A_1 \cos\theta\, \hat{r} + A_1 Sin\, \theta\, \hat{\theta} \ldots\ldots\ldots\ldots\ldots\ldots (2.7)$$

$$E_{outside} = \left(E_o + 2\frac{C_1}{r^3}\right) Cos\, \theta\, \hat{r} + \left(-E_o + \frac{C_1}{r^3}\right) Sin\, \theta\, \hat{\theta} \ldots\ldots\ldots\ldots\ldots\ldots (2.8)$$

Since $\hat{r}$ and $\hat{\theta}$ here refers to the radial distance and polar angle unit vectors in the spherical coordinate system, respectively. A_1 and C_1 are both representing the dipole moments produced the electric field inside and outside the inclusion, respectively, and given by

$$A_1 = -\left(\frac{3\varepsilon}{\varepsilon_1 + 2\varepsilon}\right) E_o \ldots\ldots\ldots\ldots\ldots\ldots (2.9)$$

$$C_1 = \left(\frac{\varepsilon_1 - \varepsilon}{\varepsilon_1 + 2\varepsilon}\right) a^3 E_o \ldots\ldots\ldots\ldots\ldots\ldots (2.10)$$

To simplify the process of calculating electric flux, assume a disk with a surface area of πa^2 is placed inside the inclusion in a plane perpendicular to the z-axis, The electric flux deviation due to polarization of inclusion can be given by

$$\Delta\emptyset_1 = 2\pi\left(\int_0^a r\varepsilon_1 E_{inside}\, dr - \int_0^a r\varepsilon E_o\, dr\right) \ldots\ldots\ldots\ldots\ldots\ldots (2.11)$$

$$= 2\pi a^2 \varepsilon E_o \left(\frac{\varepsilon_1 - \varepsilon}{\varepsilon_1 + 2\varepsilon}\right) \ldots\ldots\ldots\ldots\ldots\ldots (2.12)$$

Hent ε_1 here represents the dielectric constant of either inclusion or matrix.

In the case of single-particle polarization in the effective medium, the flux deviations should equal zero.

$$\eta_i \Delta\emptyset_i + \eta_m \Delta\emptyset_m = 0 \ldots\ldots\ldots\ldots\ldots\ldots (2.13)$$

Given that the volume fraction of the inclusion η_i can be written as *f* and the volume fraction of the matrix η_m can be written as *1-f*, therefore the *BG* formula can be expressed as (Choy, 2015)

$$f * \left(\frac{\varepsilon_i - \varepsilon}{\varepsilon_i + 2\varepsilon}\right) + (1 - f) * \left(\frac{\varepsilon_m - \varepsilon}{\varepsilon_m + 2\varepsilon}\right) = 0 \ldots\ldots\ldots\ldots\ldots\ldots (2.14)$$

This model and equation will be used to derive the optical response of the *np-S* thin films produced in this work.

2.5.2.2 Absorption and scattering by np-S

The optical properties of Ag nanostructures at the SPR are determined by the interplay between absorption and scattering phenomena. The disordered plasmonic nanopore structures are optically robust. This means that failures or defects at multiple points within the structure don't really change the optical properties of these nanostructures. Due to the random distribution of cavities and the irregular arrangement of the ligaments within the metallic nanoporous, their index of refraction is inhomogeneous (Galinski et al., 2017; Huang et al., 2016; Ron et al., 2018)

2.5.2.3 Surface plasmon resonance (SPR) and localized surface plasmon resonance (LSPR)

Surface plasmon resonance (*SPR*) is a physical phenomenon that takes place at a metal-dielectric interface; as Figure 2.19 a shows. When the frequency of an external electromagnetic wave matches the frequency of the free electron oscillations, the interaction between the electromagnetic wave and the free electrons of the metal leads to the collective oscillation of these free electrons, thereby exciting surface plasmons (Chen et al., 2011). The propagation between the incident radiation and electron surface leads to absorbing, transmitting, or scattering the radiation (Indhu et al., 2023).

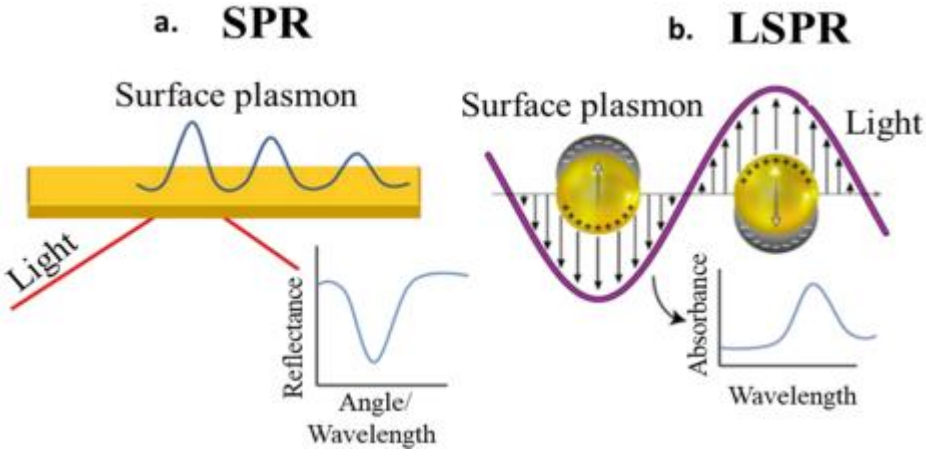

Figure 2. 19 schematic figure displays the mechanism of occurring (a) SPR at the metal-dielectric interface due to the interaction between light and conduction electrons in metal, and (b) localized surface plasmon resonance due to confining of the surface plasmon within the nanostructure as a result of the interaction between the incoming light and surface of the nanomaterial (Indhu et al., 2023)

In nanostructured materials, the interaction between the impinging electromagnetic beam and the conduction electrons in metallic nanomaterials causes the confinement of the collective oscillation of these electrons within the structure of nanomaterials. This phenomenon is known as localized surface plasmon resonance (LSPR), as it is confined to the nanostructure and occurs at the surface, as demonstrated in Figure 2.19 b. The LSPR effect is observed when the feature size of a metal ligament is far smaller than the wavelength of impinging light (λ).

When incident light interacts with the surface of a nanostructured metal, the electromagnetic field of the incoming light causes the free conduction electrons to polarize and accumulate on one side of the nanostructure particle, which leads to a net charge difference at the surface of the particle, hence forming an electric dipole as Figure 2.19 b illustrates. Therefore, an internal electric field within the metallic nanostructure is generated, which acts as a restoring force, driving the electrons back towards their equilibrium position. The produced electric field opposes the field of the incident light. Consequently, the electrons oscillate in resonance with the frequency of the incident light, resulting in LSPR (Zhao et al., 2021).

The LSPR peak of Ag in its nano-form is typically observed in the visible spectrum. It can be adjusted by controlling the feature sizes, shapes, and the dielectric function of the environment surrounding the nanoparticles. A blue shift in the LSPR peak, from 650 nm to the wavelengths between 500 and 570 nm, was observed when the ligament size of *np-S* was reduced from 100–200 nm to 50–100 nm, respectively (Morrish & Muscat, 2009), This shift is mainly caused by the enhanced surface scattering resulting from the reduced ligament size. In addition, it has been demonstrated that the increase in surface scattering within np-S is directly correlated with the reduction in pore size and the increased surface roughness of the nanoporous material (Shen & O'Carroll, 2015).

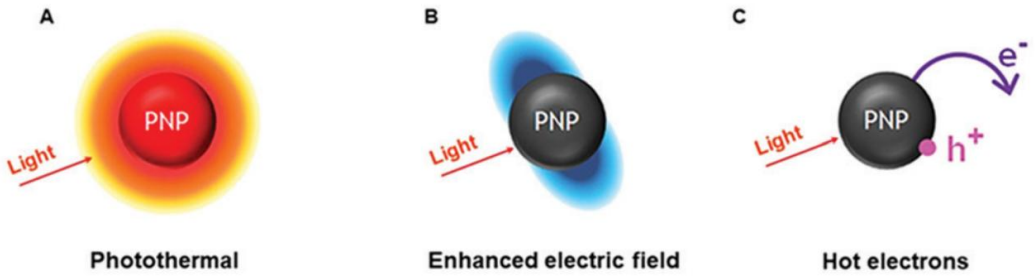

Figure 2. 20 LSPR decay mechanisms on metallic nanostructures which lead to produce (a) photo-induced heating, (b) electromagnetic field enhancement, and (c) photo-induced electron–hole pair (Zhao et al., 2021)

After excitation of LSPR, the oscillations of the plasmon can be damped through two mechanisms: radiative (scattering) and non-radiative (absorption). These two mechanisms

occur during extremely short times and extend from femtoseconds (fs) to picoseconds (ps). Regarding radiative decay, the LSPR dissipates its energy through re-emitted phonons (scattering); it occurs within a few hundred femtoseconds to a few picoseconds. On the other hand, the non-radiative decay of LSPR involves producing hot carriers (energetic electrons and holes) that can interact with the surroundings, the required time for this decay ranges between a few femtoseconds and tens of femtoseconds. The non-radiative mechanism includes the photothermal effect (increases the temperature of the plasmonic material during decay), electromagnetic field enhancement (activates nearby species), and hot carrier transfer (decay by injecting hot electrons into unoccupied states or producing electron-hole pairs that then transfer energy to the adsorbate), which are shown in Figure 2.20 (a- c). Determining which decay mechanism occurred is challenging as multiple mechanisms may happen together or sequentially (Zhao et al., 2021).

- ***LSPR and optical constant***

The effective refractive index refers to an averaged or effective value to represent the overall optical behaviour of a complex material (in our case, nanoporous material) system; it describes the propagation of electromagnetic waves within the material (Ohke et al., 1995; Speets & Kalkman, 2024). The effective refractive index of the material is influenced by refractive index of constituent phases in the nanoporous materials and porosity (Braun & Pilon, 2006). The real part of the complex refractive index is a refractive index (n), which describes the propagation of electromagnetic radiation through the material. The imaginary part is an extinction coefficient (k), which describes how much electromagnetic radiation is absorbed as it travels through the material (Fujiwara & Collins, 2019). The n and k of the material are significantly affected by the LSPR, as stated below.

As mentioned previously, when plasmonic nanoporous structures are irradiated by light, SPR is excited and becomes localized at the surface of the nanopores. Thus, strong local electric fields generate and concentrate at regions such as nanopores and the sharp edges of the ligaments in pores nanostructures, which means that the enhancement in the electrical field will vary due to the non-uniform nanopore shape. Moreover, the rough and irregular nanostructure of the nanoporous materials contributes to generating a strong electrical field at the points called hotspots. The absorption of the material increases due to the strong coupling between the electromagnetic radiation and the free electrons, which increases the k. The energy absorbed from electromagnetic radiation is dissipated via radiative or non-radiative decay

mechanisms as stated earlier. This loss of the energy, or damping, is represented by an increase in the imaginary part of the dielectric function ε_2 (Koya et al., 2021; Ron et al., 2018).

According to Kramers-Kronig relationships, Eqs. 2. 15 and 2. 16 (Peiponen et al., 1998), the real and imaginary parts of effective refractive index are directly related, which means that any change in n will lead to a change k, and vice versa.

$$n(\omega`) - 1 = \frac{2}{\pi} P \int_0^{\infty} \frac{\omega\, k\,(\omega)}{\omega^2 - \omega`^2}\, d\omega \ldots\ldots\ldots\ldots\ldots\ldots \text{(2.15)}$$

$$k(\omega`) = \frac{-2\,\omega`}{\pi} P \int_0^{\infty} \frac{n\,(\omega`) - 1}{\omega^2 - \omega`^2}\, d\omega \ldots\ldots\ldots\ldots\ldots\ldots \text{(2.16)}$$

However, due to their irregular structure, the refractive index of nanoporous materials will show anomalous dispersion and inhomogeneity (Galinski et al., 2017).

2.5.3 Electrical properties of np-S

In general, studying the electrical properties of materials focuses on describing their ability to either conduct or resist the movement of charge carriers in response to applied electric fields (Yuliza et al., 2015). These properties typically include measuring the electrical conductivity and resistivity of the materials.

According to the quantum confinement theory, and unlike the free movement of electrons in bulk materials, electron movement in nanostructured materials, such as nanoporous metals, becomes confined spatially by the potential barrier of the surface or trapped by the potential well of the quantum box. In this case, the energy levels available for the electrons to occupy become restricted, thereby causing the energy states to discretise. As the size of nanomaterials decreases, their energy band gap becomes wider, which means that high energy is required to excite the electrons from the valence band to the conduction band, thereby decreasing their electrical conductivity (Hafaiedh & Bouarissa, 2011).

On the other hand, during the flow of electrons inside a nanopore structure, they suffer from multiple scatters. The electrons scatter at the ligament boundaries, where they are redirected to interact with other electrons. The electron-electron scattering will increase with increasing the surface-to-volume ratio in nanoporous metals, thereby increasing resistive losses and reducing conductivity (Hopkins et al., 2011).

Moreover, tortuosity τ, which is defined as the ratio between the shortest pathway Δl and the Euclidean distance between the two ends of that pathway Δx as Figure 2.21 depicts, is the other factor that can affect the effective conductivity (C_{eff}) of the nanoporous materials , as shown in the expression:

$$C_{eff} = \frac{C_i * P}{\tau} \ldots\ldots\ldots\ldots\ldots\ldots \text{(2.17)}$$

Where C_i and P are intrinsic conductivity and the fraction of the conductive phase. Nanoporous metals have a highly tortuous structure as introducing the nanoporosity (ε) in the materials leads to an increase in the tortuosity according to the Eq.2.18:

$$\tau^2 = \gamma\varepsilon^{1-\alpha} \ldots\ldots\ldots\ldots\ldots\ldots \text{(2.18)}$$

Since γ and α are constants which are affected by the particle-size distribution, morphology, and porosity of nanoporous materials. The mean free path of the transported electrons through nanoporous materials is convoluted and longer than that in bulk materials, thereby electron scattering increases and hence further decrease in the electrical conductivity of the materials will be observed (Guo et al., 2021; Tjaden et al., 2018).

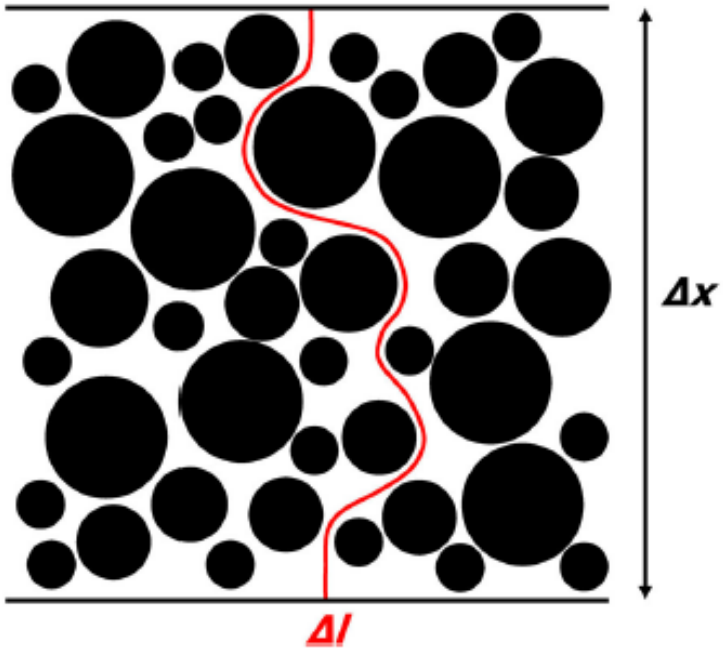

Figure 2. 21 Diagram shows the shortest path Δl through a nanopore structures of thickness Δx which used to calculate the tortuous path (Tjaden et al., 2018).

2.5.4 Antibacterial properties of np-S

Due to their great surface area-to-volume ratio, silver nanoparticles (AgNPs) enable the continuous release of Ag^+ even at low concentrations, producing antibacterial activity against a broad spectrum of microorganisms, including both Gram-positive and Gram-negative bacteria, viruses, and fungi (Faiz et al., 2018; Qing et al., 2018; Salas-Orozco et al., 2019; Vimbela et al., 2017; Zhou et al., 2012). Consequently, AgNPs are frequently used in antibacterial applications such as wound dressings (S. M. Lee et al., 2016), healthcare products (Burdușel et al., 2018), food packaging (Carbone et al., 2016), cosmetics (Kokura et al., 2010), and water purification (Tessema et al., 2024). Recent studies have reported that supporting AgNPs on mesoporous substrates such as mesoporous graphene, mesoporous silica, and

mesoporous bioactive glass significantly enhances their antibacterial action. The robust antibacterial activity is due to improving the AgNPs ' stability, eliminating the environmental toxicity associated with the release of AgNPs into the environment, preventing nanoparticle aggregation upon exposure to air or water, increasing surface area, and promoting Ag^+ ions release rates. Therefore, the porous structures make AgNPs highly efficient for various applications (Hu et al., 2012; Jorge de Souza et al., 2019; Kumar et al., 2019; Wang et al., 2014; L. Yang et al., 2019; Zhu et al., 2014).

Although the antibacterial agents produced on the mesoporous substrates provide significant benefits, it is not the only way to improve the antibacterial properties of Ag. The *np-S* is another unique and effective nanomaterial against various microorganisms.

2.5.4.1 Toxicity of np-S to bacterial cells

Only a few works in the literature have studied the antibacterial properties and toxicity of *np-S* against Escherichia coli, Staphylococcus aureus and Methicillin-resistant Staphylococcus aureus (Wang et al., 2023; Wang et al., 2019; Zhang et al., 2013). The concept of toxicity of the materials refers to any deleterious effects caused by the exposure of organisms to test materials or compounds (Marambio-Jones & Hoek, 2010). The majority of prior research concluded that *np-S* is the most effective antibacterial agent due to its ability to inhibit the growth of bacteria, which reaches higher than 95% (Wang et al., 2023). The distinctive three-dimensional (3D) nanoporous architecture, which enhances the surface area of *np-S,* makes it a superior alternative to traditional Ag metal and other Ag-based nanomaterials. The stable mechanical performance and excellent flexibility of produced *np-S* further improve its potential for environmental, medical, and wearable product applications (Wang et al., 2023).

The mechanism of antibacterial action of *np-S* has yet to be fully clarified. However, most of the recently published scientific papers this topic proposed that releases of Ag^+ ions are crucial for the antibacterial performance of *np-S*. The enhanced antibacterial activity of *np-S* is expected to increase with the concentration of Ag^+ ions release, which depends not only on the concentration of Ag but also on the ability of the solution to penetrate through the nanopore structures to reach the internal Ag ligaments. It is thought that the Ag^+ ions were released via the oxidative dissolution process of the Ag nanostructures, which occurs due to interaction with oxygen (O_2) (Choi et al., 2008) or hydrogen peroxide *(*H_2O_2*)* (AshaRani et al., 2009).

As can be seen in Figure 2.22, the dissolved Ag^+ ions interact with main bacterial cell components to kill or inhibit bacterial growth in two steps. The first step of Ag^+ ions interaction

with bacterial cells occurs on the cell envelope, and it involves destroying the peptidoglycan cell wall, plasma membrane, and the proteins attached to the membranes (Chaloupka et al., 2010; Qing et al., 2018). Ag^+ ions could strongly interact with the negatively charged compounds in the bacterial cell wall, such as carboxyl, phosphate, and amino acids found in structural proteins and enzymes. They mainly target sulfhydryl groups (-SH) in the amino acids cysteine and methionine, as well as amine groups (NH_x) in histidine, arginine, and lysine (Rai et al., 2012). Additionally, the proton motive force could be disrupted due to binding the Ag^+ ions to transported proteins found on the bacterial membrane, impeding the transport of protons and phosphate to adenosine triphosphate (ATP), which is responsible for the transfer and storage of energy within bacterial cells, causing rupturing of the plasma membrane (Klueh et al., 2000; Lok et al., 2006; Wang et al., 2019).

Intracellularly, the penetrated Ag^+ settle between the purine and pyrimidine base pairs in the nucleosides, deactivating the hydrogen bonds between the base pairs of the anti-parallel DNA strands (Hatchett & White, 1996; Monteiro et al., 2012). Some studies have indicated that the Ag^+ induce the condensation and localization of DNA in the centre of the bacterial cell, hence, inhibiting cell division and proliferation (Feng et al., 2000; Guzman et al., 2012). Ag^+ has also been found to alter the structure of ribosomes in the cytoplasm, which leads to the prevention of protein synthesis (Durán et al., 2016).

The Ag^+ release rates are influenced by various factors, including the composition of the culture media, the pH of the environment, temperature, the surface area of the antibacterial agent, the dose of the antibacterial agent, and immersion time. The following section will discuss these factors in detail.

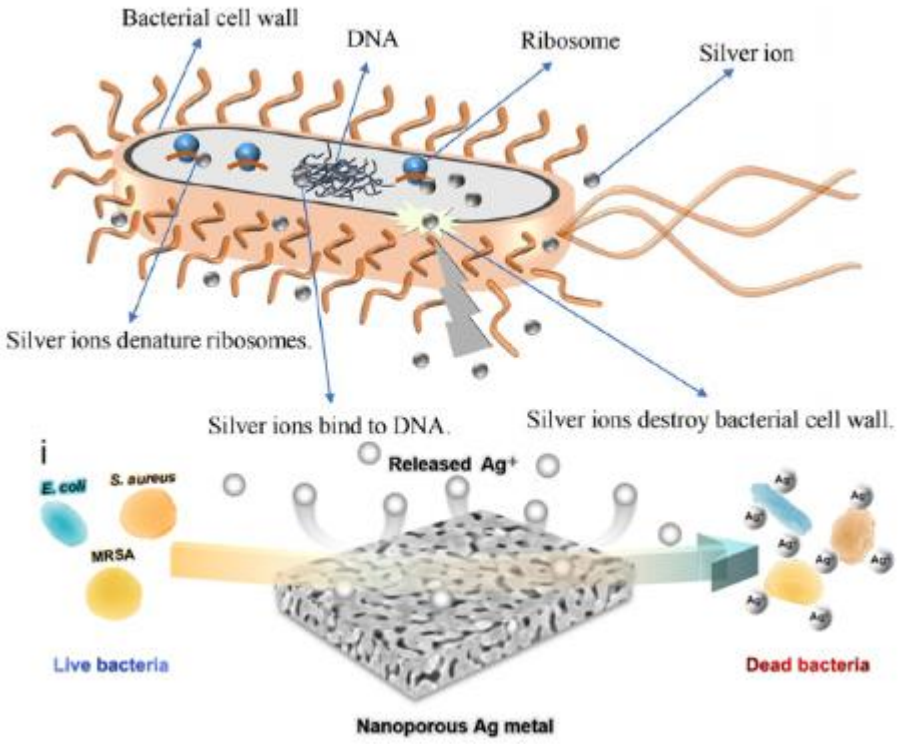

Figure 2. 22 Th proposed mechanism of the antibacterial activity of np-S relies on the release of Ag^+ which target the bacteria cell wall, destroy it, and thereby penetrate. Once inside, the Ag^+ bind with the DNA, inhibiting cell division and proliferation (Wang et al., 2023; Xiao et al., 2021).

2.5.4.2 Factors affecting the Ag^+ release rate

- ***Microstructure and specific surface area***

A higher specific surface area allows for more extensive and sustained release of Ag^+ ions, which are the primary agents responsible for the antibacterial activity. The surface charge of *np-S* shows a pronounce influence on its antibacterial activity. The electrostatic interaction between the Ag ions with positive charges and the bacterial membrane, which is charged negatively, increases the permeability of the membrane, which guaranteed the diffusion of Ag^+ ions into the cells (Mathias de Souza et al., 2024).

The surface microstructure of *np-S* enhances its antibacterial performance. The presence of nanopore structures significantly increases surface roughness, which aids in more effectively adhering bacteria and enhances their exposure to Ag^+ (Xia et al., 2020; Zheng et al., 2021). Smaller pores increase the surface area, enhancing the interaction between Ag^+ and bacterial cells. Uniform pore distribution ensures consistent antibacterial activity throughout the material, preventing "dead zones" where bacteria might survive.

- ***Immersion period***

The immersion time of *np-S* in the bacterial culture is a critical factor influencing the rate of Ag^+ ions release, hence the antibacterial efficacy and cytotoxicity of *np-S*. Previous studies have emphasized a rapid release of Ag^+ observed within the first 12 to 24 hours of immersion in the bacterial culture. The high release rate refers to the high surface area of *np-S* or the initial availability of easily accessible Ag atoms on the surface. This vast release rate of Ag^+ is followed by a stable release ascribed to the oxidation and dissolution of the deeper layers of the sponge. The slow and steady release of Ag^+ ensure a continued antibacterial performance of *np-S* over an extended period, which is beneficial for long-term antibacterial activity, preventing the regrowth of bacteria and maintaining the antimicrobial environment (Thukkaram et al., 2020; Wang et al., 2023; Wang et al., 2019).

To the best of our knowledge, there is a significant scarcity in the research that has explored the physical properties of *np-S*, especially *np-S* thin films prepared by dealloying Ag-Al alloys, including their optical, electrical, and antibacterial characteristics, leaving a wide scope for research and exploration. It is known that exploring the optical properties, including investigating the optical constants and dielectric functions of *np-S*, is important for applications in plasmonic, sensing, and photonic devices that require control of light interactions with

nanostructured materials. Moreover, examining the electrical characteristics of *np-S*, including its conductivity and resistivity, yields critical insights into the efficacy for use in electronic and energy storage devices like sensors and supercapacitors. On the other hand, investigating its antibacterial activity enables opportunities for use in environmental, biomedical, and antimicrobial applications. Therefore, studying these properties will not only address existing gaps but also open the door for new applications.

In summary, the chapter provided a literature review focusing on the key features that influence the properties of nanoporous materials. The dealloying technique as a widely used method to prepare nanoporous materials is described. The impact of nanostructure on electrical, optical, and antibacterial activity was discussed in more detail. Finally, a brief description of the SERS technique and the use of *np-S* as a Raman substrate, supercapacitor, catalytic and in medicine application was provided.

Chapter 3 Experimental procedure

3. Overview

This project has focused on investigating the physical and antibacterial characteristics of *np-S*, which are known for their potential uses in microbiology and sensing applications. To achieve a comprehensive understanding, two silver aluminium alloy ($Ag_{100-x}Al_x$) systems, which will use to prepare the *np-S* samples, were synthesized using differing strategies to ensure variability in their physical characteristics and biological functionalities. The first system is the $Ag_{100-x}Al_x$ alloy thin films, they were synthesized using a physical vapor deposition technique especially magnetron sputtering, which allows for precise control over the thickness and composition of the systems by adjusting the applied voltage and deposition time. In the second approach, the bulk $Ag_{100-x}Al_x$ alloys were prepared via melting process, involving heating the mixture of Ag and Al to a temperature (melting point) where they transition from a solid to a liquid state. This method provides control over the alloy's composition, efficiency for alloying metals that may not combine easily at room temperature.

This chapter provides an overview of the fundamental experimental approaches that are used throughout this thesis including the description of the techniques used to prepare the thin films and bulk alloys and the analytical techniques used to characterize the samples. Results will include detailed information about the techniques for preparing and characterising alloy systems.

3.1 Preparation methods

3.1.1 Magnetron sputter deposition approach

Magnetron sputter deposition is a common method for preparing uniform thin film alloys of high purity (Mwema et al., 2022). Deposition occurs in an isolated environment: a vacuum chamber houses sputter guns, and the targets positioned above them, and substrates placed below. The magnets positioned behind the targets are crucial for generating a magnetic field that confines the plasma near the surface of the targets to increase the sputtering rate.

During the sputtering process, a low pressure of inert gas, most commonly argon (Ar), is introduced into the chamber and ionised. These energetic ions hit the target material, knocking off atoms from its surface. These atoms pass through the vacuum and then land on a substrate to form the thin film coatings as Figure 3.1 (a) shows.

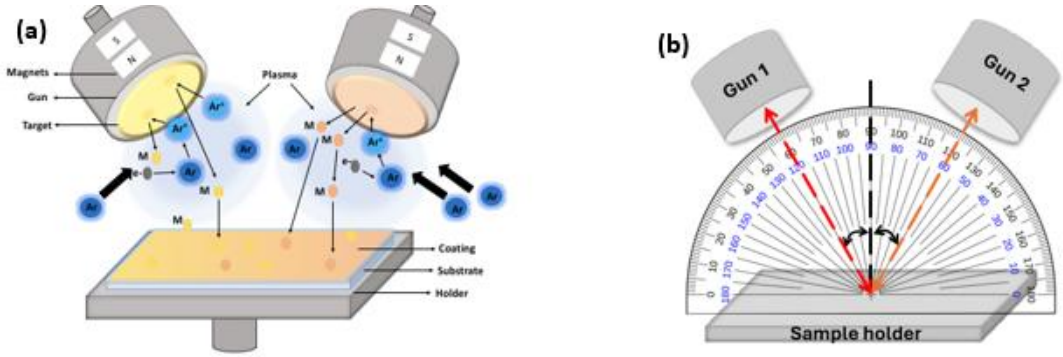

Figure 3. 1 (a) schematic picture shows the DC magnetron sputtering setup used in this project. The deposition process includes introducing a low-pressure Ar gas into the chamber and ionized to form plasma. The picture also illustrates the position of two targets (Ag and Al) which are connected to a cathode, and a substrate positioned on a holder which is placed on an anode. The produced magnetic field by the magnetron acts to confine the plasma near the surface of the targets, enhancing the sputtering rate. The ionized Ar atoms collide with the two targets, leading to eject the atoms from targets and hence deposited onto the substrate, forming a required thin film, and (b) the angle between the normal and guns.

Each target has a distinct sputter yield, which quantifies the number of atoms that are ejected from the target surface per incoming particle (Mattox, 2010). The sputtering yield of the target is influenced by the energy of the inert gas ions and the atomic number of the target (Bunshah, 1982; Frey & Khan, 2015), as shown in Figure 3.2. Understanding the sputter yield of the alloy components helps to control sputtering parameters such as applied current, deposition rate, and sputtering time, which leads to production of a uniform thin film with the desired composition and quality.

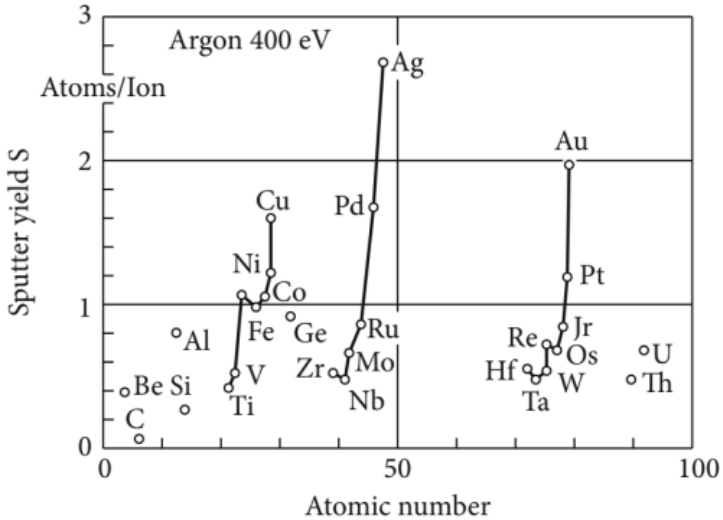

Figure 3. 2 Sputtered yield as a function of atomic number of different target at Ar^+ energy of 400 eV (Frey & Khan, 2015).

3.1.1.1 Oblique angle deposition

Oblique angle deposition (OAD), also known as glancing angle deposition (GLAD) or ballistic deposition, refers to a geometrical deposition method where the target and the substrate surface are obliquely aligned as Figure 3.1 (b) demonstrates. It has been employed in this work

to obtained thin films with high surface area and tailored nanostructures. Depositing the thin film using this geometry relies on the shadowing effect, which occurs due to directing the material flux at the substrate at an oblique angle rather than perpendicularly. Therefore, the initial nuclei or clusters of the deposited material start to form, which leads to casting shadows behind them relative to the direction of incoming flux as deposition proceeds tilted and separated nanocolumns formed because the shadowed regions may receive significantly less material as Figure 3.3 shows. The tilted degree is affected by the zenithal angle of deposition. As a result of this shadowing effect, porous and anisotropic film structures would be produced, where the physical properties of the film differ along various directions due to the aligned

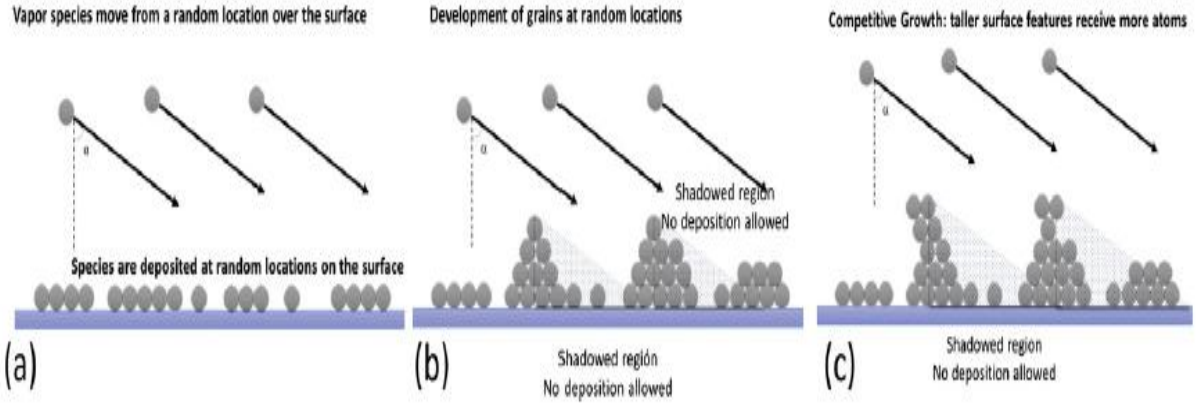

Figure 3. 3 Thin film growth using OAD geometry, (a) formation of the initial nuclei or cluster due to direct a flux at the substrate at an oblique angle, (b) and (c) the observation of shadow effect due to the accumulate of particles within certain regions (Barranco et al., 2016)

As this project aims to prepare thin film alloys with a thickness of 118 nm, the properties of the substrate material are critical as it forms the base for the coating. In this study, a glass substrate was chosen for depositing the $Ag_{100-x}Al_x$ alloy due to its smooth and defect-free surface morphology, allowing for uniform nucleation and growth of thin films, thereby reducing surface roughness and enhancing both electrical conductivity and optical transparency. Furthermore, a glass substrate is an electrically non-conductive material, ensuring that all electrical measurements are attributed to the coating without interference from the substrate (Chen, 2023; Georgiadis, 2015; Vidakovic-Koch, 2020).

Prior to alloy deposition, the substrate was cleaned using an antibacterial spray, followed by ultrasonic cleaning for 20 minutes each in acetone, ethanol, and reverse osmosis (RO) water. Finally, the substrates were dried using N_2 gas.

In the first three chapters of this project, we focus on preparing the $Ag_{100-x}Al_x$ thin film alloys with different Al concentrations and the $Ag_{100-x}Al_x$ thin film alloy with gradient composition. Three targets are used namely, titanium Ti target (99.9% purity) to deposit the

adhesion layer, and Ag and Al (99.9 purity) targets to form the coating. Our vacuum system is equipped with two guns, allowing the preparation of the alloy to be divided into two steps. The first step involves depositing 5 nm of Ti as the adhesion layer, followed by depositing a 3 nm thin layer of Ag to prevent oxidation of the Ti. The vacuum chamber is then vented to change the target for depositing 110 nm of the second layer, which is the $Ag_{100-x}Al_x$ thin film alloy. The targets are fixed at the distance of 110 mm from the holder of the substrate, with 30° angle between the normal and the target. The holder of the substrate could be set to be rotating to form homogenous thin film alloys or non-rotating to generate the gradient thin film alloy. During the sputtering process of the homogenous thin films, the substrates were rotated at 12 rev/min to promote uniform film growth.

During the deposition process, the chamber is evacuated to a base pressure greater than 10^{-4} Pa and an Ar flow maintained of 60 sccm to ensure a stable and consistent ion bombardment environment. Each gun is connected to *DC* power supply, allowing for adjustments in current to achieve the desired thickness. No heat was applied to the substrate, and the deposition was performed at room temperature, because of that increasing the substrate temperature could increase the ad-atom mobility, and hence affect the thin film microstructure (Barranco et al., 2016). Before depositing the thin film, a calibrated deposition rate for each target as a function of the current passing through the gun was calibrated by substituting the substrate holder with a crystal deposition rate monitor. The crystal monitor detects variations in resonant frequency caused by the deposition of a thin coating on its surface (Prochaska et al., 2006).

3.1.2 Melting and casting approach

Melting method, as a widely used and straightforward process, is employed to produce high-density alloys and intermetallic compounds. It entails mixing raw element constituents in stoichiometric ratios and then melting them to achieve a homogeneous molten mass. The mixture then heats to the melting temperature of the constituent with the highest melting point. The molten mass is then cast into pre-designed mold to produce the desired alloy. These methods are illustrated in Figure 3.4 (Tyagi & Ningthoujam, 2021). The quality of the resulting alloys is greatly affected by several parameters, including melting temperature, casting pressure, pouring temperature, and preheating temperature of the mold. It has been observed that decreasing the melting temperature reduces the fluidity of the molten alloy, leading to casting defects such as shrinkage. On the other hand, increasing the melting temperature can

induce the formation of hot cracks in the mold and result in porosity defects within the alloys (Dhaneswara et al., 2019).

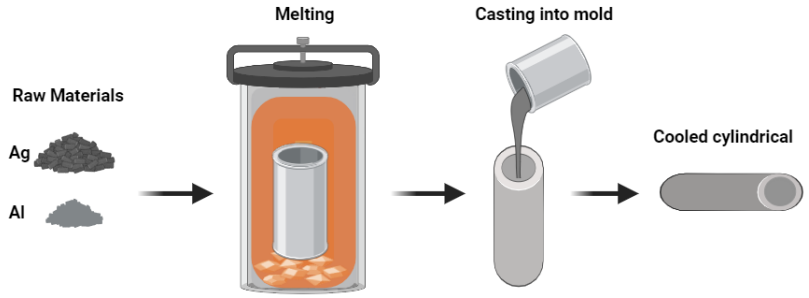

Figure 3. 4 A schematic diagram of melting and casting process that employed to prepare a AgAl alloy.

The precursor Al_xAg_{100-x} alloy was prepared via the melt casting method. Corresponding to a stoichiometry of 19.57 g of Al and 29.36 g of Ag (with the nominal composition of $Ag_{27}Al_{73}$), with a purity of 99.9 wt.%, were mixed in a clean alumina crucible and placed into a furnace for melting at 700° C to achieve the desired composition. The molten mixture was stirred and then carefully poured into a pre-heated cylindrical mold to prevent the introduction of any shrinkage defects (Suprapto et al., 2023), impurities, or air bubbles, forming a high-quality round rod of Al_xAg_{100-x} alloy mm in length and 15 mm in diameter.

The cast Ag_xAl_{100-x} alloy was subjected to homogenization heat treatment at 500 °C in a 1200C Dual Zone Split Tube Furnace (model OTF-1200X-80SL) for a holding time of 4320 minutes under a high vacuum of 8×10^{-5} torr to reduce elemental segregation. The heat treatment profile is shown in Figure 3.5. The homogenized $Ag_{100-x}Al_x$ alloy was then allowed to cool gradually to form equilibrium phases.

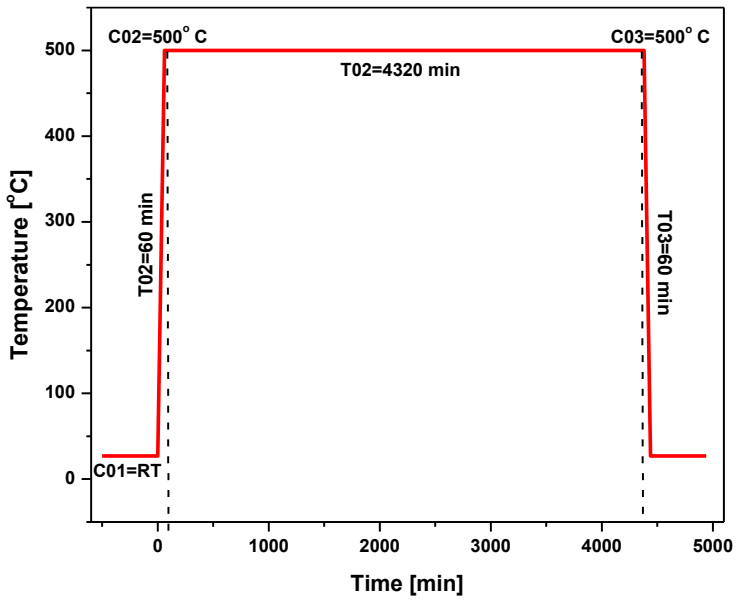

Figure 3. 5 Annealing profile used for homogenizing the as-cast alloy at 500 °C, the profile shows the parameters that need to be set up prior to starting the annealing procedures.

As can be seen in the annealing profile, the annealing process is conducted in three steps: temperature ramping, dwelling, and cooling profile. This project employs gradual ramping from room temperature to 500ºC for a 60-min ramping period to minimize thermal stress, which can cause microstructural defects or cracking. Moreover, the gradual heating ensures sufficient time for uniform heat distribution within the film, ensuring homogenization of the alloy or phase transformation begins (Afzali et al., 2016; Wang et al., 2018).

In the second step, the film dwelled for 4320 min at 500°C to ensure sufficient atomic mobility and diffusion to stabilize the alloy's composition and microstructure. It is found that higher temperatures, such as 540°C are used for homogenizing the structure, while the lower temperatures between 150 and 300°C are often used for fine-tuning precipitation and improving surface properties. Regarding dwell time, prolonged dwell time is essential as it allows for complete diffusion and phase formation, thereby creating uniform corrosion during dealloying (Afzali et al., 2016; Erlebacher et al., 2001a; Wang et al., 2018).

Finally, the annealing temperature decreases gradually from 500ºC to room temperature for a cooling period of 60 min to avoid thermal shock and prevent the formation of unwanted phases or microcracks during rapid cooling (Herrmann, 2006).

To study the physical properties of alloy thin films and bulk alloy samples, the thin films were cut into square shapes with dimensions of 1×1 cm^2, while the bulk samples were cut into discs with a thickness of 2 mm and a diameter of 12 mm as Figure 3.6 (a) and (b) demonstrates.

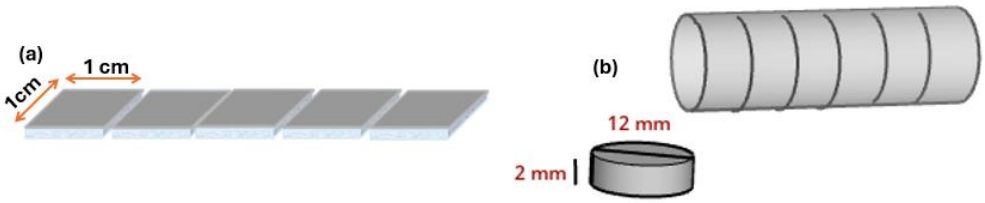

Figure 3. 6 Sketches (a) shows the way of cutting the np-S, Ag, Al, and TiO_2 thin films into square-shape with dimensions of 1 cm in width and 1 cm in length, and (b) illustrates the way of cutting the bulk sample into 8 discs with the thickness of 2 mm and diameter of 12 mm.

3.1.3 Heat treatment

Heat treatment processes involve subjecting the alloys to controlled heating and cooling cycles to alter the microstructure of the alloys and, consequently, modify their properties, such as their physical and mechanical properties. The heat treatment procedure is often necessary to

remove the defects, induce crystallization, and promote the growth of the grains. Furthermore, heat treatment can lead to further phase transitions. The efficacy of heat treatment procedures, and hence the characteristics of the resulting alloys, depend on various treatment parameters, including holding temperature, duration, and cooling process. These factors are determined based on the alloy composition and the specific attributes sought in the final product.

Within the current project, the 1200C Dual Zone Split Tube Furnace (model OTF-1200X-80SL) with the maximum heating rate of 20° C/min was used to anneal the as-deposited $Ag_{100-x}Al_x$ alloy thin films in forming gas (mixture of N_2 and H_2 gas) to avoid the oxidation of alloys' surface during annealing. The samples were placed on quartz boats and then placed inside quartz tube inside the furnace under the type K thermocouple and coil wire heating element. The samples were ramped at the maximum rate to the annealing temperature for a duration of 60 min before being cooled at the maximum rate to room temperature. The annealing profile is shown in Figure 3.7.

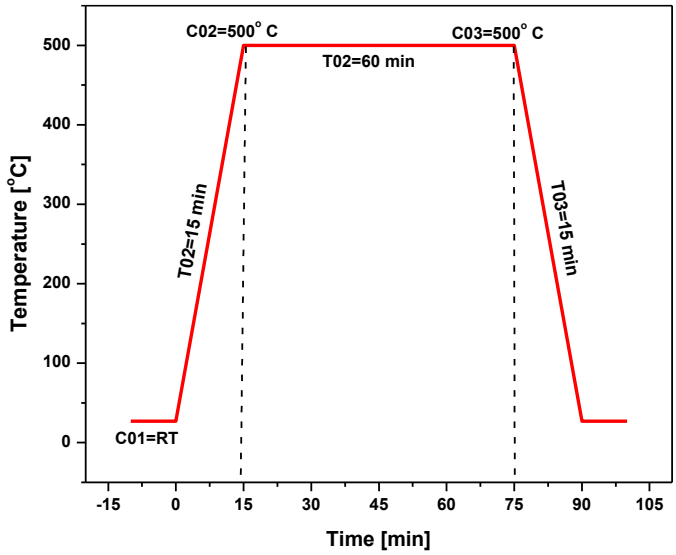

Figure 3. 7 Annealing profile used in this project showing the parameters that need to be set up prior to starting the annealing procedures.

3.1.4 Chemical dealloying

For nanoporous evolution, dealloying method as a simple and effective method has been employed to prepare the *np-S* thin films and bulk Ag sponges in this work. In our experiments we prepared *np-S* thin films and bulk Ag sponges by the selective chemical etching of Al from the $Ag_{100-x}Al_x$ thin film alloys and bulk $Ag_{100-x}Al_x$ alloys using alkaline aqueous solution to dealloy the alloy thin films and acidic aqueous solution to dealloy the bulk alloy samples. Due to the formation of intermetallic compound during the preparation and heat treatment processes of bulk Ag-Al alloys, which is resistant to dissolve in alkaline solutions,

these bulk alloys are dealloyed in acidic solutions. We selected the Al as an active component in the alloy due to direct and rapid dissolution of Al element in acidic or alkaline aqueous solutions under free corrosion conditions. Additionally, Al has a lower density (2.7 g/cm^3) compared to Ag (10.3 g/cm^3) (Mint, 1964), which further increases the diffusion rate of removal Al. Therefore, by controlling Al concentration in the alloy, we can control the speed of reaction and nanopore structures.

In this project, the dealloying process for the thin film alloys was conducted using a freshly prepared aqueous solution of NaOH at ambient temperature for different times. However, the heat treated $Ag_{100-x}Al_x$ alloys were subjected to chemical dissolution in HCl aqueous solution at room temperature, continuing the dealloying process until no obvious bubbles were formed. All samples that underwent dealloying were rinsed with fresh Milli-*Q* water for cleaning, followed by ethanol for drying. The as-dealloyed samples were stored in a vacuum desiccator to alleviate the effects of oxidation.

3.2 Characterization Techniques

3.2.1 Topography

3.2.1.1 Scanning electron microscopy (SEM)

Scanning electron microscopy is an effective technique for analysing the surfaces of samples at the nanometer to micrometre scales. SEM can provide information about the specimen's surface topography, grain orientation, chemical composition, and crystal structure due to the producing of a number of signals when the primary electron beam interacts with sample atoms as Figure 3.8 (a) demonstrates. These include Auger electrons, secondary electrons (SE), backscattered electrons (BSE), characteristic X-rays, continuum X-rays, and secondary fluorescence.

Our study focusses on understanding the SE and BSE signals, SE signal is generally utilised to generate high-resolution images of the sample surface, which provide insights into its morphology and topography, as well as BSE signal, which can also disclose information on the chemical composition and crystal orientation. Areas with higher average atomic number produce a larger quantity of backscattered electrons compared to areas with lower atomic number, resulting in a brighter appearance in the image (Goldstein et al., 2017; Mohammed & Abdullah, 2018).

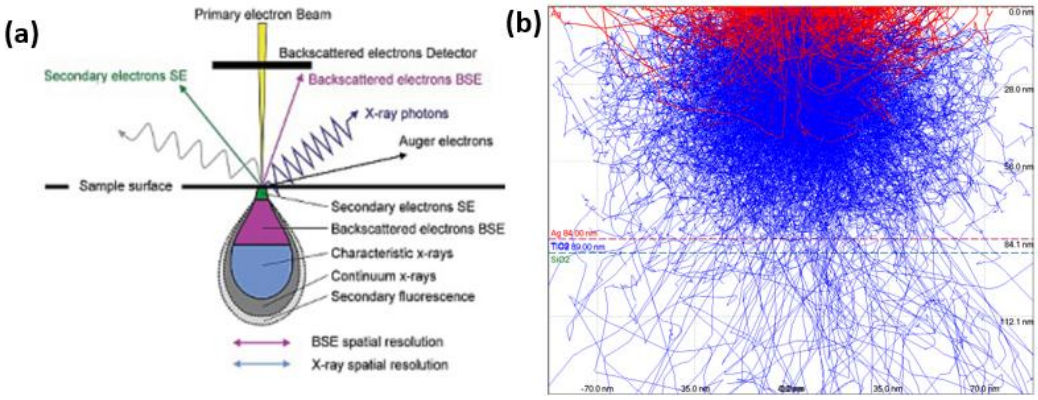

Figure 3. 8 (a) diagram of interaction volume, which shows generating variety of signals when the primary electron beam strikes the sample atoms (Kelsall et al., 2005), (b) Simulation of electron trajectories using CASINO software in np-S thin films with accelerating voltages of 5 kV and beam radius 10 nm.

For collecting SEM images and EDS spectra, the sample was mounted on aluminium stubs, cleaned using a N_2 flow, and subsequently placed in the SEM chamber. A Zeiss Supra 55VP (model field emission scanning electron microscope (FE-SEM)) was the primary instrument utilized for collecting the SEM images of the surface of the *np-S* thin films and bulk *np-S* samples. This instrument is equipped with a Schottky field emission gun, and an in-lens secondary electron detector. The primary function of this instrument was to gather topographical and morphological images for the samples under investigation. The microscope operated in high vacuum mode with a low acceleration voltage ≤5 kV to ensure that the beam interacts with the sample in an area that is very close to the surface of the sample as can be seen in Figure 3.8 (b). The SEM images were captured at high magnification and at a working distance of ≤ 4mm.

For quantitative analysis of the microstructure of the *np-S* thin films and bulk Ag sponges, a statistical analysis of the SEM images was performed using ImageJ software (Health, n.d.). The diameter of at least 100 pores and ligaments were measured to obtain accurate size distributions.

3.2.1.2 Energy Dispersive X-ray spectroscopy (EDS)

As previously discussed in Section 3.2.1.1, the signals generated from the interactions between the electron beam and sample atoms can be utilized to identify the elements within the sample.

Choosing the appropriate accelerating voltage for the electron beams that can penetrate the sample to collect information about the elemental concentrations is paramount. For thin

films with a thickness of 118 nm, defining the penetration depth of the electron beam is necessary to ensure that the analysis is confined to the film rather than the substrate. However, determining the penetration depth of the thick bulk samples can assist in identifying the volume of material being probed and the extent of beam-induced effects. For this reason, the CASINO (Monte Carlo Simulation of Electron Trajectory in Solids) software (Sherbrooke, n.d.) was used to investigate the penetration depth of electron beams with different accelerating voltages. Figure 3.9 shows that the best values for accelerating voltage in studying the thin films are 10 kV and 15 kV for the bulk samples.

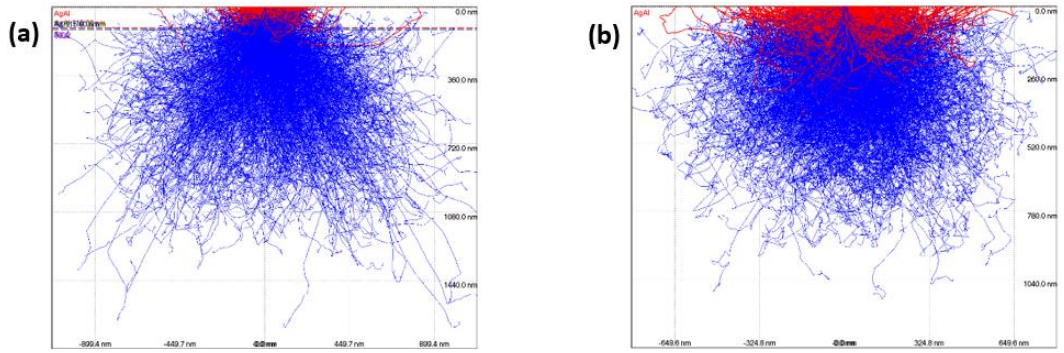

Figure 3. 9 Simulation of electron trajectories using CASINO software in (a) AgAl alloy thin films with accelerating voltages of 10 kV, beam radius 10 nm, and (b) bulk samples with accelerating voltages of 15 kV, beam radius 10 nm. red lines represent the backscattered electrons, while the blue lines indicate X-rays.

In present project, a Zeiss Evo LS15 (model scanning electron microscope (SEM)), shown in below, was utilized. This instrument equipped with a Bruker SDD XFlash 5030 detector, it provided information about the chemical composition of the investigated samples at high accelerating voltages ranging between 10 (for thin films) and 15 kV (for bulk samples), and at a working distance of 10 mm.

For each sample, the EDS spectra were acquired at five different positions. The uncertainty in the measured concentrations of the alloys and np-S thin films is within ±1 at. %; however, for the bulk Ag sponge samples, it is within ±3 at. %.

3.2.1.3 Stylus profilometer

Stylus profilometry is the most commonly used approach to measure thin film thickness due to its rapid and cost-effective performance while maintaining high accuracy and reliability. It is useful for both opaque and transparent films.

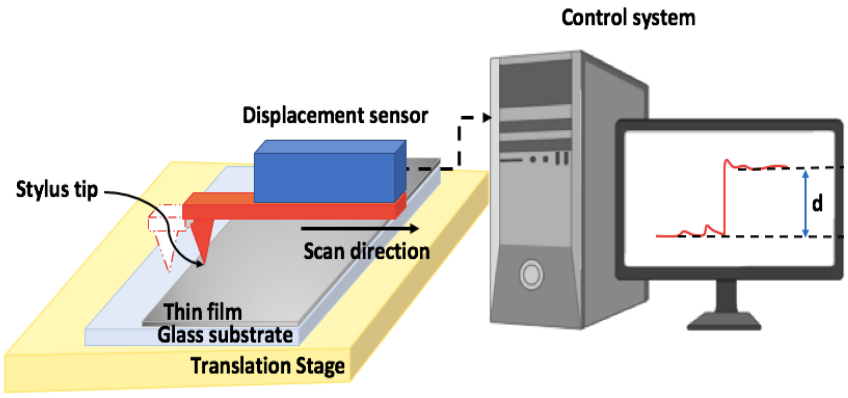

Figure 3. 10 a schematic diagram shows the profilometer configuration, the output response is shown in the monitor which is directly proportional to the variation in the surface height of the sample.

In order to measure the thickness of metal thin films, a step must be created between the coating surface and the substrate surface as Figure 3.10 illustrates. These steps were established by removing film after deposition (Ohring et al., 1992; Piegari & Masetti, 1985). The results provide a profile of the sample surface, with resolution limitations mostly due to stylus radius scratching of the film surface, substrate roughness, and vibration during measurement.

To minimize the film surface damage caused by stylus scratching, a low stylus force could be applied during the scanning. To avoid damaging the stylus, the film should be well-adhered to the substrate, and the testing surface should be cleaned. However, this technique does not require particular sample preparation.

In this work, A DektakXT (model stylus profilometer) (Bruker, USA) is employed. The stylus radius for the standard scan was 2 µm with a tracking Force of 1 mg (9.81 µN), a scanning length of 500 µm and a duration of 60 s.

3.2.1.4 Atomic force microscopy (AFM)

Atomic Force Microscopy (AFM) is a class of scanning probe microscopy (SPM) that is highly effective in imaging surface morphology and measuring surface roughness at the nanoscale. It offers extremely high magnifications of up to 10^8 and a resolution of 0.1 nm in the x and y axes, and 0.01 nm in the z axis. This instrument shows the capability to examine the surfaces of both conductive and non-conductive samples. The operation of AFM involves the scanning of a sharp tip in proximity (0.2-10 nm probe-sample separation) to the surface of the sample. It detects the forces between the tip and the surface in order to generate a topographic map (De Oliveira et al., 2012; Sanders, 2019; Tański et al., 2018).

The AFM has many advantages that include its ability to generate three-dimensional topographic images of surfaces with extremely high resolution, allowing for the visualisation

of surface features at the atomic level. Additionally, it enables imaging of dielectric material surfaces without the need to apply conductive layers and can determine surface roughness parameters without the need for additional tests. As Figure 3.11 demonstrates, this technique operates in different modes, each affecting how the tip interacts with the sample. Our study focused on non-contact where the tip oscillates and provides feedback based on its movement.

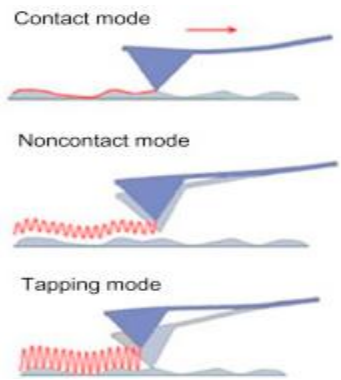

Figure 3. 11 AFM operating modes namely; contact, non-contact and tapping modes (Asmatulu & Khan, 2018)

Herein, the surface roughness of AgAl thin alloy films was measured using an XE7 (model atomic force microscope) (Park Systems, Suwon, Korea). The scans were taken in non-contact mode to avoid damaging the sample surface. The scans were performed using an NSC15 cantilever (radius of 10 nm, height of 15 µm, length of 125 µm, sensitivity of 59.99 V/µm, force constant of 40 N/m, and resonance of 325 kHz, according to the manufacturer) over an area of 2.5× 2.5 μm^2 with a resolution of 256× 256 pixels. The root mean square (RMS) surface roughness of the alloy thin films was determined using XEI data processing and analysis software (Park Systems, Suwon, Korea).

3.2.2 Crystal Structure

3.2.2.1 X-ray Diffraction (XRD)

X-ray diffraction is a powerful, and versatile analytical approach used to investigate the crystalline materials structure. This technique is non-destructive and can be employed for both qualitative and quantitative analysis of crystalline materials. It is employed in this work to identify the diffraction peaks, determine the presented phases and the crystal structures of the alloys, *np-S* thin films, and Ag sponge samples. Moreover, it can be also used to calculate the crystal size and estimated the lattice parameters of these materials.

Figure 3.12 (a) displays the conventional diffractometer using the Bragg-Brentano geometry. This geometry consists of several essential components, specifically the X-ray source, which produces a monochromatic beam of X-rays. The sample holder is positioned

opposite the source and is commonly rotated about an axis that is perpendicular to the incident X-ray beam. This rotation ensures that all crystallographic orientations are uniformly exposed. The detector, which captures the diffracted X-rays over a range of angles. In order to ensure accurate alignment, the detector and sample holder are affixed to goniometers, which enable precise modifications of their positions in relation to the incident beam. When X-ray beams interact with the electron clouds surrounding the atoms within a polycrystalline sample, the beam will penetrate to a specific depth within the sample before being fully absorbed or scattered. As demonstrated in Figure 3.12 (a), the beams also undergo scattering which leads to constructive interference of scattered waves. This results in diffracted beam when the path difference between beams 1 and 2 equals *n* times of the X-ray wavelength, satisfying Bragg's law, which can be expressed as Eq.3.1:

$$n\lambda = 2d\ sin\theta \ldots\ldots\ldots\ldots\ldots\ldots \quad (3.1)$$

Where n is integer, λ is X-ray wavelength, d is the space between the planes in the atomic lattice and θ is the diffraction angle (Bunaciu et al., 2015; Lee, 2017; ZhiLi, 2022).

The penetration depth of the X-ray in the conventional XRD analysis is several micrometers inside the sample (Brussel & Hosson, 1994). The collected XRD data is typically shown in the form of diffraction patterns displayed as a plot of the intensity of the diffracted beam against the Bragg angle (2θ) as Figure 3.12 (b) demonstrates. Peaks in the diffraction pattern indicate angle at which the atomic spacing in the material satisfies Bragg's law. Each substance has a distinct X-ray diffraction pattern, which can be likened to individual fingerprints. As Figure 3.13 shows, the positions, heights, areas, shapes and widths of XRD patterns provide critical information regarding the properties of the material under investigation. To identify an unknown sample, the diffraction pattern compared with known standards in the power diffraction database. This database provides essential information such as the chemical formula, substance name, crystallographic data, specimen data, and diffraction pattern data (Sharma et al., 2012). It can provide detailed information about crystallographic orientations, phases, structures, and other structural properties, like strain, grain size, size and degree of crystallinity, and crystal defects.

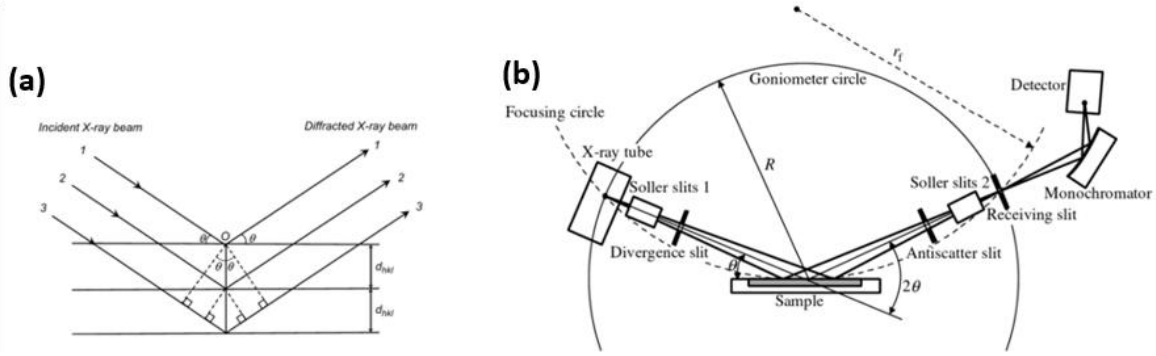

Figure 3. 12 (a) schematic diagram of the arrangement of the conventional diffractometer components which follows the Bragg-Brentano geometry (He, 2018), and (b) diffraction of the X-ray beam by the atoms of the material (ZhiLi, 2022).

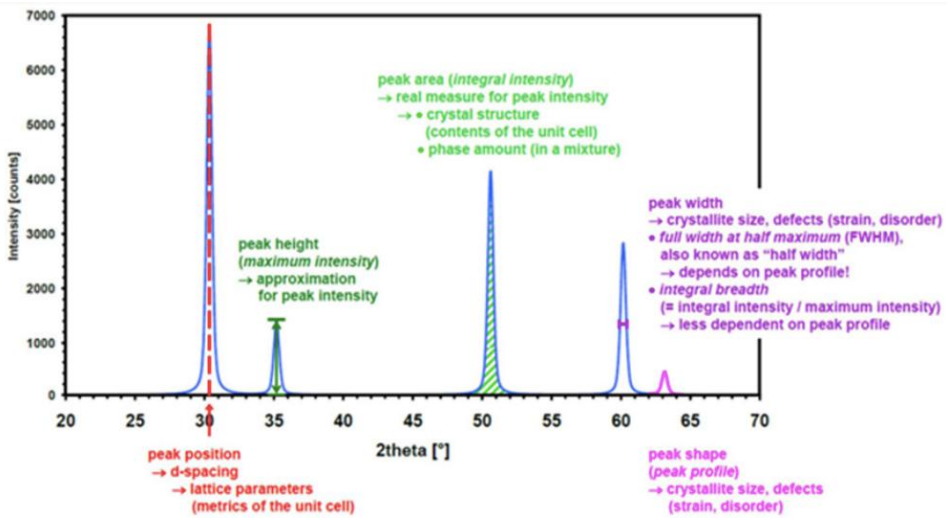

Figure 3. 13 structural information can be extracted from XRD pattern (Sharma et al., 2012)

Grazing incidence X-ray diffraction (*GIXRD*)

Grazing incidence diffraction methods are employed when the regional interest is found within surface layer of the sample. The distinct grazing diffraction setup is illustrated in Figure 3.14. The grazing incidence approach employs a very small incident angle of the *X*-ray beam on the sample, which is typically between 0.1° and 3.0°. At this shallow angle, the incident X-rays interact just with the top layers of the sample, which leads to decreasing the penetration depth of the incident X-rays. Therefore, the intense signal produces from the surface layers and weak signal from the substrate, making this XRD setting highly sensitive to the surface of the sample under investigation (Brussel & Hosson, 1994).

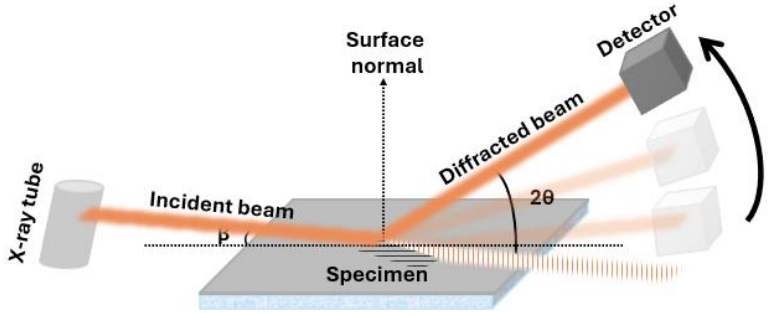

Figure 3. 14 Schematic diagram showing the grazing incidence X-ray diffraction beam (GIXRD).

The grazing incidence method has been utilised for the thin films in this work to maximise the amount of signal obtained from the thin film and minimise the amount of signal obtained from the substrate of the film,

The X-ray diffractometer utilised in this project was the Bruker D8 Discover (model X-ray diffractometer (XRD)), with Cu Kα X-rays and λ= 1.5418 Å. The instrument featured a primary beam monochromator and an LYNXEYE_XE (*0D* mode) detector. The X-rays were excited using an electron gun with an accelerating voltage of 40 kV and a current of 25 mA.

The X-ray diffraction (XRD) patterns were obtained using a grazing incidence angle of 1° and a 2θ angle spanning from 20° to 90°. For collecting the XRD patterns of the bulk Ag sponge samples, A Ni (0.02 rad) slit was inserted in the detector arm to filter out the Kβ radiation. The XRD patterns were collected with incidence angles θ between 7.5° and 40° with a step size of 0.01° and a $2\boldsymbol{\theta}$ ranging from 15° to 80° with a step size of 0.02°.

These XRD patterns provide critical insights into the crystal structure, identify the crystalline phases present, and determine their composition in the alloys and in both the np-S thin films and the bulk np-S samples. This information forms the basis for the subsequent investigations presented in this thesis.

Rietveld refinement of the XRD pattern

The Rietveld refinement method was performed using Match! software (version 4) and FullProf software (Impact, n.d.). Initially, a profile-fitting search-match was employed for qualitative analysis and identification of the phases in the alloys and sponges. Subsequently, the Rietveld refinement process was utilized for quantitative analysis by closely replicating the experimental diffraction pattern. This was achieved by fitting a model containing the crystal structure data and preferred orientation of the phases. The calculation involves the refinement of selected parameters such as zero-point, specimen displacement, scale factors, unit cell parameters, profile shape, Caglioti half-width, and background to reduce the weighted average Bragg R-factor and chi-squared (χ^2) value

3.3 Physical properties

3.3.1 Electrical resistivity measurements

3.3.1.1 Hall effect measurement

Electrical resistivity describes the opposition of the materials to the flow of electrons through it, which requires continuous pathways. In nanopore structures, the continuous ligaments can easily provide those paths for the movement of the electrons. High connectivity

of the nanostructures typically results in lower material resistivity, hence efficient electron transport. In this work, the connectivity of np-S ligaments was assessed by measuring the electrical resistivity and carrier mobility using Van der Pauw and hall effect measurements.

The Hall effect measurement is a simple method employed to investigate the electrical properties of materials. This approach relies on the Hall effect phenomenon, which occurs when a conductor carrying an electric current I is exposed to a magnetic field B, perpendicular to the current. This results in the creation of a potential difference, known as the Hall voltage V_H, whose direction is perpendicular to both the electric current and the magnetic field, as depicted in Figure 3.15. The Hall effect is caused by the Lorentz force exerted on a moving electron exposed to both an electric field and a magnetic field. The Lorentz force F is given by Eq.3.2.

$$\vec{F} = -e(\vec{E} + \vec{v} \times \vec{B}) \text{..... (3.2) (Dunlap, 2019)}$$

where e represents the electron charge, E is the electric field, v is the velocity of the electricity, and B is the magnetic field.

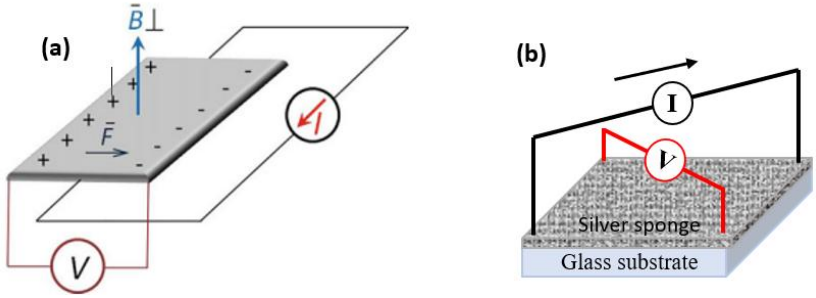

Figure 3. 15 (a) schematic diagram shows the basic arrangement of Hall effect experiment (Azarov et al., 2023), and (b) schematic diagram shows Van der Pauw method and four ohmic contacts on the np-S thin films to conduct the Hall effect measurements. In this measurement, the current is passed across opposite pair of contacts, while the voltage is measured across the other pair of contacts.

This force leads to bending and accumulation the negative charges on one side and the appearance of positive charge on the opposite side of the width. The charge accumulation continues until a state of equilibrium is achieved, at which point the Hall force perfectly balances the Lorentz force. Hence, the generated potential difference (Hall voltage) can be calculated using Eq.3.3.

$$V_H = \frac{IB}{ntq} \text{..... (3.3) (Azarov et al., 2023)}$$

Where n is the concentration of charge carrier, t is the sample thickness and q is the electric charge.

By measuring this voltage, significant information about the charge carriers type and concentration, charge density and carrier mobility in the materials under investigation can be obtained (Azarov et al., 2023; Srinivasan et al., 2023).

3.3.1.2 Van der Pauw resistivity measurement method

Van der Pauw Method is suitable for samples exhibiting irregular and arbitrarily shapes. It is frequently applied to reduce the impact of sample edge effects and the changes in size and shape of the sample on the resistivity measurements. This approach fundamentally involves the usage of four ohmic contacts, labelled as 1, 2, 3, and 4, as illustrated in Figure 3.16. Two of these probes are designated for current sourcing, while the remaining two are employed for voltage measurement. The configuration of the probes is switched to calculate different values of the electrical resistance. Typically, a set of 8 measurements is commonly taken around the sample's perimeter. Subsequently, the values are combined to calculate the resistivity. Eq.3.4 (Azarov et al., 2023; Peter & Cardona, 2010).

$$\rho = \frac{\pi}{ln2} t \frac{R_{12,34}+R_{23,41}}{2} F \ldots\ldots\ldots\ldots\ldots\ldots \text{(3.4) (Azarov et al., 2023)}$$

Where $R_{12,34}$ and $R_{23,41}$ is the electrical resistances, and are given by $R_{12,34} = \frac{V_{12}}{I_{34}}$, $R_{23,41} = \frac{V_{23}}{I_{41}}$, F is a geometrical correction factor which is equals 1 for square sample.

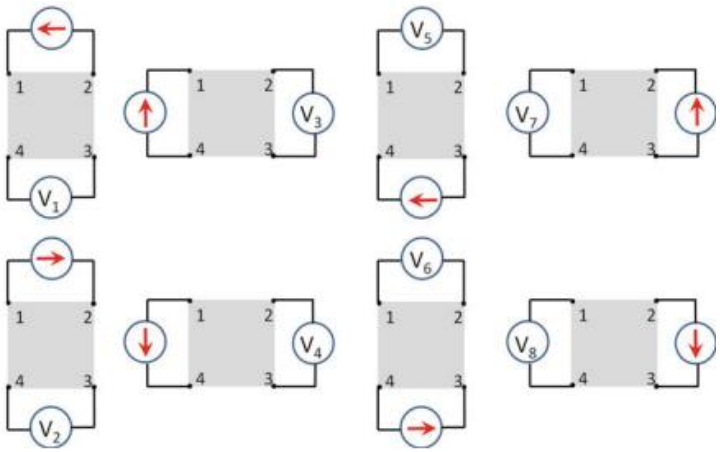

Figure 3. 16 (a) schematic diagram shows the basic experimental setup for conducting Van der Pauw resistivity measurements (Azarov et al., 2023).

In the present project, the electrical resistivity measurements of *np-S* samples were performed using ezHEMS for the four-probe van der Pauw method on a Hall effect measurement (NanoMagnetics Instruments, Oxford, United Kingdom) at the temperature *T* of 300 K, a magnetic field *B* of 0.6268 T and a current of 1 mA. The experimental geometry and the parameters were placed in Table 3.1 and Figure 3.17.

Table 3. 1 Thin films dimensions, length in mm and width in mm and thin films thicknesses employed during the resistivity measurements

Sample No.	Length (mm)	Width (mm)	Thickness (nm)
S1	9.8	9.8	89
S2	9.8	9.8	84
S3	9.8	9.8	81
S4	9.8	9.8	78
S5	9.8	9.8	71
S6	9.8	9.8	60

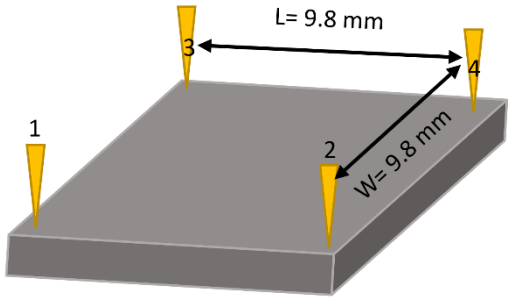

Figure 3. 17 Geometry of four-probe resistivity measurement

3.3.2 Dielectric functions and optical constant measurement

3.3.2.1 Spectroscopic ellipsometry (SE)

Spectroscopic ellipsometry is a sensitive, non-destructive, and non-contact optical technique utilized for estimating the thickness of the thin films, and determining the optical properties of various materials, thin films, interfaces, and surfaces (Politano & Versace, 2023). Therefore, this technique has been employed in this study to provide important optical properties, such as the complex dielectric function and effective refractive index of np-S thin films with different pore and ligament sizes from the measured data using appropriate optical model.

The ellipsometry measurements depend on detecting the changes in polarized light resulting from either light reflection from or light transmission through a sample. The two ellipsometry parameters Ψ, the amplitude ratio, and Δ, the phase difference between *p*-polarized and s-polarized light beam, can be measured at different wavelength of incidence light. Ψ and Δ can be related to the complex ratio of Fresnel reflection coefficients of the *p*-polarized and *s*-polarized light by the Eq.3.5:

$$\rho = \frac{\rho_p}{\rho_s} = \tan(\Psi)e^{i\Delta} \ldots\ldots\ldots\ldots\ldots\ldots (3.5)$$

The ellipsometry method is characterised by its indirect nature, the procedures that outlined in Figure 3.18 (a) were followed. The analysis of Ψ and Δ data necessitates the use of an optical model since interpreting measurement results based on their absolute values is more challenging (Fujiwara, 2007; Woollam, 2012). Figure 3.18 (b) shows an example of the optical model where an incident light wave is reflected on and transmitted through the thin film surface. The model consists of three layers, namely, air/thin film/ substrate, each layer is defined by the complex refractive index and layer thickness. Therefore, the complex quantity ρ can be written as Eq.3.6:

$$\rho\ (N_0, N_1, N_2, d, \theta_0) = \tan(\Psi)e^{i\Delta} \ldots\ldots\ldots\ldots\ldots\ldots\ldots\ldots\ (3.6)$$

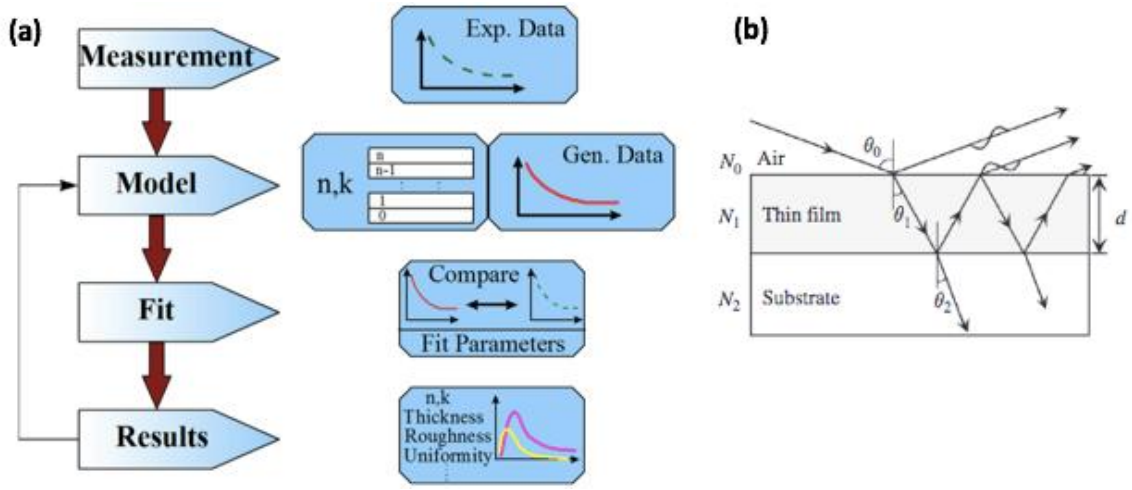

Figure 3. 18 (a) diagram depicting the procedures involved in analysing ellipsometry data (Woollam, 2012) and (b) an example of the optical model of the film consisting of three layer; air/thin film/substrate (Fujiwara, 2007).

In the current work, the optical properties of the alloy systems and *np-S* thin films were studied using a JA Woollam Variable Angle Spectroscopic Ellipsometer (VASE) (JA Woollam, Lincoln, Nebraska, USA). This instrument consists of a rotating polarizer and a fixed analyser to detect the two ellipsometry polarization parameters Δ and ψ. The ellipsometry measurements were conducted within the spectral range of 300 to 2400 nm (corresponding to photon energies ranging from 4.13 to 0.51 eV), using a wavelength step of 5 nm, at incidence angles from 65° to 75° with the angle step of 5°, and a slit width of 1700 µm.

Ellipsometry data analysis software

In order to evaluate the samples effectively, it is essential to employ an optical model simulation using WVASE ellipsometry analysis software. Two optical models were constructed to replicate the observed spectra of the as-deposited $Ag_{100-x}Al_x$ alloy thin films and *np-S* thin films. A four-layer model was used to analyse the experimental spectra of the thin

films. This model consisted of a layer composed of a rough surface, $Ag_{100-x}Al_x$ alloy with varied thicknesses, and TiO_2 layer, as well as a layer made of glass serving as the substrate (see Figure 3.19 (a)). Simultaneously, a three-layer model is employed to analyse the optical properties of de-alloyed thin films. This model comprises an EMA (Ag+void) layer with different thicknesses thickness, TiO_2 layer, and glass substrate layer, as illustrated in Figure 3.19 (b).

Due to the difficulties of obtaining the optical properties of inhomogeneous np-S thin films experimentally, an optical model, specifically the Bruggeman effective medium approximation (BEMA), is utilized to accurately calculate and predict the effective dielectric function and effective refractive index of these nanocomposite systems. In this model, the dielectric properties of Ag were utilized, while Ag fractions were estimated from the XRD refinement results which are presented in chapter 4 and 5.

The quality of the proposed optical models for extracting the optical properties of the $Ag_{100-x}Al_x$ alloys and np-S thin films was evaluated using the Mean Squared Error (MSE) values, which ranged between 1.7 and 3.6. It was found that complex samples with multilayers may have MES values more significant and still be considered acceptable (Losurdo & Hingerl, 2013). Therefore, these MSE values indicate a good agreement between the data measured by ellipsometry and the data generated using the optical model. This implies that the employed optical models are highly effective in accurately representing the optical properties of the nanocomposite systems.

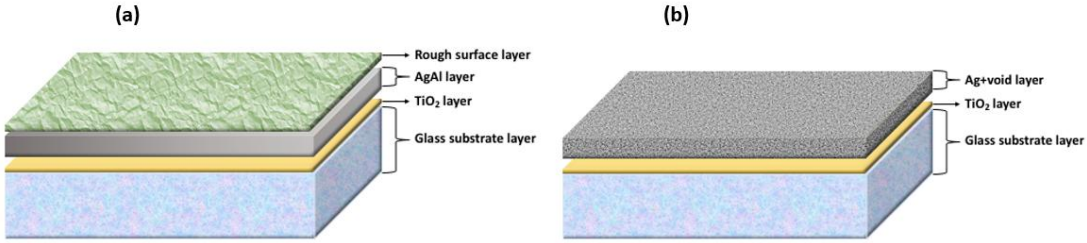

Figure 3. 19 schematic drawing of (a) the four-layers model for analysing SE spectra of gradient alloy thin films, (b) the three-layers model for analysing SE of gradient Ag nano-sponge samples.

3.3.3 Reflectance and transmittance measurement

3.3.3.1 UV-Visible spectrophotometer

A UV-Visible spectrophotometer is a commonly used instrument to investigate optical properties across a wide range of materials and sample types. It is a non-destructive, direct, precise, adaptable, and easy to use toll that can perform absolute measurements of both transmittance (T%) and reflectance (R%) within a single, integrated system and at multi-angles (Samanta, 2022; Soonmin, 2022).

Within this work, the interaction of light with *np-S* thin films, with varying ligament and pore sizes, through reflection was investigated using a universal measurement spectrophotometer (model Agilent Cary 7000) (Agilent Technologies, Agilent Technologies, Santa Clara, California, USA). This analysis was conducted over the wavelength range of 300 to 2500 nm, encompassing both the solid Ag thin film and all de-alloyed Ag-based ligament structure films.

3.3.4 Surface enhanced Raman scattering (SERS) spectroscopy

SERS has emerged as an ultra-sensitive and non-destructive surface analysis technique, capable for the detection of very low concentrations of molecules adsorbed on plasmonic nanostructure (Azimi & Docoslis, 2022; Hassanain et al., 2022; Le Ru & Etchegoin, 2009; Xie et al., 2022).

The choice of molecules for enhancing Raman signals in surface-enhanced Raman scattering (SERS) investigations is determined upon specific experimental requirements. Frequently favoured molecules include dyes such as rhodamine 6G (R6G), methylene blue, and crystal violet (CV), primarily due to their capacity for generating stronger signals and facilitating effectively bond to noble metal surfaces (Muehlethaler et al., 2017). R6G has been chosen as the probe molecule in this study. The decision was based on the fact that R6G is a highly fluorescent xanthene derivative that exhibits a molecular resonance Raman (RR) effect when stimulated within its visible absorption band at around 530 nm (Hildebrandt & Stockburger, 1984; Le Ru et al., 2007) with the enhancement as significant as 10^{14} to 10^{15} (Zhao et al., 2007). For this particular situation, a very low concentration of R6G was employed because of the exceptional sensitivity achieved by the synergistic effect of molecular resonance and surface enhancement (Hildebrandt & Stockburger, 1984). Moreover, the R6G molecules have a higher affinity for adsorption on Ag (111) (Yuan et al., 2021), which is a dominant facet for the present nanoporous thin film.

The SERS enhancement factor (EF) is a key factor for assisting the performance of a sample to be SERS substrate. It is calculated by comparing the SERS intensity I_{SERS} to the normal Raman intensity I_{NR}, as well as considering the quantity of absorbed probe molecules on the sample surface involved in SERS N_{SERS} and regular Raman signals N_{NR}. This equation can express as Eq.3.7:

$$EF = \frac{I_{SERS}/N_{SERS}}{I_{NR}/N_{NR}} \quad \text{..... (3.7) (Cara et al., 2020)}$$

The number of the molecules that contributed to the enhancement signal can be estimated by Eq.3.8:

$$N = \left(\frac{N_A M V_{probe\ solution}}{S_{substrate}}\right) \times S_{laser} \ldots\ldots\ldots\ldots\ldots\ldots \text{(3.8) (Zhang et al., 2011)}$$

Since N_A is Avogadro's number equals $6.022 \times 10^{23}\ mol^{-1}$, M is analyte molar concentration, $V_{probe\ solution}$ is analyte volume, $S_{substrate}$ is substrate size and S_{laser} is laser spot size. This employed method was described in Reference (Zhang et al., 2011).

Herein, *np-S* thin films, which have varying nanopore structures, and varying surface area with numerous active sites for the adsorption of analyte molecules, have been employed as SERS substrate. To calculate the enhancement factors of produced *np-S* thin films, Raman spectra were obtained by a Raman spectrometer system (model Renishaw inVia) (Gloucestershire, UK) with an excitation laser wavelength of 532 nm and power of 0.01 % mW. The samples were mounted under a Leica DMLB microscope (Wetzlar, Germany) equipped with a 50X/0.55 numerical aperture (NA) objective lens with a working distance of 1 mm, and the laser spot diameter was 1180 nm with the spatial resolution of 590 nm. The spectra were collected at four random points in each position with an acquisition time of 10 s. R6G with a 10^{-6} M concentration was used as the probe molecules. The dilute solution of the R6G was freshly prepared the day before experimenting and was stored in a 200 mL bottle. Before conducting the SERS measurements, A 2 µL droplet of the probe molecule is dropped on the *G-np-S* film on glass substrate for 3 h to ensure sufficient adsorption of the probe molecules onto the surface of the sample and obtain a strong signal, then washed with methanol and left to dry in the air.

3.3.5 Electrochemical surface area measurements

The mass of the prepared *np-S* thin film being too small for performing the BET measurements. Therefore, electrochemical capacitance measurements have been employed to estimate the surface area of a duplicate S6 sample, see for example Lakshmanan et al.(Lakshmanan et al., 2015). This method has been illustrated briefly in the reference (Cortie et al., 2005). The method includes using an RC electric circuit consist of a DC power supply source for producing a voltage (V_s) of 1.0 V, an external resistor (R_e) of 8 kΩ, and a double pole reversing switch connected to the np-S thin film electrodes of the capacitor. The *np-S* thin film electrodes were immersed in 0.1 M KNO_3 aqueous electrolyte. The voltage across the electrodes during the charge and discharge processes was measured using a LabJack U12 A/D

convertor. The ostensible capacitance of the electrodes could be calculated from the discharge voltage by transformation of the expression.

$$V(t) = V_0 e^{-t/RC} \quad \text{..... (3.9)}$$

to

$$ln\left(\frac{V(t)}{V_0}\right) = -t/RC \quad \text{..... (3.10)}$$

Since $V(t)$ indicates the voltage across resistance R at time t, t refers to the elapsed time, and C is the ostensible capacitance of the electrodes.

Least squares linear regression of data taken in incrementally advanced segments was used to define the slope $-1/RC$. The capacitance at 0.20 V was chosen as the datum for comparison due to the variation of the nanoporous system capacitance with time or voltage (because of the necessity for diffusive processes in the electrical double layer or pores to occur). At least five charge-discharge cycle measurements were performed on symmetrical electrodes, as shown in Figure 3.20, with the prepared capacitor immersed in the electrolyte. The capacitance was then normalized to the area of one side of a glass slide (18.75 cm²).

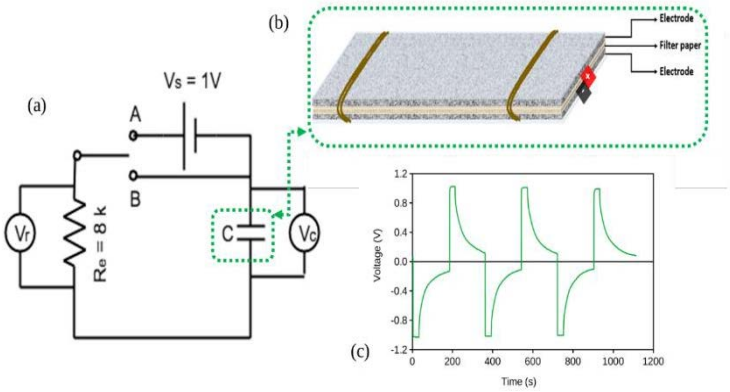

Figure 3. 20 (a) R-C circuit employed for studying the charge and discharge of the capacitor. As the circuit is connected at position A, the Vs (voltage of power supply) is equal to Vc+Vr (terminal voltage and external resistance voltage, respectively). A discharge cycle through the resistor is achieved when the circuit is connected to point B. (b) A schematic diagram of the supercapacitors used in this study consists of two sandwiches of np-S thin film electrodes with a piece of filter paper as a spacer. (c) the polarity of alternate cycles was reversed to allow for symmetrical alterations (if any) to exist on the np-S thin film electrodes.

3.4 Antibacterial properties

One of this project aims is studying the antibacterial performance of *np-S* thin films and bulk Ag sponges with different nanoporous structures against two different strains of the bacteria. *Pseudomonas aeruginosa* (*P. aeruginosa*) strain PAO1 and *Escherichia coli* (*E. coli*) strain DH5α have been chosen for this test. *P. aeruginosa* PAO1serves as a model organism

for investigating the influence of *np-S* thin films on the formed biofilm, making it an ideal candidate for evaluating the efficacy of this new antibacterial agent. However, *E. coli DH5α* as a non-pathogenic provides a convenient and safe model for antibacterial testing of both *np-S* thin films and bulk Ag sponges.

3.4.1 Agar plate colony growth

The Streak-plate protocol, which is explained in detail in reference (Sanders, 2012) and presented in Figure 3.21, has been employed in this project to grow bacterial culture and isolate bacterial colonies on an agar plate. Two agar plates were inoculated: one with *E. coli* and the other with *P. aeruginosa*. To avoid condensation from falling onto the colonies, the plate is incubated in an inverted position at 37°C for 24 h, resulting in optimal growth conditions, and then store at refrigerated temperature.

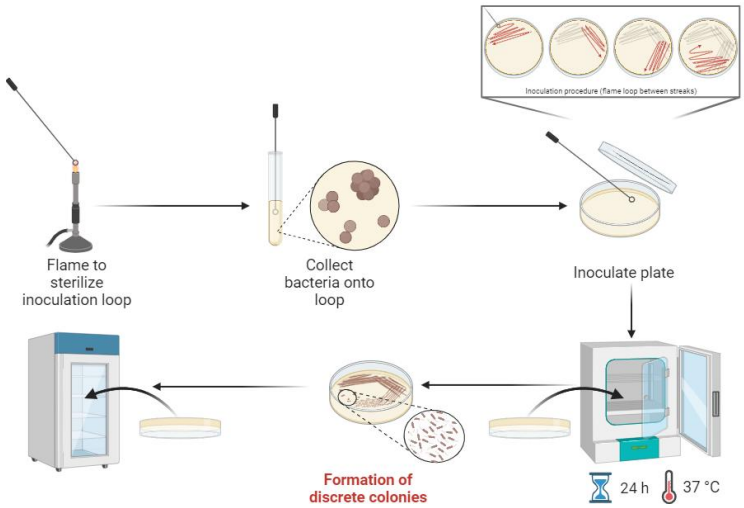

Figure 3. 21 diagram of the streak-plate method used to prepare the bacteria culture. Adapted from "streak plate method", by BioRender.com (2024). Retrieved from https://app.biorender.com/biorender-templates

3.4.2 Preparing Mueller-Hinton Broth (MHB) solution

Mueller-Hinton Broth (MHB) solution is the most common solution uses to growing a broad range of bacterial species including *E. coli* and *P. aeruginosa*. In this project, the MHB solution was prepared by adding 21 g of MHB powder to a clean, sterile container. Subsequently, 1000 mL of deionized (DI) water was added to the MHB powder in the container using a graduated cylinder. The mixture was stirred gently to fully dissolve the MHB powder and thus ensure homogeneity of the resulting solution. The solution was placed in an autoclave for 15 min for sterilizing at 121°C and then allowed to cool to room temperature.

3.4.3 Preparing the np-S thin films and bulk Ag sponges for antibacterial tests

The size uniformity is important factor for accurately studying the effect of the *np-S* thin films on bacterial growth. For this reason, each film slide was cut to the same dimensions, ensuring that the contact surface with the bacterial cells was consistent in all experimental setups. The glass cutting toll was used to cut the thin film slides to 12 coupons each coupon with the dimension of 5 mm in width and 5 mm in length as Figure 3.22 (a) depicted. Similarly, each bulk Ag sponges, bulk Ag and bulk Al discs were cut radially into six pie-shaped pieces as Figure 3.22 (b) demonstrates. Prior to conducting the experiment, the resulting thin films and bulk samples were then sterilized using an autoclave in a dry mode at 121 °C for 60 min.

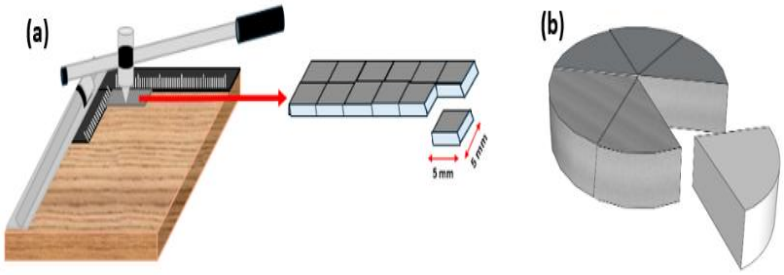

Figure 3. 22 Sketches (a) shows the use of a glass cutter tool to cut the np-S, Ag, Al, and TiO_2 thin films into square-shape with dimensions of 5 mm in width and 5 mm in length, and (b) illustrates the way of cutting the bulk samples radially into 6 pie-shaped pieces.

3.4.4 Overnight bacterial culture growth

A Single colony of the inoculated bacterial in an agar plate was touched gently by a sterile pipette tip and then transfer to a culture tube containing a 5 mL of MHB. The container should not be filled to more than one-third of its capacity to allow for proper aeration. The prepared culture tube was incubated overnight at 37°C for approximately 16 to 17 h in a shaking incubator, to promote aeration and bacterial growth. On the following day, turbidity was checked to confirm bacterial growth, and the optical density (OD) of the overnight culture was measured using a spectrophotometer, and then they were diluted into fresh MHB medium to obtain the OD of 0.05 at 600 nm and incubated for 2 h to precondition the culture prior to experimentation.

3.4.5 Dose-response assay in a 96-well microtiter plate

A 180 µL aliquot of *P. aeruginosa* culture, incubated for 2 h, was transferred into each well of a 96-well microtiter plate, with three replicates for each condition. Thin film coupons were then added to the wells, as demonstrated in Figure 3.23. After seeding the wells, the plate

was sealed with a gas-permeable membrane and then covered with its original lid. It was then incubated statically at 37°C. After 24 h of incubation, the bacterial suspension was discarded, and each well of the plate was washed twice with 200 µL of Phosphate-Buffered Saline (PBS) to remove planktonic bacteria and retain only the bacteria forming attached biofilms. Afterwards, 200 µL of CV was added to each well and kept for 20 min. Subsequently, the excess dye was discarded. Finally, the CV was dissolved with 200 µL of acetic acid per well and placed on a shaking surface for 10 min. These procedures are summarized in Figure 3.24. To ensure consistency in the results, the experiment was repeated three times under the same experimental conditions.

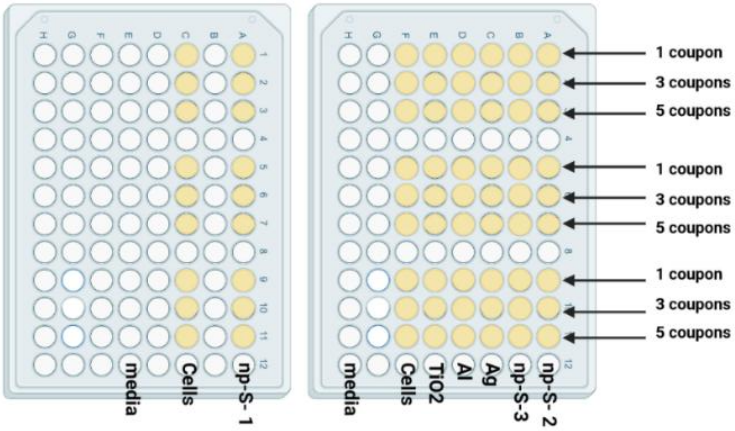

4Figure 3. 23 Top-view configuration of the 96-well plate used in dose-response assay, np-S- 1, 2 and 3 refers to np-S with the ligament size of 13.1, 22.2 and 31.6 nm, respectively.

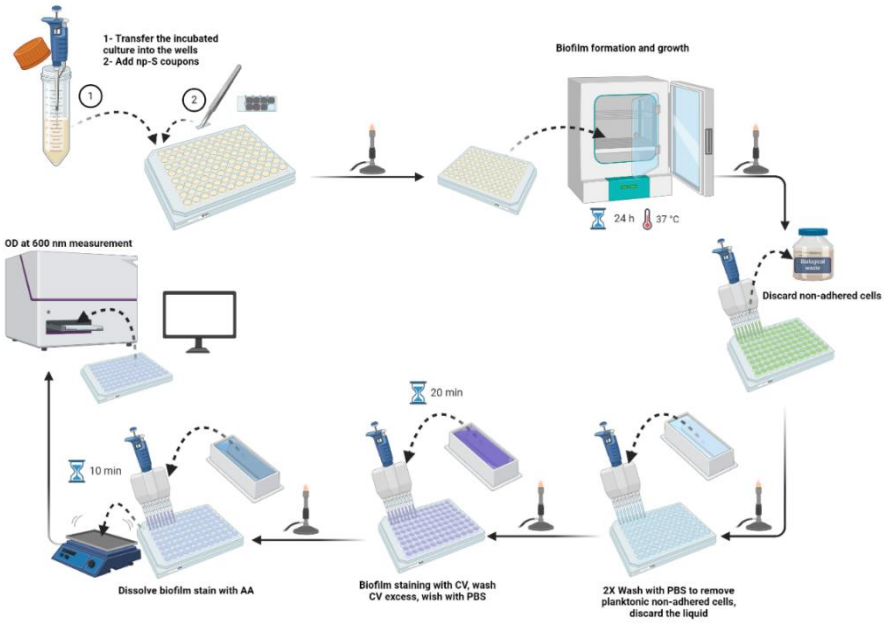

Figure 3. 24 Schematic summary showing the experimental procedure used in the dose-response assay in a 96-well micro-plate.

3.4.6 Growth inhibition assay

The growth curve of *E. coli* DH5α was recorded by turbidity measurements at 600 nm, three biological replicates and three technical replicates were prepared, totalling nine tubes for each film. The *np-S* thin films were added to each tube. One coupon of the *np-S* thin film was added to the first tube, while the second tube contains five coupons of the *np-S* thin films, followed by incubation at 37°C in a shaking incubator at 200 rpm for an additional 2 h. A 1000 µL aliquot of the culture was transferred to a cuvette to measure the OD every 2 h, up to 8 h and 4 measurements. The experimental procedures were demonstrating in Figure 3.25. The experiment was conducted three times, and the measured OD values are presented as mean ± standard deviation.

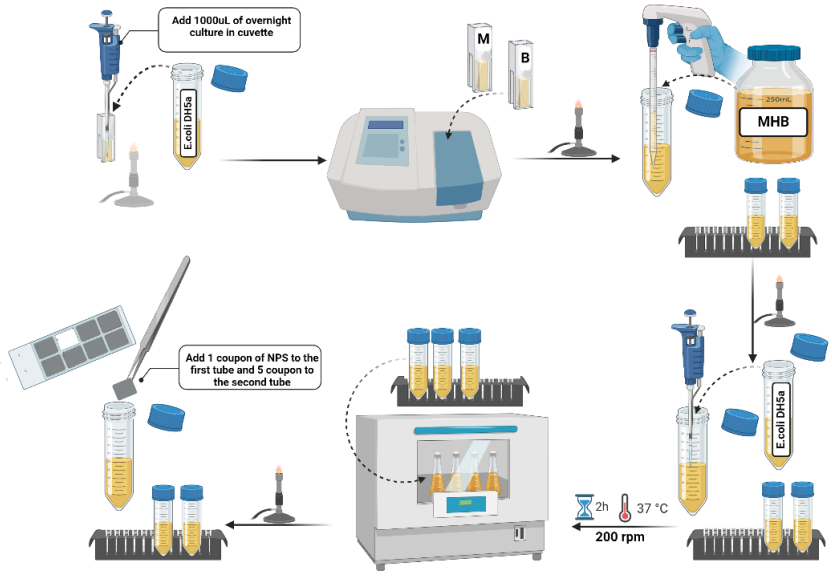

Figure 3. 25 Schematic summary represents the experimental procedure used in the growth inhibition assay.

3.4.7 Bacterial cell density measurements

Using the OD of a medium, which reflects the number of microorganism cells in the medium, to estimate and measure the growth curve is a widely employed procedure in microbiology for tracking the growth of microorganisms. OD measurements are typically performed using spectrophotometry (Krishnamurthi et al., 2021).

The OD measurements are usually conducted at a specific wavelength, normally 600 nm, which has a relatively low photon energy and will not induce autofluorescence (Godbey, 2014). As number of bacteria cells grows, the amount of incident light that arrives to the detector decreases due to increasing turbidity of bacteria suspension. Consequently, higher cell mass or

density results in less transmitted light and a higher absorbance or OD reading (Wessner et al., 2020).

The OD is measured compared to cell-free control solution according to Eq. 3.11.

$$OD = \log(\frac{1}{T}) \text{..... (3.11) (Carreira, 2017)}$$

Where T is transmittance of the light passes through the bacterial cell suspension compared to control dilution, can be calculated by finding the ratio between the intensity of the transmitted light I_t and the intensity of incident beam I_o as expressed in Eq. 3.12:

$$T = \frac{I_t}{I_o} \text{..... (3.12) (Carreira, 2017)}$$

3.4.7.1 Cell density measurement using spectrophotometer

A UV/Visible Scanning Spectrophotometer (model Shimadzu UV-1800) (Pvt.Limited Company, Uttar Pradesh, India) equipped with a tungsten halogen lamp and a silicon photodiode detector was employed for estimating the concentration of bacteria in a suspension. The measurements were conducted at a fixed wavelength of 600 nm in the absorbance mode, the measured OD is directly related to the density of bacteria cells.

3.4.7.2 Cell density measurement using microplate reader

The plate was placed in a multimode microplate reader (model Tecan Spark 20M) to measure the optical density of bacterial populations. The plate was shaken for 10 s in orbital mode before measurement.

The measured OD values of the bacterial suspension can be plotted as a function of incubation time to obtain the bacterial growth curve. It is known that the typical bacterial growth curve exhibits four phases namely, lag phase, exponential or log phase, stationary phase and death phase as Figure 3.26 demonstrates. During the lag phase, bacteria adapt to their new surroundings and there is a little to no increase in cell number depending on the environmental conditions, type of organism and medium. In the next phase, the exponential or log phase, bacterial growth begins, and rapid cell division is observed. As a result, the number of bacterial cells increases exponentially. The growth rate of bacteria in the stationary phase decelerates because of the longer intervals between bacterial cell divisions, and the rate of cell division is equal to the rate of cell death. The bacterial culture enters the death phase due to consuming the nutrient and accumulation of metabolites. This leads to a decrease in the number of viable bacteria, with increasing the number of dead cells than the number of dividing cells (Dubey, 2014; Wessner et al., 2020).

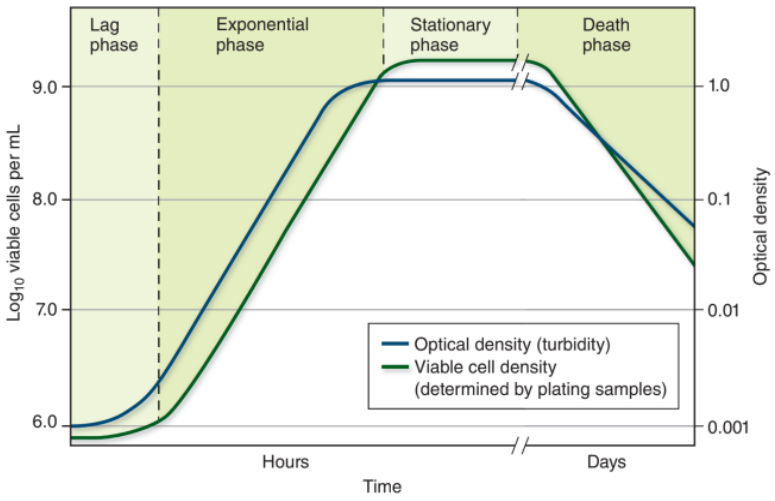

Figure 3. 26 a typical bacterial growth curve indicating four phases namely; lag, log, stationary and death phases (Wessner et al., 2020).

3.4.8 Fluorescence microscopy

Fluorescence is the term that refers to the emission of the absorbed light that occurs within the duration of nanoseconds or less. Fluorescence microscopy is a powerful and versatile optical instrument widely used in biomedical and biological fields due to its ability to provide specific, high-resolution imaging of specimens. This technique depends on the principle of fluorescence, where fluorescent dyes or proteins absorb light at a specific wavelength (excitation) and emit light at a longer wavelength (emission). The key parts of a fluorescent microscope include a light source (often a high-intensity xenon or mercury lamp, or LED), excitation and emission filters to isolate the desired wavelengths, a dichroic mirror to reflect and transmit specific wavelengths, and highly sensitive detectors such as charge-coupled devices (CCDs) or photomultiplier tubes (PMTs). Together, these elements enable the selective illumination and detection of fluorescent signals within a specimen (Kater & Nicholson, 1973; Lichtman & Conchello, 2005; Sachl & Amaro, 2023).

3.4.8.1 Staining of bacteria cells

Two different fluorescent dyes, SYTO-9 Green Fluorescent Nucleic Acid Stain (SYTO-9) and propidium iodide (PI), were employed to distinguish between live and dead bacterial cells. The green-fluorescent SYTO-9 dye, in conjunction with the red-fluorescent, PI stain, allows for simultaneous staining and differentiation of live and dead cell populations.

It is known that SYTO-9 is a green-fluorescent dye that can enter and stain bacteria with dead and live cells. on the contrary, PI is a red-fluorescent dye that stains bacteria with disrupted cell membranes, indicating cell death. By using this dual staining approach, live and dead bacteria cells within the treated and untreated samples can effectively be visualized and quantified (Stiefel et al., 2015).

A 1000 µL sample of *E. coli* culture is removed from the suspension and transferred to an Eppendorf tube, then centrifuged at 13000 rpm for 1 min to pellet the bacteria. The pelleted bacterial cells are washed twice by resuspending them in 1000 µL of PBS after discarding the supernatant, followed by another centrifugation step under the same conditions. The resulting pellets are then resuspended in PBS containing SYTO-9 stain at a concentration of 5 µM and PI dye at a working concentration of 30 µM and incubated in the dark for 10 min to allow for staining. After staining, the culture is centrifuged once more at 13000 rpm for 1 min to pellet the bacteria. A microscope slide is prepared by adding a 2 % agarose pad within a Gene Frame. The final pellet is resuspended in 100 µL of PBS, and approximately 4 µL of the culture is applied to the prepared glass slide containing agarose pad, followed by placing a coverslip over the Gene Frame to evenly distribute the agarose. The staining experiment was repeated in triplicate, and a fluorescent image was captured each time under the same conditions for statistical analysis.

3.4.8.2 fluorescent imaging

A high-performance deconvolution fluorescence microscope (model DeltaVision (DV) Elite deconvolution fluorescence microscope) (GE Healthcare, USA) is employed for fluorescent imaging to study the viability of bacteria. The microscope is set to specific excitation and emission lines: for imaging cells stained with SYTO-9, 475/28 nm excitation and 523/48 nm emission are used with the FITC filter channel, whereas cells stained with PI dye are imaged with 632/22 nm excitation and 679/34 nm emission, which identifies cells with compromised membranes. For each treatment and biological replicate, 5-6 images are captured in Z-stacks using the DV Elite SoftWoRx program and are subsequently restoratively deconvolved. The fluorescent images are then processed, and bacterial viability quantified using ImageJ software (Health, n.d.).

Statistical analysis of antibacterial tests

Analysis of variance (ANOVA) is a commonly employed statistical test for evaluating and analysing the differences in a measured variable among multiple groups to determine whether they are significantly different. Compared to other statistical methods, such as the t-test, which is limited to determining the differences between two groups at the same time, ANOVA allows the comparison between multiple groups simultaneously, as in our experiment, hence minimising the chances of errors that can occur while performing many separate tests.

Furthermore, the findings are easy to explain, using values such as the F-statistic and p-value to show if the variances between groups are statistically significant (Quinn & Keough, 2002).

The F-statistic is calculated by finding the ratio of the differences between groups to within groups. In this study, one-way ANOVA was chosen as the statistical test to compare the means of multiple groups. The F-statistic can have two possible outcomes: If the null hypothesis (H_o), which assumes the means of all groups are equal, is true, then the F- statistic value will be close to 1, meaning that the differences between groups and within groups are similar. On the other hand, if the null hypothesis is false, the F- statistic value will be greater than 1, indicating that the mean of at least one group is significantly different (Quinn & Keough, 2002).

Regarding the p-value, it provides information about whether the differences between groups are statistically significant. Similarly, there are two possible outcomes: p-value less than 0.05 ($p < 0.05$), meaning that at least one group is significantly different. On the contrary, the p-value greater than 0.05 ($p > 0.05$) suggests no significant variance between the groups (Quinn & Keough, 2002) (Knapp, 2017; van Emden, 2012).

In brief, this chapter provided important information about the techniques, methods and experimental procedures followed to prepare *np-S* as thin films and bulk. For studying their characterization such as morphology, chemical composition, and crystal structure, techniques such as SEM, EDS and XRD were employed. The electrical properties of the materials were studied using hall effect measurement and Van der Pauw resistivity measurement. Their optical properties were studied using spectroscopic ellipsometry and UV-visible spectrophotometer. This chapter describes the protocols and methods employed for study the antibacterial activity of these materials.

Chapter 4 Effect of precursor composition on the morphology and optical and electrical properties of Silver nanosponges

4. Overview

Most of the previously published works on np-S produced by dealloying of $Ag_{100-x}Al_x$ precursors have focussed on specific, fixed compositions of alloy synthesis by casting or melt spinning (Luo et al., 2020; Qiu et al., 2011a; Song, Gao, Zhang, & Zhaib, 2011; Wang et al., 2009a; Wu et al., 2015a; Zhang & Zhang, 2010; Zhang et al., 2009). Due to the segregation of Al during the preparation process, melt-route alloys of Ag-Al will generally require homogenizing the alloy. Moreover, the segregation would be observed and may not be completely suppressed even for melt-spun ribbons. On the contrary, preparing the Ag-Al alloy using magnetron sputtering technique at room temperature generates a metastable deposit that is almost homogeneous, which may be attributed to the very low diffusion rates in the solid material at the deposition temperature.

4.1 Objective of chapter

A magnetron sputtering system will be used to produce a series of $Ag_{100-x}Al_x$ alloy thin films with varying Al concentrations by controlling the applied current to one gun while the fix current will apply to the other gun during the experiment. The morphology of the produced *np-S* thin films after dealloying will be explored to investigate the impact of the Al concentration on their morphology and microstructures. The optical properties of *np-S* thin films will be studied because they are a sensitive indicator of nanoscale structure. The impact of the varying pore and ligament sizes on the optical and electrical properties will be examined.

4.2 Experimental details specific to this chapter

The $Ag_{100-x}Al_x$ thin-film alloys were magnetron co-sputtered onto glass substrates at room temperature. The composition of the film was controlled by varying the deposition rate of Al while the rate of deposition of Ag was held constant. The deposition times were adjusted so that the precursor films would all be nominally 110 nm thick. The sputtering chamber was evacuated to a base pressure of 4.7×10^{-4} Pa. The working gas was argon. During the sputtering process, the substrates were rotated at 12 rev/min to promote uniform film growth. The distance between the targets and sample holder was fixed at 110 mm, with an angle of 60°. The glass substrate was sputtered with three layers, consisting nominally of 5 nm of Ti as an adhesion layer (first layer), 3 nm of Ag (second layer), and 110 nm of Ag-Al alloy (top layer). The actual

thin films obtained were typically of the order of 115 to 120 nm in thickness. The deposition parameters are provided in Tables 4.1 and 4.2.

Table 4. 1 DC current applied to the Ti and Ag guns during deposition of adhesion layer at room temperature along with the corresponding Ti and Ag deposition rates, time of deposition, layer thickness.

Element	Current (A)	Deposition rate (nm s^{-1})	Deposition time (s)	Thickness (nm)
Ti	0.125	0.04	125	5
Ag	0.02	0.07	43	3

Table 4. 2 DC current applied to the Al and Ag guns during depositing the Al_xAg_{100-x} alloy thin films at room temperature along with the corresponding Al and Ag deposition rates, time of deposition, thin film thickness.

Sample No.	Ag gun current (A)	Ag deposition rate (nm s^{-1})	Al gun current (A)	Al deposition rate (nm s^{-1})	Deposition time (min)	Thickness (nm)
S1	0.1	0.49	0.08	0.10	3:55	109.6±0.94
S2			0.20	0.18	3:27	110.2±1.20
S3			0.24	0.21	3:15	109.7±0.94
S4			0.34	0.31	3:02	109.7±1.70
S5			0.44	0.41	2:39	110.0±1.52
S6			0.54	0.51	2:23	109.9±1.50

Dealloying was carried out in 1 M NaOH aqueous solution at room temperature for 13, 9, 7, 6, 3 and 2 min respectively for samples S1, S2, S3, S4, S5 and S6. Dealloying in NaOH concentration higher than 1M led to the film peeling off, while dealloying at much lower NaOH concentrations resulting in a high concentration of residual Al even when dealloying was conducted for a long period of time. The dealloyed samples were rinsed with deionised (DI) water, dried by ethanol and then stored in a vacuum desiccator. Films were characterized in the as-deposited state and after dealloying. The effect of an anneal in a forming gas atmosphere at 500 ºC for 60 min to enhance the crystallisation of the precursor films was also investigated.

4.3 Results and Discussion

4.3.1 Composition of as-deposited and dealloyed thin film

The chemical compositions of the matrix in the $Ag_{100-x}Al_x$ thin film alloys and the corresponding sponges were obtained using EDS, Table 4.3. The calculated relative standard deviations are estimated to be within 1%. Dealloying of the as-deposited films was relatively complete with the residual Al content of the *np-S* lying into the range 1.4 to 5.9 at.%. Residual Al at these levels has been reported in *np-S* by past workers too (Wang et al., 2009b; I. Yamauchi et al., 2003). It is evident that the as-deposited samples were all dealloyed, even, surprisingly, those with Al contents well below the 50 at.% or so of the traditional 'parting limit' (Supansomboon et al., 2014). This is not the case for the annealed samples, which hardly de-alloyed. This is evidently due, for the most part, to the formation of additional δ-Ag_2Al phase in those samples (see next section). The δ-Ag_2Al phase is well known to be resistant to corrosion in NaOH solutions (Luo et al., 2020; I. Yamauchi et al., 2003). Apparently, the

relatively defective and metastable structure of the as-deposited films renders them very susceptible to dealloying. The Al contents of the deposited surfaces are also marginally higher after annealing. We attribute this to some Al_2O_3 having been formed on the exposed surfaces of the films despite annealing having been conducted under near-vacuum conditions. The corollary to this is that the Ag content immediately below the surface would be enriched relative to the content of metallic Al.

4.3.2 Phase constitution of the thin-film alloys and de-alloyed thin films

4.3.2.1 As-deposited then de-alloyed

The Bruker D8 Discover diffractometer has been utilised in this study to collect the XRD spectra of ad-deposited and *np-S* thin films. The XRD patterns of the thin films in the as-deposited condition, which are shown in Figure 4.1 a, reveal that with a low concentration of Al (sample S1), there is a single phase – (Ag, Al) face-centred cubic crystal structure – with space group $Fm\bar{3}m$. This phase shows a weak (111) texture. This is despite the fact that the binary equilibrium phase diagram for Ag-Al shows that δ-Ag_2Al phase should have formed (Murray, 2016). Evidently, a metastable solid solution of (Ag, Al) formed instead. This is a common occurrence for magnetron sputtering at ambient temperature; there is often insufficient thermal activation of diffusive processes to crystallise complex intermetallic structures and so simple metastable closest-packed phases form instead. A transition in microstructure was observed at Al of 33.8 at. % (S2), where δ-Ag_2Al intermetallic compound with hexagonal primitive structure and space group of *P63/mmc* started to form, resulting in a mixture of two phases, namely metastable α-phase and δ-Ag_2Al. The δ-Ag_2Al usually had a strong 002 texture, but the (101), (012), (103), (112) and (004) peaks are usually also visible in the patterns for S2 through to S4. According to the XRD results, with increase of Al content from 33.8 to 52.6 at. %, the amount of $(Ag, Al)_{fcc}$ decreases while that of δ-Ag_2Al increases as indicated by the variation of diffraction peak intensities of these phases. This is as expected from the binary phase diagram of this system. Nevertheless, an examination of the binary phase diagram shows that far more δ-Ag_2Al phase should have formed, so evidently the deposit is still in a relatively metastable condition. At high Al concentrations of 62.2 and 72.6 atom % (S5 and S6), the XRD peaks show only diffraction peaks associated with a single face-centred cubic (fcc), in this case Al-rich $(Ag, Al)_{fcc}$ phase solid solution. This result for S6 is in good agreement with the results of Yang et al. (Yang et al., 2013) for their $Ag_{28}Al_{72}$ thin film prepared using a magnetron sputtering system. Although the binary phase diagram predicts some δ-Ag_2Al for lower temperatures, it will be noted that Ag is extremely soluble in (Ag,

Al)$_{fcc}$ at elevated temperatures. The absence of δ-Ag_2Al in these samples may therefore be attributed to insufficient thermal activation being available at time of deposition.

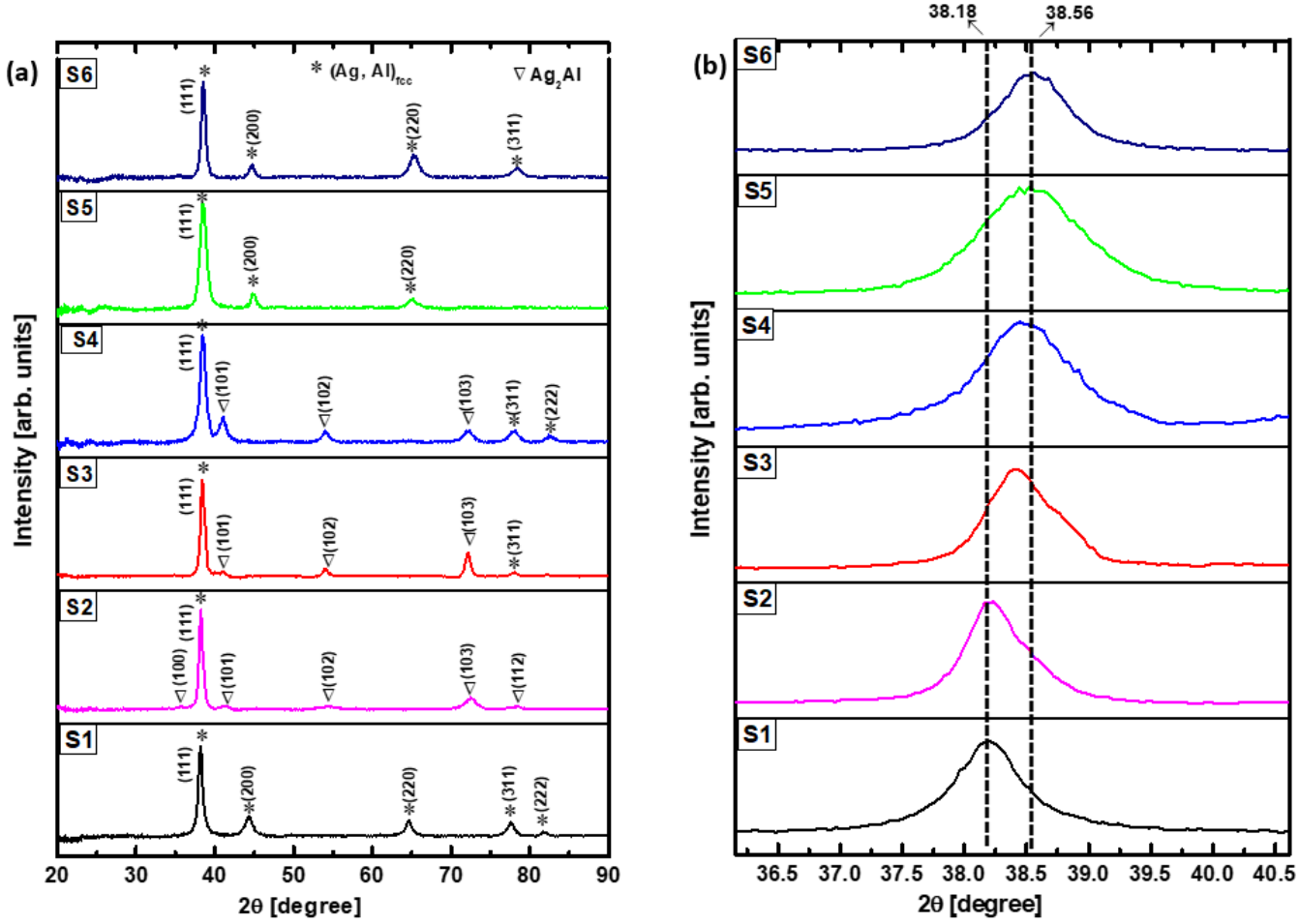

Figure 4. 1 XRD diffraction patterns of a) the as-deposited Al_xAg_{100-x} alloy thin films with different Al concentrations, the peaks are marked by different shapes of scatters representing different phases, b) enlarged (111) diffraction peak of the as-deposited alloy thin films showing a small shift of that stronger peak with increasing Al concentration.

The progressive shift of the most intense (111) diffraction peak with *2θ* at different concentrations of Al is displayed in Figure 4.1 b. The (111) peaks of the alloys shift towards the higher angle with increasing Al concentration. The lattice parameters of these thin films ranged systematically between 0.4081 ± 0.0002 nm at the lowest Al content to 0.4042 ± 0.0002 nm at the highest Al content, which corresponds to the reported values of Ag (0.40790 nm) and Al (0.40406 nm) in the Crystallography Open Database's entries ID no. 9011607 and 9012956, respectively. The measured lattice parameter values have been plotted against Al concentrations in Figure 4.2. The lattice parameter (a_0) decreases with increasing Al concentration, showing a not-quite linear relationship that is only in poor agreement with Vegard's law. The results indicate that when the Al composition is less than 40 at. %, it is the α-Ag (Al) solid solution that is dominant whereas the α-Al (Ag) solid solution exists with Al

composition higher than 60 at. %. A metastable α-phase exists between roughly 40 and 60 at. % Al.

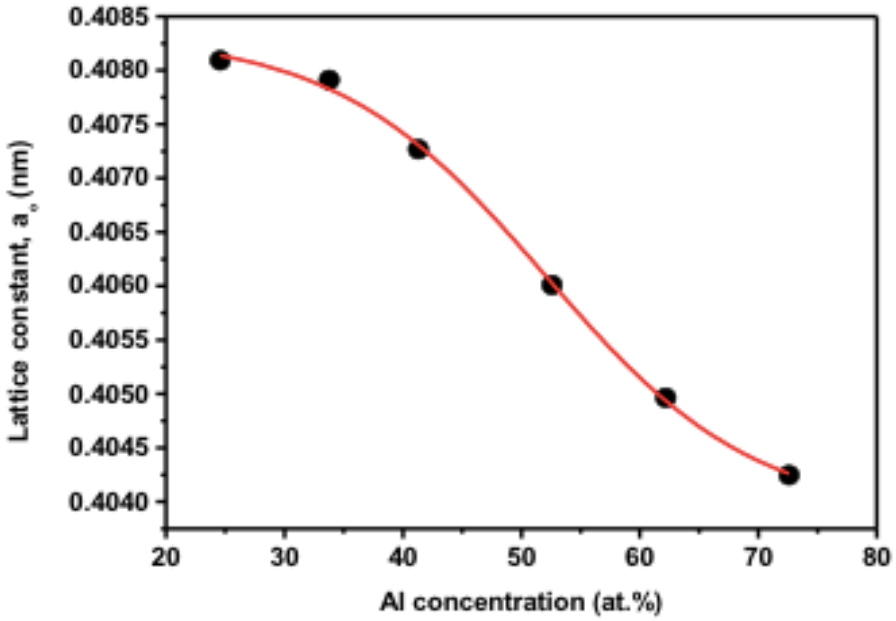

Figure 4. 2 variation in lattice constant of the as-deposited alloys as a function of changing the Al concentrations, it clearly shows that the lattice parameter values decrease with increasing Al concentration.

Rietveld refinement of the fractions of Ag and δ-Ag_2Al phases present was unstable due to the strong texture of the films and the broad nature of the peaks from these thin films. Instead, we used CRYSTALDIFFRACT's 'mixture' and 'preferred orientation' functions to estimate the amount of δ-Ag_2Al phase (balance usually being α-Ag (Al) or α-Al (Ag) phases). These results are also shown in Table 4.3. For comparison, the maximum amount of δ-Ag_2Al that could possibly form for the measured Al contents and from the published binary equilibrium diagram (Erlebacher et al.) is also listed using 500 ºC as a datum.

Table 4. 3 Composition and constituents of precursor and de-alloyed thin films. For comparison, the calculated equilibrium amount of δ-Ag_2Al at 500 °C is also shown

	S1	S2	S3	S4	S5	S6
As deposited						
Al, at. %	24.6	33.8	42.2	52.6	62.3	72.6
Approx. wt.% Ag_2Al, *XRD*	0	25-30	45-55	38-46	0	0
Equilibrium Ag_2Al, wt.%	100	100	75	65	53	36
As-deposited then de-alloyed						
Al, at. %	1.8	5.6	5.4	3.9	3.7	1.4
Approx. wt.% Ag_2Al, *XRD*	0	0	0-30	0	0-30	0
Equilibrium Ag_2Al, wt.%	0	0	0	0	0	0
Annealed						
Al, at. %	29.4	39.1	59.7	65.5	78.5	85.2
Approx. wt.% Ag_2Al, *XRD*	0	35-65	52-70	60-70	75-90	82-92
Equilibrium Ag_2Al, wt.%	85	78	57	48	24	5
Annealed then de-alloyed						
Al, at. %	6.1	10.1	25.7	43.1	54.6	71.7
Approx. wt.% Ag_2Al, *XRD*	0	70-80	80-90	65-75	90-99	90-99
Equilibrium Ag_2Al, wt.%	0	0	100	75	63	38

The *XRD* patterns of the samples de-alloyed in 1 M NaOH solution (Figure 4.3) generally showed only $(Ag, Al)_{fcc}$ solid solution, although there was also evidence for a small proportion of retained δ-Ag_2Al in some patterns of samples S3 and S5. It is evident that Al can be mostly, but not entirely, leached out using NaOH solution as a result of the significant difference in electrode potential Ag and Al. This is notwithstanding the known corrosion resistance of δ-Ag_2Al in NaOH solutions and despite the fact that samples S1 to S3 had Al contents below the traditional parting limit. The lattice parameters of these *np-S* thin films were 0.40810 ± 0.00020 nm. This is within the range of values reported for pure Ag (*cf.* the COD entry no. 9011607).

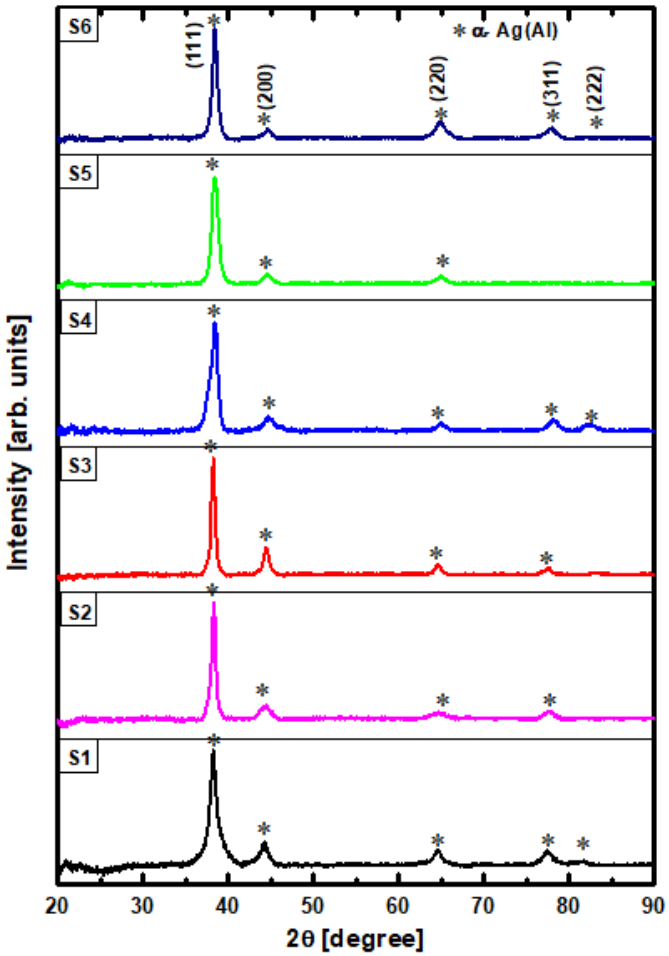

Figure 4. 3 XRD diffraction patterns of the de-alloyed Al_xAg_{100-x} thin film alloys in 1 M NaOH solution. The present peaks are assigned to diffraction from the (111), (200), (220), (311) and (222) planes of single phase which is silver.

4.3.2.2 As- deposited, annealed at 500 ºC, then de-alloyed

A duplicate of each as-deposited sample was annealed at 500ºC to see whether this would affect the morphology of the subsequent sponge. From Table 4.3 it is clear that annealing of the as-deposited films caused a marked increase in the fraction of δ-Ag_2Al. In samples S1, S2 and S3 this is likely the consequence of much of the Al in the as-deposited material having

originally being in metastable solid solution in the $(Ag, Al)_{fcc}$ phase. Annealing provided the thermal activation necessary to precipitate out an amount of δ-Ag_2Al that was closer to the equilibrium situation at 500 ºC. However, the amount of δ-Ag_2Al estimated for samples S4, S5 and S6 was far above that predicted from the equilibrium phase diagram for the measured compositions of the films. The reason for anomalously strong *XRD* peaks of δ-Ag_2Al in these samples is unknown but the phenomenon may be related to the preferred orientation being stronger than assumed and/or the fact that some of the Al had oxidized thereby enriching the ratio of Ag to metallic Al. Annealed sample S6 showed a very strong (201) texture of δ-Ag_2Al, which was unusual. Overall, the content of annealed δ-Ag_2Al also made these films much more resistant to de-alloying with the result that they still contained appreciable amounts of Al after treatment in NaOH solution. Sample S2 also appeared to also contain some $Al(OH)_3$ or other third phase that had evidently formed during de-alloying (peaks at d=4.00, 3.48, 3.10 and 2.83 Å). The XRD patterns of these films are shown in Figure 4.4.

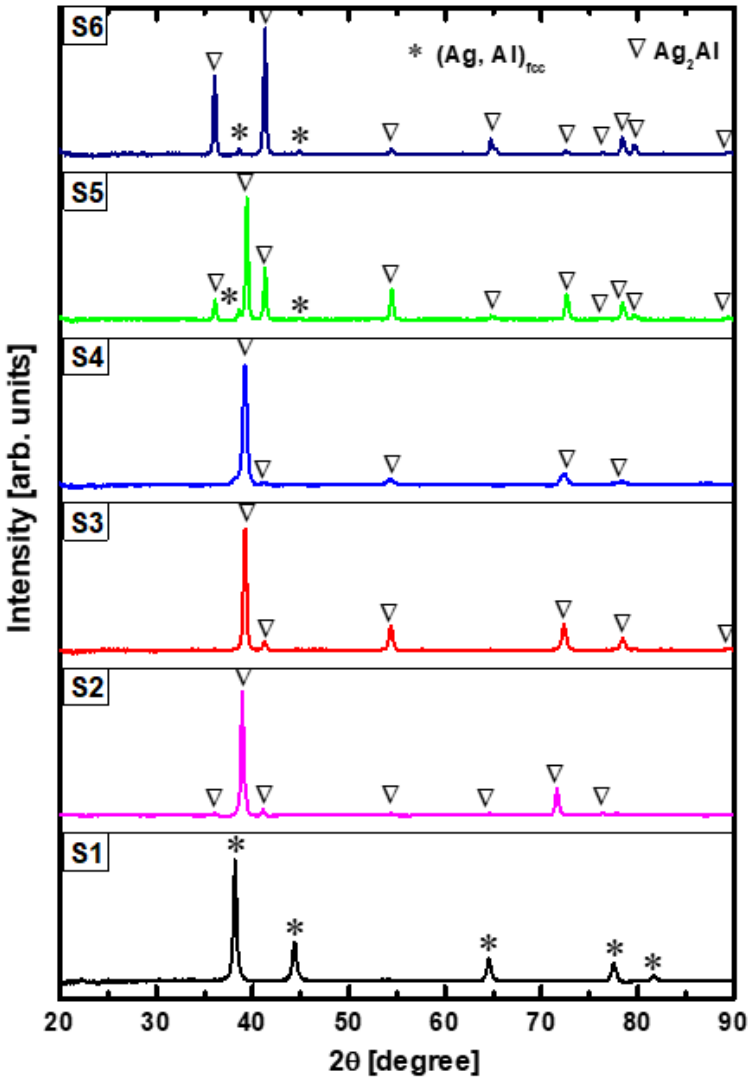

Figure 4. 4 X-ray diffraction patterns of the annealed precursor films. Comparison to the data for the as-deposited films show that there is a considerably greater amount of δ-Ag_2Al present.

4.3.3 Effect of composition in the $Ag_{100-x}Al_x$ precursor alloys on the morphology of np-S

The effect of the Al content of the precursor on the morphology of *np-S* seems controversial. For example, Yamauchi et al.(I. Yamauchi et al., 2003) reported that there was little effect of varying the Al between 61 and 85 at.%. In contrast, Wang et al.(Wang et al., 2009a) and Song et al.(Song, Gao, Zhang, & Zhai, 2011) reported a significant decrease in ligament size as Al was increased. Plane-view *SEM* images of some example regions of the present *np-S* are shown in Figure 4.5. The thin films produced by de-alloying as-deposited material all have bi-continuous spongy structures with nanoscale open-cell pores and Ag ligaments. As can be seen from these images, when the concentration of the deposited Al was low (S1), the sponge formed had pits distributed sparsely and randomly on the surface (Figure 4.5 a). Further increasing the concentration of Al in the $Ag_{100-x}Al_x$ thin film alloy brought in an appreciable change in the ligament sizes (Figure 4.5 b, c, d, e and f). There was less effect on the pore size. The mean average sizes of the ligaments and pores are summarised in Table 4.4. The ligament sizes are significantly smaller than the 90 to 450 nm and 140 to 330 nm reported for melt-spun ribbon precursors by Wang et al.(Wang et al., 2009b) and Song et al.(Song, Gao, Zhang, & Zhai, 2011) respectively. The thickness of the as-deposited films was measured using atomic force microscopy and fell with the range 118 to 121 nm.

Table 4. 4 Average pore and ligament sizes of as-deposited thin films de-alloyed in 1 M NaOH. The confidence intervals correspond to one standard deviation. The estimated surface diffusion of Ag adatoms during the de-alloying process is also given.

	S1	S2	S3	S4	S5	S6
Average pore size, nm	12.6 ± 4.9	13.9 ± 4.4	14.4 ± 4.5	15.5 ± 4.5	11.8 ± 3.1	11.1 ± 3.5
Average ligament size, nm	31.6 ± 12.8	30.6 ± 9.8	25.3 ± 8.9	22.2 ± 8.7	15.6 ± 4.4	13.1 ± 3.9
Average pore density, pores per 10,000	93	117	131	152	231	262
Surface diffusion of Ag D_s (m^2 s^{-1})	5.26×10^{-18}	4.96×10^{-18}	4.49×10^{-18}	3.93×10^{-18}	1.08×10^{-18}	0.72×10^{-18}

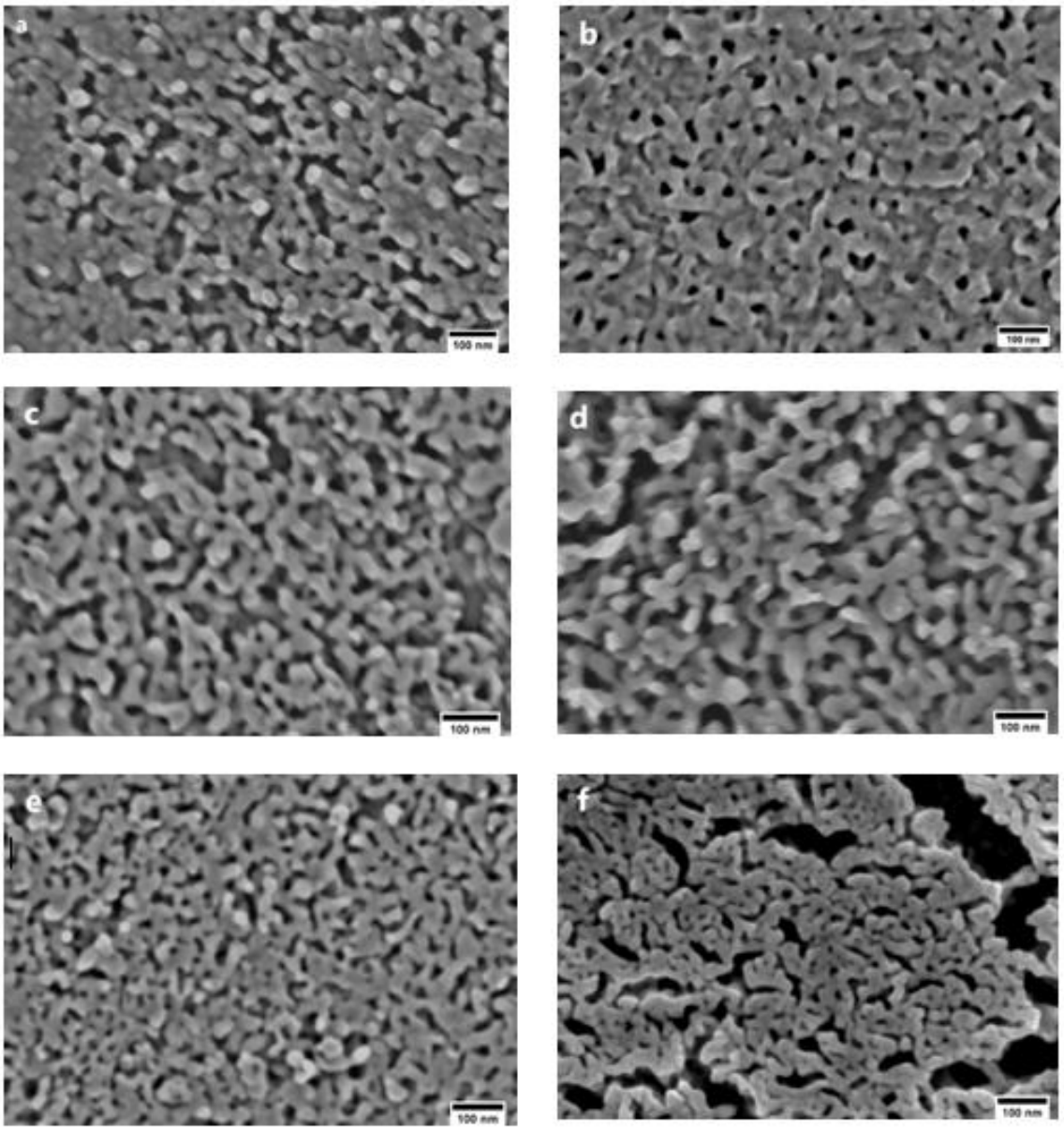

Figure 4. 5 Top-view SEM images of NP-S with the average ligament sizes of (a) S1, (b) S2, (c) S3, (d) S4, (e) S5 and (f) S6 thin films. All the top-view SEM images were scanned at high magnification and a scale bar of 100 nm.

The histograms in Figure 4.6 a- f reveal that the pore sizes of the prepared nanoporous thin films fall in the nanometer range between 2 to 27 nm, with the broad pore size distributions. Specifically, the pore sizes range from 2 to 27 nm for S1, from 2 to 27 nm for S2, from 2 to 25 nm for S3, from 2 to 26 nm for S4, from 2 to 23 nm for S5, and from 2 to 20 nm for S6. The distributions exhibit maxima between 12 and 17 nm for S1, between 12 and 15 nm for S2, between 15 and 17 nm for S3, between 15 and 22 nm for S4, between 10 and 12 nm for S5, and between 8 and 10 nm for S6, indicating significant variation in pore size depending on the variation of Al concentrations in the initial alloys. The changes pore and ligament sizes as a function of varying Al concentration in the initial alloys are depicted in Figure 4.7. It can be seen that from the results in Table 4.4, increasing the Al concentration in the primary alloys led to a linear decrease in the average ligament size and a linear increase in the average pore

size of the resulting *np-S* which peaked at 52.6 at. % Al (S4). Density of pores is shown in Figure 4.8 and Table 4.4.

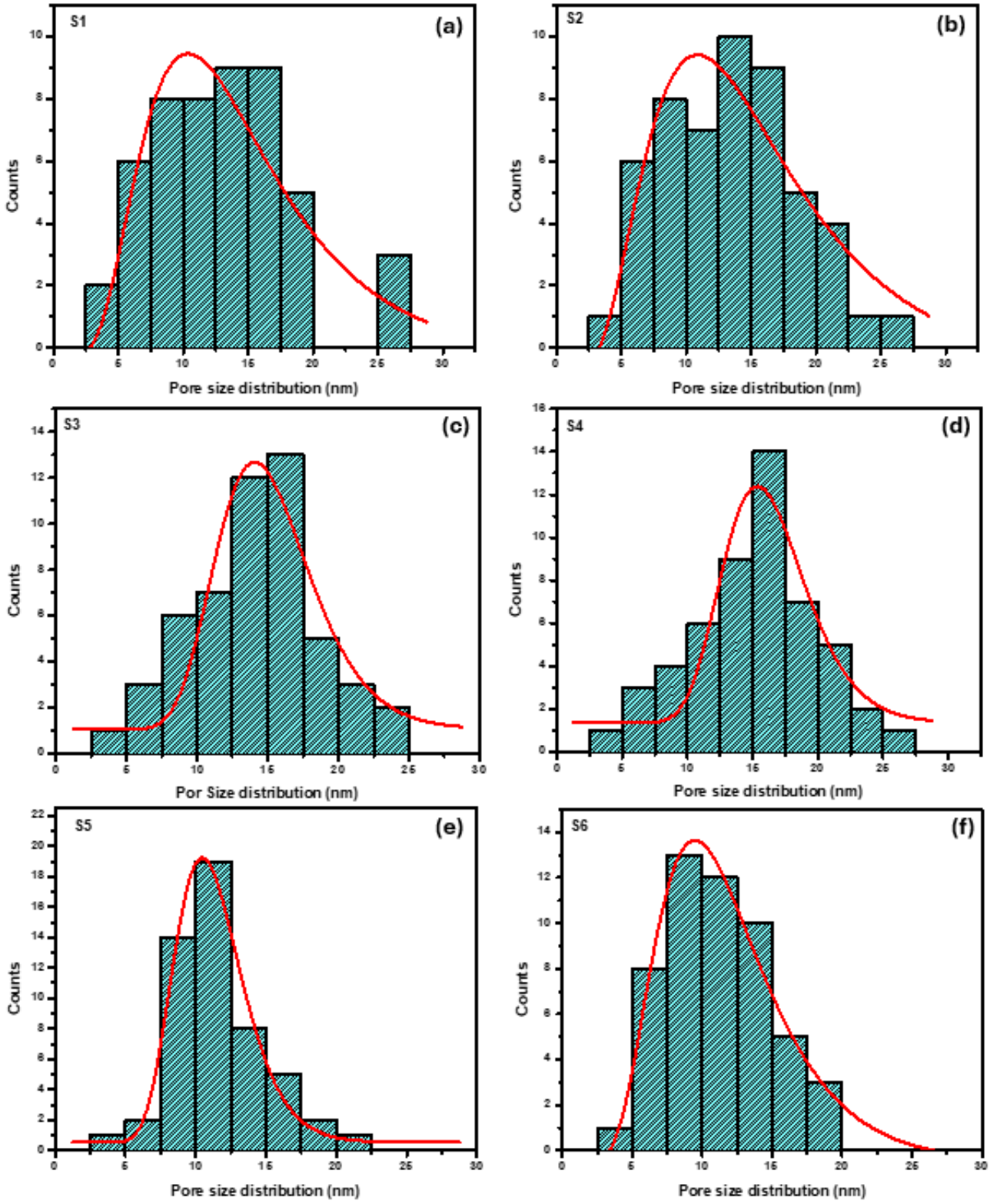

Figure 4. 6 Histograms of the pore diameter distribution of the np-S samples derived from the top-view SEM images.

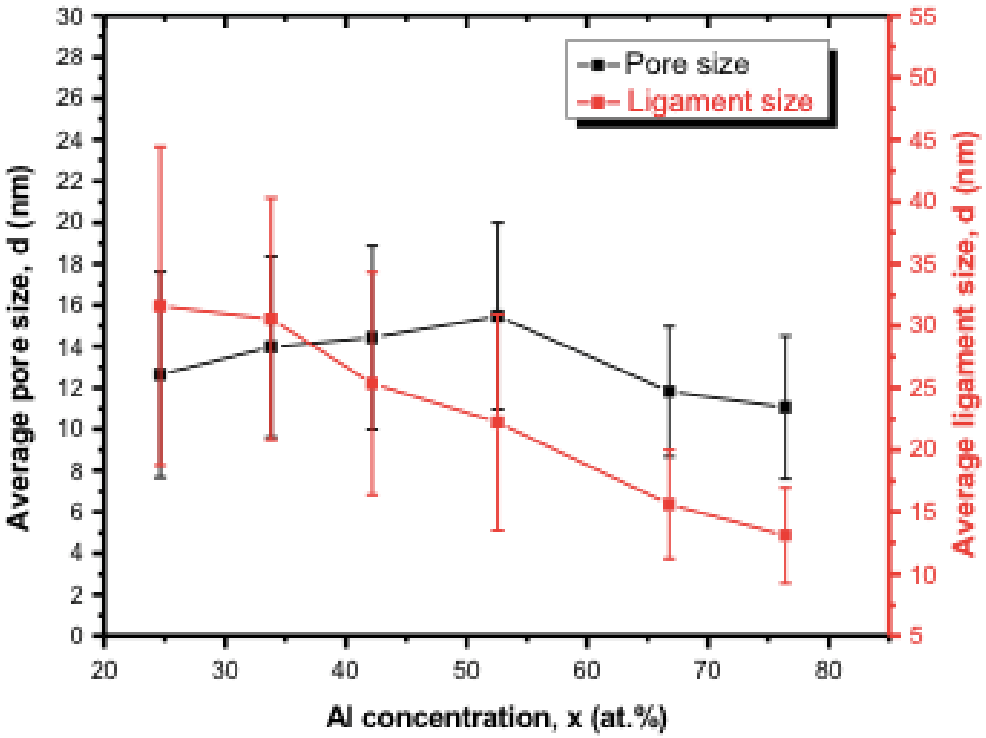

Figure 4. 7 Variations of the np-S ligament sizes and pore sizes as a function of the Al concentration in the initial alloys after dealloying in 1 M NaOH solution.

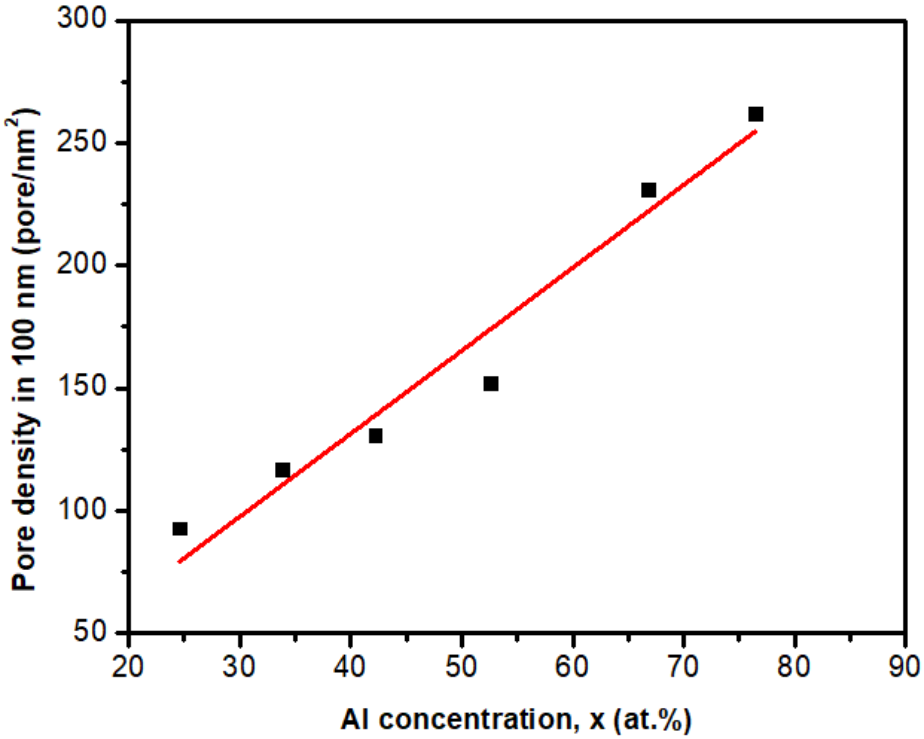

Figure 4. 8 Pore density as a function of Al concentration in the Al_xAg_{100-x} thin film alloys (filled symbols). The red line is the best linear fit for the data.

Ligament size has been shown to be related to the rate of surface diffusion of the noble metal alloys during dealloying (Ji, Wang, et al., 2011; Y. Yang et al., 2019). The latter can be estimated using Eq. 2.1. The results in Table 4.4 demonstrate that the average ligament sizes of *np-S* and the calculated surface diffusion D_s of Ag adatoms depend on the Al content in the

precursors. Increasing the Al concentration from 24.6 to 72.6 at. % led to a decrease in the ligament sizes from 31.6±12.8 to 13.1±3.9 nm, which may be attributed to lowering the surface diffusion of Ag adatoms along alloy/electrolyte interfaces from 5.26×10^{-18} to 0.72×10^{-18} m^2 s^{-1} and hence stabilising the *np-S* structure in the dealloying process. These results of D_s presented in Table 4.4 are about two orders of magnitude lower than the value (10^{-16} m^2 s^{-1}) of the surface diffusion of Ag adatoms prepared by dealloying of $Ag_{100-x}Al_x$ alloys at 363 K in H_2SO_4, H_3PO_4, $C_2H_2O_4$ and HCl solutions reported by Song and co-workers (Song, Gao, Zhang, & Zhai, 2011). Moreover, the calculated values in Table 4.4 are significantly higher than the intrinsic surface diffusion coefficients of Ag value (10^{-20} m^2 s^{-1}) by about 2 orders of magnitude (Li et al., 2017).

As mentioned earlier, the films that had been annealed before dealloying did not substantially dealloy, although their surface regions were certainly partially etched. These samples therefore are not yet converted to *np-S* although they could presumably be rendered into that state by more aggressive etching, as for example by HCl which is known to attack δ-Ag_2Al (Luo et al., 2020).

4.3.4 Electrical resistivity of the np-S thin films

It has been reported that the electrical resistivity of nanoporous materials depends on their morphology (Fujita et al., 2008; Zuruzi & Siow, 2015). The dealloyed nanoporous materials have a bicontinuous structure, where the nanoscale ligaments create interconnected networks that function as efficient channels for electron conduction. The electrical resistivity of the *np-S* thin films can be directly correlated with the average ligament size and hence, indirectly, the Al content in the precursor as Figure 4.9. The high-resolution *SEM* images in Figure 4.5 show that the *np-S* ligaments are fully percolated (connected) across the samples, providing conduction paths for electron transportation. Therefore, all the dealloyed $Ag_{100-x}Al_x$ samples formed conductive *np-S* thin films. However, we noted that the resistivities of the *np-S* thin films are higher than the resistivity of a Ag thin film comparator (1.32×10^{-8} Ω.m, which is very similar to the value of 1.59×10^{-8} Ω.m reported for bulk Ag (Fuller et al., 2002)). The identical finding has been documented by Zhang and his colleagues (Zhang et al., 2009). They found that nanoporous ribbons of gold (*NPG*), silver (*NPS*), and copper (*NPC*) had electrical resistivities that were ten to one hundred times higher than those of the bulk materials. This was attributed to the unique mechanism of the electron transport process in nanoporous metals.

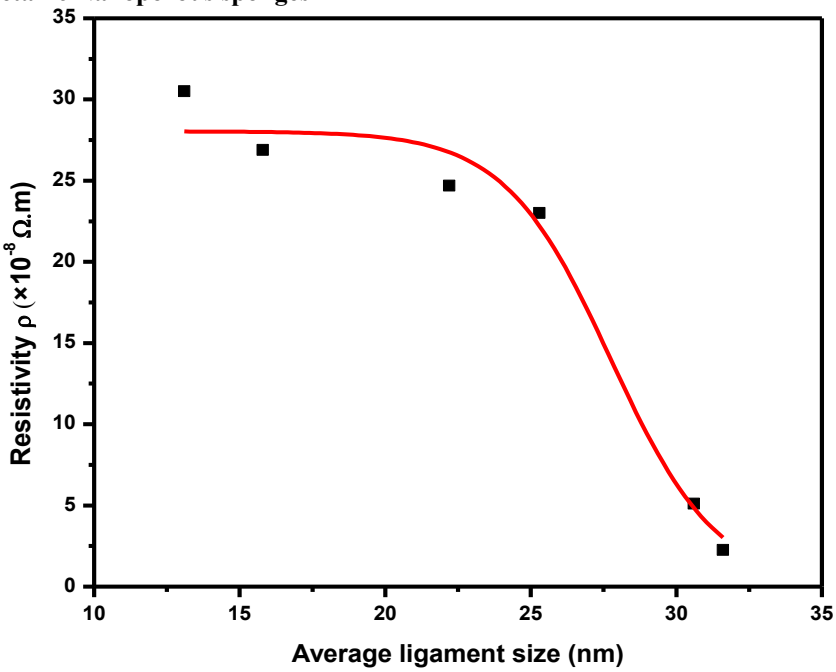

Figure 4. 9 The electrical resistivity changes as a function of the average ligament size of the np-S thin films, the curve indicates that the electrical resistivity of the sponges increases with decreasing the average ligament size.

It is well known that the presence of pores with sizes below the electron mean free path, which is roughly 57 nm at room temperature (Doremus, 2002), would have an impact on the conduction mechanism in the Ag film. Figure 4.9 indicates that the electrical resistivity of *np-S* increases with a decrease in the average ligament size. The *np-S* with 31.6 nm ligament size (S1) was ten times more conductive (ρ=2.26×10^{-8} Ω.m) than the *np-S* thin films with average sizes of 25.3 (S3), 22.2 (S4), 15.6 (S5), and 13.1 nm (S6), with their measured electrical resistivities being 2.30×10^{-7}, 2.47×10^{-7}, 2.69×10^{-7}, and 3.05×10^{-7} Ω.m respectively. The resistivity (5.10×10^{-8} Ω.m) of *np-S* with an average ligament size of 30.6 nm (S2) was anomalously high and can probably be discarded as an outlier. The electrical resistivity of *np-S* thin films goes up as the diameter of the ligaments goes down. This is because electrons scatter strongly at the points where pores and ligaments meet, and this scattering gets worse as microstructural features get smaller. This then leads to greater resistance (Fujita et al., 2008). The Hall mobility of the charge carriers in *np-S* with a ligament diameter of 31.6 nm is two orders of magnitude higher than that of *np-S* with a ligament diameter of 13.1 nm. This is true even though the carrier density of the *np-S* remained relatively unchanged with the diameter of the Ag ligaments, as Table 4.5 shows.

Table 4. 5 Carrier concentration, Hall mobility and electrical resistivity of np-S thin films deposited on glass substrate with different pore and ligament diameters

	Carrier concentration (m^{-3})	Hall mobility ($m^2.V^{-1}s^{-1}$)	Electrical resistivity (Ω.m)
S1	1.5×10^{29}	1.6×10^{-3}	2.26×10^{-8}
S2	1.9×10^{29}	1.2×10^{-3}	5.10×10^{-8}
S3	2.1×10^{29}	1.3×10^{-4}	2.30×10^{-7}
S4	2.4×10^{29}	1.0×10^{-4}	2.47×10^{-7}
S5	2.6×10^{29}	8.9×10^{-5}	2.69×10^{-7}
S6	2.9×10^{29}	3.2×10^{-5}	3.05×10^{-7}

According to Hakamada and his colleagues' research (Hakamada et al., 2016), the electrical resistivity of *np-G* increases as the size of the ligaments decreases. Similarly, the Ag foam ribbons, prepared by dealloying $Ag_{30}Al_{70}$, $Ag_{35}Al_{65}$, and $Ag_{40}Al_{60}$ alloys, exhibited increasing electrical resistivity as the porosity (pore density) volume fractions increased from 58% to 66% and to 69% (Wu et al., 2015a). Additionally, *np-G* thin films with nanostructure parameters close to the dimensions of *np-S* in this study exhibit higher electrical resistivity. The electrical resistivity of *np-G* thin films with ligament sizes of 77, 24, and 23 nm is 2.46 $\times10^{-7}$, 4.26 $\times10^{-7}$, and 5.48 $\times10^{-7}$ Ω.m, respectively. However, the measured electrical resistivity of *np-S* with the small ligament sizes is analogous to the findings by Stewart et al. (Stewart et al., 2017) for *np-S* prepared by sintering Ag nanowires at 300° C to eliminate the junction resistance between nanowires in a network. The electrical resistivity of the resulting porous structure prepared by melting the AgNWs with 6.2 μm in length and 48 nm in diameter was 2.00×10^{-7} Ω.m and for the nanoporous formed by sintering the AgNWs with 27 μm in length and 150 nm in diameter was 2.74×10^{-7} Ω.m. Moreover, the electrical resistivity of the interconnected network of particles formed by sintering the AgNPs was 2.93×10^{-7} Ω.m.

4.3.5 Electrochemical capacitance as an indicator of specific surface area

The capacitance of the as-deposited Ag-75 at. % Al alloy thin film (S6) and then the *np-S* produced from it were experimentally obtained from discharge curves of symmetric electrodes in 0.1 M KNO_3 aqueous electrolyte, Figure 4.10. As-deposited Ag-75 at% Al thin film alloy (similar to S6) had a capacitance of 67 μF cm^{-2} (sd=21μF cm^{-2}, n=6) at 0.20 V in 0.1 M KNO_3 solution. In contrast, after dealloying, the subsequent *np-S* thin film had a capacitance of 665 μF cm^{-2} (sd=124 μF cm^{-2}, n=15). Therefore, it is evident that the surface area of this sponge is about ten times larger than its starting film from an electrochemical perspective.

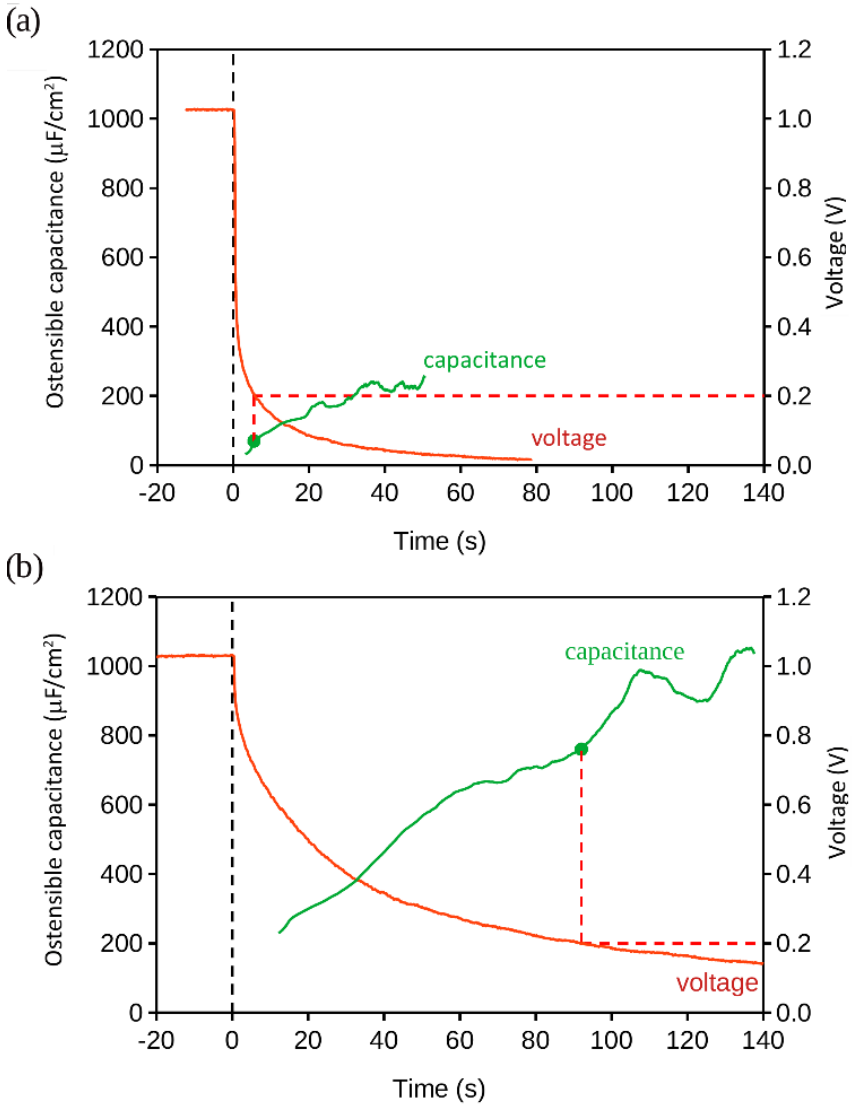

Figure 4. 10 Discharge voltages and electrochemical capacitances of (a) as-deposited Ag-75.at% Al film, and (b) np-S produced from the above film by de-alloying in NaOH. The capacitances vary with voltage and time and are compared at a datum of 0.20 V (dashed lines).

4.3.6 Optical properties of the np-S thin films as an indicator of morphology

Further insight into the structure of the dealloyed films was obtained from an analysis of their optical properties.

4.3.6.1 Dielectric permittivity

The frequency-dependent dielectric permittivity $\varepsilon(\omega)$ for non-magnetic materials is expressed as (De Silva et al., 2017) :

$$\varepsilon(\omega) = \varepsilon_1(\omega) + i\varepsilon_2(\omega) \ldots\ldots\ldots\ldots\ldots\ldots (4.1)$$

where ω is the frequency of the light, and ε_1 and ε_2 are the real and imaginary parts of the permittivity respectively. The permittivity of the dealloyed films were extracted from the ellipsometry data as described in the experimental section, and are plotted in Figure 4.11 a and b, which shows the real (ε_1) and imaginary (ε_2) dielectric permittivity of the samples. In this type of analysis, the sponges are conceptually treated as new materials in their own right, with effective permittivity that differ from that of solid Ag. Essentially, the nanocomposite material is being treated as a 'metamaterial' (A. I. Maaroof et al., 2007), albeit a rather simple one. In general, the real and imaginary components of the dielectric permittivity of the nano-plasmonic materials are the fundamental consideration when evaluating the optical and plasmonic properties (Arnold & Blaber, 2009; Cortie et al., 2019) of a material. It is worth noting that the real component of the permittivity determines the resonance frequency, which would be operating point for many devices that exploit the optical properties. The imaginary component (ε_2) of the dielectric permittivity is associated with the optical losses which arise from interband transition, intraband transition (Erwin et al., 2016), and electron surface scattering caused by grain boundaries (West et al., 2010), surface roughness (Sardana et al., 2014), lattice defects (West et al., 2010) and porosity (Sardana et al., 2014).

Inspection of Figure 4.11 a and b shows that the curves for the real part of permittivity are spread over a broad range, but all samples are less metallic than the pure Ag comparator. The curves of samples S2 to S5 do not fall in a sequence however and are all rather similar in magnitude. The situation for the complex part of the permittivity is even more irregular. Samples S2 to S5 have a complex permittivity that is more positive than that of pure Ag, attesting to the considerable electron scattering in these sponges. In contrast, samples S1 and S6 showed a lower magnitude of ε_2 at low photon energies. Importantly, the optical properties are also strongly affected by volume fraction of solid material, a factor that we will investigate below using an 'effective medium model' (*EMA*).

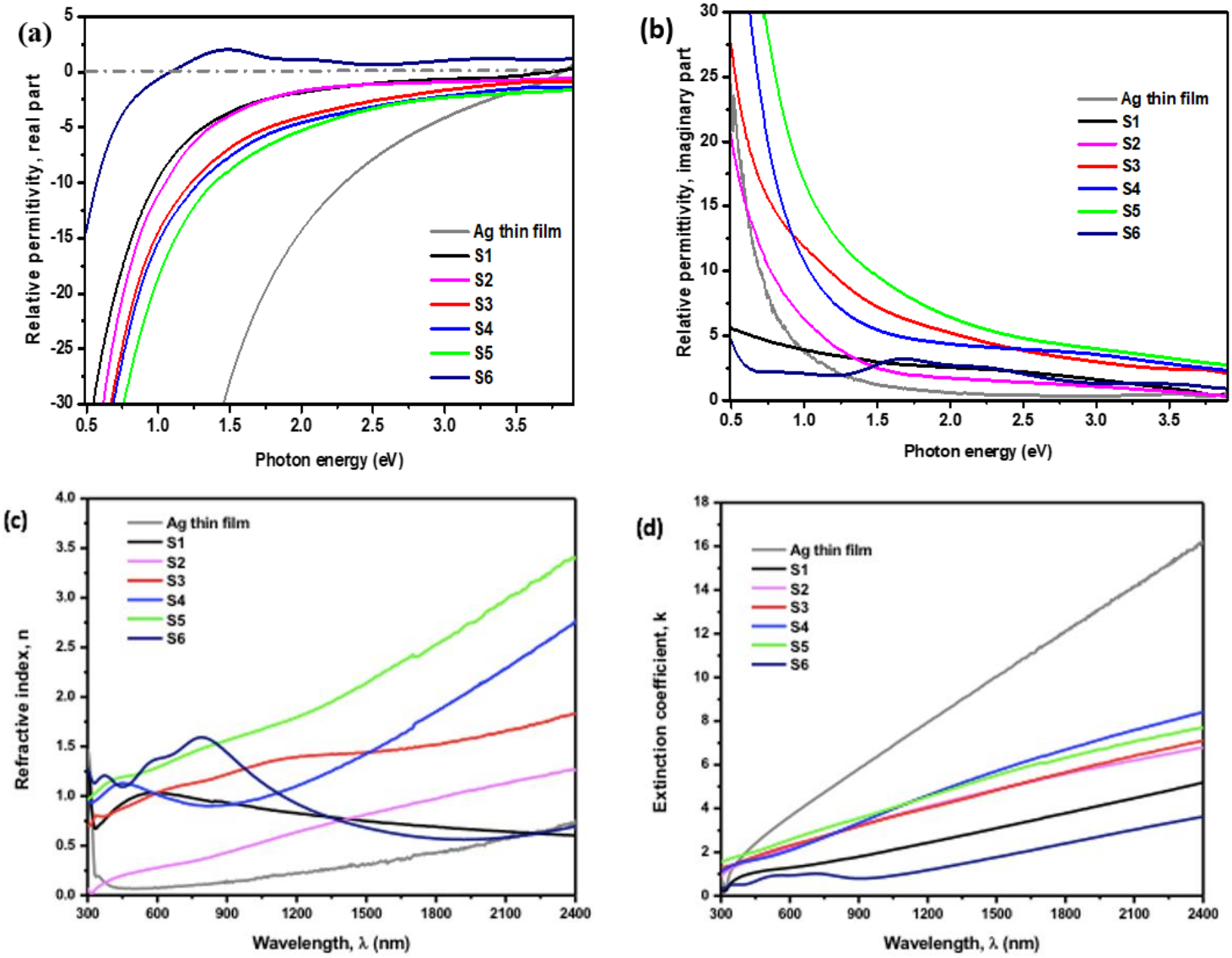

Figure 4. 11 Measured data of (a) the real part of the complex dielectric function of the np-S samples with the different average ligament sizes, (b) the imaginary part of the complex dielectric function of the np-S samples with the different average ligament sizes, and the optical constants of (c) the refractive index and (d) the extinction coefficient as a function of wavelength. (This data is for the as-deposited then de-alloyed samples. The curves for solid Ag are shown for interest but are not directly comparable to the data for the sponges.

When the characteristic size of the constituents of the material is small compared to the wavelength of the light in the media, as is the case for the present sponges, their optical response can be formulated by effective medium approximations. In these approximations, the dielectric functions of the constituents that make up the composite material are combined in an analytical relation that provides an estimate of the effective dielectric constant of the material under investigation (Garoli et al., 2018). Many EMAs have been proposed but the Bruggeman EMA is the most popular approach to obtaining the permittivity of mixed-phase films of the present type. This EMA has been exploited, for example, for the computation of the optical properties of nanoporous gold by Maaroof et al.(Maaroof et al., 2005), with the practise being subsequently taken up for *np-S* by some subsequent workers, e.g. (Detsi et al., 2014; Garoli et

al., 2018). Here we used this EMA to simulate the permittivity of sponges with varying volume fractions of metal phase, Figure 4.12. We chose to use permittivity data for Ag-6.5 at% Al for the metal phase as that composition was broadly representative of the *np-S*. The similarity in form to the experimental data is striking even if the ε_2 values of the experimental data are somewhat higher at low photon energies. Note especially that, at low volume fractions of metal, the simulation reproduces the anomalous shape of the curves for samples S1 and S6 thereby indicating that these two samples have lower volume fraction of metal than the others. We also estimated the porosity by optimizing the volume fraction of each sample against its ε_1 curve using the Bruggeman EMA. (The ε_2 curves of the sponges evidently contain additional scatter and extinction beyond that present in the thin film of the reference Ag-6.5 at.% Al sample so was not suitable for fitting against.) It was also observed that use in the Bruggeman model of the dielectric function for Al-6.5 at% Ag from de Silva et al. (De Silva et al., 2017) produced a much better fit than use of the dielectric function for pure Ag (an average least square deviation of 1.7 relative permittivity units vs 2.7 respectively). This supports the observation that the metallic portion on these sponges is Ag-Al alloy rather than pure Ag. The estimated volume fractions of Ag in each sponge are plotted in Figure 4.13. Sample S6, produced from the most Al-rich precursor has the lowest volume fraction, but the analysis indicates that all the samples have metallic volume fractions are broadly in the range of 0.4 to 0.5, with those of S1 and S6 being the lowest. This independently corroborates the unusual form of the ε_2 curves of S1 and S6 which can only be reproduced in the model by using relatively low volume fractions of metal.

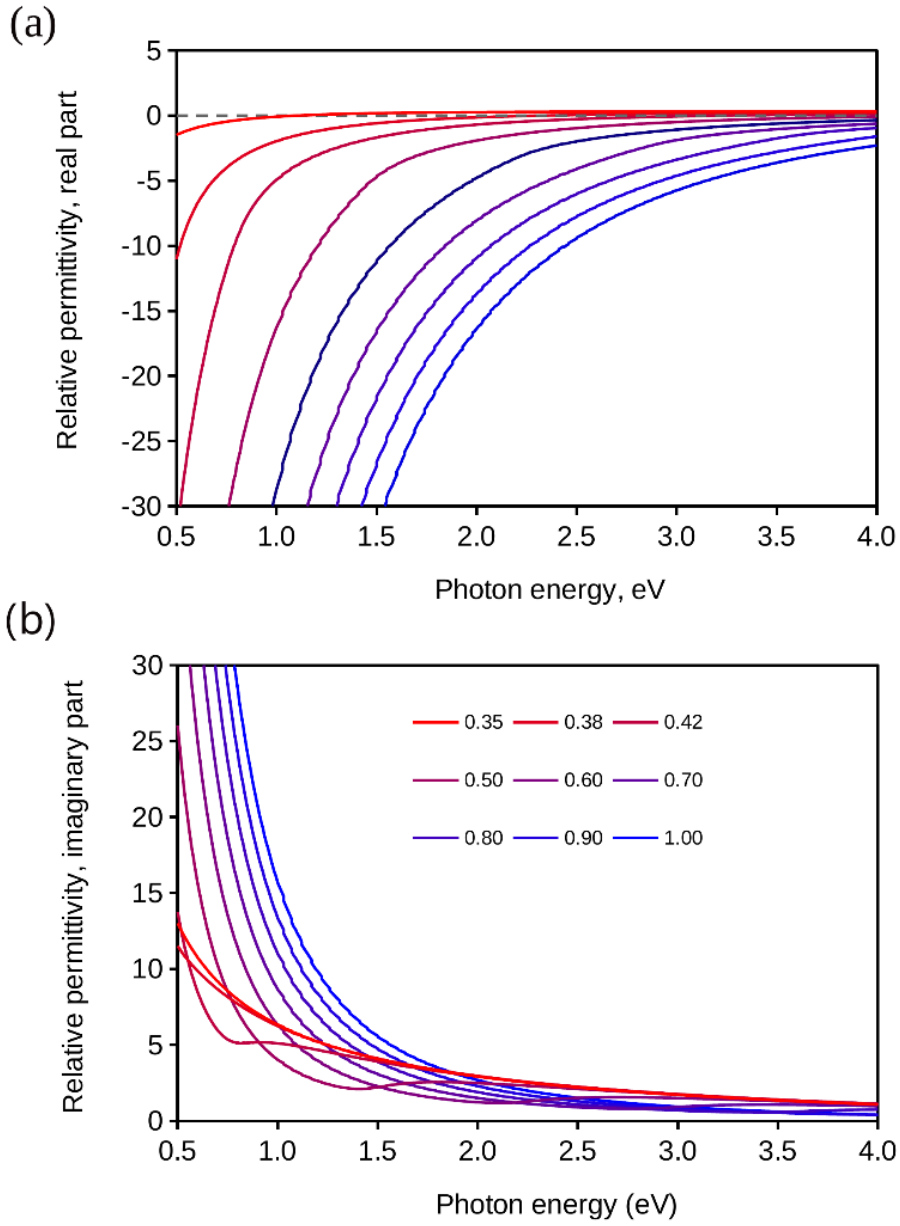

Figure 4. 12 Relative permittivity of sponges comprised of various volume fractions of Ag-6.5 at. % as calculated from the Bruggeman effective medium equation. Note that the form of the experimental data for samples S1 and S6 is qualitatively reproduced in these simulations when low volume fractions of metal are used

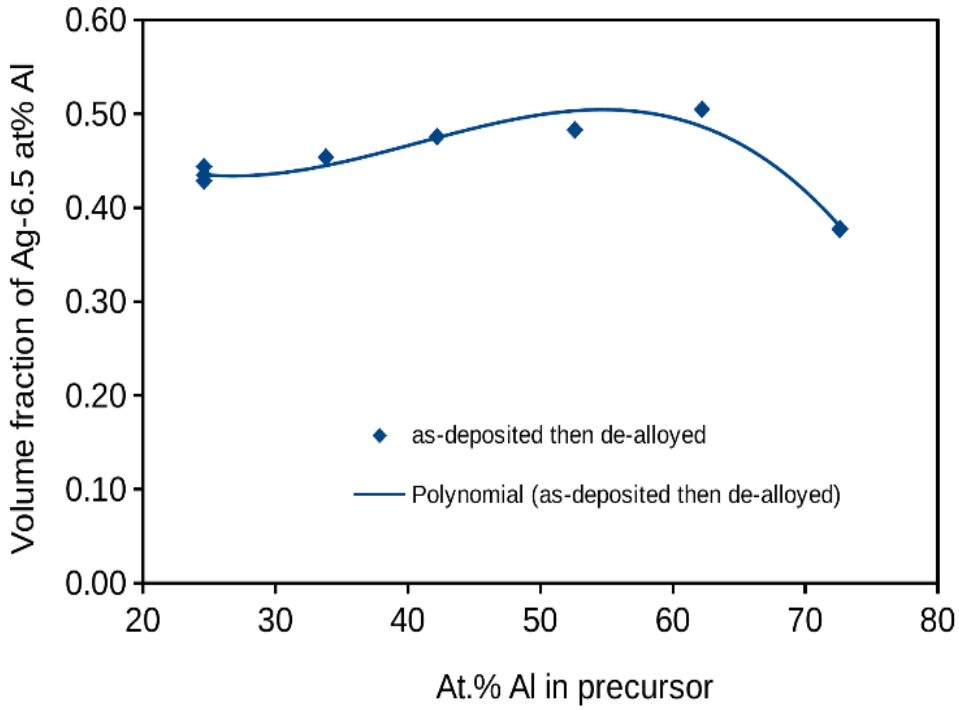

Figure 4. 13 Volume fractions of metal in the experimental sponges estimated from the real part of their permittivity using a Bruggeman model comprised of the Ag-6.5 at.% Al and voids.

4.3.6.2 Optical constants

These extracted values are presented in Figure 4.11 c and d. The optical constants are commonly described using a complex equation:

$$M(\lambda) = n(\lambda) + ik(\lambda) \quad \text{..... (4.2)}$$

The real component, *n*, is typically known as the refractive index of the material which governs a wave's phase shift and velocity as it travels through the material. The imaginary component, *k*, is referred to as the extinction coefficient and is responsible for determining the attenuation of the amplitude of the wave (Losic & Santos, 2015; Maaroof et al., 2005). Nanoporous materials can be characterised as a composite of dense materials and air. As a result, their refractive indices are determined by both the degree of porosity as well as the refractive indices of the dense materials (ligaments) (Knez, 2019; Losic & Santos, 2015).

It is apparent in Figure 4.11 c that refractive indices of all of the *np-S* thin films were larger than those of the Ag thin film in the wavelength range from 350 nm to 2250 nm. This is because the Ag thin film has a very low refractive index in this range – less than 1 – which is characteristic of metal behaviour. The refractive indices of the *np-S* thin films do not follow a consistent pattern at the lower wavelength range from 300 to 1500 nm. Nevertheless, S2 shows a refractive index that is almost identical to zero at wavelengths that are less than 350 nm, while S6 shows the highest refractive index value at this wavelength range, which follows from its

almost insulator-like behaviour. On the other hand, when the wavelength was greater than 1500 nm, S2 to S5 show high refractive indices values and exhibited a relatively less metallic behaviour.

As can be seen in Figure 4.11 d the extinction coefficient values of the *np-S* thin films and Ag thin film increase noticeably with wavelength of the incident beam. Nonetheless, the extinction coefficients of the np-S thin films still show much lower values than those of the Ag thin film. This is due to the Drude free electron response of Ag which is more developed in the Ag thin film than in the sponges. As a result, the relative attenuation of the *np-S* thin films and the Ag thin film diverges dramatically as the wavelength increases.

4.3.6.3 Reflectance of np-S thin film

The UV-Vis-NIR spectroscopy method is frequently used to measure the optical response of metallic nanostructures. In the case of non-transparent samples, such as those used in this investigation, the reflectance (*R*) spectra of the free-void Ag thin film and the de-alloyed Ag-based ligament structure films were characterised using a *UV-Vis-NIR* spectrophotometer in the wavelength range between 300 to 2500 nm.

The reflectance spectra of the free-void Ag thin film and the *np-S* samples with different average ligament sizes are presented in Figure 4.14. It can be seen that the reflectance of the Ag thin film and *np-S* with the average ligament sizes of 31.6 (S1) and 30.6 nm (S2) is expectedly high in the NIR and Vis regions of the spectra. The reflected intensity drops sharply in the UV region for these two samples, forming a dip showing the interband transition at around 310 nm (photon energy of 3.99). Unlike the other coinage metals- gold and copper, the wavelength of the absorption edge of Ag is at the short wavelength end (UV) of the visible spectrum (around a wavelength of 309 nm or photon energy of 4 eV) due to the unique position of the d-shell with respect to the Fermi level (Solé et al., 2005). In our case, the absorption edge appears as the dip in reflectance spectra due to the onset of interband transition for Ag.

Contrary to that, the reflectance spectra of *np-S* samples with the average ligament size of 25.3 (S3), 22.2 (S4), 15.6 (S5) and 13.1 nm (S6) display substantial departures from the deposited Ag thin film spectrum, as figure 12 demonstrates. The reflectance spectra of *np-S* samples are broadband, extending into the UV region with increasing the average ligament size. The LSPR bands of those samples are broad and cover most of the visible region. These shifts in the positions of the LSPR bands of nanostructure materials are due to their structural properties, as their size and shape (Aizpurua & Bryant, 2011), and their width is likely affected by the size distribution of particles (Kosović et al., 2015). Moreover, the intensities of the

reflectance spectra decrease, which means that the *np-S* thin films lose their high reflectivity and become absorptive across the spectrum due to the conversion of incident light into p-SPR (Chen et al., 2011).

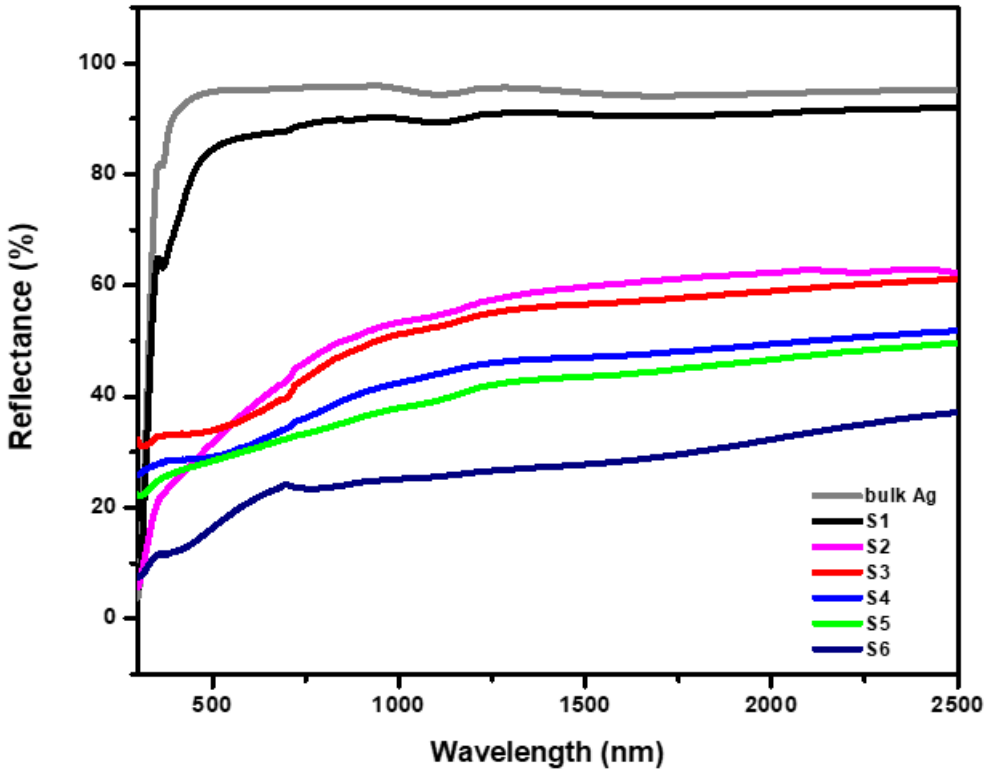

Figure 4. 14 reflectance spectra of the Ag thin film and np-S thin films with different average ligament size.

In conclusion, $Ag_{100-x}Al_x$ alloys with a range between 24.6 and 72.6 at. % Al has been successfully deposited on glass substrates. Dedealloying of the produced alloys was rapid and effective, even at Al contents well below the traditional parting limit. This is likely due to the profusion of atomic-scale structural defects in the as-deposited film, which renders it relatively susceptible to corrosion. The produced *np-S* thin films exhibited finer structure with increasing the starting Al contents.

Furthermore, the unique behaviour of the *np-S* thin films with increasing Al content is a novel finding. This led to the tuning of the average ligament size from about 32 to 13 nm, a change that was not detected for the average pore size. The density of the pores, in contrast, increased markedly as the Al content in the precursor increased. The electrochemical capacitance measurement for the *np-S* thin film produced from Ag- 75 at. % Al alloy showed a surface area that was ten times greater than its primary alloy, further highlighting the unique behaviour of these films.

The increasing electrical resistivity of the *np-S* thin films, as the average ligament decreased, has significant implications. This is evidently due to a combination of finer ligament

size and greater pore density. The dielectric permittivity of the *np-S* thin film with the average ligament size of 13 nm showed non-metallic behaviour at the higher photon energies of the spectra, and a noticeable decrease in its reflectance, which decreased sharply with decreasing the ligament size. These findings have practical applications in the field of materials science and engineering. The volume fraction of metal can be estimated by analysis of the optical properties of the sponges. Specifically, spectroscopic ellipsometry was used to extract a relative dielectric permittivity of each sponge, and the results for the real part of permittivity matched to a volume fraction estimated by use of the Bruggeman effective medium model, using a nanocomposite comprised of variable volume fractions of Ag-6.5 at.% Al and air.

Annealing the alloys before conducting dealloying was not effective because it increased the amount of the intermetallic Ag_2Al phase, formed some Al_2O_3, and consequently enhanced the Ag content in the subsurface film.

Chapter 5 Exploring the Antibacterial Power of Nanoporous Silver Coating Against Pseudomonas aeruginosa and Escherichia coli

5. Overview

Metallic silver nanostructures have been widely incorporated into antibacterial and medicinal applications due to their ability to kill or inhibit bacterial growth (Baker et al., 2005; Gunawan et al., 2020; Ivask et al., 2014; Nomier et al., 2023; Pandian et al., 2010; Raza et al., 2016). The problem associated with Ag nanoparticles their tendency to agglomerate, to form larger clusters when they are exposed to air or water (L. Yang et al., 2019). This leads to a decrease in the antibacterial efficacy of the nanoparticles. So far, various support materials have been tested to reduce agglomeration to improve the stability of AgNPs, such as mesoporous silica, mesoporous bioactive glass (BG), nanoporous metal oxide, zeolites and mesoporous graphene (M_pG) (Asli et al., 2022; Lu et al., 2014; Qing et al., 2020; L. Yang et al., 2019; Zheng et al., 2019). However, these materials have some disadvantages as antibacterial agents, including increase of the production cost, and health and environmental concerns due to leaching the AgNPs from the substrate into water (Bharti et al., 2015).

To overcome these drawbacks of AgNPs loaded on nanoporous substrate, metallic *np-S* structures have been produced. The result is like self-supporting non-aggregating Ag nanoparticles.

5.1 Objective of chapter

In this study, we aim to investigate the antibacterial activity of the *np-S* thin films with different nanopore and ligament. We have chosen the pathogenic strain Pseudomonas aeruginosa (PAO1) and the non-pathogenic strain Escherichia coli (DH5α) to provide a comprehensive approach to evaluating the antibacterial efficacy of the *np-S* thin films. This study relies on measuring the optical density of bacterial suspensions to assess bacterial growth. Additionally, cell viability will be determined by distinguishing between live and dead cells using fluorescence microscopy.

5.2 Results and Discussion

Precursor $Ag_{100-x}Al_x$ thin film alloys with x= 24.6, 52.6 and 72.6 at.%, Ag, Al and TiO_2 thin films on glass substrate were prepared using magnetron sputtering. This was followed by dealloying of the alloy thin films in 5M NaOH aqueous solution at room temperature to produce nanoporous structures, as described in chapter 4.

The average pore and ligament sizes of the produced *np-S* thin films measured from the SEM images are presented in Table 5.1. The concentration of residual Al measured using EDS technique is also shown in Table 5.1 below.

Table 5. 1 The measured chemical compositions, Average pore and ligament size, and the concentration of residual Al in the np-S thin films prepared by dealloying of Al_xAg_{100-x} thin film alloys with x= 24.6, 52.6 and 72.6 at.% in 5M NaOH at RT.

	S1	S2	S3
Al concentration (at. %)	24.6	52.6	72.6
Average pore size (nm)	12.6±4.9	15.5±4.5	11.1±3.5
Average ligament size (nm)	31.6±12.8	22.2±8.7	13.1±3.9
Residual Al concentration (at. %)	1.8	3.9	1.4

A glass cutting tool was used to cut the samples into coupons 5 mm × 5 mm square. Prior to conducting bacterial experiments, the samples were sterilized using an autoclave in a dry mode at 121 °C for 60 min. Coupons were also created from thin solid films of Ag, Al and TiO_2 with the same thicknesses and dimensions to obtain accurate, comparable, and reliable results.

5.2.1 Antibacterial performance of *np-S* thin films against P. aeruginosa

Np-S thin films were not effective in completely suppressing *Pseudomonas aeruginosa* over a 24-hour period. The optical density (OD) of the 96-well microplate, which contains untreated and treated *P. aeruginosa* with *np-S,* Ag, Al, and TiO_2 thin films, was assessed using a microplate reader after a 24-h incubation period. The *P. aeruginosa* growth was continuous, as evidenced by the measured OD values over 2.5 (higher than instrument reading). This result indicates that none of the used treatments were effective in suppressing the proliferation of *P. aeruginosa*. The persistence of substantial turbidity in the wells after adding the thin films of *np-S,* Ag, Al, and TiO_2 and incubating for 24- h, as shown in Figure 5.1, proves that these materials did not have a notable antibacterial impact on this specific bacterial strain in the given experimental conditions. The same results were reported by Wu and co-workers for nanoporous Ag foams prepared by two-step dealloying of $Ag_{30}Al_{70}$, $Ag_{35}Al_{65}$, and $Ag_{40}Al_{60}$ alloys in a 5 wt.% HCl solution at 60°C for 30 minutes, followed by treatment at 90°C for 2 hours. These produced foams did not show any antibacterial activity against *P. aeruginosa* (Wu et al., 2015b).

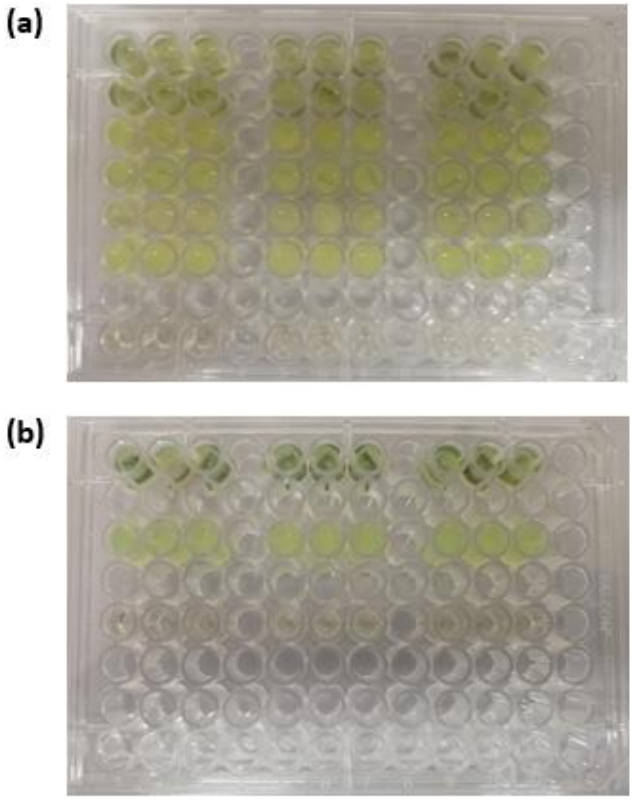

Figure 5. 1 A 96-well microplate assay used for assessing dose- response effect of np-S, Ag, Al, and TiO_2 thin films on P. aeruginosa. The turbidity of the wells shows the failure of all the treatments in completely inhibiting bacterial growth.

5.2.2 E. coli DH5α 10-h growth curve

The growth of *E. coli DH5α* cells was tracked over a 10-h period (2-h preconditioning and 8-h treating) of measurements under various experimental conditions. The graph in Figure 5.2 a, b and c shows the measured OD at 600 nm that was collected every two hours of incubation. The conditions include *E. coli* DH5α cells only as a control and *E. coli* DH5α cultures exposed to different types and amounts of treatments: *np-S* with different pore and ligament sizes (1 coupon and 5 coupons), Ag thin film (1 coupon and 5 coupons), Al thin film (1 coupon and 5 coupons), and titanium dioxide (TiO_2) (1 coupon and 5 coupons).

The OD measurements were conducted before (from 0 to 2-h) and after (from 4 to 10-h) introduction of the treatments. After 2 h of incubation, the treatment, including *np-S*, Ag, Al, and TiO_2 thin film coupons, was added to the incubated bacterial cells. The measured OD values for the period from 4 to 10 h show that all the treatment resulted in linear increase in the OD values, indicating active bacterial growth in the exponential phase. The *E. coli* cells that were treated with Ag, Al, and TiO_2 thin films and those that were not treated had identical growth curves, as shown in Figures 5.2 a, b, and c. This indicates that the presence of Ag, Al, and TiO_2 thin films in the bacterial suspension, even with an increasing number of coupons, does not measurably inhibit the exponential growth of the bacterial cells. During this period,

the OD values for *E. coli* cells alone and for treated cells with Ag, Al, and TiO_2 increased from approximately 0.6 to 1.6.

Although *E. coli* in the presence of *np-S* thin films still proliferated, a reduction in growth of *E. coli* cells was observed. The reduction was, however, to the limit of statistical significance and further work would be required to confirm the differences. The reduction was strongest for np-S thin film with a ligament size of 13.1 nm, with 5 coupons of *np-S* having a greater inhibitory effect than 1 coupon of np-S as, achieving OD of about 1.4 by the end of the 10-h period of incubation Figure 5.2 a demonstrates. Treatment with five coupons showed a stronger growth inhibition than treatment with a single coupon although the effect was unexpectedly small. *Np-S* thin films with an average ligament size of 22.2 nm show a lower reduction in bacterial growth than the 13.3 nm ligament thin films. Figure 5.2 b presents the OD values for the incubated *E. coli* cells for 4 to 10 h, indicating a slight reduction in the OD values compared to the control. *Np-S* thin films with an average ligament size of 31.6 nm do not have any inhibitory effect on the bacteria within the timeframe of the experiment, even when 5 coupons of *np-S* are added as seen in Figure 5.2 c.

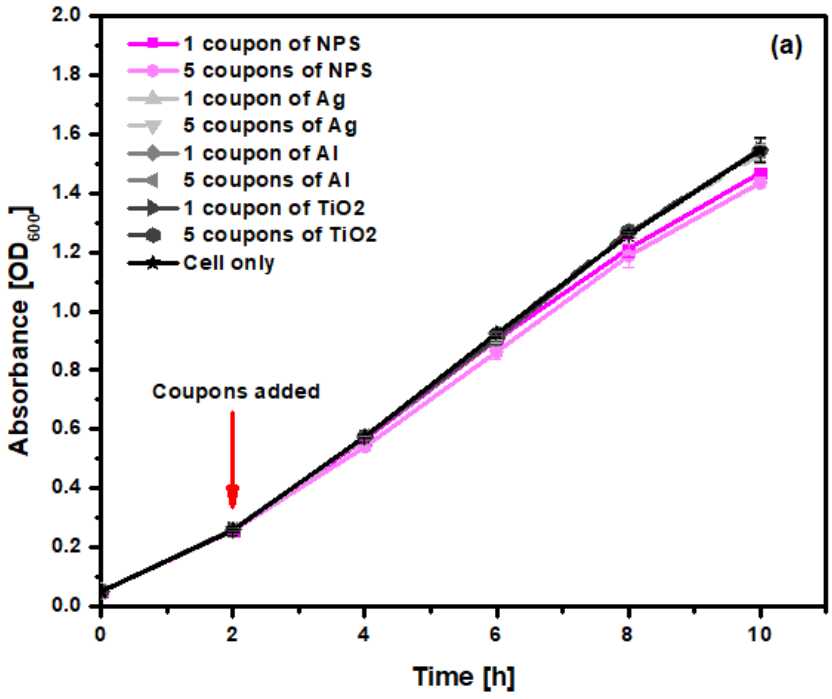

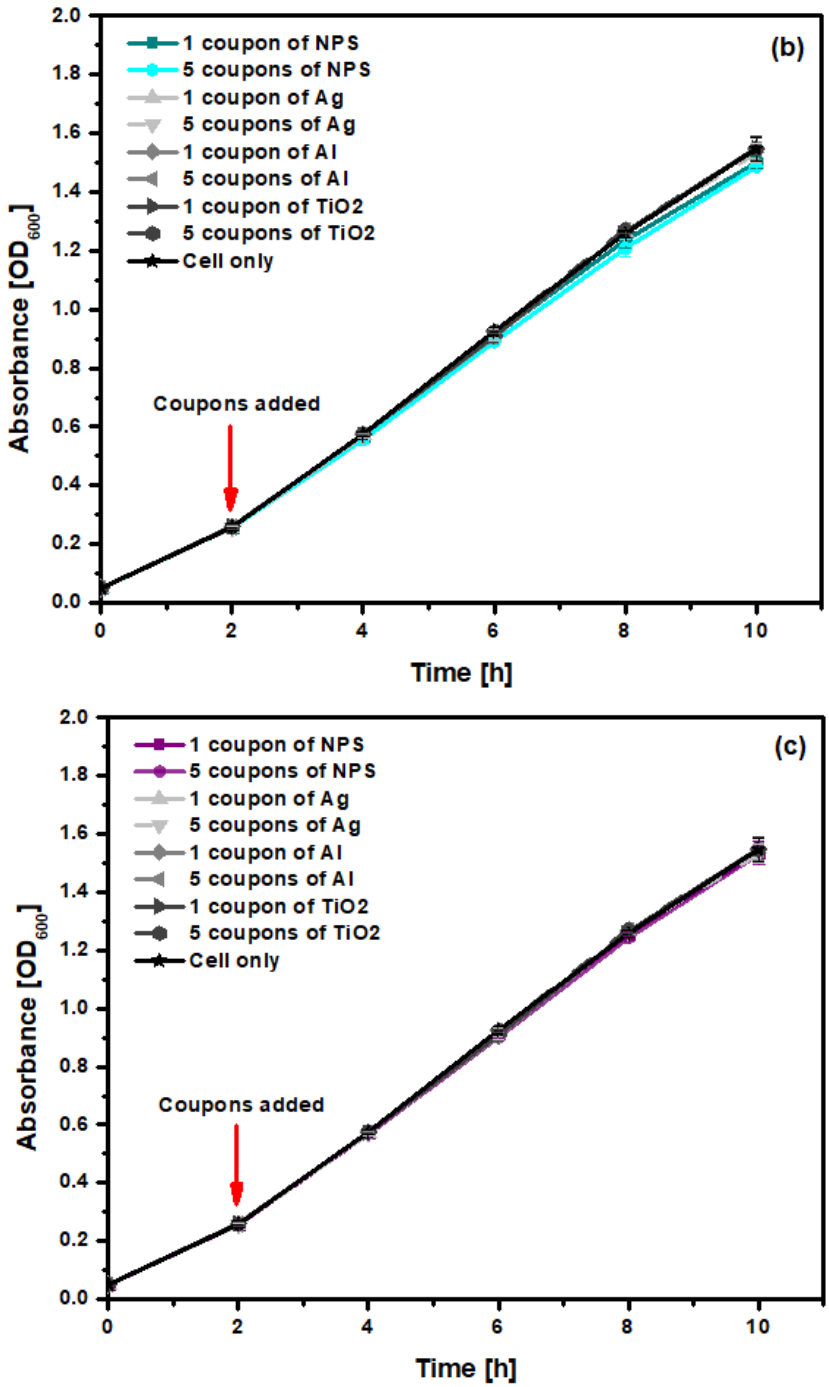

Figure 5. 2 Absorbance measurements of E. coli DH5α *at 600 nm after treating with np-S thin films with ligament size of (a) 13.1, (b) 22.2 and (c) 31.6 nm.*

5.2.3 Bacterial growth rate

The growth rate, μ of *E. coli* cells or the change in the number or mass of bacterial cells per unit time (Srivastava, 2013) during the exponential (log) phase was investigated, and can be obtained by finding the slope of the natural logarithm of OD (Ln(OD)) plotted against incubation time t as Figures 5.3 (a-i), 5.4 (a and b) and 5.5 (a and b) demonstrate using Eq.5.1:

$$\ln \frac{N_t}{N_0} = \mu(t - t_0) \quad \text{..... (5.1) (Hall et al., 2014)}$$

Where the number of bacteria cells at the final time t denoted as N_t, while N_o is the number of bacteria cells at the initial time t_o. It is assumed that the OD of a bacterial suspension is directly proportional to the number of bacteria cells in the suspension (Chatterji, 2011) although there is some literature to suggest that at larger OD values (> 1.5) multiple scattering may lead to an underestimation of the population.

The graph in Figure 5.6 a suggests that treating *E. coli* with *np-S* thin films, having an average ligament size of 13.1 nm, has minimal impact on the bacterial growth rate. The estimated growth rate of *E. coli* was 0.253 h^{-1} when exposed to five coupons of *np-S* thin films. Likewise, introducing of a single coupon of *np-S* thin film also has less influence on the growth rate of *E. coli*, with a growth rate of 0.257 h^{-1}, although slightly lower than that observed with five coupons of *np-S* thin films with uncertainty of 1%.

In comparison to the growth rate of *E. coli* treated with *np-S* thin films with an average ligament size of 13.1 nm, the introduction of *np-S* thin films with a ligament size of 22.2 nm into the *E. coli* culture results in a slight decrease in the growth rate as Figure 5.6 b shows. The growth rate of *E. coli* after adding 5 coupons of *np-S* thin films with the larger ligament size was 0.259 h^{-1}. While the addition of 1 coupon of this treatment showed no noticeable effect on the growth rate of *E. coli*, maintaining a growth rate like untreated conditions.

The growth rates of untreated and treated *E. coli* with *np-S* thin films with the ligament size of 31.6 nm, Ag, Al and TiO_2 thin films remain consistent, approximately around 0.262 h^{-1}, as figure 6c presents. This consistency confirms that the treatments used, even with increasing their concentration, do not have any effect on the bacterial growth rate. The uniform and unchanged standard deviation error bars in Figure 5.6 c further indicate that the treatments do not introduce substantial variation in growth rates.

An alternative method to express the bacterial growth rate is to calculate the time required for a bacterial population to double in number, a parameter known as the doubling time of bacterial growth. This can be determined using Eq. 5.2:

$$Doubling\ time = \frac{0.693}{\alpha} \quad \text{..... (5.2) (Ryser \& Marth, 2007)}$$

Table 5.2 below demonstrates the calculated values of doubling time for untreated and treated *E. coli* cells. The required time for *E. coli* cells to double their number increases with decreasing the average ligament size of the *np-S* thin films. Specifically, *E. coli* cells treated with 5 coupons of *np-S* thin films with a 13.1 nm ligament size required 2.74 h to double their

cell number, while 1 coupons of *np-S* thin films with a 13.1 nm ligament size and 5 coupons of *np-S* thin films with a 22.2 nm ligament size need 2.69 and 2.68 h to double their cell number. In contrast, other treatments required only 2.65 h for the *E. coli* cells to double, indicating a slight but noticeable effect of the smaller ligament size on the bacterial growth rate.

Table 5. 2 calculated growth rate using Eq.1 and doubling time using Eq.2 for untreated E. coli and treated samples using np-S-1, 2, 3 thin films with ligament size of 13.1, 22.2 and 31.6 nm, respectively, Ag, Al and TiO_2 thin films

sample	np-S-1	np-S-1	np-S-2	np-S-2	np-S-3	np-S-3	Ag	Ag	Al	Al	TiO_2	TiO_2	Cells-only
Number of coupons	1	5	1	5	1	5	1	5	1	5	1	5	-
Growth rate [h^{-1}]	0.257	0.253	0.262	0.259	0.262	0.262	0.262	0.262	0.262	0.262	0.262	0.262	0.262
Doubling time [h]	2.74	2.69	2.65	2.68	2.65	2.65	2.65	2.65	2.65	2.65	2.65	2.65	2.65

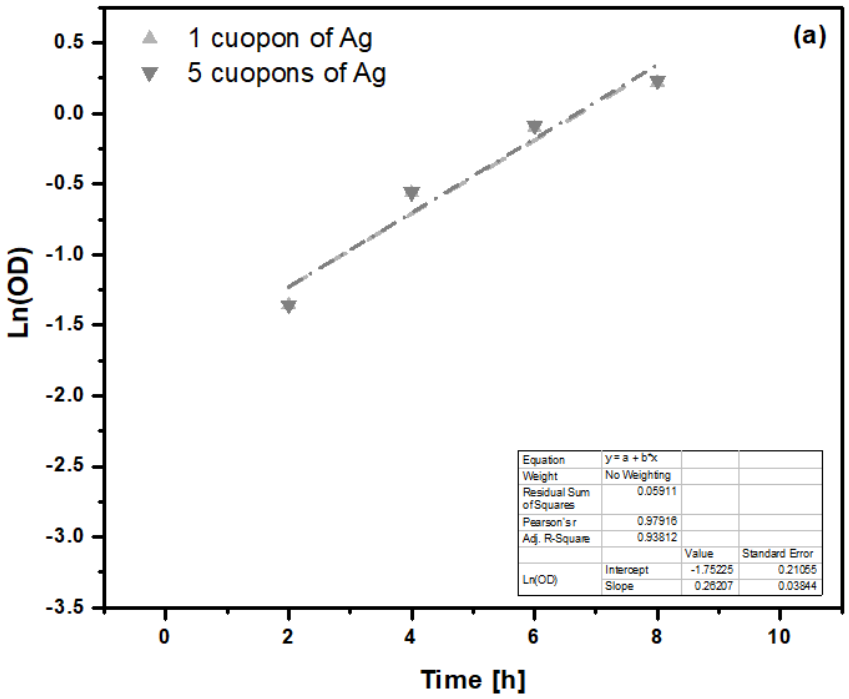

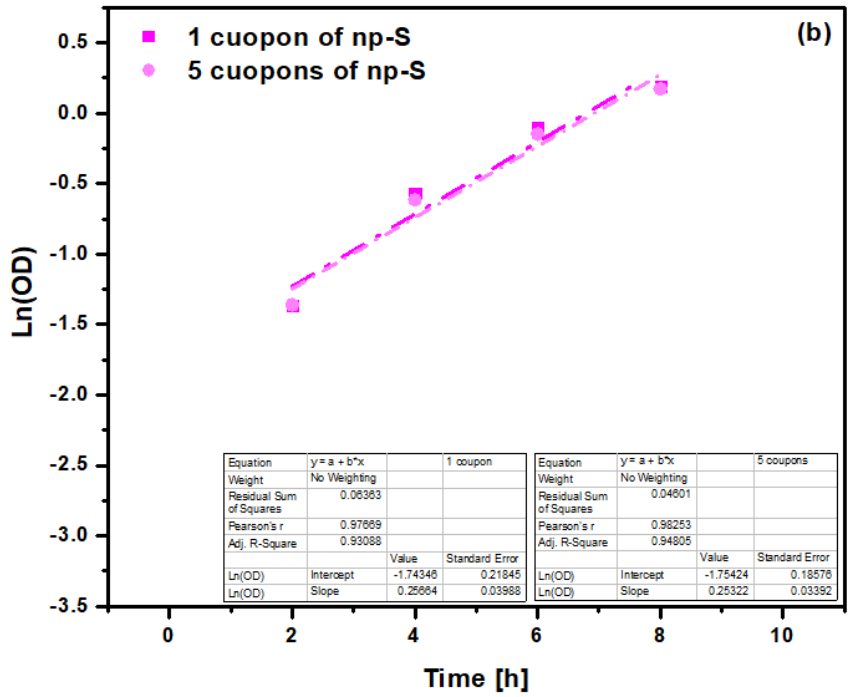

Figure 5. 3 The natural logarithm of optical density (ln OD) versus time (h) for (a) 1 and 5 coupons of Ag thin films and (b) 1 and 5 coupons of np-S with ligament size of 13.1 nm. The slope of the linear region of the curve between 2 to 8 h is used to estimate the growth rate of the E. coli culture.

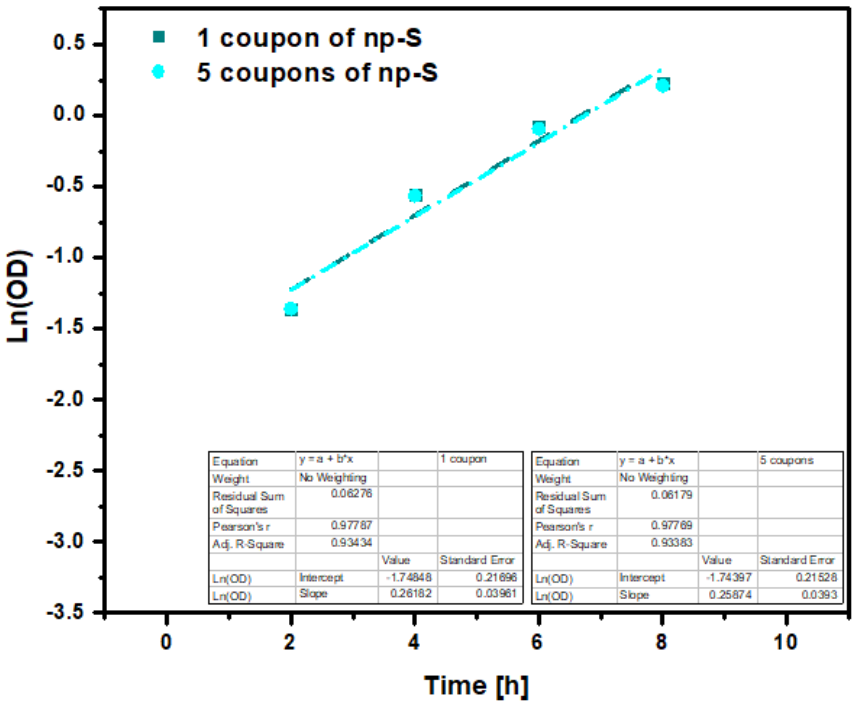

Figure 5. 4 The natural logarithm of optical density (ln OD) versus time (h) for 1 and 5 coupons of np-S with ligament size of 22.2 nm. The slope of the linear region of the curve between 2 to 8 h is used to estimate the growth rate of the E. coli culture.

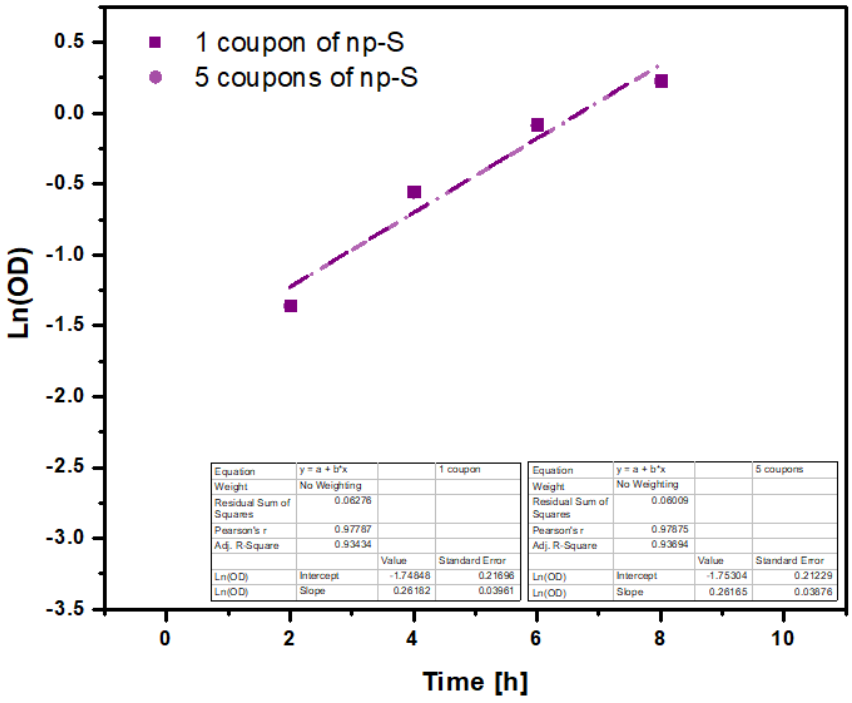

Figure 5. 5 The natural logarithm of optical density (ln OD) versus time (h) for 1 and 5 coupons of np-S with ligament size of 31.6 nm. The slope of the linear region of the curve between 2 to 8 h is used to estimate the growth rate of the E. coli culture.

5.2.4 Biomass growth

An alternative method to understand bacterial growth over a given period of time, is related to the total mass of living organisms in a given population during that period (Cunningham & Cunningham, 2014; IGNACIMUTHU, 2019). This parameter is a biomass growth of organisms, it can be calculated using the following equation (Eq. 5.3):

$$Biomass\ growth\ (\%) = \frac{Sample\ OD_{600} - blank\ OD_{600}}{Control\ OD_{600} - blank\ OD_{600}} \times 100 \ldots\ldots\ldots\ldots\ldots\ldots \quad (5.3)$$

(Kungolos, 2006)

The bar graph in Figure 5.6 a, b, and c presents the biomass growth percentage of treated *E. coli* cells relating to untreated cells over a 10-hour period. After the initial 2-h period, treatments were added to the *E. coli* suspension, leading to observable changes in the growth dynamics.

Upon addition of the *np-S* thin films, a slight decrease in the biomass growth percentage of treated *E. coli* cultures was noted. Specifically, *E. coli* treated with 1 coupon of *np-S* thin films with a ligament size of 13.1 nm exhibited a biomass growth percentage of 95%. Increasing the concentration of *np-S* thin films to 5 coupons resulted in a further reduction of the biomass growth percentage to 92%. This indicates a dose-dependent effect of the *np-S* thin films on the bacterial growth, with higher concentrations leading to more significant growth inhibition.

On the other hand, treating *E. coli* with 5 coupons of *np-S* thin films with a ligament size of 22.2 nm led to a biomass growth percentage of 96%, suggesting a slightly lesser inhibitory effect compared to the smaller ligament size. Other treatments, regardless of their type or quantity, did not measurably reduce the exponential growth of the bacterial cultures, as evidenced by the almost similar growth percentages across all treatments. This consistency indicates that most treatments had minimal impact on the overall biomass growth, with the exception of the *np-S* thin films, which demonstrated a measurable effect based on their concentration and ligament size.

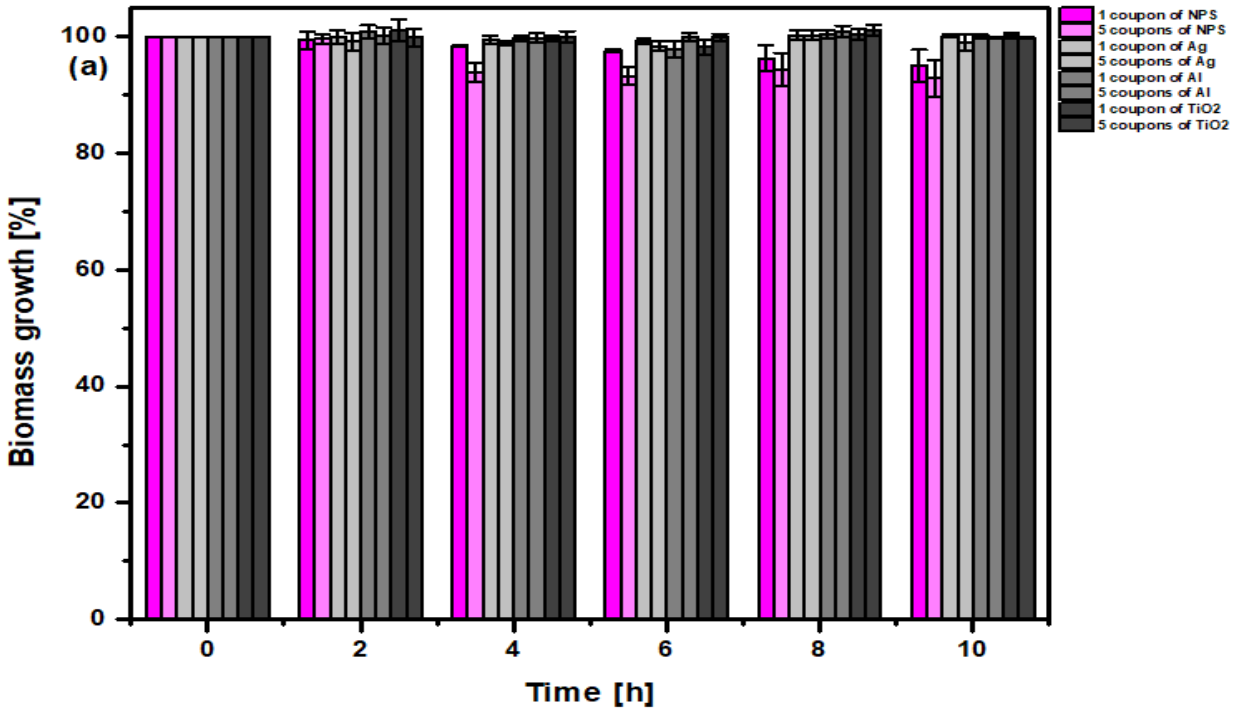
(a)
Biomass growth [%]
Time [h]
0
20
40
60
80
100
0
2
4
6
8
10
1 coupon of NPS
5 coupons of NPS
1 coupon of Ag
5 coupons of Ag
1 coupon of Al
5 coupons of Al
1 coupon of TiO2
5 coupons of TiO2

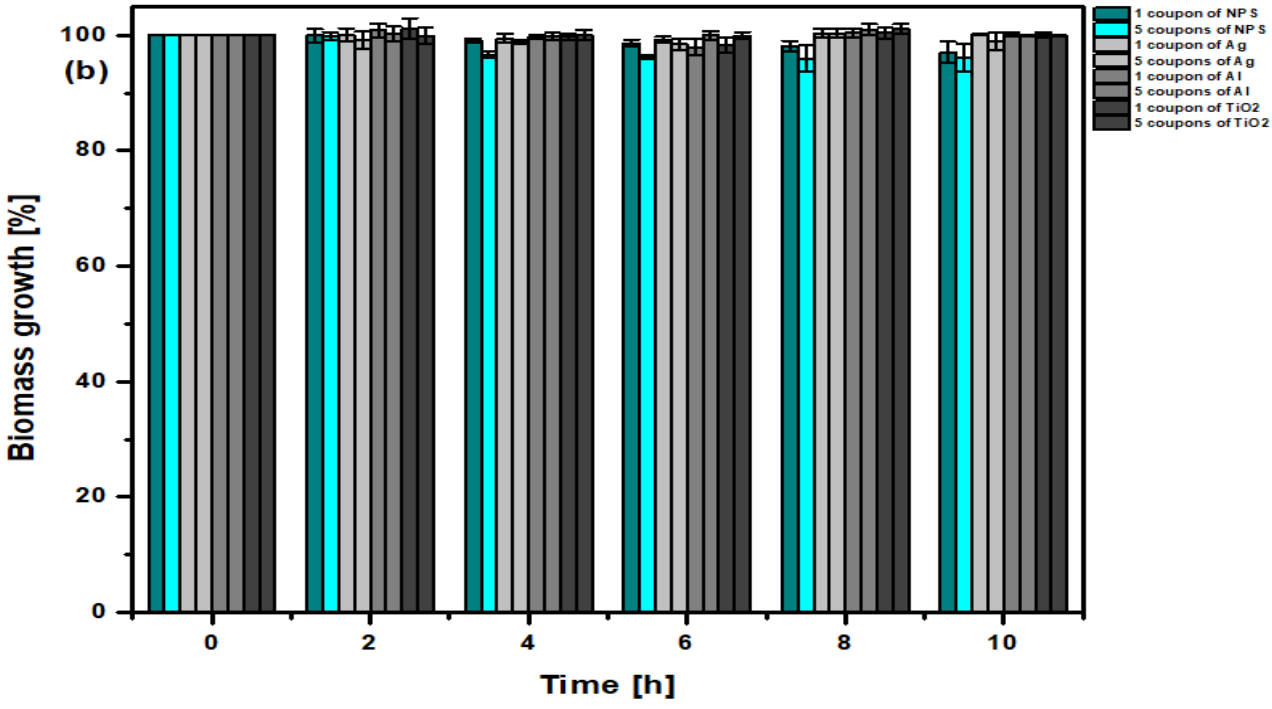
(b)
Biomass growth [%]
Time [h]
0
20
40
60
80
100
0
2
4
6
8
10
1 coupon of NPS
5 coupons of NPS
1 coupon of Ag
5 coupons of Ag
1 coupon of Al
5 coupons of Al
1 coupon of TiO2
5 coupons of TiO2

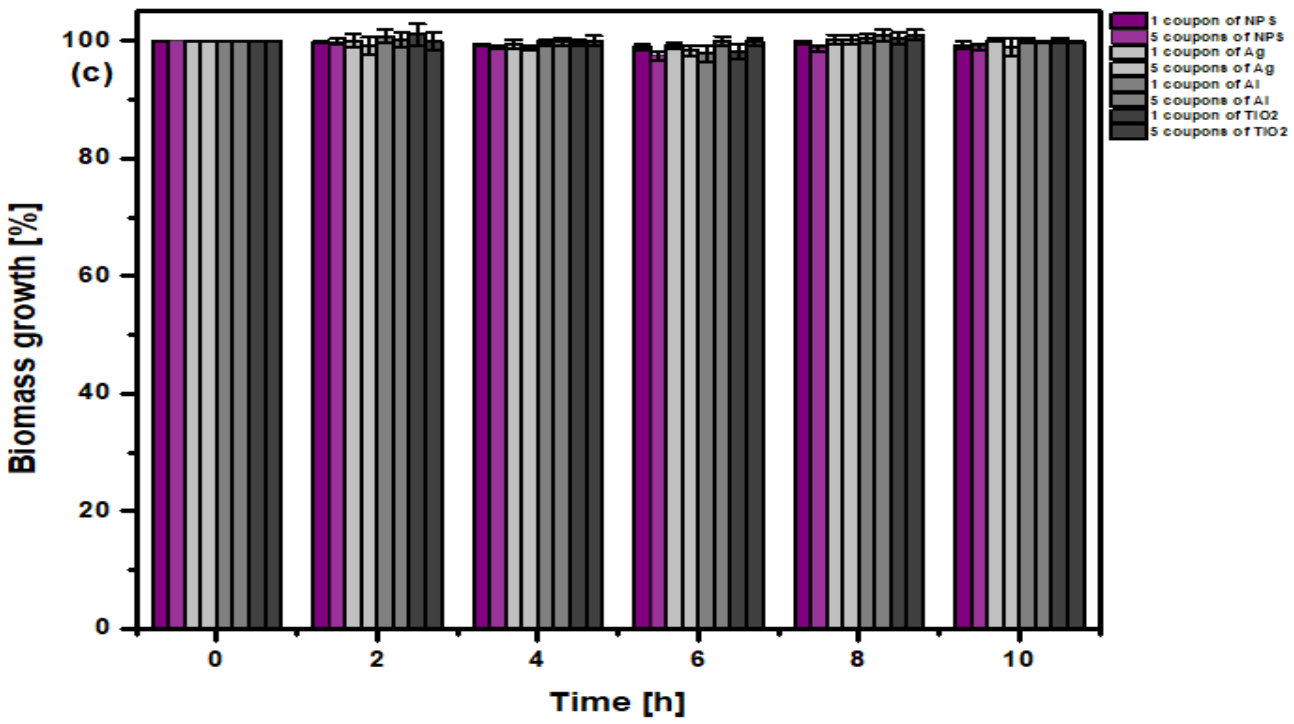

Figure 5. 6 Biomass growth of E. coli DH5α after treating with np-S thin films with ligament size of (a) 13.1, (b) 22.2 and (c) 31.6 nm.

5.2.5 Cell viability

The differences in the ratio of viable to non-viable cells between treated and untreated samples serve as a direct measure of the antibacterial performance of the targeted thin films. Therefore, for further examination of the antibacterial effectiveness of the treatments used, including *np-S,* Ag, Al, and TiO_2 thin films, at least nine fluorescent images of each treatment and an untreated E. *coli* culture were collected. For this reason, two different fluorescent dyes, SYTO-9 and PI, were employed to distinguish between live and dead bacterial cells. The green-fluorescent SYTO-9 dye, in conjunction with the red-fluorescent, PI stain, allows for simultaneous staining and differentiation of live and dead cell populations.

The representative fluorescence microscopic images of treated and untreated *E. coli* are shown in Figure 5.7 a, b, c, d, and e. The presented images display rod-shaped cell bodies, with the width between 0.5 and 1.4 µm and the length between 0.9 and 3.1 µm. Moreover, elongated rod-shaped E. coli cells with the length between 4 and 47 µm were observed in all fluorescence images. When compared with the literature, *E. coli* DH5α typically has a length ranging from 1 to 3 µm and a width of approximately 0.5 µm (Huang et al., 2018). The elongation in *E. coli* cells can be caused by inhibition of cell division which will lead to filamentous cell formation. Moreover, suppression of the Min proteins by RcsB prevents the formation of the Z ring in rod-shaped cells, leading to elongated cells. The presence of antibacterial agents such as

nanoporous metals can induce filamentation in bacteria as an adaptive mechanism to survive adverse conditions. Lastly, nutrient starvation may be one reason for cell elongation (Poole, 2019).

The cell viability can be defined as the ratio of the number of live cells to the total number of cells (both live and dead) (Měřička et al., 2021). The calculated values of *E. coli* cells viability depicted in Figure 5.8; the untreated *E. coli* cells viability reached 97.0±7%. Similarly, the treated *E. coli* with Ag, Al and TiO_2 thin films exhibited the cells viability of 96.1±6%, 96.1±9%, and 96.1±7%, respectively. In contrast, a slight decrease in viability was observed, with 87.0±6% after treating *E. coli* with *np-S* thin film with ligament size of 13.1

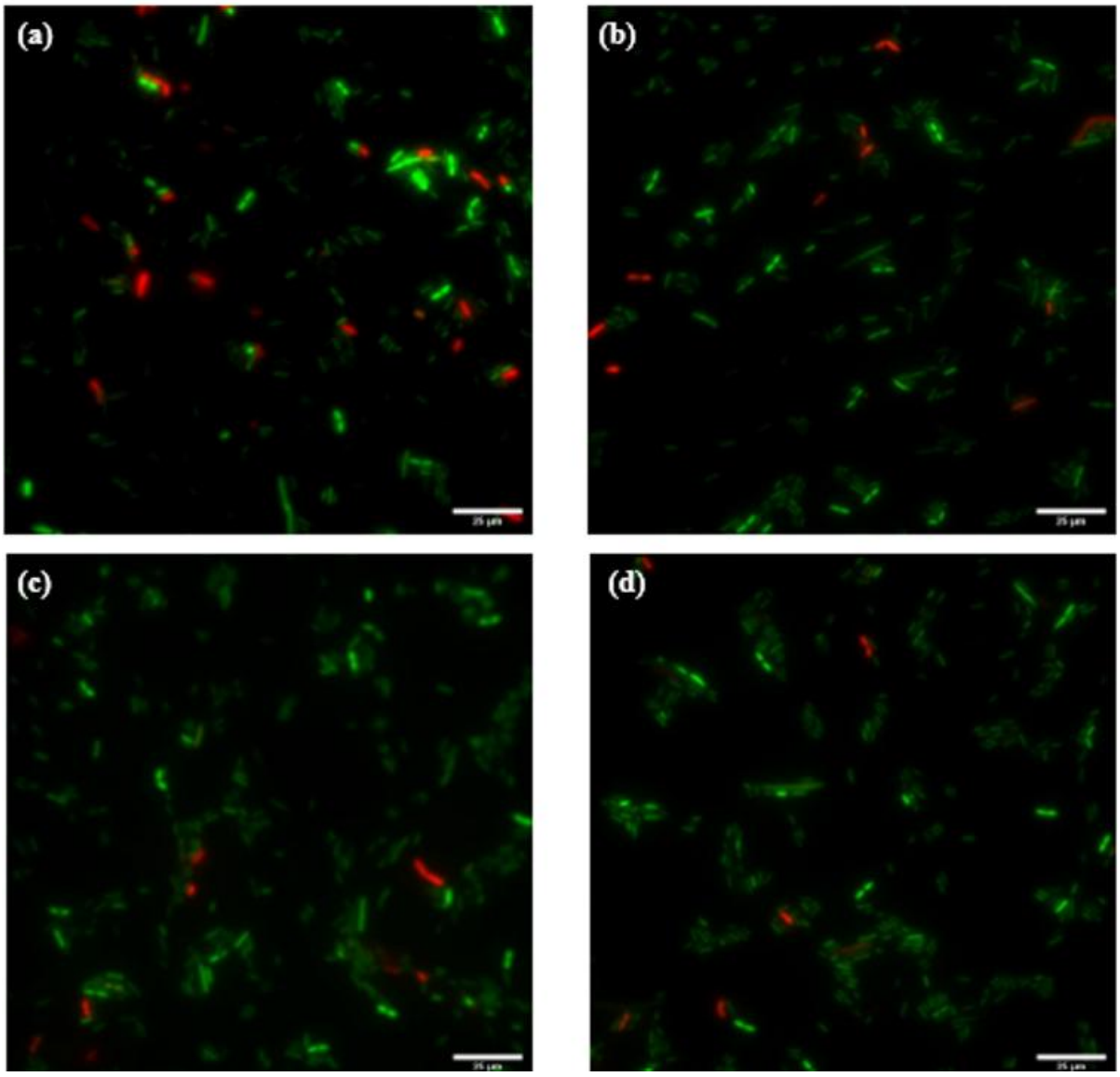

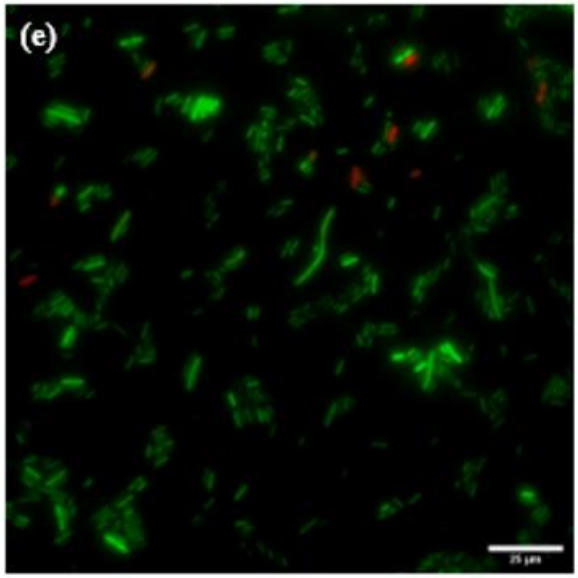

Figure 5. 7 Fluorescence microscopic images of E. coli DH5α strain after treating for 6 h with (a) np-S thin films with ligament size of 13.1 nm, (b) Ag thin films, (c) Al thin films, (d) TiO_2 thin films, and (e) without any treatment. Viable E. coli cells appear as green rods while non-viable E. coli cells shown as red rods.

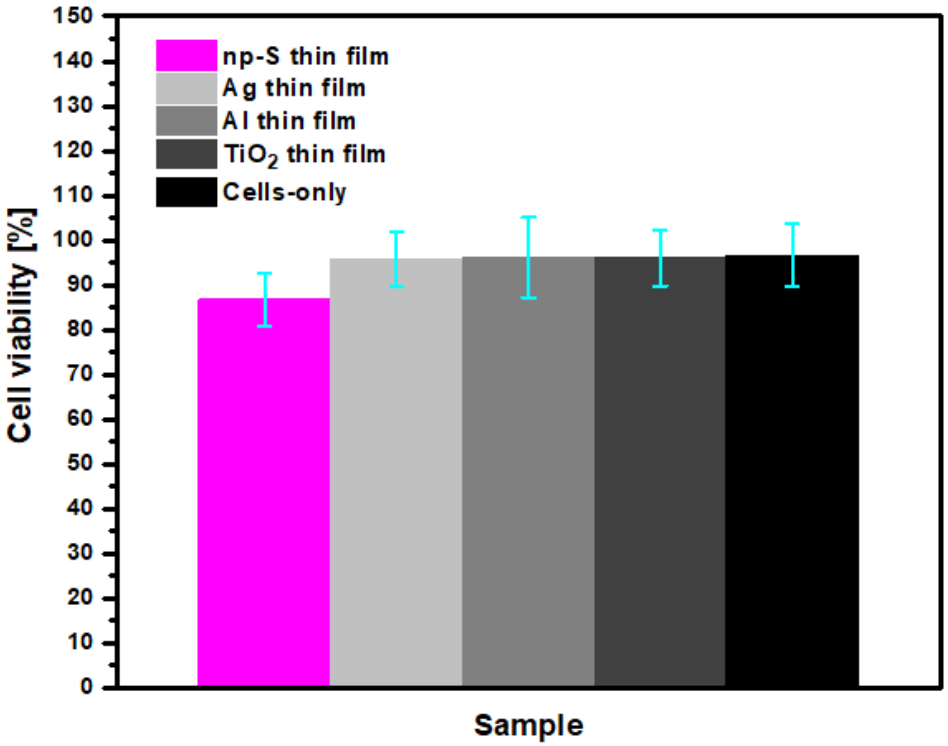

Figure 5. 8 Cell viability of E. coli DH5α after treating for 6 h with np-S thin films with ligament size of 13.1 nm, Ag thin films, Al thin films, and TiO_2 thin films. The presented graph demonstrates the mean values ±standard deviations for live

The toxic mechanism of silver in its nanostructures against a broad range of microorganisms is still not fully resolved. According to the existing literature, two main proposed mechanisms are well-established; direct-contact killing and ion-mediated killing (Baker et al., 2005; Dakal et al., 2016). Nanoporous materials with a high surface area provide numerous active sites for releasing Ag^+ ions, which can subsequently lead to the disruption of

bacterial membranes. In this study, *np-S* thin films with an average pore size of 11.1 nm exhibit a surface area that is ten times greater than that of their corresponding alloy counterparts (see Chapter 7), thereby offering significantly more active sites for Ag^+ ions release. On the other hand, the average pore size of the used *np-S* thin films in this work was small ranging from 11.1 to 15.5 nm. These sizes are considerably smaller than the smallest dimension of both *P. aeruginosa* and *E. coli* DH5α, which are approximately 1 μm and 0.5 μm, respectively (Huang et al., 2018; Wu et al., 2015b). Therefore, the bacterial cells are unable to penetrate the nanopore structure of the thin films. This observation demonstrates that the antibacterial performance of the thin films is likely due to increasing the surface area of the thin films rather than internal bacteria absorption. In regard to the direct-contact mechanism, the antibacterial action of nanoporous metals does seem to be due to damaging the bacteria cell wall or even weakening its cell wall, which is a common mechanism for metal nanoparticles and other antibacterial agents. However, the negative hyperpolarization of bacteria cell walls may be the main reason for the antibacterial activity of nanoporous metals. This change in the electrical state of the bacteria cell wall in turn leads to delicately disrupt ion channels, which are crucial for regulating the flow of ions into and out of the bacteria cell, thereby impairing bacterial function (Miyazawa et al., 2018). The reported antibacterial activity of nanoporous gold (*NPG*) against *E. coli* (K-12) was attributed to the hyperpolarization of the bacterial cell wall by *NPG*. This observation was recorded after 400 μL of the bacterial culture was dropped onto NPG and then incubated for 48 h (Miyazawa et al., 2018).

Despite their enhanced surface area which promotes active sites for direct contact with the bacteria and for releasing Ag^+ ions, the produced *np-S* thin films demonstrated very low antibacterial performance, which may be attributed to many reasons such as large volume of bacterial suspension (Duggan et al., 2024) relative to the *np-S* thin films' surface area, which may lead to saturated the surface of the np-S thin film with bacteria, thereby decrease the area for releasing Ag^+ and for contact. Moreover, relative humidity may contribute to decreasing the effectiveness of np-S as antibacterial agent. Hakamada and co-workers studied the antibacterial activity of nanoporous gold (NPG) against *Escherichia coli* and *Staphylococcus epidermidis* by dropping 400 μL of suspension onto the surface of *NPG*, flat gold (*FG*) and control. The samples were incubated for up to 24 h, in a humidity-controlled environment at 35°C. They concluded that the antibacterial performance of *NPG* is highly affected by relative humidity (RH). *NPG* became less effective at a low RH of 15% and at a high RH of 90%. At 15 % RH, the bacterial suspension dried out, causing bacterial death. While at 90% RH, the

increased thickness of the suspension prevented direct contact between the antibacterial agent and the bacteria. Moreover, they found that the antibacterial performance of *NPG* is highly affected by the pore size, *NPG* with small pore size (20 nm) demonstrated higher antibacterial activity than *NPG* with large pore size (50 nm), especially at RH of 60%. (Hakamada et al., 2017).

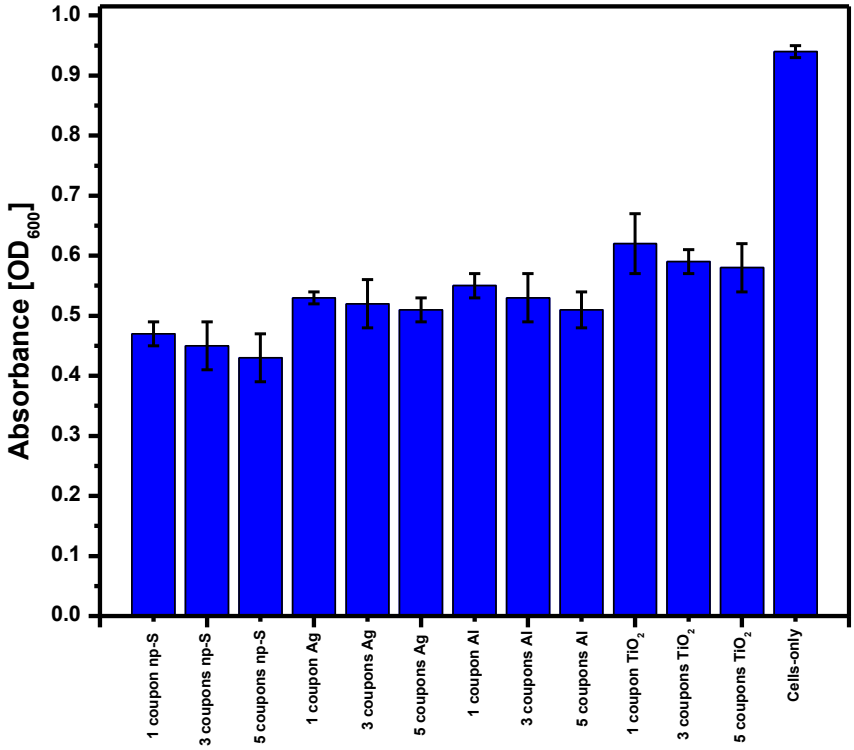

Figure 5. 9 The measured absorbance using microplate reader.

Finally, the growth of *E.coli* DH5α cells were also tested after 24-h incubation at 37°C. In this case, the measured OD using microplate reader indicates that, comparison to the measured OD using spectrophotometer after 8-h incubation, there is a great reduction in measured OD values for the treated *E. coli* cells from 1.5 to 0.55. This implies that the bacteria are entering the death phase, in which the number of cells dying out exceeds number of new cells being formed. Moreover, the high decrease in OD values for the treated *E. coli* DH5α cells compared to the untreated bacterial cells reveals that the *np-S,* Ag, Al, and TiO_2 thin films are effective in killing the bacterial cells. The treatments are causing a more significant decline in bacterial density, which may be attributed to the use of small volume of bacterial suspension, proving their enhanced antibacterial performance as Figure 5.9 shows.

In conclusion, the antibacterial activity of np-S thin films with different pore and ligament sizes was tested against two different gram-negative bacterial strains, *Pseudomonas aeruginosa (P. aeruginosa)* strain PAO1 and *Escherichia coli* (*E. coli*) strain DH5α. Two

protocols have been employed to measure bacterial density: the dose-response assay in a 96-well microtiter plate and the growth inhibition assay. The results indicated that *np-S* thin films with varying pore size, ligament size and doses were ineffective in inhibiting *P. aeruginosa* growth. However, the spectrophotometer recorded a slight reduction in the density of *E. coli* DH5α by *np-S* thin film with the smallest pore and ligament size, suggesting a modest antibacterial effect on this strain.

Chapter 6 Gradient Nanoporous Silver Thin Film: Correlating Compositionally with Optical Properties and Surface Enhanced Raman Scattering

6. Overview

Traditionally, the nanostructure variation in *np-S* has been achieved through separate sample preparation and processing. This conventional method can result in inconsistent conditions between each step. In this chapter, a novel technique has been employed to create a continuously changing composition across a substrate in a single deposition process coupled with a simultaneous, single-step dealloying procedure. By fabricating different nanostructures under uniform conditions, this method allows for a more accurate comparison between different sections of the *np-S* by reducing experimental variability. This is crucial for a clear understanding of how nanostructure variations impact the properties of the material.

6.1 Objective of chapter

This study aims to use a magnetron-sputtered system to create a thin film of an $Ag_{100-x}Al_x$ alloy. The constant current will apply to the two deposition guns during the deposition process. However, the rotation of the sample holder will be discontinued. The aim is to obtain the thin film with varying Al content. This crystal structure and composition of alloy thin film will be examined under EDS and XRD at different positions to investigate the effect of this method on the Al content and crystal structure of the film. The dielectric permittivities and optical constants at the same positions will be extracted by modelling the ellipsometry data. The obtained film will be used as a surface-enhanced Raman substrate after applying R6G as a Raman probe, and then the Raman signal will be collected at the same positions.

6.2 Experimental details specific to this chapter

The Al_xAg_{100-x} alloy thin film with a gradient composition and was sputter deposited by DC magnetron sputtering onto a 76 mm × 26 mm glass slide substrate. Before deposition, the substrate was cleaned with antibacterial spray then ultrasonically cleaned with acetone, ethyl alcohol and Milli-Q water for 20 min in each solvent and blow-dried under nitrogen gas. Ag, Al and Ti targets with a purity of 99.99% were used as sputter targets. The glass substrate was covered by three layers of 5 nm of Ti as an adhesion layer (first layer), followed by 3 nm of pure Ag (second layer), and finally by the Ag-Al alloy (top layer). The purpose of depositing Ag layer is to guarantee that the thin film adheres to the underlying substrate and inhibits the

adhesion layer from being oxidized during changing the targets. To ensure a gradient composition and thickness across the long axis of the sample was realized, the deposition process was performed with a nonrotating sample holder. The sputtering chamber was evacuated to a base pressure of 5.9×10^{-4} Pa in argon ambient. The Ar flow was set to a fixed rate of 60 sccm. The guns were tilted at 26° relative to the substrate normal, with a gap spacing of approximately 84 mm between the target and substrate. The DC current applied to each target is summarized in Table 6.1.

Table 6. 1 Sputter deposition parameters for preparing gradient Al_xAg_{100-x} alloy thin film.

layer	Material	Current (A)	Deposition rate (nm/s)	Thickness (nm)	Deposition time (s)
Adhesion layer 1	Ti	0.130	0.04	5	327
2	Ag	0.040	0.11	3	43
Ag-Al alloy layer 1	Al	0.340	0.2	Gradient	756
	Ag	0.040	0.11		

The whole sample was subjected to dealloying process which was conducted using a freshly prepared aqueous solution of 0.5 M NaOH at room temperature with varying durations due to the differences in Al concentration, as demonstrated in Table 6.2. The sample that underwent dealloying was rinsed with fresh Milli-Q water for cleaning, followed by ethanol for drying. The dealloyed sample was stored in a vacuum desiccator to reduce oxidation.

Table 6. 2 Al concentration in the gradient Al_xAg_{100-x} thin film alloy and dealloying time in 0.5 M NaOH

Sample No.	p1	p2	p3	p4	p5	p6	p7	p8	p9	p10	p11	p12	p13	p14	p15
Position from sample centre (cm)	**-3.5**	**-3**	**-2.5**	**-2**	**-1.5**	**-1**	**-0.5**	**0**	**0.5**	**1**	**1.5**	**2**	**2.5**	**3**	**3.5**
Al concentration (at. %)	38	40	42	48	51	55	59	60	62	66	70	76	78	80	81
Dealloying time (min)	27	25	23	21	19	17	15	13	11	9	7	6	4	3	2

The data were collected at fifteen points along the film surface as Figure 6.1 shows; the distance between each two points was 5 mm.

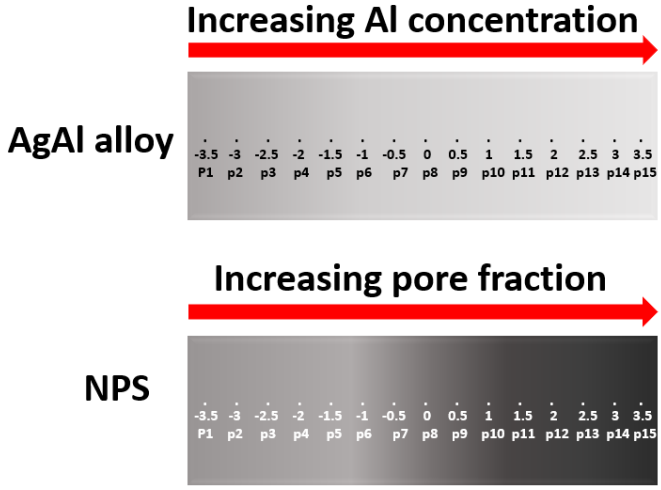

Figure 6. 1 A schematic figure illustrating the top-view of the sample surface of (a) the gradient thin film alloy and (b) the gradient nanoporous silver thin film, showing the points where data was collected.

6.3 Results and Discussion

6.3.1 Investigation chemical composition and thickness of alloy and G-np-S thin films

The elemental composition of the position dependent Al_xAg_{100-x} thin film alloy was determined by EDS. As seen in Table 6.3, the Al concentration ranges from 38 to 81 at. %. The approximate thickness of the G-Al_xAg_{100-x} alloy was measured at each position. The measured thickness values are listed in Table 6.3. It is found that the thickness of the alloy layer increases with the increase in Al content because the deposition rate from the Al target is higher than that from the Ag target.

The EDS analysis of the *G-np-S* sample revealed the presence of residual Al through dealloying in the 0.5 M NaOH solution; the results are shown in Table 6.3 below. The results in Table 6.3 indicate that the residual Al content of the dealloyed sample increased with increasing the Ag concentration in the precursor alloy. Previous studies on *np-S* through the process of dealloying melt-spun Al-Ag alloy ribbons in 20 wt % NaOH aqueous solution have provided evidence that *np-S* typically retains a certain amount of residual Al, typically in the range of several atom percent (Wang et al., 2009b). Hence, it is justifiable to conclude that the tiny quantity of residual Al identified using EDS is expected to be trapped inside the Ag ligaments as a solid solution, especially with the Al concentration between 81 and 48 at.%. In contrast, the residual Al at the high Ag concentration (alloy with less than 48 at.% Al) refers to the existence of the δ-Ag_2Al, which is stable in an alkaline solution and can be partially dealloyed in the alkali solution (Wang et al., 2009b) (I Yamauchi et al., 2003).

Table 6. 3 Chemical composition, thickness of the gradient Al_xAg_{100-x} thin film alloy, and thickness of G-np-S thin films extracted from the ellipsometry model.

Sample No.	Alloy composition	Thickness (nm)	Thickness of G-np-S (nm)	Concentration of residual Al (at. %)
p1	62 at. % Ag- 38 at. % Al	114	85	19.4
p2	60 at. % Ag- 40 at. % Al	129	93	15.1
p3	58 at. % Ag- 42 at. % Al	137	102	12.4
p4	52 at. % Ag- 48 at. % Al	143	109	10.6
p5	49 at. % Ag- 51 at. % Al	160	123	11.1
p6	45 at. % Ag- 55 at. % Al	181	141	10.6
p7	41 at. % Ag- 59 at. % Al	193	156	9.1
p8	40 at. % Ag- 60 at. % Al	206	163	8.8
p9	38 at. % Ag- 62 at. % Al	219	170	8.6
p10	34 at. % Ag- 66 at. % Al	223	184	8.1
p11	30 at. % Ag- 70 at. % Al	227	189	7.7
p12	24 at. % Ag- 76 at. % Al	252	193	7.8

p13	22 at. % Ag- 78 at. % Al	261	206	7.4
p14	20 at. % Ag- 80 at. % Al	273	234	6.1
p15	19 at. % Ag- 81 at. % Al	301	256	5.8

6.3.2 Phase constitution of the G-AlxAg100-x alloy and G-np-S thin films

Three crystallographic phases can be identified from the G- Al_xAg_{100-x} diffraction patterns as shown in Figure 6.2, face-centred cubic (*fcc*) α-Ag (with Al in solid solution) phase, hexagonal close packing (*hcp*) δ-Ag_2Al phase and face-centred cubic (*fcc*) $(Ag, Al)_{fcc}$ phase.

Two phases, δ-Ag_2Al and $(Ag, Al)_{fcc}$, are present in some samples. Those results are at the positions of p1, p2, and p3 show one predominant peak at 38.9° and other small peaks at 41°, 72° corresponding to δ-Ag_2Al intermetallic phase with hexagonal primitive structure and space group of *P63/mmc*. A minimal amount of a solid solution (*fcc*) metastable α- phase is revealed by peaks at 44° and 78°, assigned to the diffraction from (200) and (311) planes.

Similarly, the same two phases were detected at the positions of p4, p5, p6 and p7 where the Al concentration increased further, as Figure 6.2 a and b demonstrated. However, the XRD in Figure 6.2 a and b show that the substantial diffraction peak shifts from 38.9° due to an increasing contribution from the $(Ag, Al)_{fcc}$ (111) peak at 38.64°. The other three diffraction peaks grow at the 2θ values of 44.80°, 65.28°, and 78.40°, attributed to the (200), (220), and (311) diffraction planes of a single face-centred cubic $(Ag, Al)_{fcc}$ phase with space group $Fm\bar{3}m$. The peak shift may be due to the small size of the Al atom compared to the Ag atoms in the δ-Ag_2Al phase, whose volume fraction increases with increasing the Ag content (Zhao et al., 2017), which may lead to the reduction of the unit cell as Figure 6.3 shows. At these positions, the amount of δ-Ag_2Al intermetallic phase with hexagonal primitive structure and space group of P63/mmc started to decrease, just one peak at around 2θ value of 41.8° with an exceedingly small intensity was detected, and the peak can be ascribed to the (101) diffraction plane. These results for the positions from p1 to p6 are in good agreement with the results of Mao et al. (Mao et al., 2016) for their gradient AgAl thin films prepared using a magnetron sputtering system.

The XRD diffraction pattern in Figure 6.2 b and c clearly demonstrate that at the positions of p8, p9, p10, p11, p12, p13, p14 and p15, the δ-Ag_2Al phase disappeared, and the precursor AgAl alloy consists of one distinct phase, namely, face-centred cubic (*fcc*) metastable α-phase phase with space group $Fm\bar{3}m$. The detected XRD peaks were designated to the diffraction of the (111), (200), (220), (311), and (222) planes. The absence of δ-Ag_2Al phase at these positions can be linked to inadequate thermal activation during the deposition process.

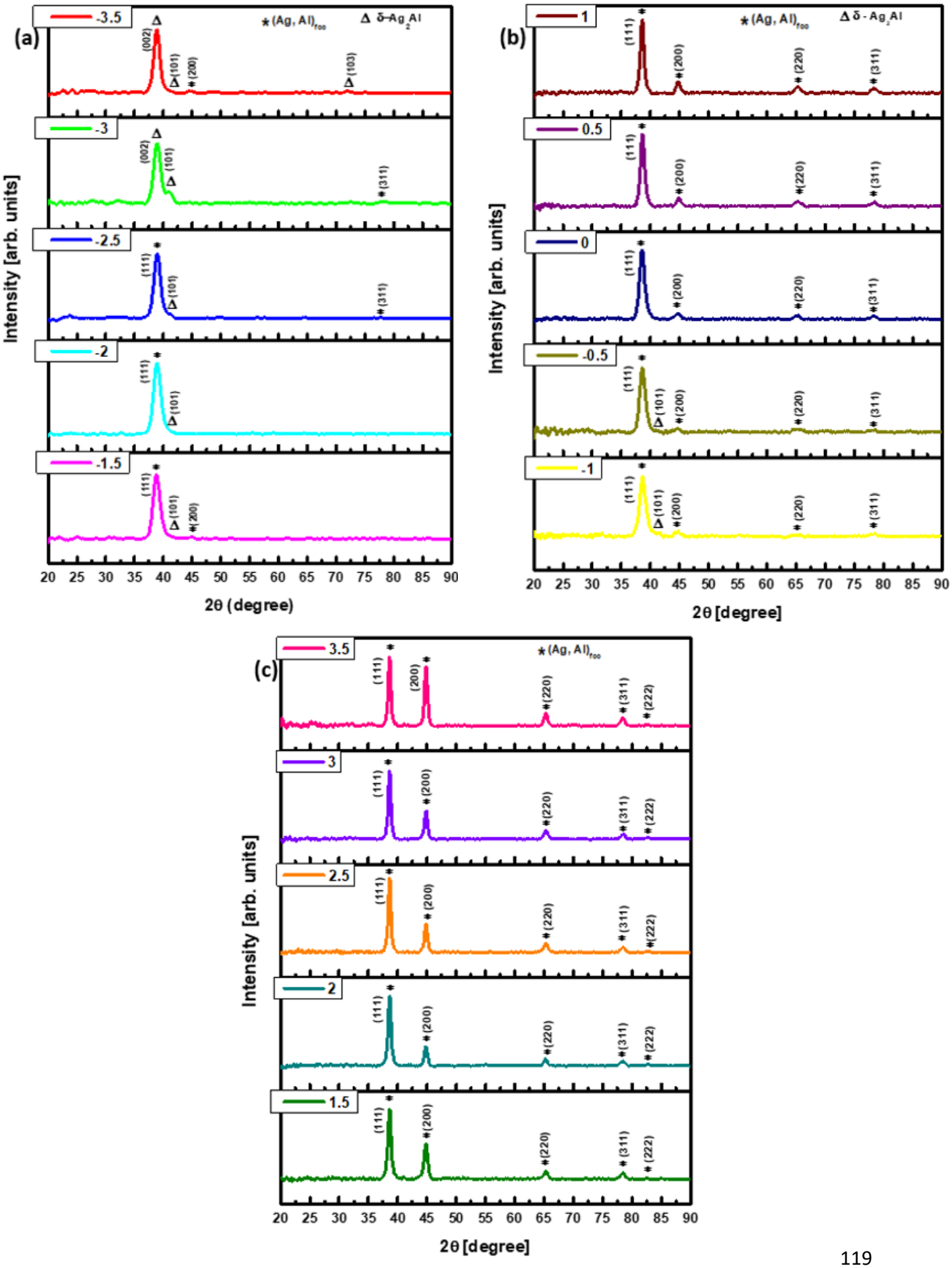
(a)
-3.5
-3
-2.5
-2
-1.5
★(Ag, Al)fcc
Δ δ-Ag2Al
(002)
(101)
(200)
(103)
(311)
(111)
Intensity [arb. units]
2θ (degree)
(b)
1
0.5
0
-0.5
-1
(220)
2θ [degree]
(c)
3.5
3
2.5
2
1.5
(222)

Figure 6. 2 XRD diffraction patterns of the as-deposited gradient Al_xAg_{100-x} alloy thin film with different Al compositions, a) at position p1, p2, p3, p4 and p5 b) at the position of p6, p7, p8, p9 and p10, and c) at the position of p11, p12, p13, p14 and p15. The patterns illustrate that the alloy thin film consists of three distinct phases: (fcc) α-Ag (Al) phase, (hcp) δ-Ag_2Al phase and (fcc) α-Ag (Al) phase. The patterns show that the δ-Ag_2Al phase existed with decreasing Al content, whereas the α- Al (Ag) phase dominates when the concentration of Al increased.

The lattice parameters and unit-cell volume of the gradient thin film at different positions varied systematically between 0.417 nm and 7.269 nm^3 for the lowest Al content, and between 0.405 nm and 6.626 nm^3 for the highest Al content. These values are consistent with the reported values of Ag (0.417 nm and 7.262 nm^3) and Al (0.405 nm and 6.623 nm^3) in the Crystallography Open Database's entries ID no. 9013053 and 9611602, respectively. The lattice parameter and unit-cell volume values have been graphed against their corresponding positions as Figure 6.3 illustrated. The lattice parameter and unit-cell volume exhibit a drop as the Al concentration increases, indicating a non-linear relationship that deviates significantly from Vegard's law.

The crystal structure of a dealloyed G-Al_xAg_{100-x} alloy thin film in 0.5 M NaOH aqueous solution at room temperature was investigated using *GIXRD*. As displayed in Figure. 6.4 a, b and c, the initial $(Ag, Al)_{fcc}$ phase completely disappeared, and the δ-Ag_2Al intermetallic phase was partially dissolved upon de-alloying in 0.5 M NaOH solution. A new set of peaks emerged at the 2θ values of 38.24°, 44.4°, 64.8°, 77.6° and 82.1°, which can be ascribed to the diffraction of the (111), (200), (220), (311) and (222) planes of (fcc) metastable α-phase with space group $Fm\bar{3}m$. The residual (hcp) δ-Ag_2Al phase was observed at the position of p1, p2 and p3, at the 2θ values of 38.9°, 41.4° and 71.8°, and the peaks assigned to the diffraction of (002), (101) and (103) planes. The lack of complete dealloying of δ-Ag_2Al can be attributed to the stability of δ-Ag_2Al on alkali (Wang et al., 2009b) (I Yamauchi et al., 2003).

The lattice parameters and unit-cell volume of the gradient *np-S* at various places were measured to be 0.4078905533 ± 0.0006608158 nm and 6.7863204 ± 0.0329982848 nm^3, respectively, as depicted in Figure 6.4. This falls within the reported range of values for pure Ag, as indicated by the COD entry number 9011607.

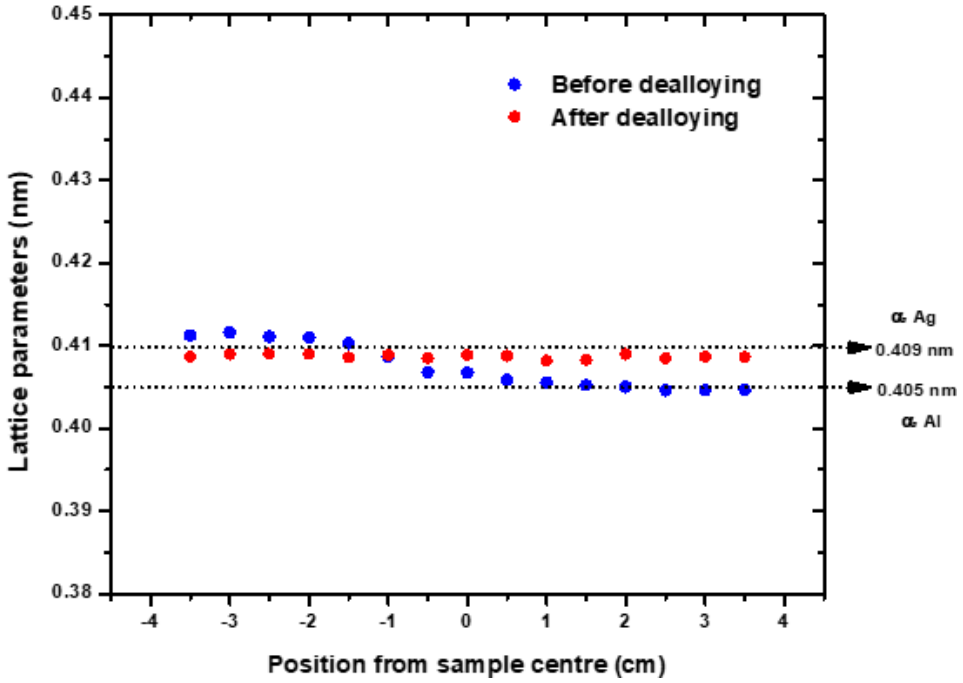

Figure 6. 3 The relationship between the lattice parameter in the α- Al (Ag) and α- Ag (Al) phases and position along the gradient Al_xAg_{100-x} alloy and np-S thin films, the lattice parameter.

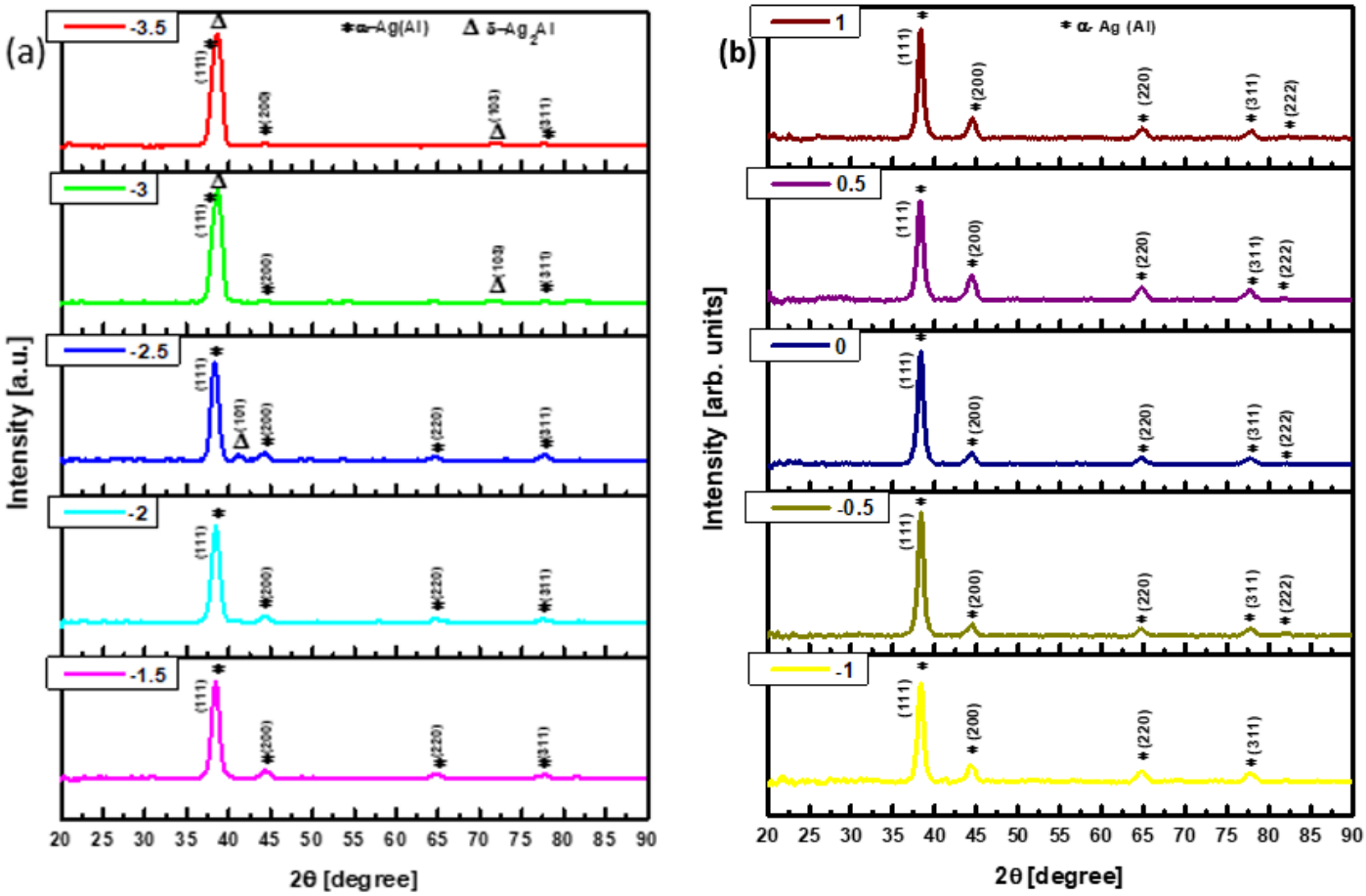

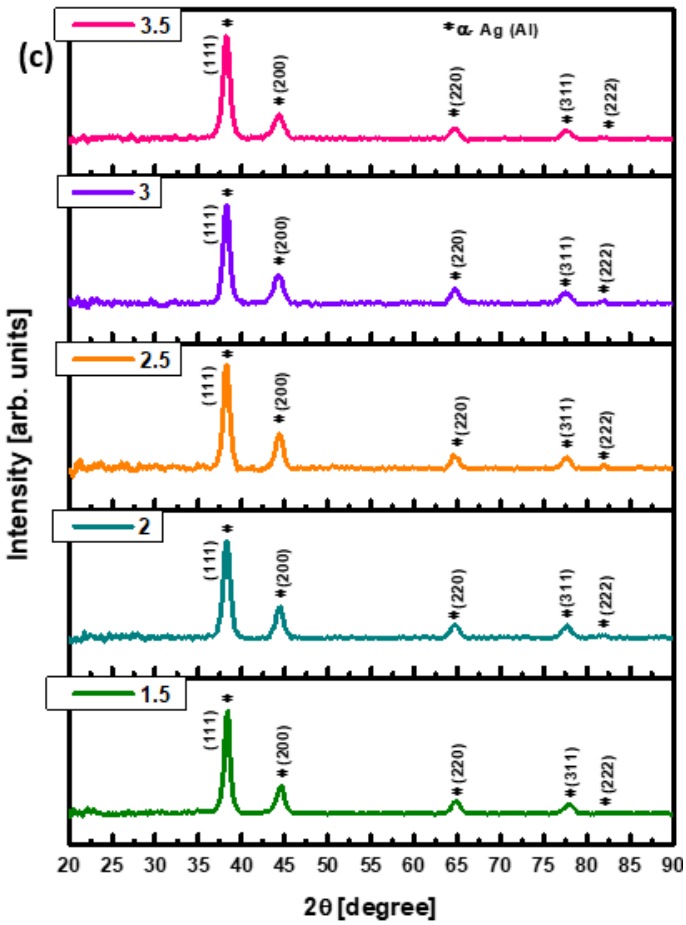

Figure 6. 4 XRD patterns of the de-alloyed gradient nano-porous silver (G-np-S) thin film, a) at the position of p1, p2, p3, p4 and p5 b) at the position of p6, p7, p8, p9 and p10, and c) at the position of p11, p12, p13, p14 and p15. The patterns demonstrate that the α-Al phase and δ-Ag_2Al phase were dissolved upon dealloying in NaOH solution, and the Ag atoms left behind at the passive surface, which exhibit small nanopores structure.

6.3.3 Influence of changing the Al concentration on the morphology of the G-np-S thin film

Nanostructure of the *G-np-S* thin film formed through the chemical dealloying of the G-Al_x Ag_{100-x} alloy (x= 38 to 81at.%) in the 0.5 M NaOH solution are shown clearly in top-view SEM images presented in Figure 6.5 (a-o). The surface morphologies of the nanoporous exhibit homogeneous and bi-continuous ligament-pore structures with length scales of several tens of nanometers.

For the sponges formed at the distance of p1, p2 and p3, as *SEM* images in Figure 6.5 (a-c) shows, the nanoporous structure of G-*np-S* can be observed at higher magnification *SEM* images (insets), no apparent cracks can be remarked on the surface views of the fabricated gradient sponges as low magnification SEM images show. With the decrease of the Ag content in the precursor alloy thin film, the surface morphologies of the resulting *G-np-S* change obviously, as Figure 6.5 (c-o) displays. A small number of tiny cracks with lengths between a

few nanometers to several hundred nanometers start to form and can be detected on the surface of the sponges generated at p4, p5 and p6, as demonstrated in Figure 6.5 (d-f). The dimensions and quantity of the cracks progressively increase in the subsequent positions at p7 to p15. The presence and characteristics of cracks in the sponges depend on their original composition, whereby a lower Ag content in the precursor alloy corresponds to a higher occurrence of cracks as demonstrated in Figure 6.5 (d-o). Some large cracks can reach several micrometers in length and sub-micrometers in width, as Figure 6.5 (f-o). Cracks are frequently observed in nanoporous metals, including nanoporous gold films (Lu et al., 2007; Sun & Balk, 2008), monolithic nanoporous copper (Hayes et al., 2006), *np-S* films (Li & Lu, 2021; Yuan et al., 2021), monolithic *np-S* ribbons (Wang et al., 2009b), and so forth. The mechanisms behind the formation of the cracks remain poorly understood till now. However, several research groups have investigated the underlying causes of crack formation. According to Sun et al. (Sun & Balk, 2008) and Lu et al. (Lu et al., 2007), it has been postulated that the presence of cracks in *NPG* can be attributed to the phenomenon of volume shrinking. Hayes and co-workers (Hayes et al., 2006) argued that the presence of cracks in the monolithic *NPC* can be attributed to many reasons, including residual stress, capillary forces resulting in "mud-cracking," or coherency stresses between the alloy and the dealloyed copper. Wang and colleagues (Wang et al., 2009b) have suggested that the presence of cracks in monolithic NPS may be attributed to residual stress resulting from the significant volume reduction.

The formation of the nanopore structures by dissolving parent alloy to produce bicontinuous and interconnected pore/ligament occurred by the contribution of two main processes: (i) roughing due to the dissolving of active atoms, which has a lower electrode potential and (ii) coarsening process caused by the surface diffusion of less active atoms to the rearrangement and growth of ligaments and pores, which interact in a complex mechanism (Chen & Sieradzki, 2013; Yi Ding et al., 2004; Erlebacher et al., 2001b; Yu et al., 2008). The variations in the dissolution rate of the active element and the surface diffusion of noble metal can both cause different stress and, thus, the distinct architecture of nanoporous structures (Wang et al., 2009b) (Huang et al., 2017). The findings in Table 6.4 indicate that the surface diffusion rate D_s (derived using Equation 2.1) of Ag adatoms is influenced by the concentration of Al component in the initial alloy; the surface diffusion rate of Ag increases with decreasing the Al concentration.

Consequently, the augmentation of the Al concentration from 38 to 81 atomic percent (at.%) resulted in a reduction in the surface diffusion of Ag adatoms along the interfaces of the

alloy and electrolyte, which decreased from 1.82×10^{-19} to 0.32×10^{-19} m^2 s^{-1}. Therefore, the fine and tiny pores demonstrated in the high magnification SEM images in Figure 6.5 (n and o) can be attributed to the partial immobilization of Ag atoms, which impedes the surface diffusion of Ag atoms along the ligaments. The values of D_s provided in Table 6.4 exhibit a significant decrease of almost three orders of magnitude compared to the surface diffusion value (10^{-16} m^2s^{-1}) of Ag adatoms obtained by the dealloying process of Ag-Al alloys at 363 K in various solutions, including H_2SO_4, H_3PO_4, $C_2H_2O_4$ and HCl solutions, as reported by Song et al. (Song, Gao, Zhang, & Zhai, 2011). Furthermore, the calculated values presented in Table 6.4 exhibit a higher significance level than Ag's intrinsic surface diffusion coefficients, which have a value of (10^{-20} m^2 s^{-1}) by almost one order of magnitude (Li et al., 2017).

Table 6. 4 The calculated Ag surface diffusion rates during the dealloying process, it is clearly demonstrated moving to the position with higher Al concentration led to decrease surface diffusion.

Sample No.	p1	p2	p3	p4	p5	p6	p7	p8	p9	p10	p11	p12	p13	p14	p15
Position from sample centre (cm)	-3.5	-3	-2.5	-2	-1.5	-1	-0.5	0	0.5	1	1.5	2	2.5	3	3.5
Ag surface diffusion (SD) ($\times10^{-19}$ nm^2s^{-1})	1.87	1.68	1.51	1.48	1.47	1.41	1.36	1.37	1.35	1.34	1.35	1.32	1.04	0.29	0.32

Additional investigations into the *G-np-S* film's nanopore structure, as shown in Figure 6.5 inset, reveal that the measured pore and ligament diameters fall within the 10 to 30 nm range and that their diameters increase linearly with the precursor alloy's Ag content. According to the research, pore and ligament sizes between 1 and 100 nm show a highly sensitive *SERS* surface (Kleinman et al., 2013).

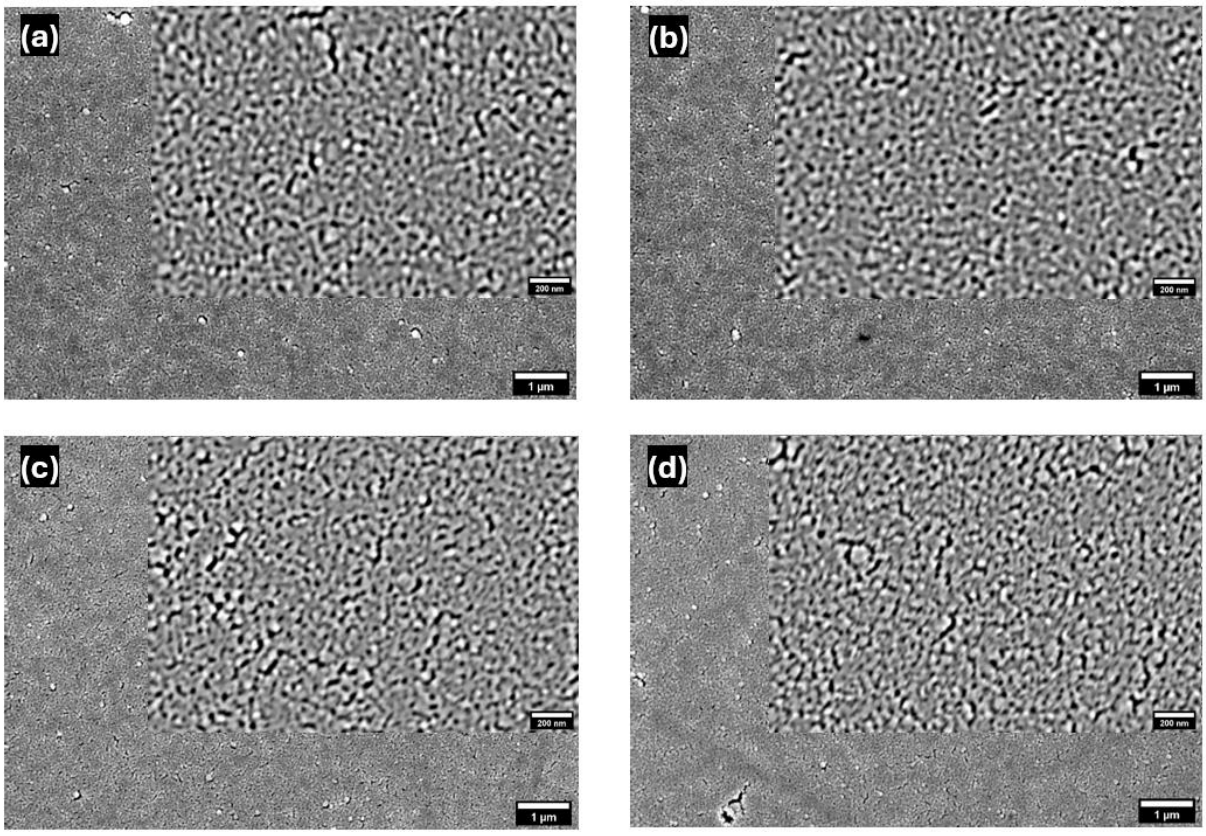

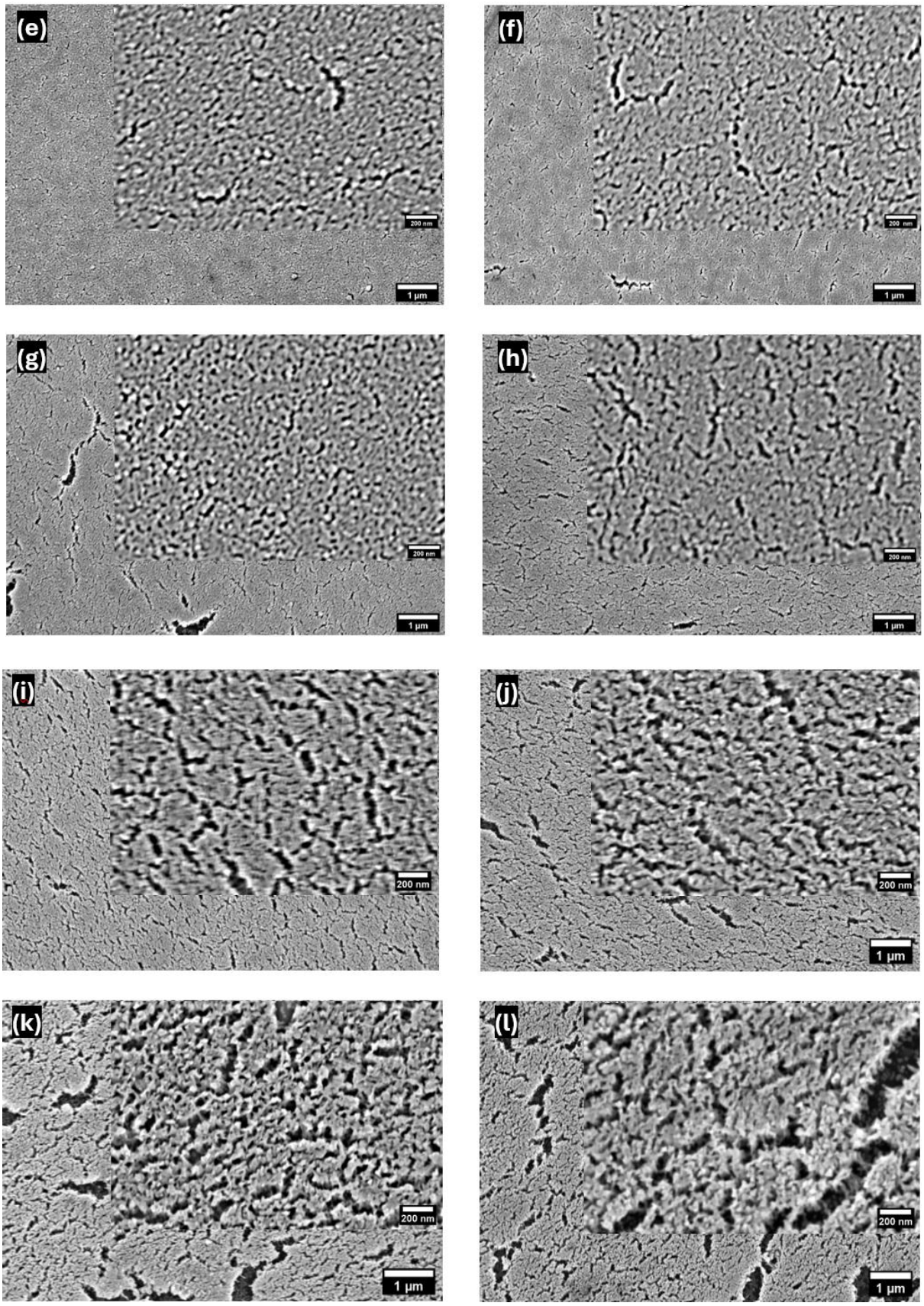
(e)
200 nm
1 µm
(f)
200 nm
1 µm
(g)
200 nm
1 µm
(h)
200 nm
1 µm
(i)
200 nm
(j)
200 nm
1 µm
(k)
200 nm
1 µm
(l)
200 nm
1 µm

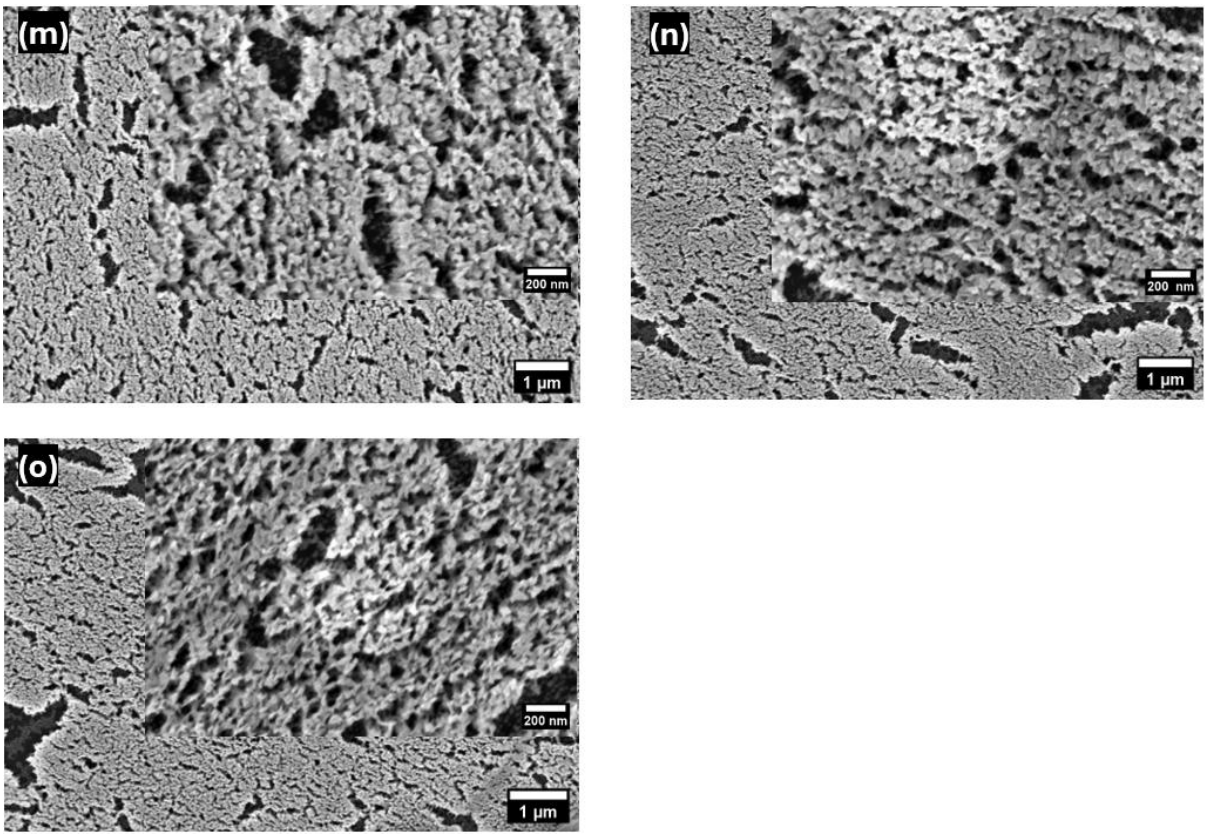

Figure 6. 5 Top-view SEM images collected at different distances from the centre of the G-np-S, (a) at p1, (b) p2, (c) p3, (d) p4 (e) p5, (f) p6, (g) p7, (h) p8, (i) p9, (j) p10, (k) p11, (l) p12, (m) p13, (n) p14 and (o) p15. The low-magnification SEM images clearly show the existence of cracks on the surface of the sponges (scale bar 1 µm), and the high-magnification images (inset) demonstrate the nano-porous structure of the sponges (scale bar 200 nm).

It is evident from Figure 6.6 that the pore is smaller in diameter compared to the ligament. Beyond that, as the relationship in Figure 6.7 shows, the density of the pore decreases when moving along the sponge from p1 to p15.

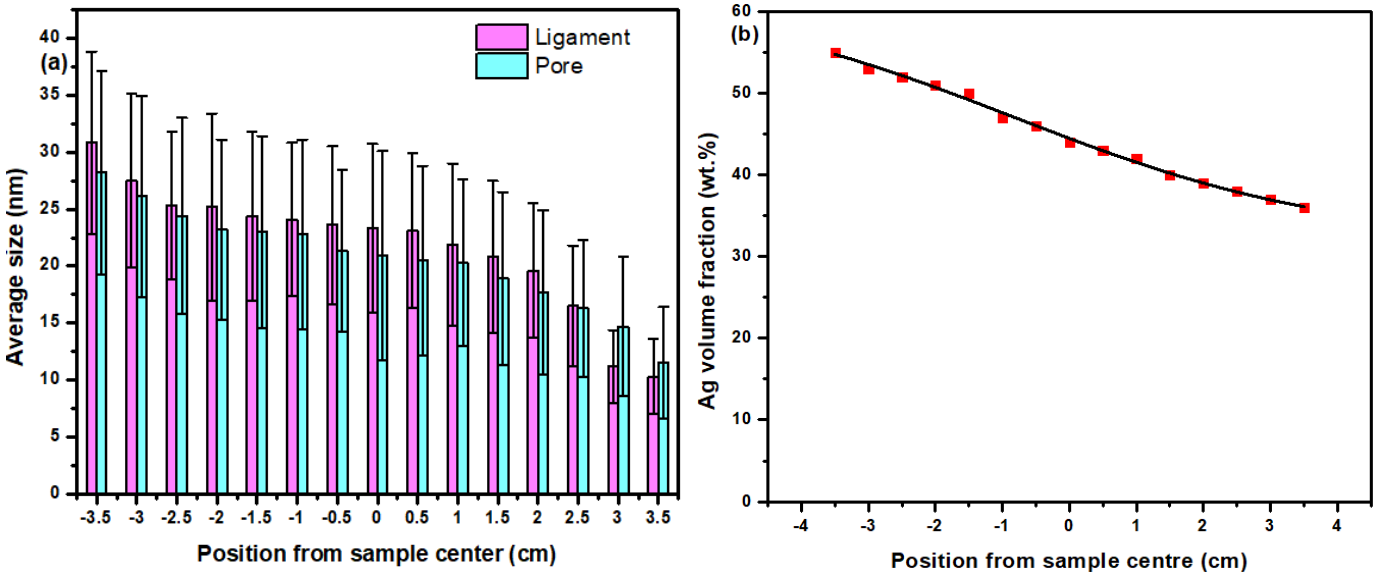

Figure 6. 6 (a) Histogram of the average pore size (red) and average ligament size (blue) of the G-np-S of 100 measurements using imageJ software, and error bars indicate. (b) the volume fraction of Ag extracted from XRD refinement of the diffraction patterns and used for modelling the ellipsometry data.

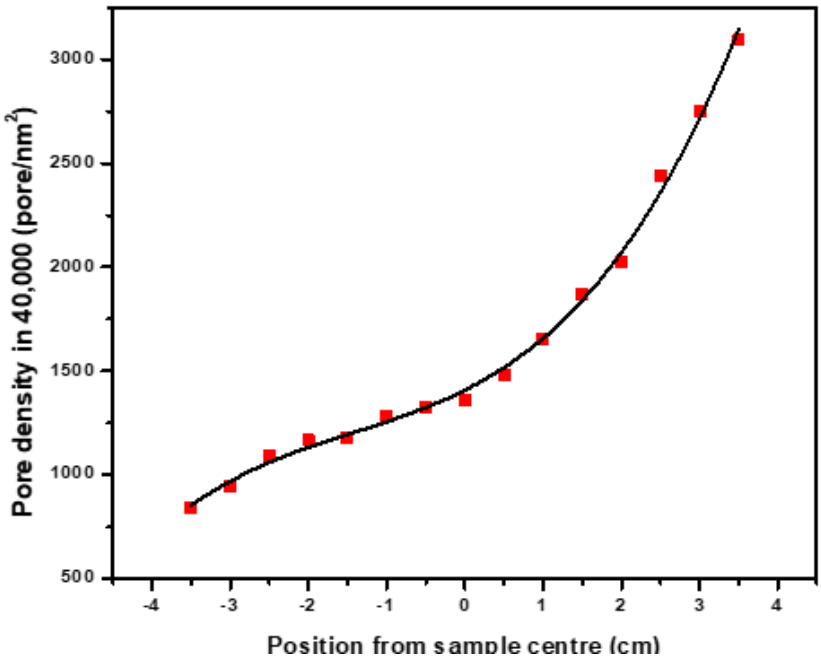

Figure 6. 7 Position dependence of pore density of G-np-S thin film (shown by filled symbols).

6.3.4 Effect of nanoporous structure on the optical properties

The plasmonic behaviour of nonmagnetic nanomaterials during the interaction with electromagnetic waves is commonly characterized by its intrinsic properties, such as dielectric permittivity (effective dielectric functions) or optical functions (effective refractive index) (Y. Li et al., 2021). Investigate the permittivity $\varepsilon(\omega)$ of the involves analysing the real ε_1, which represents the polarization ability caused by the electric field, and imaginary ε_2 portions, which corresponds to energy losses resulting from this phenomenon (West et al., 2010). Figures 6.8 (a, b, c, and d) and 6.9 (a, b, c, and d) show the generated ε_1 and ε_2 as functions of photon energy, along with the refractive index *n* and extinction coefficient *k* as functions of wavelength for the *G-np-S* and alloy thin films, respectively. Two optical models, depicted in Figure 3.18, were designed to obtain the optical properties of the material by studying the interaction between polarized light and the gradient alloy and *np-S* thin films.

The optical properties of the gradient morphology *np-S* thin film, interacting with electromagnetic radiation with photon energies ranging from 0.49 to 4.1 eV, are demonstrated in Figure 6.8 (a, b, c, and d). Pore and ligament size and their distribution are significant factors affecting the optical properties of nanoporous materials, as these dimensions influence the scattering mean free path of photons. Moreover, non-uniform distribution and irregular shape of pores and ligaments in nanopore structures lead to the occurrence of anisotropic scattering (Dixon et al., 2007).

The investigation of Figure 6.8 a indicates that the nanoporous silver thin film with gradient morphologies exhibits a red shift in the plasma frequencies, ranging from 3.70 eV at position P7 to 0.78 eV at position P15. However, the expected red shift of the plasma frequencies from positions P1 to P6 cannot be noticed, as the measurements did not extend beyond a photon energy of 4.1 eV. The plasma frequencies of the *np-S* at positions P1 to P6 expected to be higher than the frequency of the incident electromagnetic field. As a result, the np-S at these positions displays a negative real part of the dielectric function due to the high density of free electrons, behaving like bulk metallic material (Wiederrecht, 2010). At these positions, the nanoporous silver exhibits average pore sizes larger than 20 nm, ligament sizes larger than 23 nm, and silver volume fractions exceeding 45 wt.%. The oscillating free electrons reflect the incident electromagnetic radiation, at the same time, a significant portion of the radiation is absorbed by the *np-S* due to increased surface plasmon resonance, leading to an increase in the imaginary part of the dielectric function, as demonstrated in Figure 6.8 b. Many studies revealed that the high ε_2 values are related to the optical losses that result from interband transition, intraband transition (Erwin et al., 2016), and electron surface scattering by grain boundaries (West et al., 2010), surface roughness (Sardana et al., 2014), lattice defects (West et al., 2010), and porosity (Sardana et al., 2014).

However, the real dielectric function ε_1 for *np-S* formed at positions from p7 to p15 increases with the increase of photon energies in the near-infrared range and then reaches zero at specific photon energies (0.78, 0.93, 0.99, 1.09, 1.74, 1.75, 1.98, 2.85, and 3.70 eV) at corresponding distances from the center of the sample (p7 to p15) as Figure 6.8 a (inset) shows, and beyond these photon energies, the real part of the dielectric constant becomes positive. The *np-S* thin film at these positions exhibits a significant shift from the natural Epsilon-Near-Zero (ENZ) photon energy for the bulk Ag. These ENZ transitions indicated a red-shift in the plasma frequency ω_p compared to the bulk silver value reported by literature, which is a real fraction of their permittivity that becomes essentially zero in the ultraviolet range (Zeman & Schatz, 1987), as Figure 6.8 a shows. This observation is consistent with those obtained by other studies, which indicated that the plasma frequency ω_p of nanoporous gold exhibits a spectral red-shift due to its lower density than bulk materials (Abbas I Maaroof et al., 2007; Ruffato et al., 2011). Furthermore, several studies have demonstrated that the porosity of nanoporous materials has a huge influence on the plasma frequency (Carton et al., 2013; Smith & Earp, 2009). Hence, the red-shift observed in the ω_p can be ascribed to the reduction in pore diameter from 21 to 11 nm and ligament diameter from 23 to 10 nm, combined with the decrease in the

fraction of Ag from 46% to 36% as shown in Figure 6.8 b. This frequency is often called the shielded plasma frequency ω_p^*, which is lower than ω_p (Abbas I Maaroof et al., 2007). Based on the effective medium theory, noble metals can be incorporated into a dielectric host medium to create ENZ materials at visible or near-infrared frequencies (Gao et al., 2013; Sihvola, 1999). As the fraction of the Ag metal decreases, a lesser amount of the electromagnetic wave travels through the material, resulting in reduced optical losses as Figure 6.8 b demonstrates. Conversely, field localization weakens, and the electromagnetic field expands across a greater volume (Jakšić et al., 2018).

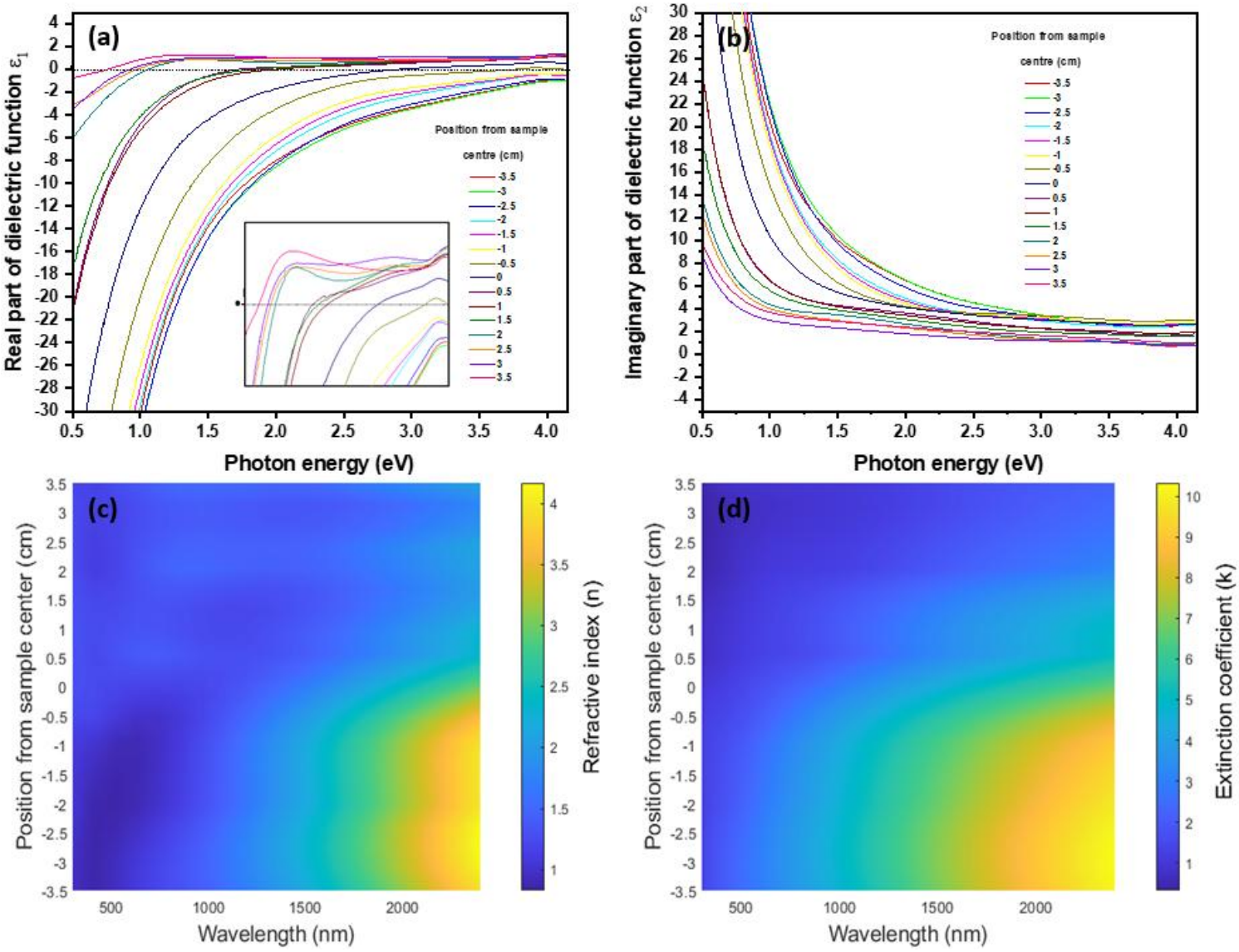

Figure 6. 8 Variation of dielectric permittivity with photon energy at different positions on the G-np-S thin film, (a) real parts ε_1, (b) imaginary parts ε_2, and colour map of (c) refractive index n and (d) extinction coefficient (k) as a function of position at each spatial position of the G-np-S thin film.

Upon examination of ε_1 and ε_2 of the gradient alloy thin film, which is displayed in Figure 6.9 a and b, it is evident that ε_1 values invariably remain negative, indicating a metallic

nature of the gradient alloy at all positions of the gradient thin film. Figure 6.9 b demonstrates that as the Al concentration decreases, ε_2 exhibits an increase, especially at photon energy values ranging from 1.5 to 4.1 eV. On the other hand, colour maps in Figure 6.9 c and d show that both n and k indicate a linear relationship with position (Al concentration) across the whole range of the wavelengths. This finding is compatible with the dielectric permittivity data presented in Figure 6.9 a and b, demonstrating a linear relationship with composition (position) and providing further evidence of their linear dependency on composition.

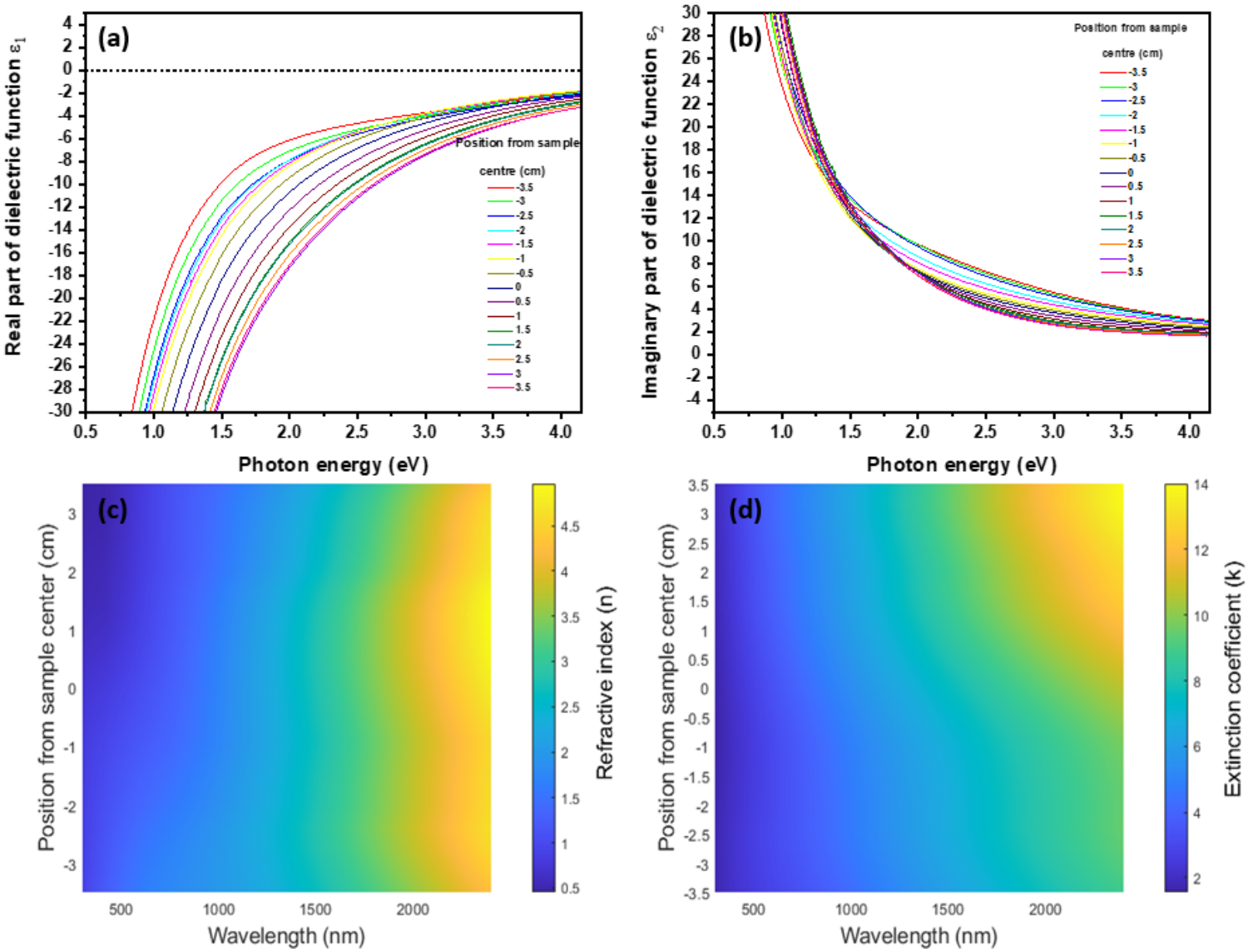

Figure 6. 9 Position dependence Al concentration) of optical properties of gradient alloy thin film, (a) real, (b) imaginary part of dielectric permittivity, (c) refractive index, and (d) extension coefficient of optical constant.

The small peak observed at a photon energy of about 3.9 to 4 eV in Figure 6.8 a is assigned to interband transitions from *4d*-band to *5sp*-band (Erwin et al., 2016), since the onset of interband transitions for Ag occurs at about 3.9 to 4 eV (Irani et al., 1971; Johnson & Christy, 1972). The results depicted in Figure 6.8 a demonstrates that the nanoporous structures formed

at various locations on *G-np-S* thin film exhibit plasmonic solid behavior. This is evident from the fact that the wavelength position of interband transitions, determined by the metal composition, remains relatively constant even when the void content varies (Abbas I Maaroof et al., 2007).

Due to the small nanopore feature sizes compared to the wavelength of the wave (λ), localized surface plasmon resonance (LSPR) can be induced across the electromagnetic spectrum, from ultraviolet (UV) to near-infrared (NIR) (Koya et al., 2021). The resonance position is affected by several factors, including the nanoparticles' dimensions and morphology, as well as the properties of the surrounding medium. It helps to manipulate the resonance throughout a broad spectrum of frequencies (García, 2011; Kreibig & Genzel, 1985). As displayed in Figure 6.8 a, the peak at the short photon energies is sensitive to the change of the nanostructure sizes; it becomes narrower, and a redshift is observed as the pore and ligament sizes and Ag fraction decrease. This peak can be assigned to *LSPR* excitation.

It is known that introducing nanopore structures into a material is an appropriate way to achieve material with a reduced refractive index (Liu et al., 2012). Figure 6.8 c represents the refractive index map as a wavelength function. The data demonstrates a positive correlation between pore size and refractive index. The regions located at distances ranging from p7 to p1 exhibit the lowest refractive index values within the infrared (IR) spectrum. Subsequently, the refractive index experiences a gradual increase at subsequent positions due to the progressive increase of the pore diameters. This phenomenon can be attributed to the correlation between the increase of pore diameter, the increase of light scattering and the resulting prolongation of light path or light trapping (Pham et al., 2012).

6.3.5 Effect of nanoporous structure on the SERS intensity

To showcase the SERS capability of the prepared *G-np-S* thin film, R6G has been chosen as the probe molecule. The decision was based on the fact that R6G is a highly fluorescent xanthene derivative that exhibits a molecular resonance Raman (RR) effect when stimulated within its visible absorption band at around 530 nm (Hildebrandt & Stockburger, 1984; Le Ru et al., 2007) with the enhancement as significant as 10^{14} to 10^{15} (Zhao et al., 2007). For this particular situation, a very low concentration of R6G was employed because of the exceptional sensitivity achieved by the synergistic effect of molecular resonance and surface enhancement (SERS) (Hildebrandt & Stockburger, 1984). Moreover, the R6G molecules have a higher affinity for adsorption on Ag (111) (Yuan et al., 2021), which is a dominant facet for the present nanoporous thin film.

The SERS spectra of a 10^{-6} M concentration of R6G on four distinct SERS substrates, namely glass substrate, Ag thin film substrate, gradient alloy thin film substrate, and *G-np-S* thin film substrate, are displayed in Figure 6.10. It is evident that the G6R did not produce any SERS signals when the spectra were acquired using the identical acquisition procedure and conditions on the glass slide, Ag thin film, and alloy thin film substrates, which can be attributed to the low surface roughness of the thin film alloy, measured to be 3. It is important to note that a surface morphology with a roughness scale of 50~200 nm is essential for achieving a significant enhancement factor (Tian et al., 2002).

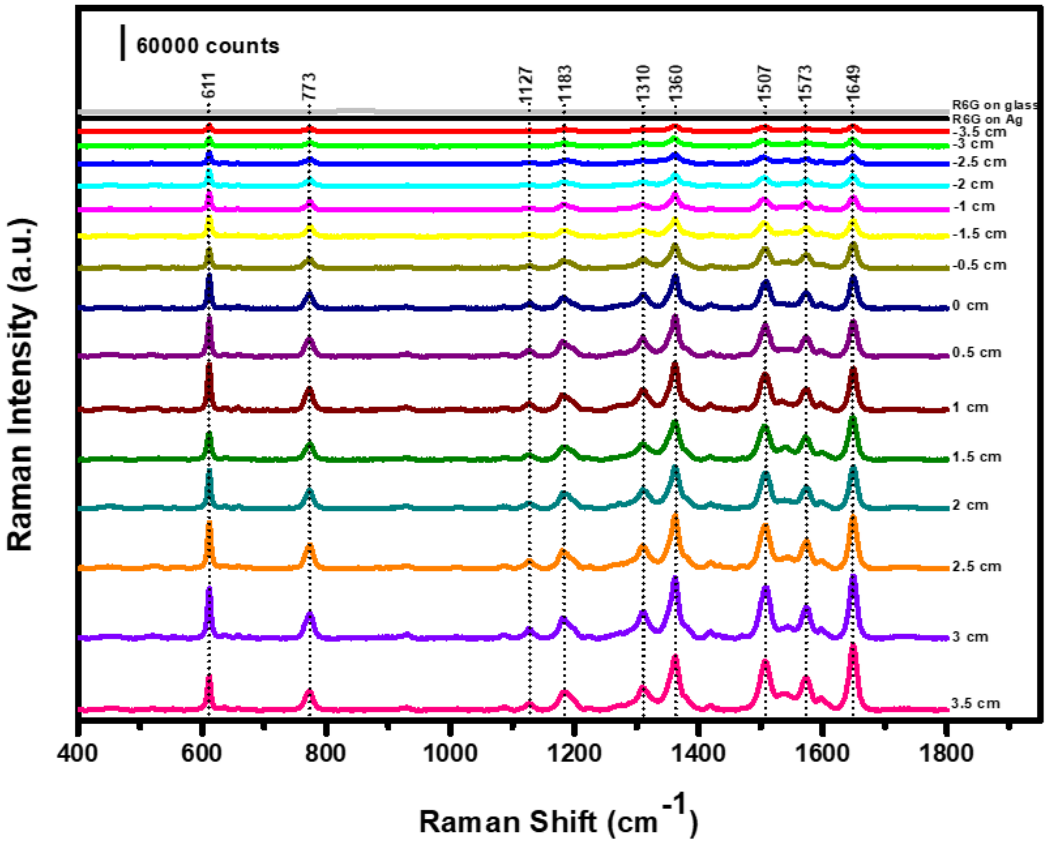

Figure 6. 10 SERS spectra of R6G on the G-np-S thin film collected at different positions.

The intense Raman bands of the R6G dye adhered at 15 positions on the *G-np-S* thin film were recorded at specific wavenumbers: 611 cm^{-1} (corresponding to the C-C-C in-plane bending vibration), 773 cm^{-1} (associated with the C-H out-of-plane bending), 1127 cm^{-1}, 1183 cm^{-1} (related to the C-H in-plane bending), 1310 cm^{-1}, 1573 cm^{-1} (assigned to the N-H in-plane bending) (Wu et al., 2016), 1360 cm^{-1}, 1573 cm^{-1}, and 1649 cm^{-1} (indicative of the aromatic C-C stretching vibration) (Yuan et al., 2021). These results are consistent with those available in the literature (Hildebrandt & Stockburger, 1984; Huang et al., 2017; Kudelski, 2005; Le Ru et al., 2007; R. Li et al., 2014; Qian et al., 2007; Wu et al., 2016; Zhang et al., 2011). The experiment was repeated several times to strengthen the credibility of the results, with *SERS*

spectra collected from four random points at each position, as shown in Figure 6.11. The standard deviation was then calculated based on the SERS intensity at the Raman band of 1649 cm^{-1}.

Because the pores and ligaments are smaller than the laser-beam spot (approximately 1 μm in diameter), it is feasible to obtain almost identical spectra from different locations at the same position using the same acquisition process. The low values of standard deviation demonstrate this, as Figure 6.11 shows. The spectra exhibit variations in both bandwidth and relative intensity at different locations. The G6R on the *np-S* structure formed at p15 displayed the most intense SERS signal, particularly at 1183, 1360, 1507, and 1649 cm^{-1} Raman bands. It is found that the intensity of the Raman band of 1649 cm^{-1} for the *np-S* evolute at p15 is more than 11 times greater than that at p1, as shown in Figure 6.10 and Figure 6.11. Structurally, at this position, the *np-S* exhibits the smallest pore and ligament diameter (11 and 10 nm, respectively) compared to other sites, as Figure 6.5 and Figure 6.6 a show. Furthermore, a gradual decrease in the SERS intensities was observed as moved along the x-axis of the *G-np-S* thin film, corresponding to a decrease in the sizes of the pore and ligament. The Raman intensity exhibited its minimum values at p1 (distance of -3.5 cm from the sample's centre), corresponding to the produced *np-S* with the largest pore and ligament sizes of 28 and 31 nm, respectively. Numerous studies have indicated that enhancing the Raman signal depends on nanopore size. According to Qian et al. (Qian et al., 2007), the Raman band of R6G at 1650 cm^{-1} on *np-Au* with average pore sizes of 5 nm exhibited an intensity 100 times higher than that of R6G on *np-Au* with average pore sizes of 700 nm. The signal enhancement of Raman for the R6G on *NPS* was less significant, as stated by Li and his colleagues (R. Li et al., 2014). They found that the intensity of R6G at 1650 cm^{-1} was almost one order of magnitude higher for the *NPS* with average pore sizes of 25 nm than that of big pore sizes of 100 nm. On the contrary, the nanoporous copper (*NPC*) with average pore sizes of 34 nm displayed a significant intensity at the wavenumber of 1650 cm^{-1}, compared to the *NPC* with larger pore sizes of 118 nm (Chen et al., 2009).

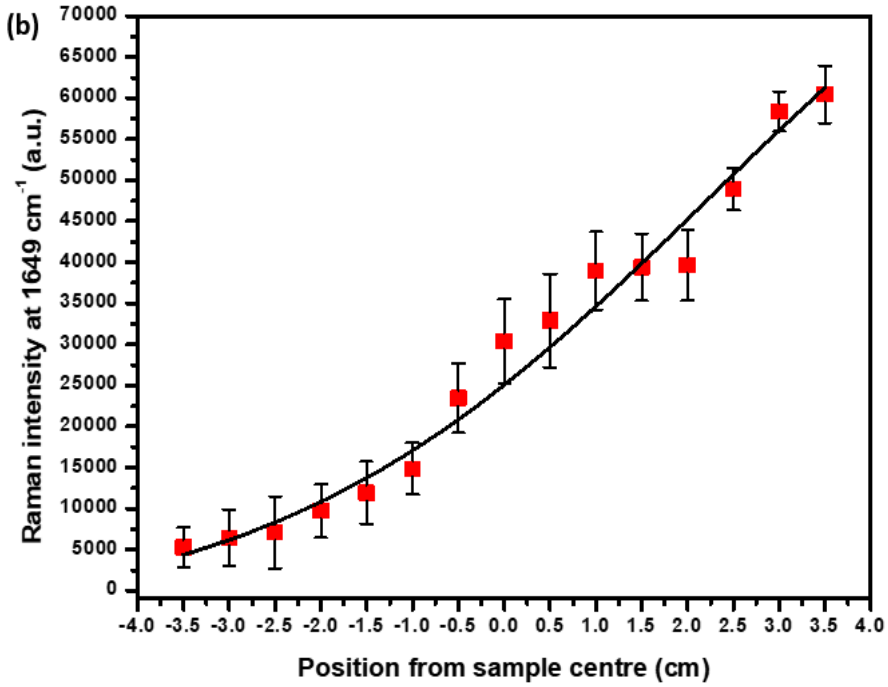

Figure 6. 11 position dependence of the R6G at 1649 cm^{-1} of the aromatic C-C stretching. The solid line is a guide to the eye. The error bars indicate ±5000.

In general, SERS activity of the *G-np-S* thin film can be attributed to various factors, including the high surface area of the nanopore structures, which provides a multitude of spots for probe molecules to adhere, then detect the signals from a more significant number of molecules, hence enhancing the signal. Moreover, the electromagnetic (EM) enhancement mechanism plays a significant role in enhancing Raman signals, which is linked to enhanced local fields resulting from surface plasmon resonance excitation (Ko et al., 2008; Qian et al., 2007; Sur & Chowdhury, 2013). According to Figure 6.8 a, the *np-S* structure at p15 displayed the most intense LSPR peak in the visible region. This structure has an average pore size of 11 nm. Figure 6.8 a shows that the peak was close to the wavelength of the excitation laser. According to Wu and his colleagues, the Raman enhancement seems unrelated to the *SPR* spectral position but was instead linked to the size of the nanoparticles (Wu et al., 2016). As shown in Figure 6.8 a, the LSPR peaks became weaker and broader, increasing the nanopore sizes as they moved from p14 to p7. Eventually, the LSPR disappeared for the *np-S* generated at the sites from p6 to p1. However, the SPR is known to be highly responsive to the dielectric permittivity of the surrounding medium in contact with the metal surface. Consequently, the resonance positions could be altered when the R6G molecules are adsorbed on the *np-S* thin film, even with just a few molecules binding events (Garoli et al., 2019). Additionally, the *EM* enhancement could be raised due to the high-density "hot spots" that can emerge at the subwavelength porous matrix (Garoli et al., 2019), as well as at nanoparticle junctions and flat metal surfaces that sustain plasmon resonances. Many studies indicated that molecules

confined within the narrow gaps between metal nanoparticles significantly enhance Raman signals.

The active sites of SERS are not exclusively caused by the EM enhancement near the metal surface but also results from the effect of chemical enhancement (Baia et al., 2005; Balmes et al., 2005; R. Li et al., 2014; Moskovits & Jeong, 2004; Qian et al., 2007). As the R6G, which is cationic, can bind to the surface of the gradient nanopore structure thin film, lead to complete charge transfer from the *np-S* to the dye (Zhao et al., 2007) and hence enhance the Raman signal.

Calculating the EF is a critical factor to evaluate the effectiveness of the *G-np-S* thin film as a SERS substrate. The EF was calculated using Eqs. 3.8 and 3.9, which are presented in the methodology section, and following the method described in Reference (Zhang et al., 2011). Table 4 below illustrates the EF of *G-np-S* at different positions.

Table 6. 5 Enhancement factor calculated using Eqs. 3.8 and 3.9 at different positions on the surface of the G-np-S thin film

Sample No.	Position from sample centre (cm)	Enhancement factor (EF)
p1	**-3.5**	3.43×10^{6}
p2	**-3**	4.19×10^{6}
p3	**-2.5**	4.61×10^{6}
p4	**-2**	6.30×10^{6}
p5	**-1.5**	7.73×10^{6}
p6	**-1**	9.64×10^{6}
p7	**-0.5**	1.52×10^{7}
p8	**0**	1.97×10^{7}
p9	**0.5**	2.14×10^{7}
p10	**1**	2.53×10^{7}
p11	**1.5**	2.56×10^{7}
p12	**2**	2.58×10^{7}
p13	**2.5**	3.18×10^{7}
p14	**3**	3.79×10^{7}
p15	**3.5**	3.93×10^{7}

The EF values are directly correlated with the pore sizes, as evidenced by the data presented in Table 6.5. Decreasing the size of nanopores enhances the Raman signals and, thereby, the *EF*. Notably, the EF values obtained in this study are higher than those reported for *np-S* substrates in the literature review section, even when employing comparable concentrations of the probe molecules. This is also clear when comparing data for nanoporous copper substrates (Hu et al., 2018). The findings are consistent with EF values reported for nanoporous gold (Fang et al., 2014).

It can conclude that the magnetron sputtering system has been used effectively to produce a gradient $Ag_{100-x}Al_x$ alloy with a broad range of Al compositions between 38 and 81 at.%, by applying constant current to the two targets. As the Al content in the precursor alloy

increases from 38 to 81 at. %, the average pore and ligament sizes decrease gradually from 28 to 11 nm and from 30 to10 nm, respectively. These results indicate a clear correlation between the Al content in the starting alloy and the pores density, average pore and ligament sizes.

Varying the Al concentration in the precursor alloy allows for control of the formation of cracks after dealloying in a 0.5 M NaOH solution. The cracks form when the Al content increases from 48 to 81 at.%, and their diameter becomes broad. The nanopore structures typically get finer at these positions. The mechanism behind the formation of the cracks after dealloying is not fully understood yet. The proposed mechanism assumed that the cracks may be formed due to volume shrinking, residual stress, capillary forces resulting in "mud-cracking," or coherency stresses between the alloy and the dealloyed film.

A red shift towards longer wavelengths was observed in the plasma frequency ω_p when the average pore size decreased from 21 to 11 nm, the average ligament size from 23 to 10 nm, and the Ag fraction from 46 to 36 wt.%. This trend indicated a decrease in metallic behaviour. The *np-S* thin film with Al concentrations between 59 and 81 at.%, displayed non-metallic behavior at the wavelengths ranging from 350 to 1610 nm, respectively. The *np-S* produced by dealloying the $Ag_{100-x}Al_x$ alloy with Al content between 60 and 81 at.% demonstrated lower optical constants due to increased pore density.

Due to the electromagnetic and chemical effects, *G-np-S* showed a superior intense Raman signal at the Raman band of 1694 cm^{-1}. The SERS activities of the *G-np-S* thin film are pore size-dependent; *np-S* with the small pore diameter exhibited the strongest SERS enhancement and highest enhancement factor of 3.93×10^7.

Chapter 7 Impact of Heat Treatment Prior to Dealloying on Nanostructure and Antibacterial Performance of Silver Sponges

7. Overview

Heat treatment process is a simple and effective method used in the processing and microstructural modification of metals. This process facilitates the recovery and recrystallization of deformed structures, resulting in the formation of more homogenous and refined grains with fewer lattice defects. By subjecting metals to controlled heating and cooling cycles, heat treatment can enhance mechanical properties, reduce internal stresses, and improve overall material performance (Ghosh et al., 2019; Zhao et al., 2020).

7.1 Objective of chapter

Herein, we explore the impact of heat-treatment conducted before the dealloying process on the nanostructure of the produced sponges. The $Ag_{100-x}Al_x$ alloy used was prepared by casting the pure Ag and Al, followed by homogenization annealing. The $Ag_{100-x}Al_x$ alloys were next subjected to dealloying in 2 M HCl aqueous solution to create the nanoporous structure. Electrochemical measurements to estimate the capacitance of the bulk Ag sponge electrodes was then conducted. The antibacterial activity of the Ag sponges with varied nanoporous structure against *E. coli* DH5α was also studied.

7.2 Experimental details specific to this chapter

Bulk Ag-Al alloy was prepared using melting and casting method, and then alloy was homogenized through a heat treatment under high vacuum as described in chapter 3. Homogenized alloy discs were heat treated for 24 h at the temperature from 350 °C to 500 °C, as shown in Table 7.1, to alter the properties of the homogenized alloy and its microstructure and relieve the stress introduced during the preparation process. The annealed samples were quenched in an ice brine path to prevent the formation of unwanted phases during the cooldown process and to preserve the microstructure. The heat treatment profile is shown in Figure 7.1.

Table 7. 1 Temperatures for homogenizing and heat treating the bulk alloys, and dealloying times employed for preparing the Ag sponges

Sample	Temperature (°C)	Dealloying time (h)
Homogenized alloy	500	-
T1- quenched	500	168
T2- quenched	450	168
T3- quenched	400	168
T4- quenched	350	168
H1- homogenized	500	7
H2- homogenized	500	16

H3- homogenized	500	28
H4- homogenized	500	35

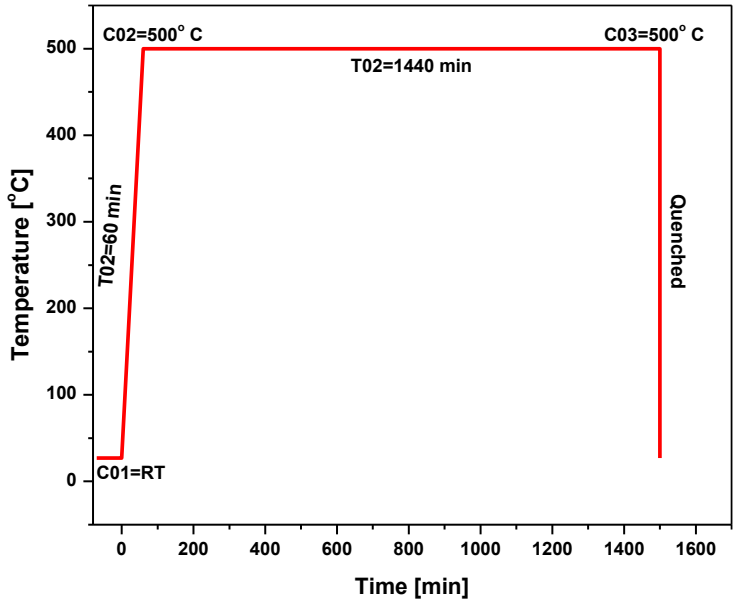

Figure 7. 1 Time- temperature profile used for heat treating the homogenized alloy to obtain the required microstructures.

The bulk alloy discs were subjected to chemical dissolution of Al in a 2 M hydrochloric acid (HCl) aqueous solution at room temperature, continuing the dealloying process until no obvious bubbles were formed. Meanwhile, the homogenized alloy discs were dealloyed in the same concentration of HCl solution for different durations, as listed in Table 7.1. The dealloyed alloys were rinsed with Milli-Q water, followed by ethanol, and then blow-dried with nitrogen. The as-dealloyed samples were kept in a vacuum desiccator to reduce oxidation.

The XRD patterns were collected using an X-ray diffractometer (Bruker D8 Discover diffractometer) in θ-2θgeometry equipped with a copper K-alpha (Cu Kα) radiation with a wavelength of approximately 1.5418 Å, primary beam monochromator and LYNXEYE_XE (0D mode) detector. The X-rays were excited using an electron gun with an accelerating voltage of 40 kV and a current of 25 mA. A Ni (0.02 rad) slit was inserted in the detector arm to filter out the Kβ radiation. The XRD patterns were collected with incidence angles between 7.5° and 40° with a step size of 0.01° and a 2θ ranging from 15° to 80° with a step size of 0.02°.

7.3 Results and Discussion

7.3.1 Determination of chemical composition of bulk alloys and Ag sponges

The chemical composition of elements in homogenized, and quenched bulk alloys was determined using the EDS technique, as shown in Table 7.2. The EDS patterns (not included

in this manuscript) were acquired at five different positions on the round discs of the bulk alloys. The values in Table 7.2 represent the average Al and Ag concentration values and standard error. The small standard error values confirm the compositional homogeneity of the homogenized and quenched alloys. These minor variations in the concentrations of Ag and Al components observed between the round discs are owing to the compositional fluctuations within the primary cylinder alloy.

Table 7. 2 Elemental compositions of homogenized alloy at 500 ℃, and heat-treated alloys at temperatures between 350 ℃ and 500 ℃.

Sample	Heat treatment temperature (°C)	concentration (at.%)	
		Ag	Al
T1	500	18±0.6	82±0.6
T2	450	17±0.4	83±0.4
T3	400	19±0.7	81±0.7
T4	350	17±0.3	83±0.3

The EDS measurements of the elemental composition of the dealloyed bulk samples revealed that, even though the alloys were submerged in the HCl solution until no bubbles were observed, the presence of Al was still detected by the EDS. The most probable causes for the presence of the Al include the formation of intermetallic compounds (Ag_2Al) during the preparation and heat treatment processes, which are more resistant to dissolution (Wang et al., 2009b). Moreover, the formation of a protective oxide layer (Al_2O_3) on the surface of the alloy when exposed to air or during the dealloying process may prevent the dissolution of Al in HCl solutions (Boukerche et al., 2014). Additionally, the saturation of the solution with dissolved Al ions may lead to the re-precipitation or adsorption of Al onto the surface of the Ag sponges (McCue, Gaskey, et al., 2016). The measured concentrations of the elements present in the dealloyed samples are shown in Table 7.3.

Table 7. 3 Elemental compositions of elements present in bulk Ag sponges prepared by dealloying the annealed Al_xAg_{100-x} alloys at different temperatures and by dealloying the homogenized Ag_xAl_{100-x} alloys at 500 ℃ for various durations.

	Sample	concentration (at.%)	
		Ag	Al
Dealloyed for 168 h	T1-quenched at 500°C	91±0.5	9±0.5
	T2-quenched at 450°C	93±0.8	7±0.8
	T3-quenched at 400°C	80±1.7	20±1.7
	T4-quenched at 350°C	86±0.4	14±0.4
Annealed at 500°C	H1-dealloyed for 7 h	33±0.6	67±0.6
	H2-dealloyed for 16 h	48±1.3	52±1.3
	H3-dealloyed for 28 h	61±0.8	39±0.8
	H4-dealloyed for 35 h	73±0.4	27±0.4

7.3.2 Crystal structure and phase constitution

Referring to the binary $Ag_{100-x}Al_x$ phase diagram in Figure 7.2 (Porter & Easterling, 2009), at the temperatures between 350° to 500°C, two phases form in alloys with Al concentrations greater than 42 at. % and lower than 89 at. %. These two phases are α-Ag (Al) face-centred cubic (*fcc*) crystal structure – with space group $Fm\bar{3}m$, and δ-Ag_2Al intermetallic compound with hexagonal closed packing (*hcp*) structure and space group of *P63/mmc*.

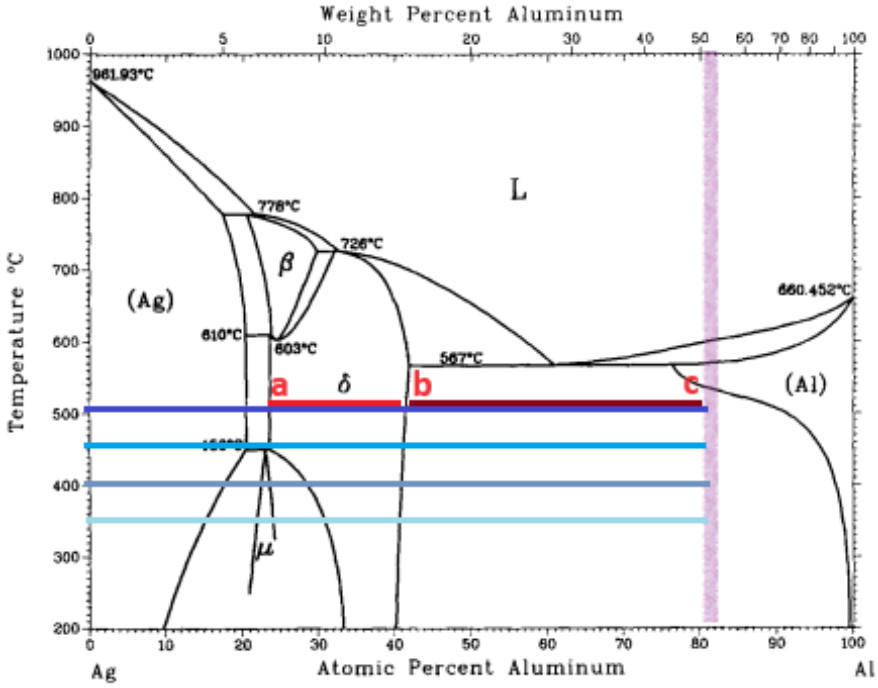

Figure 7. 2 Temperature–composition $Ag_{100-x}Al_x$ alloy phase diagram (McAlister, 1987)

The XRD diffraction patterns in Figure 7.3 confirmed the presence of these two phases in the homogenized and heat-treated alloys. These findings confirm that no new phases were observed to form during the heat-treatment processes, which means the alloy system is thermodynamically stable before and after applying heat treatment (Barron et al., 2022). The most intense peaks with the plane of (002), (101), (102), and (103) in the XRD patterns in Figure 7.3 indicate that the δ-Ag_2Al intermetallic phase with space group of *P63/mmc* and lattice parameter a of 0.288 nm and c of 0.458 nm is dominant. Whereas, the other planes including (111), (200), (220), and (311) assigned for the α -Al (Ag) phase with space group of $Fm\bar{3}m$ and lattice parameter a of 0.4048 nm. The Ag component exists here as a solid solution of Ag in the α-Al matrix, but most of the Ag exist in the δ-Ag_2Al phase. Moreover, the XRD patterns of the treated alloys indicated the formation of Al_2O_3 during the heat treatment process, which exhibits high corrosion resistance in the low concentration HCl aqueous solution

(Curkovic & Jelaca, 2009), and also can prevent the diffusion of atoms or ions which acts as a diffusion barrier, hence enhance the stability of alloys (Li et al., 2022).

It can be observed from the XRD patterns in Figure 7.3 a that, the peak intensities of the homogenized alloy significantly decreased after heat treatment, as well as the intensity of the diffraction peaks of the heat-treated alloys exhibited slight decrease with increasing the treatment temperatures, this effect can be explained based on the Debye-Waller factor, also called the temperature-factor. According to Debye-Waller theory, the atoms in the subjected alloy to the temperature will experience significant thermal vibrations which leads to atomic displacements from their equilibrium positions. As treatment temperature increases, coherent elastically diffracted x-rays reduce due to increase the atomic vibrions, causing weak diffraction signals (Levi & Suhl, 1979).

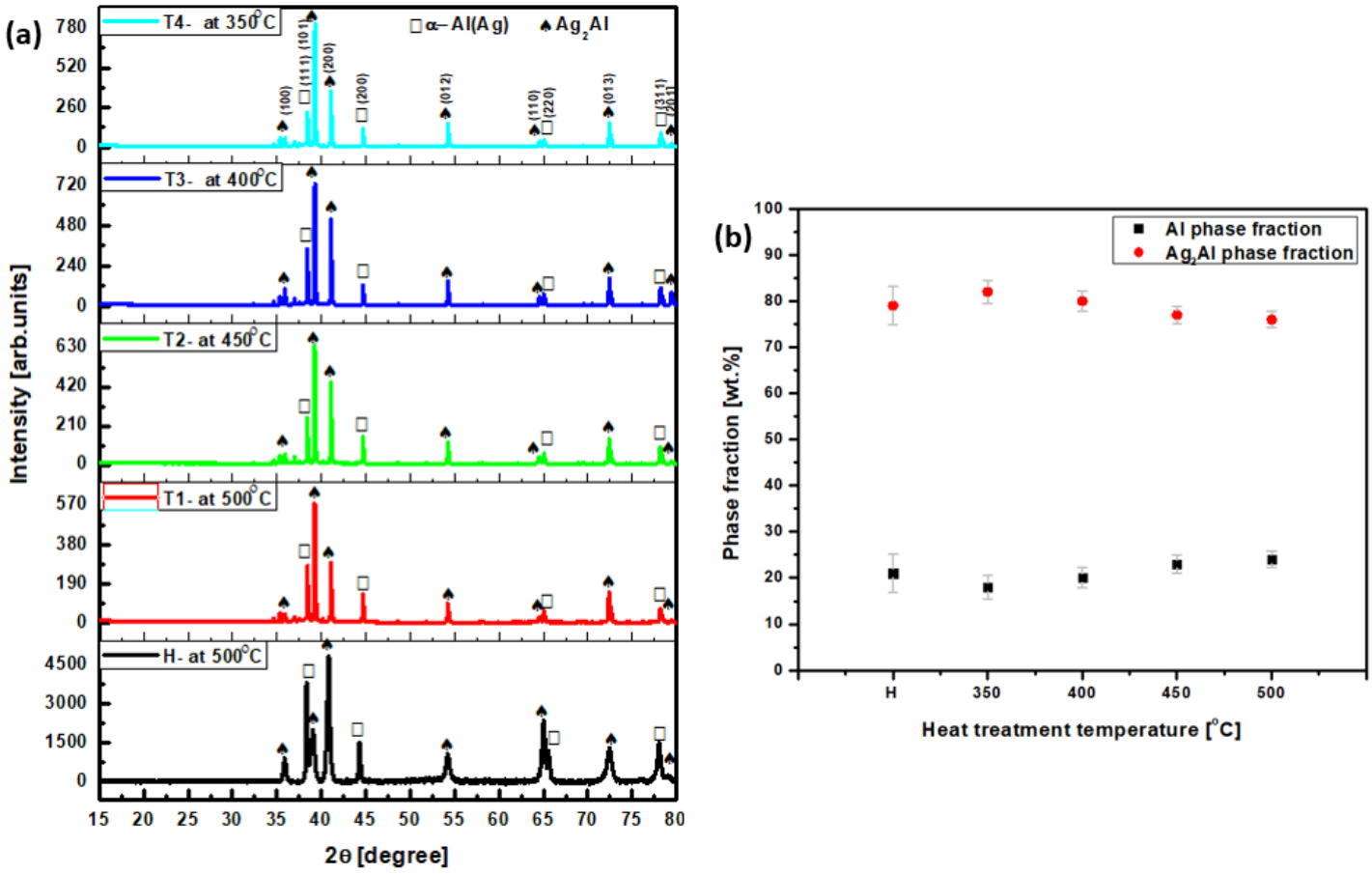

Figure 7. 3 a) XRD diffraction patterns of the homogenized and quenched alloys at 500 ℃, 450 ℃, 400 ℃, and 350 ℃, showing the two phases namely, α-Al and Ag_2Al, and (b) the fraction of Al, and Ag_2Al phases present in the alloys, as determined from the Rietveld refinement.

Table 7. 4 Peak positions, lattice parameters 'a' and 'c', unit-cell volume and crystal sizes 'D' of the homogenized and quenched alloys extracted from XRD patterns

Sample	Phase	
	Ag_2Al	Al

	2θ [°]	(hkl)	D [nm]	CIF	a [nm]	c [nm]	Unit-cell volume [nm^3]	2θ [°]	(hkl)	D [nm]	CIF	a [nm]	Unit-cell volume [nm^3]
H- at 500°C	35.79	(100)	0.38	1509589	0.288	0.458	3.29	38.44	(111)	1.16	4313217	0.405	6.65
	39.11	(002)	0.68					44.64	(200)	1.20			
	41.00	(101)	0.40					65.03	(220)	1.23			
T1- at 500°C	35.34	(100)	1.44	1509589	0.288	0.458	3.29	38.45	(111)	2.24	4313217	0.405	6.65
	39.25	(002)	0.89					44.68	(200)	1.53			
	41.10	(101)	1.44					65.04	(220)	2.74			
T2- at 450°C	35.90	(100)	1.45	1509589	0.288	0.458	3.29	38.43	(111)	1.73	4313217	0.405	6.65
	39.25	(002)	1.74					44.68	(200)	1.94			
	41.10	(101)	1.85					65.04	(220)	1.73			
T3- at 400°C	35.90	(100)	1.91	1509589	0.288	0.458	3.29	38.45	(111)	1.87	4313217	0.405	6.65
	39.27	(002)	1.87					44.70	(200)	2.09			
	41.10	(101)	2.04					65.06	(220)	1.89			
T4- at 350°C	35.92	(100)	0.95	1509589	0.288	0.458	3.29	38.45	(111)	1.77	4313217	0.405	6.65
	39.27	(002)	1.77					44.72	(200)	1.80			
	41.12	(101)	1.69					65.08	(220)	1.93			

The fractions of the α-Al (Ag) and δ-Ag_2Al phases detected in the bulk alloys can be determined using the Rietveld method. The results in Figure 7.3 b revealed that the fraction of δ-Ag_2Al phase is higher than the fraction of α-Al (Ag) phase in all the alloy samples. The standard errors of the phase fractions are small. The obtained fraction of the phases presented in homogenized alloy were 79 wt.% of δ-Ag_2Al phase and 21 wt.% of α-Al (Ag). Whereas the δ-Ag_2Al phase fractions in the quenched alloys at 500°, 450°, 400°, and 350°C were 76, 77, 80, and 82 wt.%, and the α-Al (Ag) phase fractions were 24, 23, 20, and 18 wt.%, respectively. These values were compared with the phase fraction values estimated from the binary phase diagram shown in Figure 7.1. According to the quantity rule (also known as the second lever rule), the fractions of phases present in the alloy can be estimated as the ratio of the length of the arm (ab length or bc length in Figure 7.1) opposite each phase to the total length of the tie-line (ac length in Figure 7.1) (Tisza, 2001). The extracted δ-Ag_2Al phase fractions in the quenched alloys at 500°, 450°, 400°, and 350°C were 77.8, 77.8, 81.4, and 83.3 wt.%, and the α-Al (Ag) phase fractions were 22.2, 22.2, 18.6, and 16.7 wt.%, respectively, which is very close to those values determined using the Rietveld method. The well-matched phase fractions from the binary phase diagram and Rietveld analysis confirm the stability of the phases during the heat treatment.

The influence of homogenization and heat treatment temperatures on the crystallite sizes of the alloys was investigated. The XRD patterns, as shown in Figure 7.3 a, reveal that all the alloys exhibit a crystalline structure because the patterns exhibit sharp, and well-defined peaks. It can be seen that the XRD peaks become sharper after heat treatments, with the

sharpest peaks observed following heat treatment at 500°C, compared to 350°C. The crystallite size (D) was estimated using the Debye-Scherrer formula:

$$D = \frac{0.9\,\lambda}{\beta\,cos\theta} \text{..... (2) (Rijesh et al., 2018)}$$

Where λ is the X-ray wavelength in nm, β is the full width at half maximum of the peak in radian and θ is Bragg's diffraction angle in degree.

The calculated crystallite sizes are presented in Table 7.1. The results indicated that the crystallite size of the alloy increase with increasing the treatment temperature, for example, the crystal size D of (111) plane in α-Al (Ag) phase increases from 1.77 nm at 350°C to 2.24 at 500°C which indicated as a more crystalline alloy. This increase in crystallite size and peak sharpness with increasing treatment temperatures refers to the growth of grains and reduction of defects, hence alloy homogenization (Muhammed Shafi & Chandra Bose, 2015).

The evolution of nanoporosity during the dealloying process involves the dissolution of the more electrochemical active component (Al atoms) at the surface of the alloy through a rapid reaction between the Al atoms from the α-Al (Ag) and δ-Ag_2Al phases and the HCl solution. The HCl solution was used here based on the findings of Yamauchi and his co-workers in their previous report. Their study indicated that the δ-Ag_2Al phase presented in the rapidly solidified Ag_xAl_{100-x} alloys with x= 15, 20, 25, 30 and 39 at.% is resistant to leaching in NaOH solution, preventing its dissolution and contribution to the formation of nanoporous structures (I. Yamauchi et al., 2003).

During dealloying process, the Al atoms dissolve in HCl solution, producing Al^{3+} ions, and H_2 gas, which is released as air bubbles during the dealloying reaction (1) and (2):

$$2\,Al_{(s)} + 6\,HCl_{(aq)} \rightarrow 2\,AlCl_{3\,(aq)} + 3\,H_{2(g)}\uparrow \text{..... (1)}$$

$$2Ag_2Al_{(s)} + 8HCl_{(aq)} \rightarrow 4Ag_{(s)} + 2AlCl_{3\,(aq)} + 3H_{2(g)}\uparrow \text{..... (2)}$$

The residual Ag component diffuse along alloy/electrolyte interfaces and agglomerates to form interconnected and continuous nanoporous structures (Wang et al., 2009b). According to Detsi and co-workers, the dealloying process involves the complete dissolution of the Al from α-Al (Ag) phase first, followed by the selective removal of the intermetallic δ-Ag_2Al phase (Detsi et al., 2012; Wang et al., 2009b), creating a sufficient number of voids (Ji, Zhang, et al., 2011). These voids became filled by aggregating surface Ag atoms. Consequently, Al atoms with lower coordination diffuse to the alloy/electrolyte interface (Moore et al., 2002). Leaching Al out of the α-Al(Ag) phase can be effectively achieved at room temperature (Qiu et al., 2011b). The Ag remains as a porous structure after the Al is removed. The XRD

diffraction patterns of the as-dealloyed alloys in Figure 7.4 a shows that the α-Al (Ag) phase undergoes complete dealloying in HCl. Therefore, the XRD peaks due to α-Al (Ag), the (111), (200), (220) and (311) peaks at 2θ=38.4°, 44.7°, 65.1°, and 78.2° are not present in the diffraction patterns of the dealloyed samples, indicate the complete removal of α-Al (Ag) phase. Meanwhile, there is a reduction in the diffraction intensity of the δ-Ag_2Al phase, suggesting partial leaching of the Al content from the δ-Ag_2Al phase during the dealloying process. The resultant Ag sponges are primarily composed of a face-centred cubic (fcc) α-Ag phase (CIF#9011607) with the expected (111), (200), (220) and (311) peaks, characterized by a space group of $Fm\bar{3}m$, and a lattice parameter a of 0.4079 nm. Moreover, a minor amount of un-dealloyed δ-Ag_2Al phase within the structure is observed, as shown in Figure 7.4 b. This implies that the δ-Ag_2Al phase cannot be completely dealloyed when immersed in the HCl solution (Wang et al., 2009b). The Ag sponge diffraction peaks are broader when compared to those of the alloys which can be ascribed to the presence of ligament and pore nanostructures.

Figure 7.5 a present the XRD patterns of the as-dealloyed alloys, all subjected to the same concentration of HCl solution but dealloyed for varying durations. The results indicate the continuing presence of the Al phase in the alloy when immersed in the HCl solution for shorter periods, specifically 7 and 16 h. The concentration of the residual Al atoms and the dealloying duration as Figure 7.5 b demonstrated. After 28 h of dealloying, the peaks corresponding to the α-Al (Ag) phase completely disappeared, and only the peaks of α-Ag (Al) and δ-Ag_2Al phases were detected.

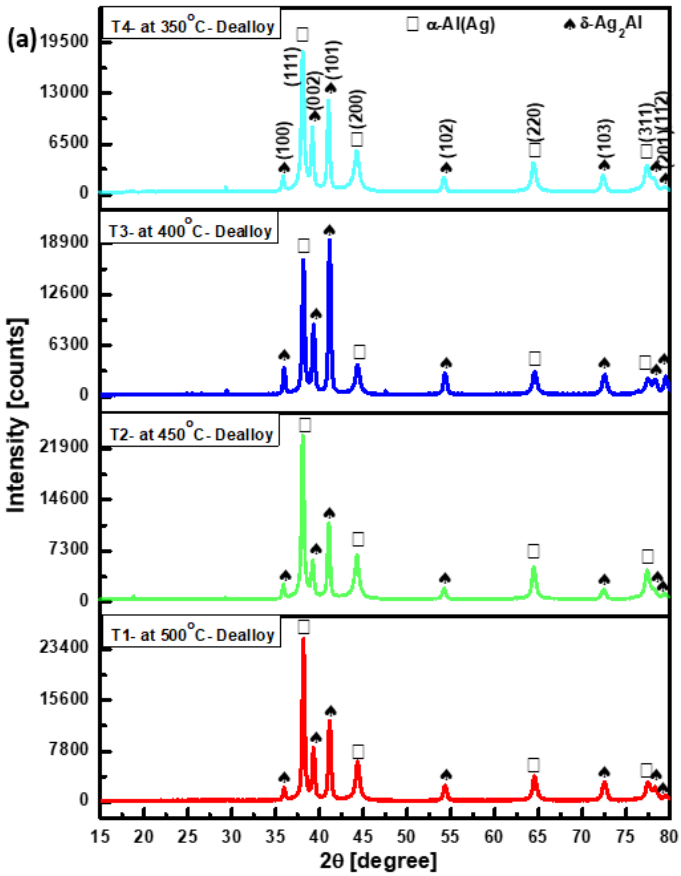

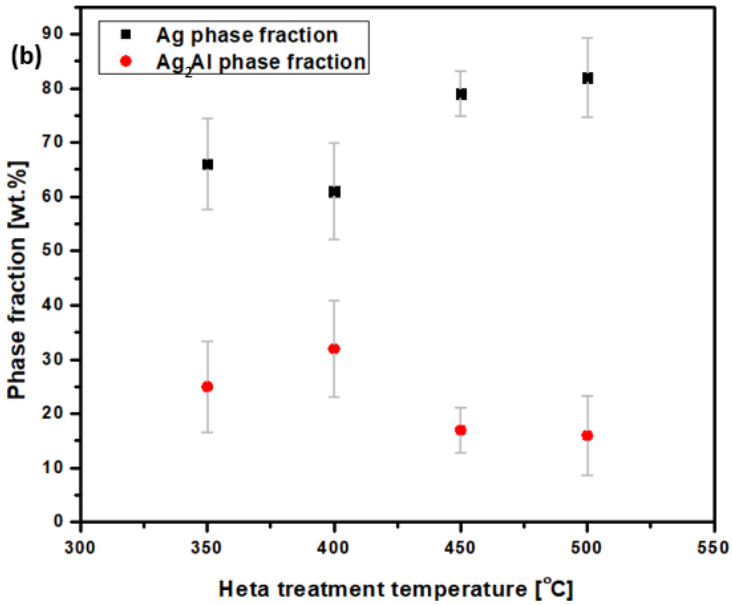

Figure 7. 4 XRD diffraction patterns of the dealloyed alloys quenched from 500 ℃, 450 ℃, 400 ℃, and 350 ℃, reflecting the presence of the Ag_2Al phase after dealloying in 2M HCl, and (b) the fractions of the primary phases, Ag and Ag_2Al, present in the as-dealloy specimens, as determined from the Rietveld refinement

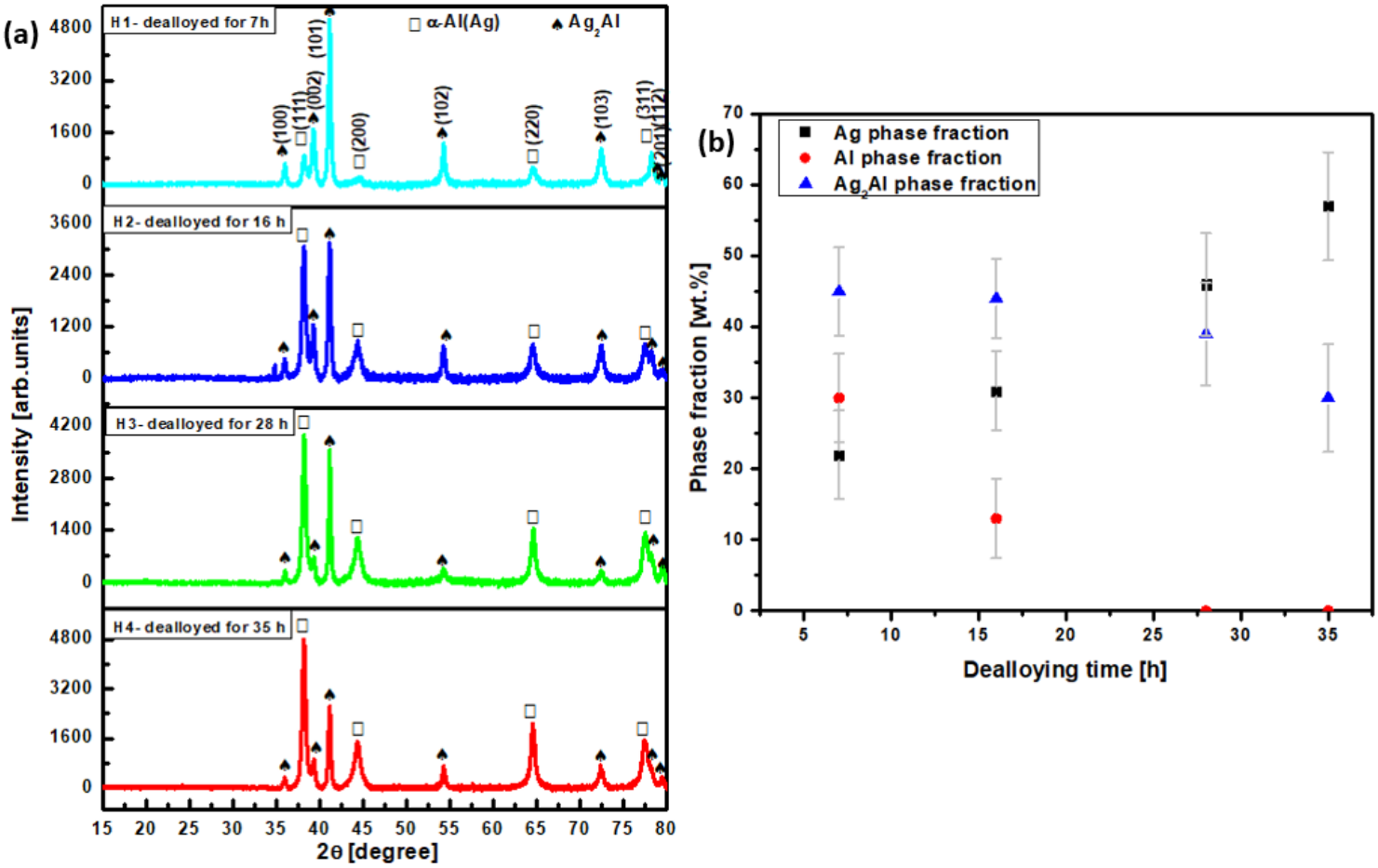

Figure 7. 5 XRD diffraction patterns of the dealloyed specimens prepared by dealloying homogenized alloys in 2M HCl for different periods of time: 7, 16, 28, and 35 h, and (b) the phase fraction in wt.% of the primary phases, Ag and Ag_2Al, present in the as-dealloyed specimens, as determined from the Rietveld refinement.

7.3.3 Microstructure of Ag sponges prepared by dealloying heat-treated alloys

The formation of Ag sponges with hierarchical structures during the dealloying process in HCl solution for bulk $Ag_{100-x}Al_x$ alloys, with x between 81 and 83 at.%, is shown in Figure 7.6 a- d. The plan-view SEM micrographs in Figure 7.6 reveal that the selective dissolution of Al atoms from the bulk $Ag_{100-x}Al_x$ alloys leads to the evolution of three-dimensional, bicontinuous structures featuring interpenetrating ligament and open-pore architectures, which align with the XRD results.

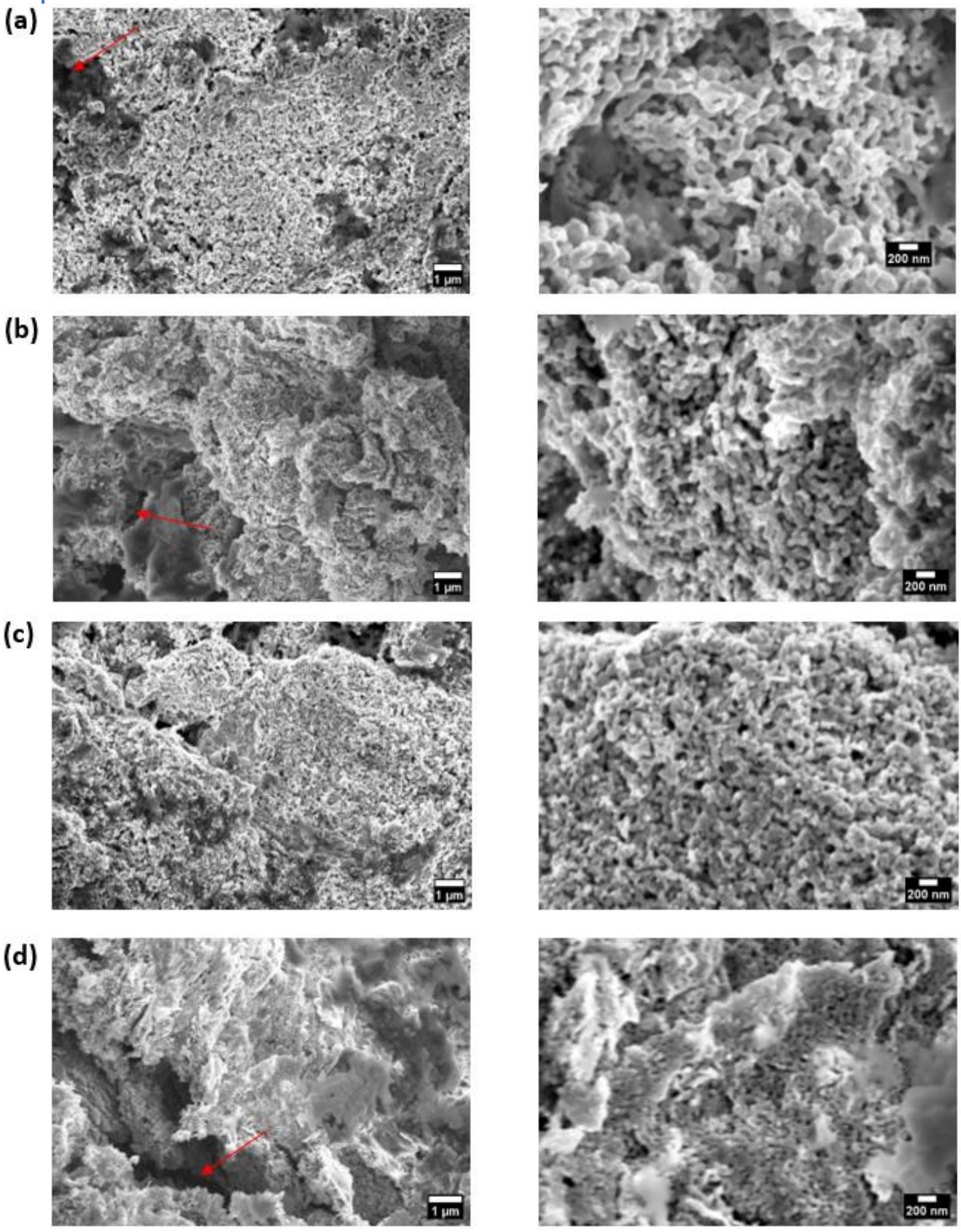

Figure 7. 6 Top-view SEM images showing the microstructure of Ag sponges prepared by dealloying the annealed $Ag_{23}Al_{77}$ alloys in 2M HCl solution for the same durations and at different treatment temperatures (a) at 500 ℃, (b) at 450 ℃, (c) at 400 ℃, and (d) at 350 ℃. The SEM images in the left column were captured at a lower magnification with a scale bar of 1 µm, whereas the images in the right column were taken at a higher magnification with a scale bar of 200 nm. The red arrows indicated the presence of cracks.

The average width of pores and ligaments of the produced bulk sponges were estimated from SEM images and measured using ImageJ software, specifically utilizing the straight-line tool, as detailed in Table 7.5. It is concluded that the smallest measured ligaments were with the size greater than 30 nm, which is higher than the measured ligament we found in chapter 4 and 6 for *np-S* prepared by dealloying the $Ag_{100-x}Al_x$ alloys in alkaline solution (NaOH). Nonetheless, the obtained results are consistent with the findings of Ding et al. (2004). They observed that dealloying of AuAl alloy in acidic conditions leads to the coarsening of Au ligaments (Y. Ding et al., 2004). Similarly, in this study, the produced bulk sponges exhibited an increase in the average pore and ligament sizes with higher heat treatment temperatures prior to dealloying, indicating that the heat treatment impacted the microstructure of the sponges.

Table 7. 5 Average ligament and pore sizes in nm of the Ag sponges prepared by dealloying the quenched Ag_xAl_{100-x} alloys in 2M HCL for the same durations, and Ag surface diffusion

Dealloyed sample	T1 at 500°C	T2 at 450°C	T3 at 400°C	T4 at 350°C
Average Ligament diameter (nm)	58.5±17.9	45.9±12.9	45.2±18.2	31.1±8.3
Average Pore diameter (nm)	50.8±19.6	49.4±20.9	40.1±12.8	36.1±14.3
Surface diffusion of Ag, Ds (m^2s^{-1})	3.86×10^{-15}	1.46×10^{-15}	1.37×10^{-15}	0.308×10^{-15}

The histograms depicted in Figure 7.7 a- d demonstrate that the pore sizes are within the nanometer range, with the broad pore size distributions in the Ag sponges. Specifically, the pore sizes range from 20 to 120 nm for T1 heat-treated at 500°C, from 10 to 130 nm for T2 heat-treated at 450°C, from 10 to 110 nm for T3 heat-treated at 400°C, and from 10 to 90 nm for T4 heat-treated at 350°C. The distributions exhibit maxima between 30 and 50 nm for T_1, between 30 and 40 nm for T_2, between 40 and 50 nm for T_3, and between 20 and 30 nm for T_4, indicating significant variation in pore size depending on the annealing temperature of the alloys prior to dealloying.

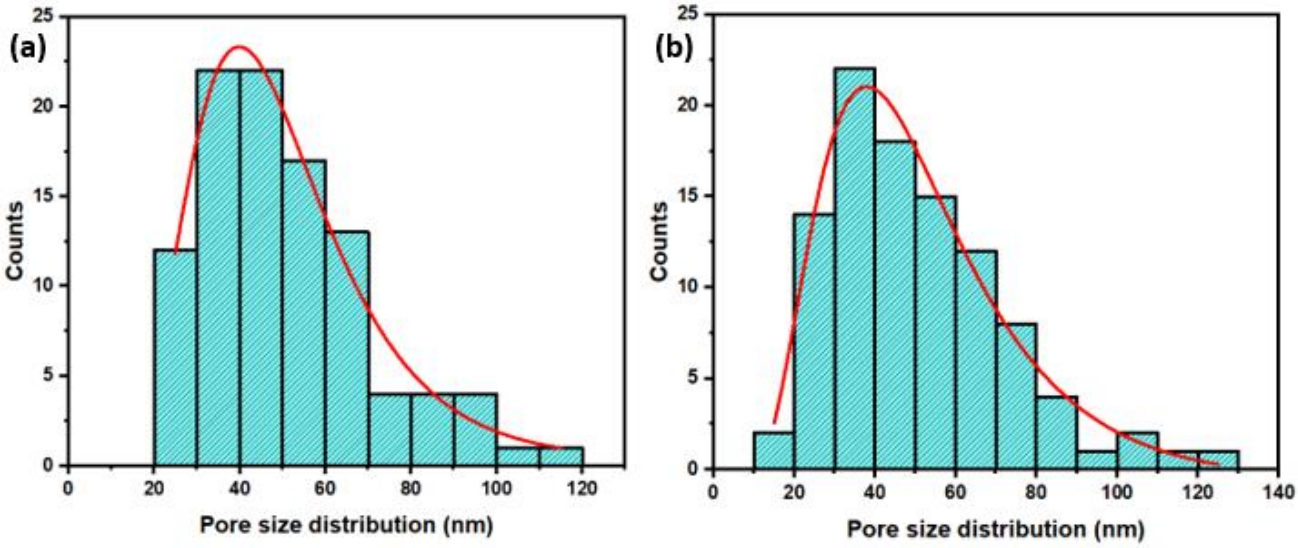

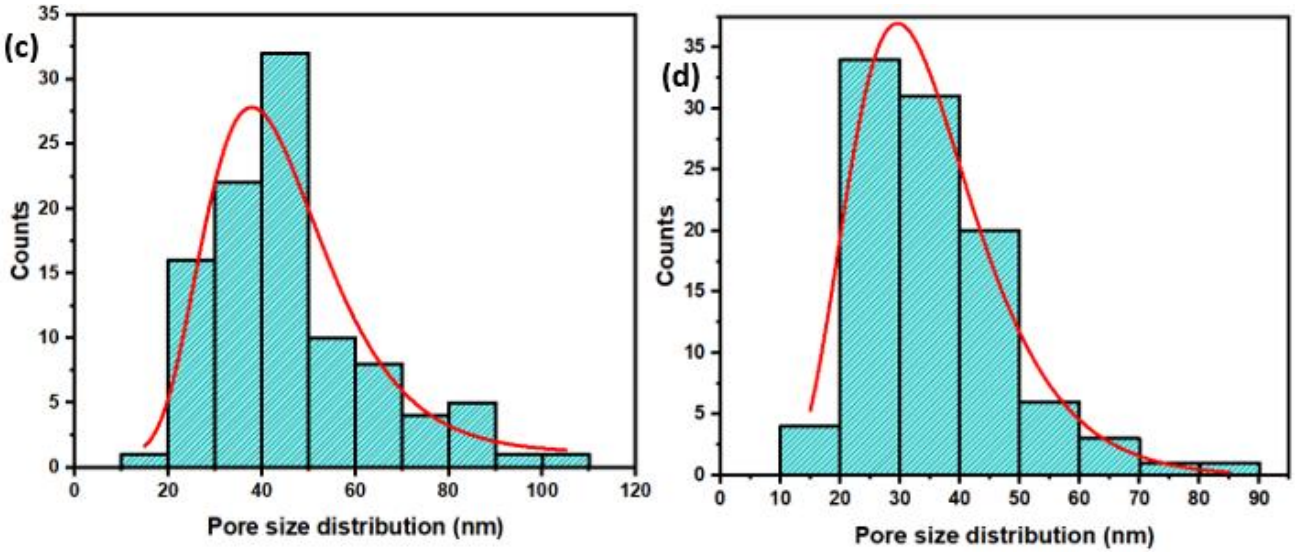

Figure 7. 7 Pore size distribution histogram (a) for sample T_1 annealed at 500℃, (b) for sample T_2 annealed at 450℃, for sample T_3 annealed at 400℃ and (d) for sample T_4 annealed at 350℃.

According to Eq. 2.1, a linear relationship exists between the ligament size of the Ag sponges and surface diffusivity, which describes surface diffusion-controlled coarsening D_s of columns of the Ag atoms. The largest ligaments were observed for the Ag sponge derived from the 500° C pre-heated $Ag_{100-x}Al_x$ alloy indicating the Ag atoms have higher surface diffusion rate. Numerous studies have reported that the surface diffusion rate of heat-treated precursors is faster than that of those without any treatment (X.-l. Tan et al., 2012), which may be attributed to the decreased surface tension at the alloy surface with increasing heat treatment temperatures. This reduction in surface tension promotes the diffusion of the more noble component at the interface between the ribbon and solution (Zhao et al., 2022). The Ag sponges obtained in this study exhibited higher surface diffusion values compared to the sponges produced by dealloying $Ag_{100-x}Al_x$ alloy thin films in NaOH, as discussed in Chapters 4 and 6 of this thesis. According to Wang et al. (2009) this difference may result from variations in internal stress due to differing dissolution rates of components, variations in surface diffusion of the components, as well as the viscosity of the dealloying solution (Wang et al., 2009a).

7.3.4 Microstructure of Ag sponges prepared by dealloying untreated alloys

To investigate the impact of heat-treatment and dealloying times on the microstructure of bulk Ag sponges, four discs of untreated Ag-Al alloy were dealloyed for different durations, ranging from 7 to 35 h (after 35 h of dealloying, no H_2 bubbles were observed which indicated that the dealloying process finished). It can be observed that no obvious nanoporous structures were formed when the dealloying of homogenized and untreated alloys were conducted for only 7 and 16 h, as demonstrated in Figures 7.8 a and b. Instead, large cracks were seen,

reaching several micrometers in length and increasing in width with the extended dealloying time of 28 h. As Figure 7.8 c and d shows, the evolution of pore structures began to appear after dealloying for 35 h, with the mean pore and ligament diameters of the formed Ag sponge being approximately 49.6 ± 25.3 nm and 60.3 ± 26.5 nm, respectively. The mean pore and ligament diameters decreased when the alloy was immersed for 2100 min in HCl solution, with the measured mean pore and ligament diameters being 31.7 ± 15.3 nm and 46.6 ± 15.2 nm, respectively. The incomplete dealloying of the homogenized but untreated alloys may be attributed to the formation of an oxide layer, as previously mentioned, or the creation of more stable intermetallic phase during homogenization that are less reactive in HCl (Boukerche et al., 2014; Qiu et al., 2011b; Wang et al., 2009b; R. Zhang et al., 2018).

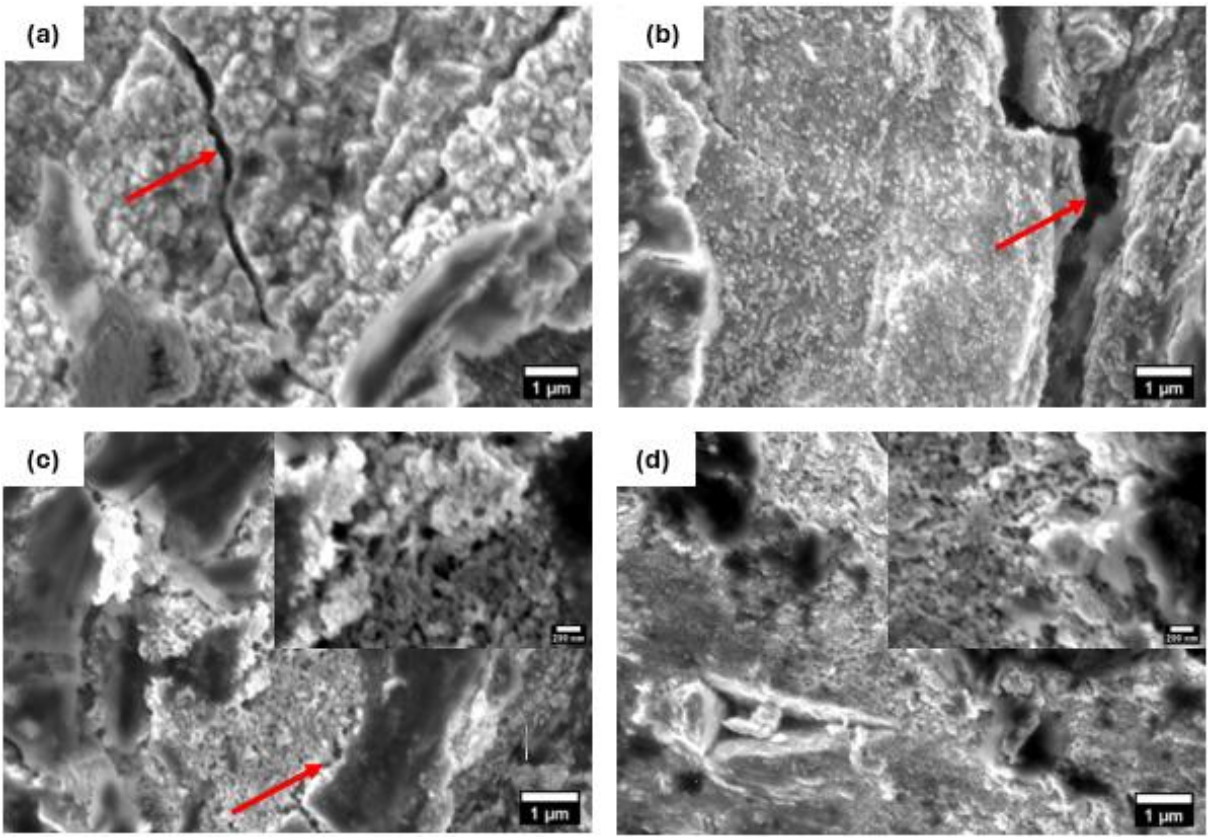

Figure 7. 8 Top-view SEM images of Ag sponges prepared by dealloying $Ag_{23}Al_{77}$ alloy in 2M HCl at room temperature for (a) 420 min, (b) 960 min, (c) 1680 min and (d) 2100 min. The images indicate that nanoporous structures did not form after dealloying for 7 and 16 h. In contrast, pore structures began to emerge after 28 and 35 h of dealloying, as inset images show. The SEM images were captured at a lower magnification with a scale bar of 1 µm, whereas the inset images were taken at a higher magnification with a scale bar of 200 nm. The red arrows indicated the presence of cracks.

7.3.5 Bulk Ag sponges as electrode in a supercapacitor

Bulk Ag sponges were tested as electrodes in an aqueous supercapacitor. The square wave charge/discharge cycles of asymmetrical electrodes (one electrode is bulk Ag sponge and the other is bulk AgAl alloy) in 0.1 M KNO_3 aqueous electrolyte are illustrated in Figures 7.9

(a- d). As can be seen in the figure, a constant current was applied to charge the bulk Ag sponge electrodes, which led to an increase in the voltage until 1 V was reached. The charging period was extended to 60 s, followed by a discharge cycle down to 0.50 V to release some of the stored electrical energy. The duration of this discharge differs from one electrode to another which depends on the surface area of the Ag sponge electrodes. Five charge and discharge cycles were recorded, with the final discharge cycle being much deeper. The capacitance of each two-electrode system was then determined in order to provide an estimate of the electrochemically active surface area. Here the estimated capacitance up to 60 s after the final discharge started was plotted in Figure 7.10 (a- d).

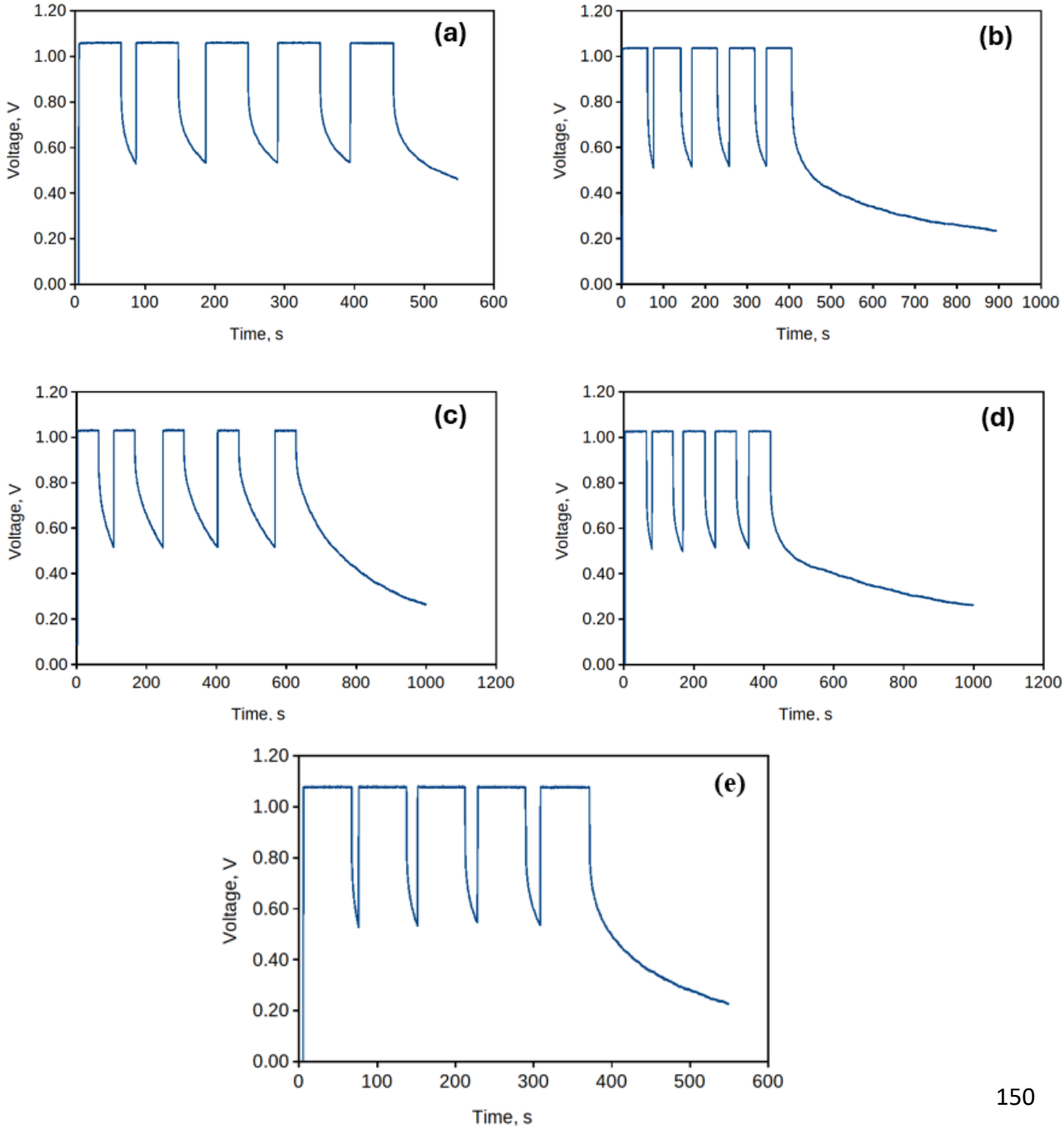

Figure 7. 9 Voltage against time plots for five charge/discharge cycles for bulk Ag sponge electrodes, (a) T1 sample heat-treated at 500 ℃, (b) T2 sample heat-treated at 450 ℃, (c) T3 sample heat-treated at 400 ℃, and (d) T4 sample heat at 350 ℃, and (e) as-cast alloy+ not dealloyed.

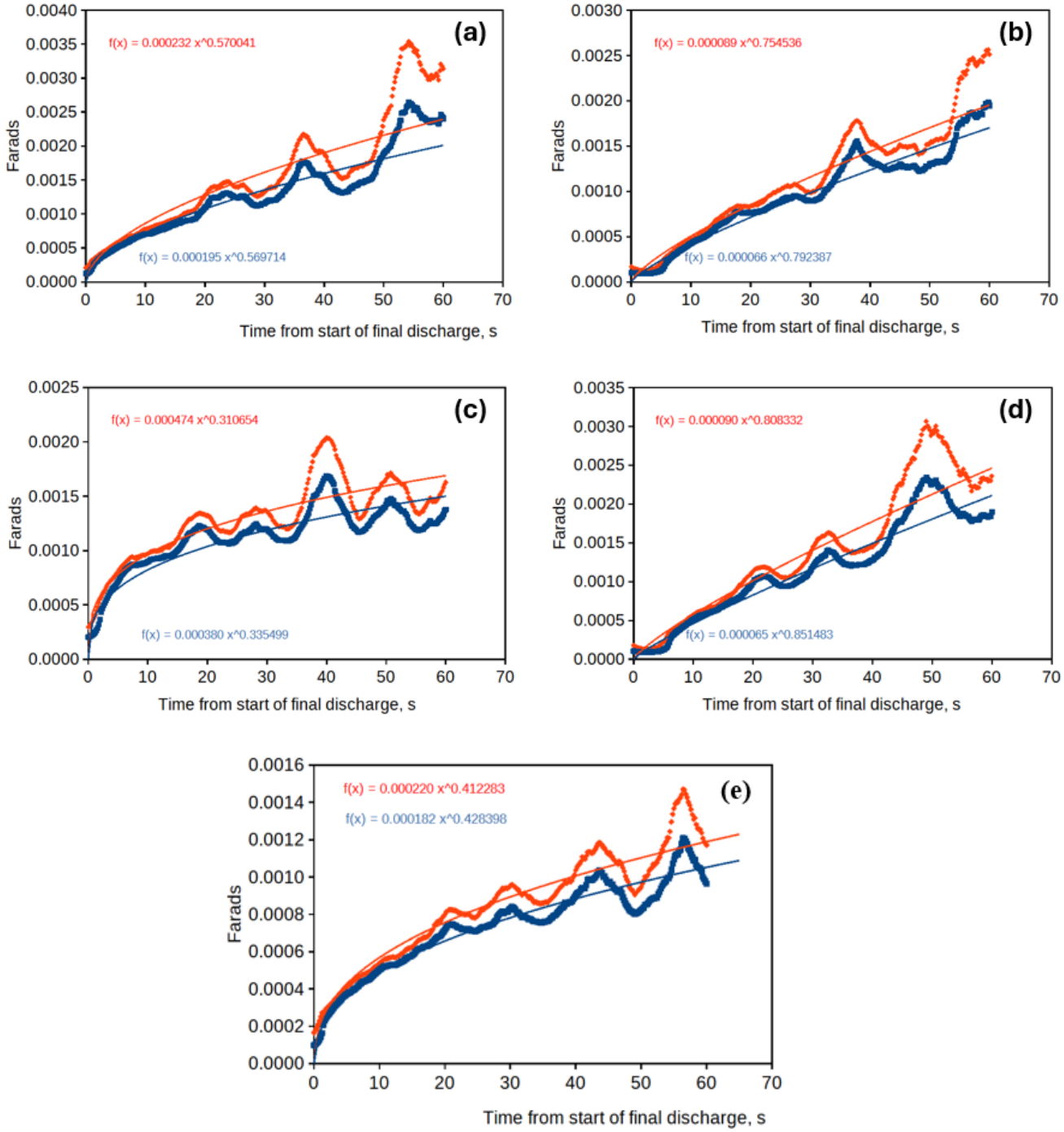

Figure 7. 10 Estimated capacitance (in Farads) as a function of time for bulk Ag sponge electrodes, (a) T1 sample heat-treated at 500 ℃, (b) T2 sample heat-treated at 450 ℃, (c) T3 sample heat-treated at 400 ℃, (d) T4 sample heat at 350 ℃, and (e) as-cast alloy+ not dealloyed. The high estimated capacitance in red, and the low estimated capacitance in blue

The graphs show that the capacitance of the bulk Ag sponge electrodes increases over time and/or decrease in cell voltage. This indicates that there is either some diffusion of ions out of deep channel OR that there is a redox process that produces energy at the lower voltages. The possibility of redox activity that occurs at the electrode surface after multiple and

reversible charge/ discharge cycles leading to an increase in the charge storage capability through Faradaic reactions is the most likely (Ansari et al., 2022). Moreover, the graph demonstrates similar oscillations in every case, which may be attributed to the same dynamic processes in each electrode. It may be due to successive redox reactions occurring on the surface or maybe to different ionic species successively coming off the sponge surface.

A 10 s running filter was applied to the data to make the fluctuating data smoother and reduce the noise to make the trend more visible, followed by applying the linear fitting to estimate the capacitance. The high estimated capacitance (indicated in red) and the low estimated capacitance (shown in blue) might indicate slight differences in the capacitance evolves raging between190 to 385 as Table 7.6 demonstrates. Compared to the as-cast bulk alloy capacitance, bulk Ag sponges exhibited high estimated capacitance 2 times larger for T1, 1.6 times larger for T2, 1.4 times larger for T4, 2.1 times larger for T4.

Table 7. 6 high and low estimated capacitances of bulk Ag sponges heat-treated at different temperature before dealloying

Sample	T1-dealloy	T2- dealloy	T3- dealloy	T4- dealloy	As-cast
High estimated capacitance (µF)	2394	1955	1691	2464	1190
Low estimated capacitance (µF)	2009	1693	1501	2123	1152
Difference (µF)	385	262	190	341	38

The above results show that the highest capacitance values were recorded for the Ag sponge with the lowest and highest pore sizes, which means that the nanoporous structure had no impact on the capacitor performance.

7.3.6 Growth Inhibition of E. coli by Bulk Ag Sponges prepared from treated alloys

The growth of *E. coli* bacteria in the presence of Ag nanosponges, Ag and Al were investigated and evaluated by measuring the OD at 600 nm during their interaction. The growth curve results indicated that the optical density, which reflects the bacterial cell density, increased with increasing the incubation times, as illustrated in Figure 7.11. However, a smaller increase in the measured OD was observed after 6 h of exposure of the *E. coli* culture to nanosponges. This reduced growth was more marked when the culture was exposed to nanosponges prepared from the heat-treated alloy at higher temperatures 450° and 500° C. Smooth Ag and Al specimens produced no noticeable inhibition on bacterial growth.

Statistical analysis was performed using the ANOVA statistical method to compare the OD values of the different replicates by calculating F and p-values. The F-value can be found by calculating the variance ratio between the means of the replicates to the variance within the replicates, while the p-value determines whether the differences in OD values of these different

replicates are statistically significant or not, P>0.05 indicates good consistency and reliability in the measurements of OD between treatments and controls (Knapp, 2017; van Emden, 2012). The results showed that the F-values was 0.179 and P-value was 0.98, which reflected that the OD measurements are consistent across different replicates of the same treatment.

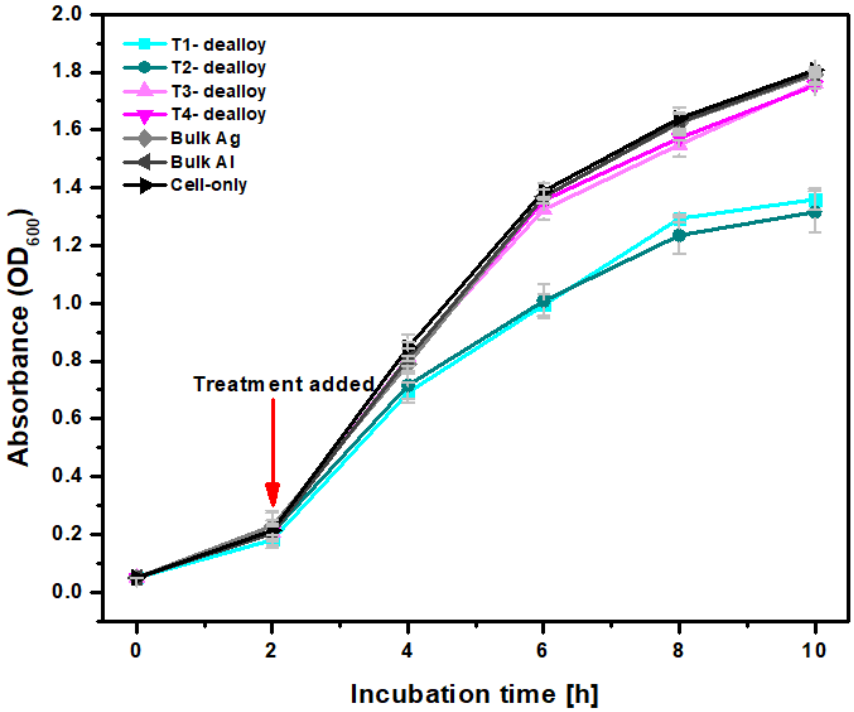

Figure 7. 11 Absorbance measurements of E. coli DH5α at 600 nm after treatment with Ag nanosponges prepared by heat-treating the Al_xAg_{100-X} at different temperatures ranging from 350 to 500 ℃, bulk Ag and bulk Al. The area shaded in yellow indicates the lag phase, while the area shaded with purple refers to the exponential phase.

The growth inhibition was determined on the basis of the measured values of OD obtained for the *E. coli* suspension treated with Ag sponges, bulk Ag and bulk Al over a 6-h test period. The inhibition was calculated according to Eq. 7.1.

$$I = \frac{control\ (OD_{8\,h}) - treated\ (OD_{8h})}{control\ (OD_{8\,h}) - control\ (OD_{0h})} \times 100 \ldots\ldots\ldots\ldots\ldots\ldots \text{(7.1) (Doskocz et al., 2017)}$$

Since $control\ (OD_{8\,h})$ and $control\ (OD_{0\,h})$ are the optical density of the bacterial dilution at 8 h and 0 h of incubation, respectively, $treated\ (OD_{8\,h})$ is the optical density of the bacterial suspension after treating with Ag sponges for 8 h.

The growth of E. coli was inhibited by 26% following treatment with Ag sponges prepared by dealloying T1, which was quenched at 500°C, as Figure 7.12 demonstrated. This inhibition increased slightly to 28% when the suspension was treated with Ag sponges prepared by dealloying T2, quenched at 450°C. In contrast, significantly lower inhibition rates of 2.6% and 3% were observed for treatments with Ag sponges produced by dealloying T4 (quenched at 350°C) and T3 (quenched at 400°C), respectively. For comparison, bulk Ag and bulk Al exhibited minimal inhibition, with percentages of 0.9% and 0.5%, respectively.

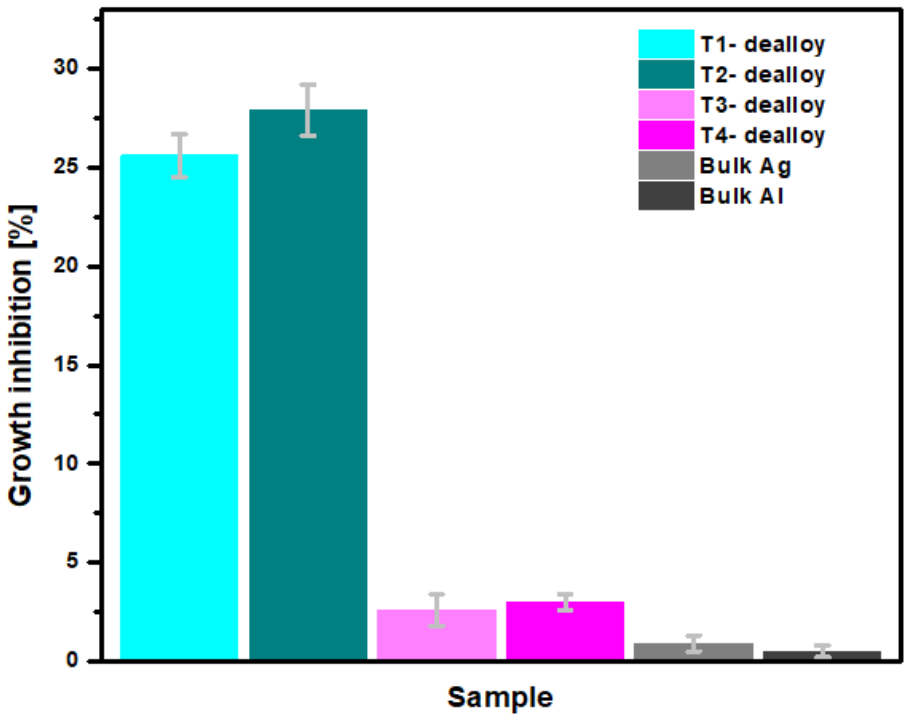

Figure 7. 12 Effect of treatment with ag sponges, bulk Ag and bulk Al on the growth of E. coli

7.3.7 Growth rate of *E. coli*

According to OD vs. time curves presented in Figure 7.11, two phases of bacterial growth were noticed namely, lag phase and exponential phase. The lag phase refers to the initial period in the bacterial population life, in this phase the bacteria begin to adapt to their new surroundings before commencing exponential growth, typically covering the first two hours of incubation. This is followed by the exponential phase, where rapid cell division is observed (Wessner et al., 2020).

The bacterial growth rate (α) during the exponential phase, which is describes the change in the number or mass of bacterial cells per unit time (Srivastava, 2013), was estimated using the relationship:

$$\ln \frac{N_t}{N_0} = \alpha(t - t_0) \quad \text{..... (7.2) (Hall et al., 2014)}$$

Where N_t is the number of bacteria cells at the final time t, and N_o is the number of bacteria cells at the initial time t_o. It is confirmed that the OD of a bacterial suspension is directly proportional to the number of bacteria cells in the suspension (Dr. S. Sivakalai, 2023). Consequently, to estimate the growth rate, we use the slope of the natural logarithm of OD (Ln (OD)) plotted against time t as Figure 7.13 (a- c) shows. *E. coli* doubling time was calculated from Eq.7.3.

$$Doubling\ time = \frac{0.693}{\alpha} \quad \text{..... (7.3) (Ryser \& Marth, 2007)}$$

The growth rate of *E. coli* treated with bulk Ag sponges is influenced by the pore and ligament sizes, as well as the concentration of residual Al. It was observed that an increase in pore and ligament sizes, coupled with a decrease in residual Al concentration, resulted in a reduced growth rate of *E. coli*. As illustrated in Figure 7.13 (a-c) and detailed in Table 7.7, the Ag sponges prepared by dealloying T1 quenched at 500°C (characterized by the largest pore and ligament sizes and the lowest residual Al concentration) exhibited the lowest *E. coli* growth rate at 0.189 h^{-1} ± 1.173, leading to a longer doubling time of 3.67 hours. When the pore and ligament sizes decreased from 50.8±19.6 and 58.5±17.9 nm to 49.4±20.9 and 45.9±12.9 nm, respectively, the growth rate decreased slightly to 0.183 h^{-1} ± 1.147, reducing the doubling time to 3.79 hours. Notably, the bacterial growth rate increased by 82.24% and 78.91% for Ag sponges prepared by dealloying T3 quenched at 400°C and T4 quenched at 350°C, respectively, compared to T2 quenched at 450°C. This increase in growth rate is likely attributed to the higher concentrations of residual Al, which were 20 at.% and 14 at.% for T3 and T4, respectively.

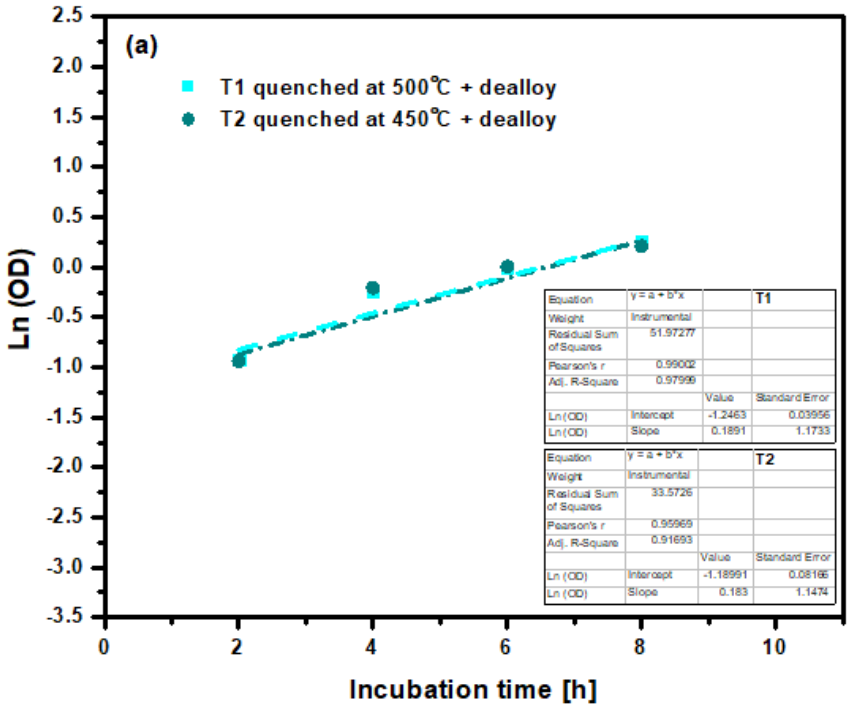

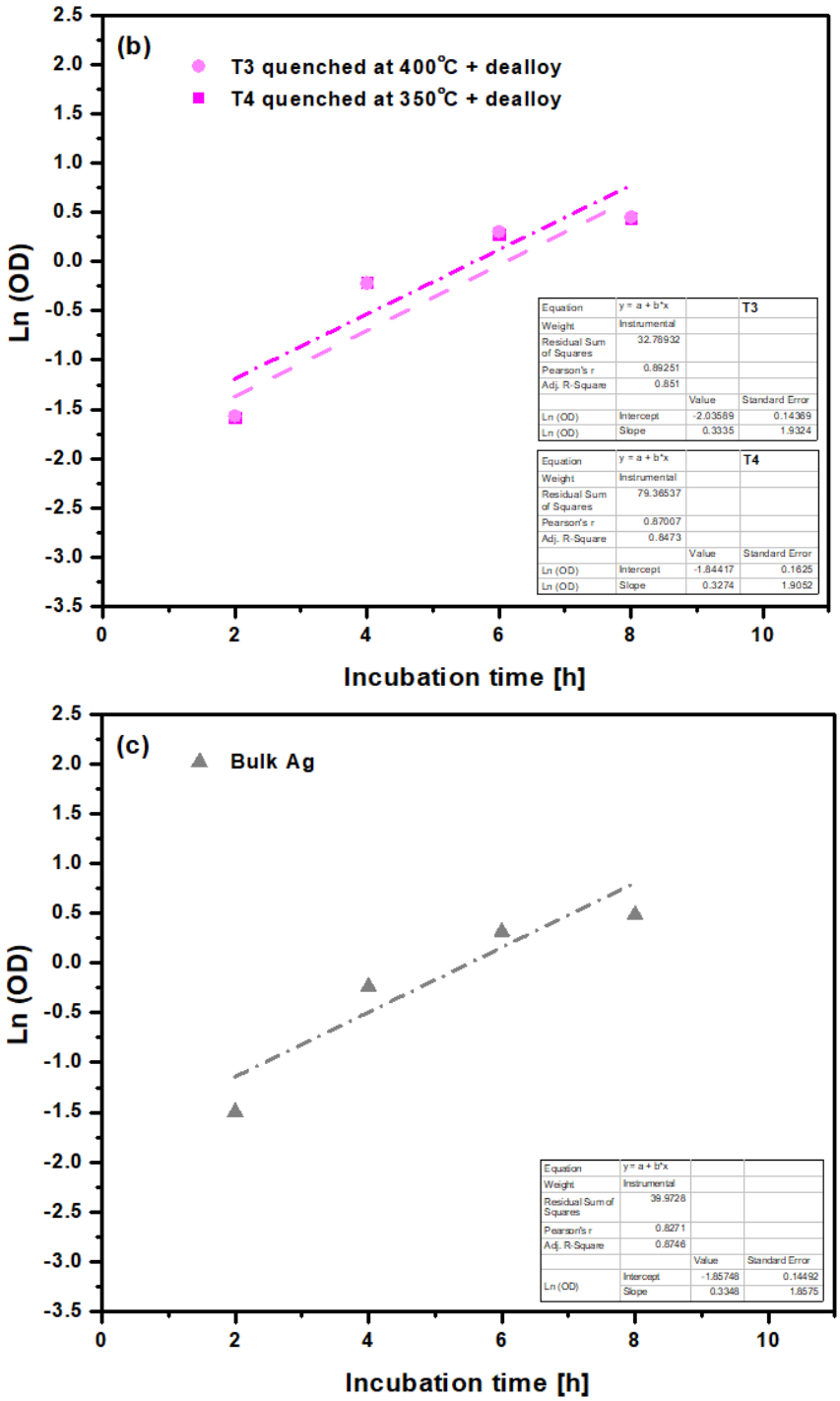

Figure 7. 13 The natural logarithm of optical density (ln OD) versus time (h) for (a) T1 quenched at 500 ℃ and T2 quenched at 450 ℃, (b) T3 quenched at 400 ℃ and T4 quenched at 350 ℃ and (c) bulk Ag. The slope of the linear region of the curve between 2 to 6 h is used to estimate the growth rate of the E. coli culture.

Table 7. 7 calculated values of the growth rate and doubling time of E. coli without treating and after treating with the Ag sponges, bulk Ag and bulk Al. The doubling time was calculated based on the growth rates observed in Figure 7.13.

Sample	T1-dealloy	T2- dealloy	T3- dealloy	T4- dealloy	Bulk Ag	Bulk Al	Cells-only
Growth rate [h^{-1}]	0.189	0.183	0.334	0.327	0.335	0.342	0.336
Doubling time [h]	3.67	3.79	2.07	2.12	2.07	2.03	2.06

7.3.8 Cell viability

The antibacterial activities of the Ag sponges against *E. coli* DH5α were further inspected using the live/dead two-color staining fluorescence method. This process relies on probing the permeability of the bacterial membrane, which serves as a marker for the viability of bacterial cells. Images in Figure 7.14 show the representative fluorescence microscopic images of *E. coli* DH5α treated with Ag sponges, bulk Ag, and bulk Al. All the presented images display rod-shaped cell bodies, with a width between 0.7 and 1.8 µm and the length between 1 and 3.2 µm. Moreover, elongated rod-shaped *E. coli* DH5α cells with a length between 5 and 30 µm were observed in all fluorescence images. The cell viability can be estimated using Eq.7.4 (Měřička et al., 2021):

$$Viability\ (\%) = \frac{sum\ of\ live\ cells}{sum\ of\ all\ (live+dead)\ cells} \times 100 \ldots\ldots\ldots\ldots\ldots\ldots (7.4)$$

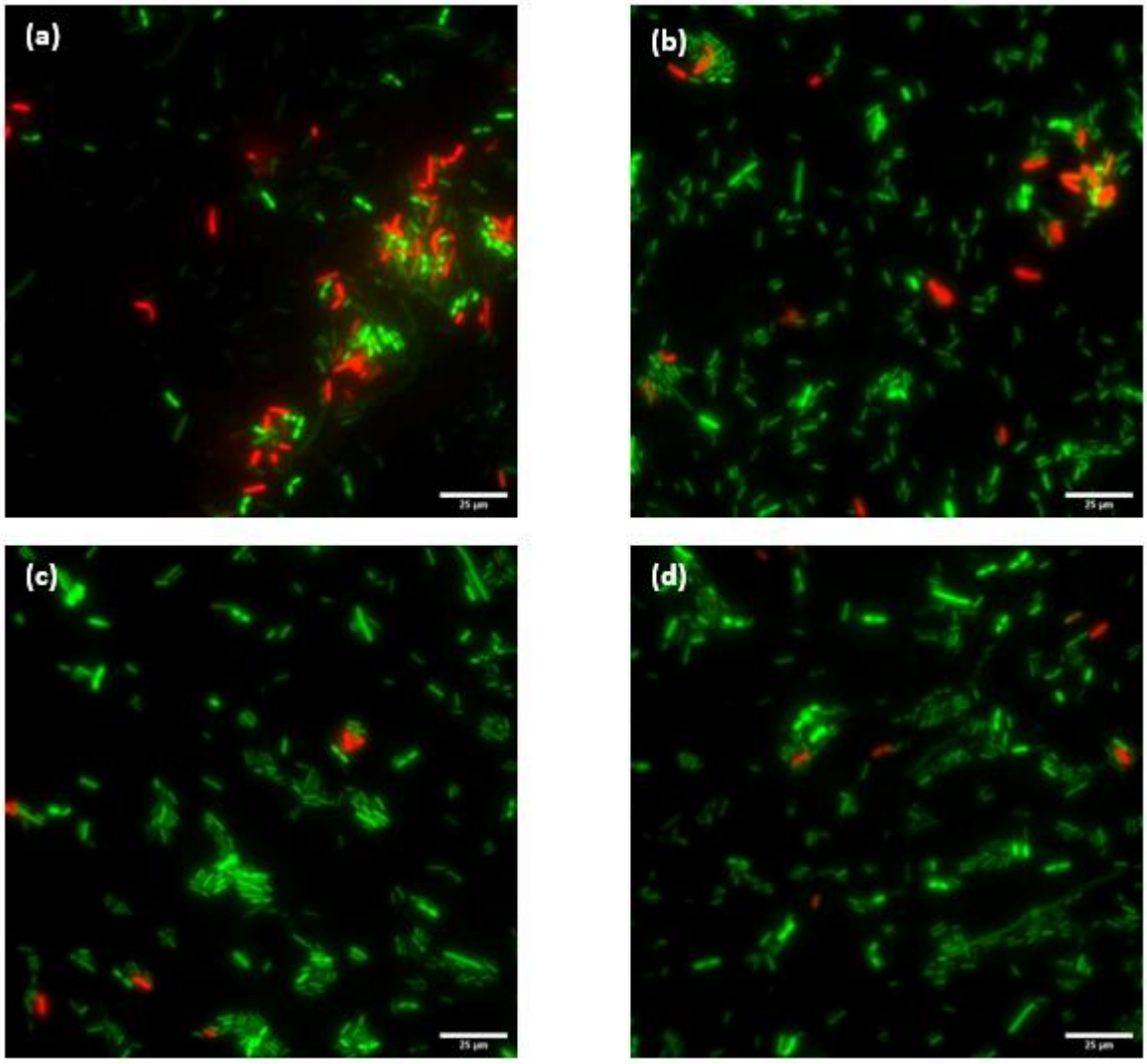

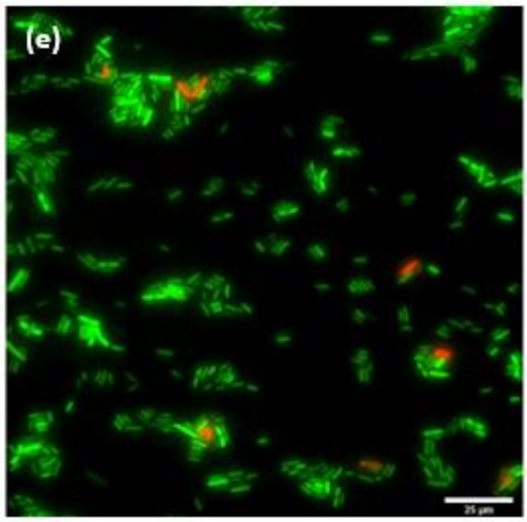

Figure 7. 14 Fluorescence microscopic images of E. coli DH5α strain after treating for 6 h with (a) Ag sponges prepared by dealloying the heat-treated alloy at 450℃ (T2), (b) Ag sponges prepared by dealloying the heat-treated alloy at 350℃ (T4), (c) bulk Ag, (d) bulk Al, and (e) without any treatment. Viable E. coli cells appear as green rods while non-viable E. coli cells shown as red rods.

The results in Figure 7.15 indicate that the calculated cell viability of *E. coli* was high, reaching 96.7±4.0% without treatment. After treatment with bulk Ag and Al, cell viability remained similarly high at 96.1±4.3% and 95.9±5.7%, respectively. A slight decrease in viability was observed, with 93.1±6.0% after treating *E. coli* with Ag sponges produced from the heat-treated alloy at 350°C (T4). However, a more significant reduction in cell viability, to 72.0±6.3%, was recorded after treatment for 6 h with Ag sponges produced by dealloying the heat-treated alloy at 450°C (T2).

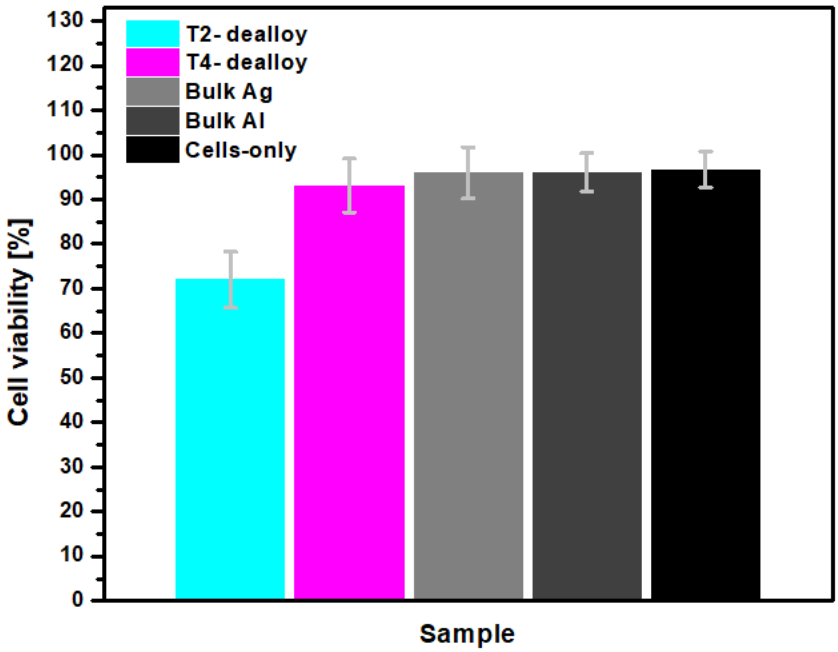

Figure 7. 15 Cell viability of E. coli DH5α after treating for 6 h with Ag sponges prepared by dealloying the heat-treated alloy at 450℃, Ag sponges prepared by dealloying the heat-treated alloy at 350℃, bulk Ag, and bulk Al. The presented graph demonstrates the mean values ±standard deviations for live cells.

The antibacterial properties of Ag sponges are closely linked to their morphologies. The produced Ag sponges feature small pore sizes ranging between 35 and 51 nm, significantly smaller than the width of *E. coli* DH5α, which is approximately 0.5 μm (Huang et al., 2018). This indicates that bacteria cannot penetrate the pores of the Ag sponges, suggesting that their antibacterial activity is primarily due to surface interactions rather than internal absorption of bacteria. These interactions are facilitated by the presence of ligaments ranging from 30 to 59 nm, which provide a substantial surface area for bacterial contact and for releasing Ag^{+}.

7.3.9 Growth Inhibition of E. coli by Bulk Ag Sponges prepared from untreated alloys

The impact of microstructure of bulk Ag sponges and residual Al concentration on bacterial growth was further explored. As shown in Figure 7.16, an increase in Al concentration notably affects the antibacterial action of the sponges. Specifically, Figure 7.16 illustrates that measured OD values increase with higher Al concentrations. A direct correlation between the residual aluminum (Al) content in the silver (Ag) sponges and the growth rate of *E. coli* DH5α was observed. The highest bacterial growth rate, 0.334 h^{-1}, was recorded for the Ag sponge dealloyed for 7 h. This rate decreased slightly with prolonged dealloying time, reaching 0.332 h^{-1} at 16 h. After 35 h of dealloying, the growth rate further declined to 0.328 h^{-1}. These values closely align with the growth rates observed for bulk Ag, bulk Al, and untreated cells. Higher concentrations of residual Al may limit the available surface area for bacterial interaction by covering or blocking some active silver sites. This can reduce the effectiveness of the antibacterial properties of the sponges by diminishing the surface interactions crucial for their function (Qiu et al., 2011b).

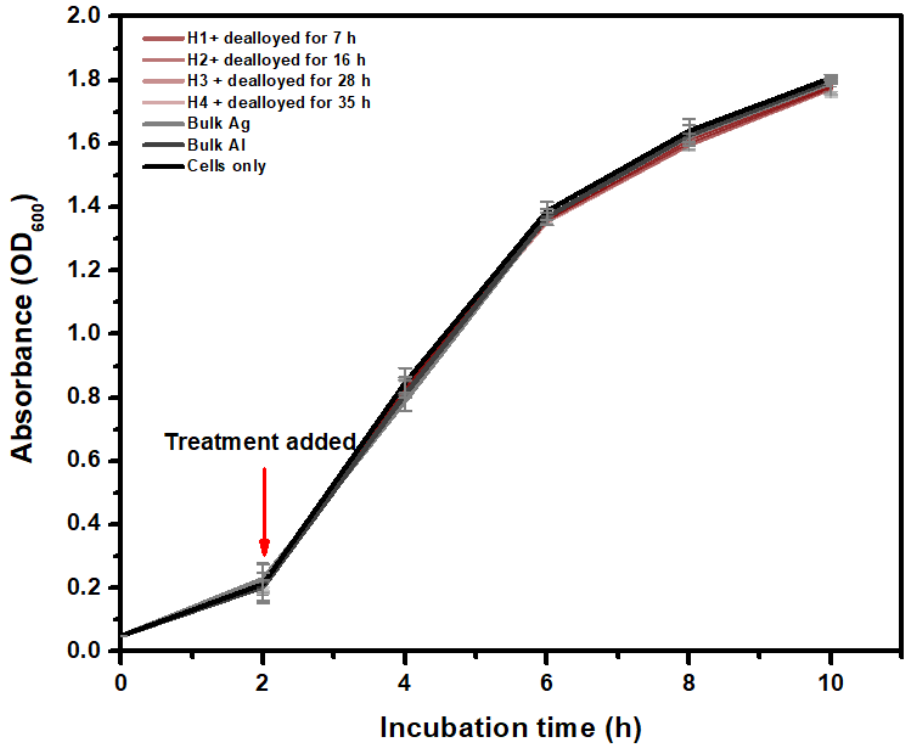

Figure 7. 16 The measured values of the absorbance versus incubation time, the area shaded in yellow indicates the lag phase, while the area shaded with purple refers to the exponential phase.

The findings above indicate that homogenization and heat treatment enhance the microstructure of Ag sponges, thereby improving their antibacterial performance. Higher quenching temperatures (500°C and 450°C) result in stronger inhibition (26-28%) due to reduced residual Al and increased Ag surface exposure. In contrast, the high residual Al content in Ag sponges prepared from untreated alloys correlates with higher bacterial growth rates, likely due to the lack of a well-formed nanoporous structure.

A proposed antibacterial mechanism for Ag sponges involves the sustained release of Ag^+ from the ligament surface into the culture media. These silver ions then attach to the negatively charged bacterial cell walls (Wang et al., 2023). The unique three-dimensional self-supported structure of the Ag sponges helps to avoid the self-aggregation often seen with traditional antibacterial nanoparticles (Hu et al., 2012; Zheng et al., 2019; Zhu et al., 2014), allowing for a continuous and controlled release of silver ions. This enhances their interaction with bacterial cells and improves antibacterial efficacy. For example, Ag sponges prepared by dealloying $Cu_{57}Ag_{40}La_3$ (at.%) alloy ribbons in 0.25 mol/L HNO_3 at room temperature for 90 hours, with ligament sizes of 119 ± 12 nm and pore sizes of 78 ± 9 nm, exhibited high antibacterial performance against *E. coli, Staphylococcus aureus*, and methicillin-resistant *Staphylococcus aureus* (MRSA), with antibacterial rates exceeding 95% (Wang et al., 2023). On the contrary, Ag sponges prepared by dealloying $Mg_{65}(Ag_xCu_{1-x})_{25}Y_{10}$ (x = 0, 0.5, 0.75, and 1.0, at%) alloys in 0.04 M H_2SO_4 for 50 minutes, with a specific surface area of 7.06 m^2/g and average ligament size of 31 nm, demonstrated lower antibacterial activity compared to Ag-Cu alloy sponges due to lower concentrations of released Ag ions (0.1 mg/L), highlighting the importance of ligament size and ion release rates in antibacterial performance. The superior chemical stability of Ag further enhances its potential for sustained antibacterial action (Wang et al., 2019). In another study, NPS/Fe_3O_4 nanocomposites with a specific surface area of 5 m^2/g, prepared by chemical dealloying of rapidly solidified Al–Ag–Fe precursors in 20 wt.% NaOH at 90±5°C, with ligament/pore sizes ranging from 20 to 50 nm, displayed excellent antibacterial properties against *E. coli* K12. The antibacterial efficacy was evaluated by counting *E. coli* colonies on LB agar plates incubated for 18 hours at 30°C (Zhang et al., 2013). Controlling experimental conditions, such as maintaining a relative humidity of about 60%, is crucial for investigating the antibacterial actions of metallic nanoporous structures. For instance, nanoporous gold (*NPG*) demonstrates excellent antibacterial properties against

Escherichia coli and *Staphylococcus epidermidis* under controlled humidity conditions (Hakamada et al., 2017).

In conclusion, the heat-treatment of the bulk $Ag_{100-x}Al_x$ alloy prior to the dealloying process successfully produced *np-S* with different nanostructure sizes, as evidenced by increased pore and ligament sizes with increasing the temperatures from 350 to 500°C. However, despite these altering in the nanostructure, it appears to be no clear correlation between the nanoporous and ligament sizes and the capacitance performance of these bulk Ag sponges. However, sponges with large pores and ligament sizes demonstrated a good antibacterial effect.

Conclusion and future work

Nanoporous materials have size-dependent physical and chemical properties. This means the control of the morphology of nanoporous sponges can tune the materials for different applications. The nanoporous morphology can be adjusted by changing the composition of the precursor alloy and the dealloying conditions, such as time, temperature, and electrolyte type and concentration. This work focused on fabricating *np-S* nanostructures with different morphologies by tuning the composition of primary alloys using different routes.

A general method of controlling the morphology of *np-S* films was demonstrated, by varying the composition of the precursor alloy before dealloying in NaOH. This method was applied to the formation of *np-S* thin films by varying the current in a single gun during magnetron co-sputtering of the precursor alloy. Homogenized Ag-Al alloy thin films were prepared by rotating the sample holder during deposition while a gradient composition was achieved by keeping the sample holder static.

Np-S thin films with different ligament and pore sizes were produced and it was shown that these different morphologies resulted in different physical properties. It was found that decreasing the pore and ligament size in nanoporous structures with increasing Al content led to increased electron scattering evidenced by a reduction in electrical conductivity. Similarly, decreasing pores and ligaments size led to decreased light reflectance by nanoporous material due to increasing light scattering within the nanofeatures. The *np-S* films behaved as an optical metamaterial in the visible region with a large real dielectric function at short wavelengths, lower energy loss as indicated by the imaginary part of the dielectric function, anomalous refractive index, and low light absorption, as the extinction coefficient demonstrated. Material with a high real dielectric function and low absorption can be used in applications such as second-harmonic generation, a possibility which could be cosidered in future work. *Np-S* exhibited non-metallic behavior with increasing Al content from 59 and 81 at.%, at wavelengths ranging from 350 to 1610 nm, respectively. The *np-S* produced by dealloying the $Ag_{100-x}Al_x$ alloy with Al content between 60 and 81 at.% demonstrated lower optical constants due to increased pore density. Due to the electromagnetic and chemical effects, *G-np-S* (gradient *np-S*) showed a superior intense Raman signal at the Raman band of 1694 cm^{-1}. The SERS activities of the *G-np-S* thin film are pore size-dependent; *np-S* with the small pore diameter exhibited the strongest *SERS* enhancement and highest enhancement factor of 3.93×10^7.

The antibacterial performance of these *np-S* thin films was examined against *Pseudomonas aeruginosa* (*P. aeruginosa*) strain PAO1 and *Escherichia coli* (*E. coli*) strain DH5α. A dose-response assay in a 96-well microtiter plate and a growth inhibition assay protocol were used in this study. The results demonstrated that *np-S* thin films with varying pore size, ligament size and doses were ineffective in inhibiting *P. aeruginosa* growth due to the formation of strong biofilm, which acts as a barrier to prevent the Ag^{+} from interacting with the bacteria. On the other hand, the measured OD values using a spectrophotometer indicated a slight reduction in the density of *E. coli* DH5α by np-S thin film with the small pore and ligament size (11.1 and 13.1 nm, respectively), which indicate a small antibacterial effect of np-S on this strain. These findings open the door for future studies, which involve studying the antibacterial effect of nanoporous Ag using different protocols, such as the spread plate method. The bacterial colony number should be counted and analyzed for colony-forming unit (CFU). The light exposure should be controlled as Ag particles are known catalyse organic reactions under illumination.

Morphology of *np-S* was also controlled by heat-treatment of the bulk $Ag_{100-x}Al_x$ alloy prior to dealloying process, as evidenced by increased pore and ligament sizes corresponding to increasing annealing temperatures from 350 to 500°C. However, despite these altering in the nanostructure, it appears to be no clear correlation between the nanoporous and ligament sizes and the electrochemical capacitance performance of these bulk Ag sponges. However, a more significant reduction in cell viability, to 72.0±6.3%, was recorded after treatment for 6 h with Ag sponges produced by dealloying the heat-treated alloy at 450°C compared to untreated bacterial suspension which demonstrated high cell viability 96.7±4.0%. This suggests that factors other than pore and ligament sizes may have a more critical impact in determining these properties, such as the concentration of residual Al in the alloys after dealloying.

This work has highlighted the versatility of *np-S* and, in particular, how its microstructure can be controlled by producing it by dealloying $Ag_{100-x}Al_x$ precursors.

In general, nanoporous structures with different morphology and feature sizes were produced by adjusting the composition of the alloy using different routes. The work serves as a platform for the continued development of this fascinating nanomaterial.

References

Abid, N., Khan, A. M., Shujait, S., Chaudhary, K., Ikram, M., Imran, M., Haider, J., Khan, M., Khan, Q., & Maqbool, M. (2022). Synthesis of nanomaterials using various top-down and bottom-up approaches, influencing factors, advantages, and disadvantages: A review. *Advances in Colloid and Interface Science*, *300*, 102597.

Afzali, P., Yousefpour, M., & Borhani, E. (2016). Evaluation of the effect of ageing heat treatment on corrosion resistance of Al–Ag alloy using electrochemical methods. *Journal of materials research*, *31*(16), 2457-2464.

Ahmad, T., Nazim, A., Farooq, U., Khan, H., Jain, S. K., Ubaidullah, M., & Ahmed, J. (2020). Biosynthesis, characterization and photo-catalytic degradation of methylene blue using silver nanoparticles. *Materials Today: Proceedings*, *29*, 1039-1043.

Aizpurua, J., & Bryant, G. (2011). Coupling in Metallic Nanoparticles: Approaches to Optical Nanoantennas. *Handbook of Nanophysics*, *3*, 24-01. https://doi.org/10.1201/9781420075458-28

Ansari, M. Z., Ansari, S. A., & Kim, S.-H. (2022). Fundamentals and recent progress of Sn-based electrode materials for supercapacitors: A comprehensive review. *Journal of energy storage*, *53*, 105187. https://doi.org/10.1016/j.est.2022.105187

Ariga, K., Vinu, A., Yamauchi, Y., Ji, Q., & Hill, J. P. (2012). Nanoarchitectonics for mesoporous materials. *Bulletin of the Chemical Society of Japan*, *85*(1), 1-32.

Arnold, M. D., & Blaber, M. G. (2009). Optical performance and metallic absorption in nanoplasmonic systems. *Optics express*, *17*(5), 3835-3847.

Aromaa, J., Kekkonen, M., Mousapour, M., Jokilaakso, A., & Lundström, M. (2021). The Oxidation of Copper in Air at Temperatures up to 100 °C. *Corrosion and materials degradation*, *2*(4), 625-640. https://doi.org/10.3390/cmd2040033

Asane, J., Qi, Z., Biener, M., Liberman, V., & Noginov, M. (2018). Optical properties of nanoporous gold foams. *AIP Advances*, *8*(9), 095302. https://doi.org/https://doi.org/10.1063/1.5030128

AshaRani, P. V., Low Kah Mun, G., Hande, M. P., & Valiyaveettil, S. (2009). Cytotoxicity and Genotoxicity of Silver Nanoparticles in Human Cells. *ACS nano*, *3*(2), 279-290. https://doi.org/10.1021/nn800596w

Asli, B., Abdelkrim, S., Zahraoui, M., Mokhtar, A., Hachemaoui, M., Bennabi, F., Ahmed, A. B., Sardi, A., & Boukoussa, B. (2022). Catalytic reduction and antibacterial activity of MCM-41 modified by silver nanoparticles. *Silicon*, *14*(18), 12587-12598. https://doi.org/https://doi.org/10.1007/s12633-022-01963-6

Asmatulu, R., & Khan, W. S. (2018). *Synthesis and applications of electrospun nanofibers*. Elsevier. https://doi.org/https://doi.org/10.1016/C2017-0-00516-5

Ates, M. (2016). Graphene and its nanocomposites used as an active materials for supercapacitors. *Journal of solid state electrochemistry*, *20*(6), 1509-1526. https://doi.org/10.1007/s10008-016-3189-4

Azarov, A., Hallén, A., & Radamson, H. H. (2023). Electrical Characterization of Semiconductors: I–V, C–V and Hall Measurements. In *Analytical Methods and Instruments for Micro-and Nanomaterials* (pp. 197-240). Springer. https://doi.org/https://doi.org/10.1007/978-3-031-26434-4_7

Azimi, S., & Docoslis, A. (2022). Recent advances in the use of surface-enhanced Raman scattering for illicit drug detection. *Sensors*, *22*(10), 3877. https://doi.org/https://doi.org/10.3390/s22103877

Baboian, R. (2005). *Corrosion Tests and Standards: Application and Interpretation*. ASTM International. https://books.google.com.au/books?id=8C7pXhnqje4C

Baia, M., Baia, L., & Astilean, S. (2005). Gold nanostructured films deposited on polystyrene colloidal crystal templates for surface-enhanced Raman spectroscopy. *Chemical Physics Letters*, *404*(1-3), 3-8.

Baker, C., Pradhan, A., Pakstis, L., Pochan, D. J., & Shah, S. I. (2005). Synthesis and antibacterial properties of silver nanoparticles. *Journal of nanoscience and nanotechnology*, *5*(2), 244-249. https://doi.org/https://doi.org/10.1166/jnn.2005.034

Balmes, O., Bovin, J.-O., Malm, J.-O., & Xu, H. (2005). Homogeneous surface-enhanced Raman scattering observed from self-assembled gold nanoparticle films deposited from the liquid–liquid interface. *Vibrational spectroscopy*, *37*(2), 189-193.

Bao, M., Wang, J., Feng, X., Luo, J., & Sun, J. (2024). *Nanometal Catalysis in Organic Synthesis*. Springer Nature Singapore. https://books.google.com.au/books?id=FycVEQAAQBAJ

Barbillon, G., Faure, A. C., El Kork, N., Moretti, P., Roux, S., Tillement, O., Ou, M., Descamps, A., Perriat, P., & Vial, A. (2007). How nanoparticles encapsulating fluorophores allow a double detection of biomolecules by localized surface plasmon resonance and luminescence. *Nanotechnology*, *19*(3), 035705.

Barranco, A., Borras, A., Gonzalez-Elipe, A. R., & Palmero, A. (2016). Perspectives on oblique angle deposition of thin films: From fundamentals to devices. *Progress in materials science*, *76*, 59-153. https://doi.org/10.1016/j.pmatsci.2015.06.003

Barron, P. J., Carruthers, A. W., Dawson, H., Rigby, M. T., Haigh, S., Jones, N. G., & Pickering, E. J. (2022). Phase stability of V-based multi-principal element alloys. *Materials Science and Technology*, *38*(13), 926-939.

Barsuk, D., Zadick, A., Chatenet, M., Georgarakis, K., Panagiotopoulos, N. T., Champion, Y., & Jorge Jr, A. M. (2016). Nanoporous silver for electrocatalysis application in alkaline fuel cells. *Materials & Design*, *111*, 528-536. https://doi.org/https://doi.org/10.1016/j.matdes.2016.09.037

Beg, S., Rahman, M., Jain, A., Saini, S., Midoux, P., Pichon, C., Ahmad, F. J., & Akhter, S. (2017). Nanoporous metal organic frameworks as hybrid polymer–metal composites for drug delivery and biomedical applications. *Drug Discovery Today*, *22*(4), 625-637.

Bekana, D., Liu, R., Li, S., & Liu, J.-F. (2019). Fabrication of nanoporous silver film by dealloying Ag/α-Fe2O3 nanocomposite for surface-enhanced Raman spectroscopy. *Sensors and Actuators B: Chemical*, *286*, 94-100. https://doi.org/https://doi.org/10.1016/j.snb.2019.01.114

Bharti, C., Nagaich, U., Pal, A., & Gulati, N. (2015). Mesoporous silica nanoparticles in target drug delivery system: A review. *International Journal of Pharmaceutical Investigation*, *5*(3), 124-133. https://doi.org/10.4103/2230-973X.160844

Białous, A., Gazda, M., Grochowska, K., Atanasov, P., Dikovska, A., Nedyalkov, N., Reszczyńska, J., Zaleska-Medynska, A., & Śliwiński, G. (2016). Nanoporous TiO2 electrode grown by laser ablation of titanium in air at atmospheric pressure and room temperature. *Thin solid films*, *601*, 41-44.

Biener, J., Nyce, G. W., Hodge, A. M., Biener, M. M., Hamza, A. V., & Maier, S. A. (2008). Nanoporous plasmonic metamaterials. *Advanced materials*, *20*(6), 1211-1217.

Biener, J., Wittstock, A., Zepeda-Ruiz, L., Biener, M., Zielasek, V., Kramer, D., Viswanath, R., Weissmüller, J., Bäumer, M., & Hamza, A. (2009). Surface-chemistry-driven actuation in nanoporous gold. *Nature Materials*, *8*(1), 47-51.

Biswas, A., Bayer, I. S., Biris, A. S., Wang, T., Dervishi, E., & Faupel, F. (2012). Advances in top–down and bottom–up surface nanofabrication: Techniques, applications & future prospects. *Advances in Colloid and Interface Science*, *170*(1-2), 2-27.

Boukerche, I., Djerad, S., Benmansour, L., Tifouti, L., & Saleh, K. (2014). Degradability of aluminum in acidic and alkaline solutions. *Corrosion science*, *78*, 343-352. https://doi.org/10.1016/j.corsci.2013.10.019

Braun, M. M., & Pilon, L. (2006). Effective optical properties of non-absorbing nanoporous thin films. *Thin solid films*, *496*(2), 505-514. https://doi.org/10.1016/j.tsf.2005.08.173

Brussel, B. v., & Hosson, J. T. M. D. (1994). Glancing angle x-ray diffraction: A different approach. *Applied Physics Letters*, *64*(12), 1585-1587.

Bryche, J.-F., Tsigara, A., Bélier, B., de La Chapelle, M. L., Canva, M., Bartenlian, B., & Barbillon, G. (2016). Surface enhanced Raman scattering improvement of gold triangular nanoprisms by a gold reflective underlayer for chemical sensing. *Sensors and Actuators B: Chemical*, *228*, 31-35.

Bunaciu, A. A., UdriŞTioiu, E. G., & Aboul-Enein, H. Y. (2015). X-ray diffraction: instrumentation and applications. *Critical reviews in analytical chemistry*, *45*(4), 289-299.

Bunshah, R. F. (1982). Deposition technologies for films and coatings: developments and applications. *(No Title)*.

Burdușel, A.-C., Gherasim, O., Grumezescu, A. M., Mogoantă, L., Ficai, A., & Andronescu, E. (2018). Biomedical applications of silver nanoparticles: an up-to-date overview. *Nanomaterials*, *8*(9), 681.

Campbell, F. C. (2008). *Elements of Metallurgy and Engineering Alloys*. ASM International. https://books.google.com.au/books?id=6VdROgeQ5M8C

Cao, J., Liu, H.-L., Yang, J.-M., Li, Z.-Q., Yang, D.-R., Ji, L.-N., Wang, K., & Xia, X.-H. (2020). SERS detection of nucleobases in single silver plasmonic nanopores. *ACS sensors*, *5*(7), 2198-2204.

Capaccio, A., Sasso, A., & Rusciano, G. (2021). A simple and reliable approach for the fabrication of nanoporous silver patterns for surface-enhanced Raman spectroscopy applications. *Scientific Reports*, *11*(1), 22295. https://doi.org/https://doi.org/10.1038/s41598-021-01727-z

Cara, E., Mandrile, L., Sacco, A., Giovannozzi, A. M., Rossi, A. M., Celegato, F., De Leo, N., Hönicke, P., Kayser, Y., & Beckhoff, B. (2020). Towards a traceable enhancement factor in surface-enhanced Raman spectroscopy. *Journal of Materials Chemistry C*, *8*(46), 16513-16519. https://doi.org/https://doi.org/10.1039/D0TC04364H

Carbone, M., Donia, D. T., Sabbatella, G., & Antiochia, R. (2016). Silver nanoparticles in polymeric matrices for fresh food packaging. *Journal of King Saud University. Science*, *28*(4), 273-279. https://doi.org/10.1016/j.jksus.2016.05.004

Carreira, S. C. (2017). *Rapid Cell Magnetisation Using Cationised Magnetoferritin*. Springer International Publishing. https://books.google.com.au/books?id=qCopDwAAQBAJ

Carton, O., Ghaymouni, J., Lejeune, M., & Zeinert, A. (2013). Optical characterization of porous sputtered silver thin films. *Journal of Spectroscopy*, *2013*.

Carvill, J. (2014). *Mechanical Engineer's Data Handbook*. Butterworth-Heinemann. https://books.google.com.au/books?id=6-VdBgAAQBAJ

Chaloupka, K., Malam, Y., & Seifalian, A. M. (2010). Nanosilver as a new generation of nanoproduct in biomedical applications. *Trends in biotechnology (Regular ed.)*, *28*(11), 580-588. https://doi.org/10.1016/j.tibtech.2010.07.006

Chatterji, A. K. (2011). *Introduction to Environmental Biotechnology*. Prentice-Hall of India Pvt.Limited. https://books.google.com.au/books?id=075-IOj7ZlgC

Chaturvedi, S., Dave, P. N., & Shah, N. K. (2012). Applications of nano-catalyst in new era. *Journal of Saudi Chemical Society*, *16*(3), 307-325.

Chauvin, A., Txia Cha Heu, W., Tessier, P.-Y., & El Mel, A.-A. (2016). Impact of the morphology and composition on the dealloying process of co-sputtered silver-aluminum alloy thin films. *Physica Status Solidi. B: Basic Solid State Physics*, *253*(11), 2167-2174. https://doi.org/10.1002/pssb.201600604

Chen, H.-A., Long, J.-L., Lin, Y.-H., Weng, C.-J., & Lin, H.-N. (2011). Plasmonic properties of a nanoporous gold film investigated by far-field and near-field optical techniques. *Journal of Applied Physics*, *110*(5), 054302. https://doi.org/https://doi.org/10.1063/1.3631824

Chen, L., Lang, X., & Chen, M. (2013). Dealloyed nanoporous metals. *Nanoporous Materials: Synthesis and Applications*, 125-182.

Chen, L. Y., Yu, J. S., Fujita, T., & Chen, M. W. (2009). Nanoporous copper with tunable nanoporosity for SERS applications. *Advanced Functional Materials*, *19*(8), 1221-1226.

Chen, Q., & Sieradzki, K. (2013). Spontaneous evolution of bicontinuous nanostructures in dealloyed Li-based systems. *Nature materials*, *12*(12), 1102-1106.

Chen, Y. (2023). *Surface Plasmon Resonance Imaging: Basic Theory and Practical Methodology*. Springer Nature Singapore. https://books.google.com.au/books?id=CiTJEAAAQBAJ

Cheng, I., & Hodge, A. (2014). High temperature morphology and stability of nanoporous Ag foams. *Journal of porous materials*, *21*, 467-474.

Chi, H., Wang, C., Wang, Z., Zhu, H., Mesias, V. S. D., Dai, X., Chen, Q., Liu, W., & Huang, J. (2020). Highly reusable nanoporous silver sheet for sensitive SERS detection of pesticides. *Analyst*, *145*(15), 5158-5165.

Choi, O., Deng, K. K., Kim, N.-J., Ross, L., Surampalli, R. Y., & Hu, Z. (2008). The inhibitory effects of silver nanoparticles, silver ions, and silver chloride colloids on microbial growth. *Water research (Oxford)*, *42*(12), 3066-3074. https://doi.org/10.1016/j.watres.2008.02.021

Choy, T. C. (2015). *Effective medium theory: principles and applications* (Vol. 165). Oxford University Press.

Cortie, M. B., Arnold, M. D., & Keast, V. J. (2019). Quest for zero loss : unconventional materials for plasmonics. *Adv. Mater.*, *32*(18), 1904532. https://doi.org/doi: 10.1002/adma.201904532

Cortie, M. B., Maaroof, A. I., & Smith, G. B. (2005). Electrochemical capacitance of mesoporous gold. *Gold Bull.*, *38*(1), 15-23. https://doi.org/https://doi.org/10.1007/BF03215223

Cousins, K., & Zhang, R. (2019). Highly porous organic polymers for hydrogen fuel storage. *Polymers*, *11*(4), 690.

Crawley, G. M. (2017). *Energy storage*. World Scientific Publishing Co. Pte. Ltd.

Cunningham, W., & Cunningham, M. (2014). *Ebook: Environmental Science: A Global Concern*. McGraw-Hill Education. https://books.google.com.au/books?id=HoZvEAAAQBAJ

Curkovic, L., & Jelaca, M. F. (2009). Dissolution of alumina ceramics in HCl aqueous solution. *Ceramics international*, *35*(5), 2041-2045. https://doi.org/10.1016/j.ceramint.2008.11.007

Dakal, T. C., Kumar, A., Majumdar, R. S., & Yadav, V. (2016). Mechanistic Basis of Antimicrobial Actions of Silver Nanoparticles. *Frontiers in microbiology*, *7*, 1831-1831. https://doi.org/10.3389/fmicb.2016.01831

De Oliveira, R., Albuquerque, D., Cruz, T., Yamaji, F., & Leite, F. (2012). *Measurement of the nanoscale roughness by atomic force microscopy: basic principles and applications* (Vol. 3).

De Silva, K. S., Keast, V. J., Gentle, A., & Cortie, M. B. (2017). Optical properties and oxidation of α-phase Ag–Al thin films. *Nanotechnology*, *28*(9), 095202. https://doi.org/https://doi.org/10.1088/1361-6528/aa5782

Detsi, E., Salverda, M., Onck, P. R., & De Hosson, J. T. M. (2014). On the localized surface plasmon resonance modes in nanoporous gold films. *Journal of Applied Physics*, *115*(4), 044308. https://doi.org/https://doi.org/10.1063/1.4862440

Detsi, E., Vuković, Z., Punzhin, S., Bronsveld, P. M., Onck, P. R., & De Hosson, J. T. M. (2012). Fine-tuning the feature size of nanoporous silver. *CrystEngComm*, *14*(17), 5402-5406. https://doi.org/https://doi.org/10.1039/C2CE25313E

Dey, T. (2023). Microplastic pollutant detection by Surface Enhanced Raman Spectroscopy (SERS): a mini-review. *Nanotechnology for environmental engineering*, *8*(1), 41-48. https://doi.org/10.1007/s41204-022-00223-7

Dhaneswara, D., Fajar Fatriansyah, J., Ramadhan, R., & Ashari, A. (2019). The Effect of Melting Temperature Aluminum Metal Casting Using Mixed Degasser Based Sodium Fluoride and Sodium Nitrate. *MATEC Web of Conferences*, *269*, 7001. https://doi.org/10.1051/matecconf/201926907001

Ding, Y., Kim, Y. J., & Erlebacher, J. (2004). Nanoporous Gold Leaf: "Ancient Technology"/Advanced Material. *Advanced materials (Weinheim)*, *16*(21), 1897-1900. https://doi.org/10.1002/adma.200400792

Ding, Y., Kim, Y. J., & Erlebacher, J. (2004). Nanoporous gold leaf:“Ancient technology”/advanced material. *Advanced materials*, *16*(21), 1897-1900.

Ding, Y., & Zhang, Z. (2016). *Nanoporous metals for advanced energy technologies*. Springer.

Dixon, M. C., Daniel, T. A., Hieda, M., Smilgies, D. M., Chan, M. H., & Allara, D. L. (2007). Preparation, structure, and optical properties of nanoporous gold thin films. *Langmuir*, *23*(5), 2414-2422.

Dong, X.-Y., Gao, Z.-W., Yang, K.-F., Zhang, W.-Q., & Xu, L.-W. (2015). Nanosilver as a new generation of silver catalysts in organic transformations for efficient synthesis of fine chemicals. *Catalysis Science & Technology*, *5*(5), 2554-2574.

Doremus, R. H. (2002). Optical properties of small clusters of silver and gold atoms. *Langmuir*, *18*(6), 2436-2437.

Doskocz, N., Affek, K. A., & Załęska-Radziwiłł, M. (2017). Effects of aluminium oxide nanoparticles on bacterial growth. 9th Conference on Interdisciplinary Problems in Environmental Protection and Engineering EKO-DOK,

Dr. S. Sivakalai, D. V. A. R. D. R. K. C. D. A. K. Y. D. K. P. S. (2023). *Textbook of PHARMACEUTICAL MICROBIOLOGY*. Shashwat Publication. https://books.google.com.au/books?id=-uHgEAAAQBAJ

Dubey, R. C. (2014). *Advanced Biotechnology*. S. Chand Limited. https://books.google.com.au/books?id=SKgrDAAAQBAJ

Duggan, K., Ijaz, M. K., McKinney, J., & Maillard, J.-Y. (2024). Reviewing the evidence of antimicrobial activity of glycols. *Journal of applied microbiology*, *135*(4). https://doi.org/10.1093/jambio/lxae071

Dunlap, R. A. (2019). *Electrons in Solids: Contemporary Topics*. Morgan & Claypool Publishers.

Durán, N., Nakazato, G., & Seabra, A. B. (2016). Antimicrobial activity of biogenic silver nanoparticles, and silver chloride nanoparticles: an overview and comments. *Applied microbiology and biotechnology*, *100*(15), 6555-6570. https://doi.org/10.1007/s00253-016-7657-7

El-Kalliny, A. S., Abdel-Wahed, M. S., El-Zahhar, A. A., Hamza, I. A., & Gad-Allah, T. A. (2023). Nanomaterials: a review of emerging contaminants with potential health or environmental impact. *Discover Nano*, *18*(1), 68.

Emregül, K., & Aksüt, A. A. (2000). The behavior of aluminum in alkaline media. *Corrosion science*, *42*(12), 2051-2067.

Erlebacher, J. (2004). An atomistic description of dealloying: porosity evolution, the critical potential, and rate-limiting behavior. *Journal of The Electrochemical Society*, *151*(10), C614.

Erlebacher, J., Aziz, M. J., Karma, A., Dimitrov, N., & Sieradzki, K. (2001a). Evolution of nanoporosity in dealloying. *Nature*, *410*, 450-435. https://doi.org/https://doi.org/10.1038/35068529

Erlebacher, J., Aziz, M. J., Karma, A., Dimitrov, N., & Sieradzki, K. (2001b). Evolution of nanoporosity in dealloying. *nature*, *410*(6827), 450-453.

Erwin, W. R., Zarick, H. F., Talbert, E. M., & Bardhan, R. (2016). Light trapping in mesoporous solar cells with plasmonic nanostructures. *Energy & Environmental Science*, *9*(5), 1577-1601. https://doi.org/https://doi.org/10.1039/C5EE03847B

Faiz, M. B., Amal, R., Marquis, C. P., Harry, E. J., Sotiriou, G. A., Rice, S. A., & Gunawan, C. (2018). Nanosilver and the microbiological activity of the particulate solids versus the leached soluble silver. *Nanotoxicology*, *12*(3), 263-273. https://doi.org/10.1080/17435390.2018.1434910

Fang, C., Shapter, J. G., Voelcker, N. H., & Ellis, A. V. (2014). Electrochemically prepared nanoporous gold as a SERS substrate with high enhancement. *RSC advances*, *4*(37), 19502-19506.

Faure, A.-C., Barbillon, G., Ou, M., Ledoux, G., Tillement, O., Roux, S., Fabregue, D., Descamps, A., Bijeon, J.-L., & Marquette, C. A. (2008). Core/shell nanoparticles for multiple biological detection with enhanced sensitivity and kinetics. *Nanotechnology*, *19*(48), 485103.

Feng, Q. L., Wu, J., Chen, G. Q., Cui, F. Z., Kim, T. N., & Kim, J. O. (2000). A mechanistic study of the antibacterial effect of silver ions on Escherichia coli and Staphylococcus aureus. *Journal of biomedical materials research*, *52*(4), 662-668. https://doi.org/10.1002/1097-4636(20001215)52:4<662::AID-JBM10>3.0.CO;2-3

Forouzandeh, P., Kumaravel, V., & Pillai, S. C. (2020). Electrode Materials for Supercapacitors: A Review of Recent Advances. *Catalysts*, *10*(9), 969. https://doi.org/10.3390/catal10090969

Frey, H., & Khan, H. R. (2015). *Handbook of thin film technology*. Springer.

Fujita, T., Okada, H., Koyama, K., Watanabe, K., Maekawa, S., & Chen, M. (2008). Unusually small electrical resistance of three-dimensional nanoporous gold in external magnetic fields. *Physical review letters*, *101*(16), 166601. https://doi.org/https://doi.org/10.1103/PhysRevLett.101.166601

Fujiwara, H. (2007). *Spectroscopic ellipsometry: principles and applications*. John Wiley & Sons.

Fujiwara, H., & Collins, R. W. (2019). *Spectroscopic Ellipsometry for Photovoltaics: Volume 1: Fundamental Principles and Solar Cell Characterization*. Springer International Publishing. https://books.google.com.au/books?id=1TSDDwAAQBAJ

Fuller, S. B., Wilhelm, E. J., & Jacobson, J. M. (2002). Ink-jet printed nanoparticle microelectromechanical systems. *Journal of Microelectromechanical systems*, *11*(1), 54-60.

Gadag, R. V., & R. V. Gadag, A. N. S. (2010). *Engineering Chemistry*. I.K. International Publishing House Pvt. Limited. https://books.google.com.au/books?id=oRrK-bSl_fgC

Galinski, H., Fratalocchi, A., Döbeli, M., & Capasso, F. (2017). Light Manipulation in Metallic Nanowire Networks with Functional Connectivity. *Advanced optical materials*, *5*(5), np-n/a. https://doi.org/10.1002/adom.201600580

Gao, J., Sun, L., Deng, H., Mathai, C. J., Gangopadhyay, S., & Yang, X. (2013). Experimental realization of epsilon-near-zero metamaterial slabs with metal-dielectric multilayers. *Applied Physics Letters*, *103*(5).

García, M. A. (2011). Surface plasmons in metallic nanoparticles: fundamentals and applications. *Journal of Physics D: Applied Physics*, *44*(28), 283001.

Garoli, D., Calandrini, E., Bozzola, A., Toma, A., Cattarin, S., Ortolani, M., & De Angelis, F. (2018). Fractal-like plasmonic metamaterial with a tailorable plasma frequency in the near-infrared. *ACS Photonics*, *5*(8), 3408-3414. https://doi.org/https://doi.org/10.1021/acsphotonics.8b00676

Garoli, D., Calandrini, E., Giovannini, G., Hubarevich, A., Caligiuri, V., & De Angelis, F. (2019). Nanoporous gold metamaterials for high sensitivity plasmonic sensing. *Nanoscale Horizons*, *4*(5), 1153-1157.

George, E. P., Raabe, D., & Ritchie, R. O. (2019). High-entropy alloys. *Nature reviews materials*, *4*(8), 515-534.

Georgiadis, K. (2015). *The Failure Mechanisms of Coated Precision Glass Molding Tools*. Apprimus Wissenschaftsverlag. https://books.google.com.au/books?id=21x9DwAAQBAJ

Ghosh, A., Ghosh, M., & Kalsar, R. (2019). Influence of homogenisation time on evolution of eutectic phases, dispersoid behaviour and crystallographic texture for Al–Zn–Mg–Cu–Ag alloy. *Journal of Alloys and Compounds*, *802*, 276-289. https://doi.org/10.1016/j.jallcom.2019.06.091

Godbey, W. T. (2014). *An Introduction to Biotechnology: The Science, Technology and Medical Applications* (1 ed., Vol. 11). Elsevier Science. https://doi.org/10.1016/C2013-0-18161-5

Goldstein, J. I., Newbury, D. E., Michael, J. R., Ritchie, N. W., Scott, J. H. J., & Joy, D. C. (2017). *Scanning electron microscopy and X-ray microanalysis*. springer.

Goodall, R. (2013). Porous metals: Foams and sponges. In *Advances in powder metallurgy* (pp. 273-307). Elsevier.

Górecki, R., Polo, C. C., Kalile, T. A., Miqueles, E. X., Tonin, Y. R., Upadhyaya, L., Meneau, F., & Nunes, S. P. (2023). Ptychographic X-ray computed tomography of porous membranes with nanoscale resolution. *Communications Materials*, *4*(1), 68.

Griffiths, E., Wilmers, J., Bargmann, S., & Reddy, B. D. (2020). Nanoporous metal based composites: Giving polymers strength and making metals move. *Journal of the Mechanics and Physics of Solids*, *137*, 103848.

Groysman, A. (2009). *Corrosion for Everybody*. Springer Netherlands. https://books.google.com.au/books?id=OHsKYj8T9z8C

Gulzar, U., Goriparti, S., Miele, E., Li, T., Maidecchi, G., Toma, A., De Angelis, F., Capiglia, C., & Zaccaria, R. P. (2016). Next-generation textiles: from embedded supercapacitors to lithium ion batteries. *Journal of materials chemistry. A, Materials for energy and sustainability*, *4*(43), 16771-16168. https://doi.org/10.1039/c6ta06437j

Gunawan, C., Faiz, M. B., Mann, R., Ting, S. R., Sotiriou, G. A., Marquis, C. P., & Amal, R. (2020). Nanosilver targets the bacterial cell envelope: the link with generation of reactive oxygen radicals. *ACS applied materials & interfaces*, *12*(5), 5557-5568. https://doi.org/https://doi.org/10.1021/acsami.9b20193

Guo, X., Zhang, C., Tian, Q., & Yu, D. (2021). Liquid metals dealloying as a general approach for the selective extraction of metals and the fabrication of nanoporous metals: A review. *Materials today communications*, *26*, 102007. https://doi.org/10.1016/j.mtcomm.2020.102007

Güzel, R. (2018). Synthesis of Silver Nanoparticles. In. IntechOpen. https://doi.org/10.5772/intechopen.75363

Guzman, M. P., Dille, J. P., & Godet, S. P. (2012). Synthesis and antibacterial activity of silver nanoparticles against gram-positive and gram-negative bacteria. *Nanomedicine*, *8*(1), 37-45. https://doi.org/10.1016/j.nano.2011.05.007

Hafaiedh, A., & Bouarissa, N. (2011). Quantum confinement effects on energy gaps and electron and hole effective masses of quantum well AlN. *Physica. E, Low-dimensional systems & nanostructures*, *43*(9), 1638-1641. https://doi.org/10.1016/j.physe.2011.05.013

Hakamada, M., Kato, N., Miyazawa, N., & Mabuchi, M. (2016). Water-adsorption effect on electrical resistivity of nanoporous gold. *Scripta Materialia*, *123*, 30-33.

Hakamada, M., Taniguchi, S., & Mabuchi, M. (2017). Antibacterial activity of nanoporous gold against Escherichia coli and Staphylococcus epidermidis. *Journal of materials research*, *32*(9), 1787-1795. https://doi.org/10.1557/jmr.2017.157

Hall, B. G., Acar, H., Nandipati, A., & Barlow, M. (2014). Growth rates made easy. *Molecular biology and evolution*, *31*(1), 232-238. https://doi.org/10.1093/molbev/mst187

Han, T., Ruan, H., Cao, S., Guan, Y., Tang, D., & Yang, X. (2021). *Photoelectric Materials and Devices*. World Scientific.

Hassanain, W. A., Johnson, C. L., Faulds, K., Graham, D., & Keegan, N. (2022). Recent advances in antibiotic resistance diagnosis using SERS: focus on the “Big 5” challenges. *Analyst*, *147*(21), 4674-4700. https://doi.org/https://doi.org/10.1039/D2AN00703G

Hatchett, D. W., & White, H. S. (1996). Electrochemistry of Sulfur Adlayers on the Low-Index Faces of Silver. *Journal of physical chemistry (1952)*, *100*(23), 9854-9859. https://doi.org/10.1021/jp953757z

Hayes, J., Hodge, A., Biener, J., Hamza, A., & Sieradzki, K. (2006). Monolithic nanoporous copper by dealloying Mn–Cu. *Journal of Materials Research*, *21*(10), 2611-2616.

He, B. B. (2018). *Two-dimensional X-ray Diffraction*. John Wiley & Sons.

Health, N. I. o. (n.d.). *ImageJ*. Retrieved November 3, 2020 from https://imagej.nih.gov/ij/download.html

Hemanth, N., Mohili, R. D., Patel, M., Jadhav, A. H., Lee, K., & Chaudhari, N. K. (2022). Metallic nanosponges for energy storage and conversion applications. *Journal of Materials Chemistry A*, *10*(27), 14221-14246.

Herrmann, J. W. (2006). *Handbook of Production Scheduling*. Springer US. https://books.google.com.au/books?id=DX9CAAAAQBAJ

Hildebrandt, P., & Stockburger, M. (1984). Surface-enhanced resonance Raman spectroscopy of Rhodamine 6G adsorbed on colloidal silver. *The Journal of Physical Chemistry*, *88*(24), 5935-5944.

Hopkins, P. E., Serrano, J. R., Phinney, L. M., Li, H., & Misra, A. (2011). Boundary scattering effects during electron thermalization in nanoporous gold. *Journal of Applied Physics*, *109*(1), 013524-013524-013525. https://doi.org/10.1063/1.3530866

Hu, G., Xiao, L., Tong, P., Bi, D., Wang, H., Ma, H., Zhu, G., & Liu, H. (2012). Antibacterial hemostatic dressings with nanoporous bioglass containing silver. *International journal of nanomedicine*, *7*(default), 2613-2620. https://doi.org/10.2147/IJN.S31081

Hu, Z., Wang, J., Li, R., Xu, C., Liu, X., Wang, Y., Fu, E., & Lu, Z. (2018). Ion irradiation-enhanced raman scattering on nanoporous copper. *Langmuir*, *34*(43), 13041-13046.

Huang, C. Z., Ling, J., Wang, J., & Media, C. S. P. (2018). *Elastic Light Scattering Spectrometry*. De Gruyter. https://books.google.com.au/books?id=gTCGDwAAQBAJ

Huang, J., Liu, C., Zhu, Y., Masala, S., Alarousu, E., Han, Y., & Fratalocchi, A. (2016). Harnessing structural darkness in the visible and infrared wavelengths for a new source of light. *Nature nanotechnology*, *11*(1), 60-66. https://doi.org/10.1038/nnano.2015.228

Huang, J., Liu, Y., He, X., Tang, C., Du, K., & He, Z. (2017). Gradient nanoporous gold: a novel surface-enhanced Raman scattering substrate. *RSC advances*, *7*(26), 15747-15753.

Huber, N., Viswanath, R. N., Mameka, N., Markmann, J., & Weißmüller, J. (2014). Scaling laws of nanoporous metals under uniaxial compression. *Acta Materialia*, *67*, 252-265. https://doi.org/10.1016/j.actamat.2013.12.003

IGNACIMUTHU, S. (2019). *Environmental Studies*. MJP Publisher. https://books.google.com.au/books?id=W9CbDwAAQBAJ

Impact, C. (n.d., July 15, 2024). *Match! - Phase identification from powder diffraction*. Retrieved April 9, 2024 from https://www.crystalimpact.com/match/download.htm#download

Indhu, A. R., Keerthana, L., & Dharmalingam, G. (2023). Plasmonic nanotechnology for photothermal applications - an evaluation. *Beilstein Journal of Nanotechnology*, *14*(1), 380-419. https://doi.org/10.3762/BJNANO.14.33

Irani, G., Huen, T., & Wooten, F. (1971). Optical properties of Ag and α-phase Ag-Al alloys. *Physical review B*, *3*(8), 2385.

Ivask, A., ElBadawy, A., Kaweeteerawat, C., Boren, D., Fischer, H., Ji, Z., Chang, C. H., Liu, R., Tolaymat, T., & Telesca, D. (2014). Toxicity mechanisms in Escherichia coli vary for silver nanoparticles and differ from ionic silver. *ACS nano*, *8*(1), 374-386. https://doi.org/https://doi.org/10.1021/nn4044047

Jakšić, Z., Obradov, M., Jakšić, O., Isić, G., Vuković, S., & Radović, D. V. (2018). Methods of decreasing losses in optical metamaterials. *Facta Universitatis, Series: Electronics and Energetics*, *31*(4), 501-518.

Jalas, D., Canchi, R., Petrov, A. Y., Lang, S., Shao, L., Weissmüller, J., & Eich, M. (2014). Effective medium model for the spectral properties of nanoporous gold in the visible. *Applied Physics Letters*, *105*(24). https://doi.org/10.1063/1.4904714

Jayram, N. D., Sonia, S., Poongodi, S., Kumar, P. S., Masuda, Y., Mangalaraj, D., Ponpandian, N., & Viswanathan, C. (2015). Superhydrophobic Ag decorated ZnO nanostructured thin film as effective surface enhanced Raman scattering substrates. *Applied Surface Science*, *355*, 969-977. https://doi.org/https://doi.org/10.1016/j.apsusc.2015.06.191

Ji, H., Wang, X., Zhao, C., Zhang, C., Xu, J., & Zhang, Z. (2011). Formation, control and functionalization of nanoporous silver through changing dealloying media and

elemental doping. *CrystEngComm*, *13*(7), 2617-2628. https://doi.org/https://doi.org/10.1039/C0CE00900H

Ji, H., Zhang, C., Xu, J., Zhao, C., Wang, X., & Zhang, Z. (2011). On the vacancy-controlled dealloying of rapidly solidified Mg–Ag alloys. *CrystEngComm*, *13*(15), 4846-4849.

Jibowu, T. (2016). A review on nanoporous metals. *Front Nanosci Nanotech*, *2*(4), 165-168.

Jin, Y., Li, R., Zuo, L., & Zhang, T. (2017). Correlation between dealloying conditions and coarsening behaviors of nanoporous silver produced by chemical dealloying of Ca-Ag metallic glass. *Journal of Alloys and Compounds*, *695*, 1600-1609.

Jing, Z., Dong, Y., & Zhang, L. (2024). Nanoporous silver fabricated with pretreated Ag-Al alloy toward surface enhanced Raman sensing. *Nanotechnology*, *35*(32), 325703. https://doi.org/10.1088/1361-6528/ad4559

Johnson, P. B., & Christy, R.-W. (1972). Optical constants of the noble metals. *Physical review B*, *6*(12), 4370.

Jorge de Souza, T. A., Rosa Souza, L. R., & Franchi, L. P. (2019). Silver nanoparticles: An integrated view of green synthesis methods, transformation in the environment, and toxicity. *Ecotoxicology and environmental safety*, *171*, 691-700. https://doi.org/10.1016/j.ecoenv.2018.12.095

Joudeh, N., & Linke, D. (2022). Nanoparticle classification, physicochemical properties, characterization, and applications: a comprehensive review for biologists. *Journal of Nanobiotechnology*, *20*(1), 262.

Kater, S. B., & Nicholson, C. (1973). *Intracellular staining in neurobiology* (1st 1973. ed.). Springer-Verlag. https://doi.org/10.1007/978-3-642-87123-8

Keir, D., & Pryor, M. (1980). The dealloying of copper-manganese alloys. *Journal of The Electrochemical Society*, *127*(10), 2138.

Kelsall, R. W., Hamley, I. W., & Geoghegan, M. (2005). *Nanoscale Science and Technology*. https://doi.org/10.1002/0470020873

Khan, I., Saeed, K., & Khan, I. (2019). Nanoparticles: Properties, applications and toxicities. *Arabian journal of chemistry*, *12*(7), 908-931.

Kim, M., Jeong, G. H., Lee, K. Y., Kwon, K., & Han, S. W. (2008). Fabrication of nanoporous superstructures through hierarchical self-assembly of nanoparticles. *Journal of materials chemistry*, *18*(19), 2208-2212.

Kleinman, S. L., Frontiera, R. R., Henry, A.-I., Dieringer, J. A., & Van Duyne, R. P. (2013). Creating, characterizing, and controlling chemistry with SERS hot spots. *Physical Chemistry Chemical Physics*, *15*(1), 21-36.

Klueh, U., Wagner, V., Kelly, S., Johnson, A., & Bryers, J. D. (2000). Efficacy of silver-coated fabric to prevent bacterial colonization and subsequent device-based biofilm formation. *Journal of biomedical materials research*, *53*(6), 621-631. https://doi.org/10.1002/1097-4636(2000)53:6<621::AID-JBM2>3.0.CO;2-Q

Knapp, H. (2017). *Intermediate Statistics Using SPSS*. SAGE Publications. https://books.google.com.au/books?id=OCekDgAAQBAJ

Knez, M. (2019). *World Scientific Reference Of Hybrid Materials (In 3 Volumes)* (Vol. 17). World Scientific.

Ko, H., Singamaneni, S., & Tsukruk, V. V. (2008). Nanostructured surfaces and assemblies as SERS media. *Small*, *4*(10), 1576-1599.

Kokura, S. M. D. P., Handa, O. M. D. P., Takagi, T. M. D. P., Ishikawa, T. M. D. P., Naito, Y. M. D. P., & Yoshikawa, T. M. D. P. (2010). Silver nanoparticles as a safe preservative for

use in cosmetics. *Nanomedicine*, *6*(4), 570-574. https://doi.org/10.1016/j.nano.2009.12.002

Kosović, M., Balarin, M., Ivanda, M., Đerek, V., Marciuš, M., Ristić, M., & Gamulin, O. (2015). Porous silicon covered with silver nanoparticles as surface-enhanced Raman scattering (SERS) substrate for ultra-low concentration detection. *Applied spectroscopy*, *69*(12), 1417-1424. https://doi.org/https://doi.org/10.1366/14-07729

Kou, T., Li, D., Zhang, C., Zhang, Z., & Yang, H. (2014). Unsupported nanoporous Ag catalysts towards CO oxidation. *Journal of Molecular Catalysis A: Chemical*, *382*, 55-63.

Koya, A. N., Zhu, X., Ohannesian, N., Yanik, A. A., Alabastri, A., Proietti Zaccaria, R., Krahne, R., Shih, W.-C., & Garoli, D. (2021). Nanoporous metals: From plasmonic properties to applications in enhanced spectroscopy and photocatalysis. *ACS nano*, *15*(4), 6038-6060. https://doi.org/https://doi.org/10.1021%2Facsnano.0c10945

Kreibig, U., & Genzel, L. (1985). Optical absorption of small metallic particles. *Surface Science*, *156*, 678-700.

Krishna, K. S., Sandeep, C. S., Philip, R., & Eswaramoorthy, M. (2010). Mixing does the magic: a rapid synthesis of high surface area noble metal nanosponges showing broadband nonlinear optical response. *ACS nano*, *4*(5), 2681-2688.

Krishnamurthi, V. R., Niyonshuti, I. I., Chen, J., & Wang, Y. (2021). A new analysis method for evaluating bacterial growth with microplate readers. *Plos one*, *16*(1), e0245205-e0245205. https://doi.org/10.1371/journal.pone.0245205

Kudelski, A. (2005). Raman studies of rhodamine 6G and crystal violet sub-monolayers on electrochemically roughened silver substrates: Do dye molecules adsorb preferentially on highly SERS-active sites? *Chemical Physics Letters*, *414*(4-6), 271-275.

Kudernac, T., Lei, S., Elemans, J. A., & De Feyter, S. (2009). Two-dimensional supramolecular self-assembly: nanoporous networks on surfaces. *Chemical Society Reviews*, *38*(2), 402-421.

KukáShon, J., SungáKong, S., ManáKim, J., HyunáKo, C., YunáLee, Y., HeeáHwang, S., & AháYoon, J. (2009). Facile synthesis of highly ordered mesoporous silver using cubic mesoporous silica template with controlled surface hydrophobicity. *Chemical communications*(6), 650-652.

Kulkarni, P., Baron, P. A., & Willeke, K. (2011). *Aerosol Measurement: Principles, Techniques, and Applications*. Wiley. https://books.google.com.au/books?id=ETvXooNW4-EC

Kumar, A., Mariappan, C. R., & Sarahan, B. S. (2019). Antibacterial and structural properties of mesoporous Ag doped calcium borosilicate glass-ceramics synthesized via a sol-gel route. *Journal of non-crystalline solids*, *505*, 431-437. https://doi.org/10.1016/j.jnoncrysol.2018.11.024

Kungolos, A. (2006). *Environmental Toxicology*. WIT Press. https://books.google.com.au/books?id=hx4ztCG8Nf8C

Kurowska-Tabor, E., Gawlak, K., Hnida, K., Jaskuła, M., & Sulka, G. D. (2016). Synthesis of porous thin silver films and their application for hydrogen peroxide sensing. *Electrochimica Acta*, *213*, 811-821. https://doi.org/https://doi.org/10.1016/j.electacta.2016.08.007

Kwon, H., Lee, S. H., & Kim, J. K. (2015). Three-Dimensional Metal-Oxide Nanohelix Arrays Fabricated by Oblique Angle Deposition: Fabrication, Properties, and Applications. *Nanoscale research letters*, *10*(1), 369-369. https://doi.org/10.1186/s11671-015-1057-2

Lakshmanan, C., Viswanath, R. N., Polaki, S. R., Rajaraman, R., Dash, S., & Tyagi, A. K. (2015). Surface area of nanoporous gold: Effect on temperature. *Electrchimica Acta*, *182*, 565-572. https://doi.org/https://doi.org/10.1016/j.electacta.2015.09.104

Laskar, A. L., Bocquet, J. L., Brébec, G., & Monty, C. (2012). *Diffusion in Materials*. Springer Netherlands. https://books.google.com.au/books?id=PzTwCAAAQBAJ

Lawanstiend, D., Gatemala, H., Nootchanat, S., Eakasit, S., Wongravee, K., & Srisa-Art, M. (2018). Microfluidic approach for in situ synthesis of nanoporous silver microstructures as on-chip SERS substrates. *Sensors and Actuators B: Chemical*, *270*, 466-474.

Le Ru, E. C., Blackie, E., Meyer, M., & Etchegoin, P. G. (2007). Surface enhanced Raman scattering enhancement factors: a comprehensive study. *The Journal of Physical Chemistry C*, *111*(37), 13794-13803.

Le Ru, E. C., & Etchegoin, P. G. (2009). A quick overview of surface-enhanced Raman spectroscopy. *Principles of surface-enhanced Raman spectroscopy*, 1-27. https://doi.org/http://dx.doi.org/10.1016/B978-0-444-52779-0.00007-6

Lee, M.-J., Lim, S.-H., Ha, J.-M., & Choi, S.-M. (2016). Green synthesis of high-purity mesoporous gold sponges using self-assembly of gold nanoparticles induced by thiolated poly (ethylene glycol). *Langmuir*, *32*(23), 5937-5945.

Lee, M. (2017). *X-Ray diffraction for materials research: from fundamentals to applications*. CRC Press.

Lee, S. M., Park, I. K., Kim, Y. S., Kim, H. J., Moon, H., Mueller, S., Arumugam, H., & Jeong, Y.-I. (2016). Superior absorption and retention properties of foam-film silver dressing versus other commercially available silver dressing. *Biomaterials research*, *20*(1), 22-22. https://doi.org/10.1186/s40824-016-0069-z

Levi, A. C., & Suhl, H. (1979). Quantum theory of atom-surface scattering: Debye-Waller factor. *Surface science*, *88*(1), 221-254. https://doi.org/10.1016/0039-6028(79)90577-6

Li, C., Freiberg, K., Tang, Y., Lippmann, S., & Zhu, Y. (2022). Formation of Nanoscale Al2O3 Protective Layer by Preheating Treatment for Improving Corrosion Resistance of Dilute Fe-Al Alloys. *Materials*, *15*(22), 7978. https://doi.org/10.3390/ma15227978

Li, C., Zhang, T., Zhang, M., Jin, Y., Zuo, L., Xu, H., & Li, R. (2017). Fabrication of fine spongy nanoporous Ag-Au alloys with improved catalysis properties. *Progress in Natural Science: Materials International*, *27*(6), 658-663. https://doi.org/https://doi.org/10.1016/j.pnsc.2017.05.002

Li, G., Zhang, W., Luo, N., Xue, Z., Hu, Q., Zeng, W., & Xu, J. (2021). Bimetallic nanocrystals: Structure, controllable synthesis and applications in catalysis, energy and sensing. *Nanomaterials*, *11*(8), 1926.

Li, R., Liu, X., Wang, H., Wu, Y., Chu, X., & Lu, Z. (2014). Nanoporous silver with tunable pore characteristics and superior surface enhanced Raman scattering. *Corrosion science*, *84*, 159-164. https://doi.org/https://doi.org/10.1016/j.corsci.2014.03.023

Li, R., Liu, X., Wang, H., Wu, Y., & Lu, Z. P. (2015). Development of electrochemical supercapacitors with uniform nanoporous silver network. *Electrochimica Acta*, *182*, 224-229. https://doi.org/10.1016/j.electacta.2015.09.069

Li, R., Liu, X., Wang, H., Zhou, D., Wu, Y., & Lu, Z. (2016). Formation mechanism and characterization of nanoporous silver with tunable porosity and promising capacitive performance by chemical dealloying of glassy precursor. *Acta Materialia*, *105*, 367-377. https://doi.org/https://doi.org/10.1016/j.actamat.2015.12.042

Li, W., Lv, S., Wang, Y., Zhang, L., & Cui, X. (2019). Nanoporous gold induced vertically standing 2D NiCo bimetal-organic framework nanosheets for non-enzymatic glucose biosensing. *Sensors and Actuators B: Chemical*, *281*, 652-658. https://doi.org/https://doi.org/10.1016/j.snb.2018.10.150

Li, Y., Zhou, Z., He, Y., & Li, H. (2021). *Epsilon-near-zero Metamaterials*. Cambridge University Press.

Li, Z., & Lu, X. (2021). Nanoindentation for mechanical behaviour characterization of nanoporous silver fabricated through dealloying. *Bulletin of Materials Science*, *44*, 1-7.

Li, Z., Lu, X., Li, B., Bai, L., & Wang, Q. (2015). Research on electrochemical oxidation of formaldehyde on the nanoporous silver electrode in alkaline solution. *ECS Electrochemistry Letters*, *4*(6), H24.

Li, Z., Lu, X., & Qin, Z. (2013). Formation of nanoporous silver by dealloying Ag22Zn78 alloy at low temperature in H2SO4. *Int. J. Electrochem. Sci*, *8*, 3564-3571. https://doi.org/https://doi.org/10.1016/S1452-3981(23)14412-9

Li, Z., Zhang, C., Tian, J., Zhang, Z., Zhang, X., & Ding, Y. (2014). Highly selective oxidation of organosilanes with a reusable nanoporous silver catalyst. *Catalysis Communications*, *53*, 53-56.

Lichtman, J. W., & Conchello, J.-A. (2005). Fluorescence microscopy. *Nature methods*, *2*(12), 910-919.

Lim, H., Kim, D., Kwon, G., Kim, H.-J., You, J., Kim, J., Eguchi, M., Nanjundan, A. K., Na, J., & Yamauchi, Y. (2020a). Synthesis of uniformly sized mesoporous silver films and their SERS application. *The Journal of Physical Chemistry C*, *124*(43), 23730-23737.

Lim, H., Kim, D., Kwon, G., Kim, H.-J., You, J., Kim, J., Eguchi, M., Nanjundan, A. K., Na, J., & Yamauchi, Y. (2020b). Synthesis of Uniformly Sized Mesoporous Silver Films and Their SERS Application. *Journal of physical chemistry. C*, *124*(43), 23730-23737. https://doi.org/10.1021/acs.jpcc.0c07234

Lin, B., Kong, L., Hodgson, P. D., & Dumée, L. F. (2014). Impact of the De-Alloying Kinetics and Alloy Microstructure on the Final Morphology of De-Alloyed Meso-Porous Metal Films. *Nanomaterials (Basel, Switzerland)*, *4*(4), 856-878. https://doi.org/10.3390/nano4040856

Liu, K., Zhao, Q., Li, B., & Zhao, X. (2022). Raman Spectroscopy: A Novel Technology for Gastric Cancer Diagnosis. *Frontiers in bioengineering and biotechnology*, *10*, 856591-856591. https://doi.org/10.3389/fbioe.2022.856591

Liu, L. Q., Wang, X. L., Jing, M., Zhang, S. G., Zhang, G. Y., Dou, S. X., & Wang, G. (2012). Broadband and omnidirectional, nearly zero reflective photovoltaic glass. *Advanced materials*, *24*(47), 6318-6322.

Liu, X., Ronne, A., Yu, L.-C., Liu, Y., Ge, M., Lin, C.-H., Layne, B., Halstenberg, P., Maltsev, D. S., & Ivanov, A. S. (2021). Formation of three-dimensional bicontinuous structures via molten salt dealloying studied in real-time by in situ synchrotron X-ray nano-tomography. *Nature communications*, *12*(1), 3441.

Liu, Y., Huang, J., Wang, X., Tsai, M., & Wang, Z. (2018). Nanoporous foam fabricated by dealloying AgAl thin film through supercritical fluid corrosion. *RSC advances*, *8*(24), 13075-13082. https://doi.org/https://doi.org/10.1039/C8RA00463C

Liu, Y., Mai, S., Li, N., Yiu, C. K., Mao, J., Pashley, D. H., & Tay, F. R. (2011). Differences between top-down and bottom-up approaches in mineralizing thick, partially demineralized collagen scaffolds. *Acta biomaterialia*, *7*(4), 1742-1751.

Liu, Y., Zhang, Y., Ding, H., Xu, S., Li, M., Kong, F., Luo, Y., & Li, G. (2013). Self-assembly of noble metallic spherical aggregates from monodisperse nanoparticles: their synthesis and pronounced SERS and catalytic properties. *Journal of Materials Chemistry A*, *1*(10), 3362-3371.

Lok, C.-N., Ho, C.-M., Chen, R., He, Q.-Y., Yu, W.-Y., Sun, H., Tam, P. K.-H., Chiu, J.-F., & Che, C.-M. (2006). Proteomic Analysis of the Mode of Antibacterial Action of Silver Nanoparticles. *Journal of proteome research*, *5*(4), 916-924. https://doi.org/10.1021/pr0504079

Losic, D., & Santos, A. (2015). *Electrochemically engineered nanoporous materials* (Vol. 220). Springer.

Losurdo, M., & Hingerl, K. (2013). *Ellipsometry at the nanoscale*. Springer.

Lu, R., Zou, W., Du, H., Wang, J., & Zhang, S. (2014). Antimicrobial activity of Ag nanoclusters encapsulated in porous silica nanospheres. *Ceramics international*, *40*(2), 3693-3698. https://doi.org/10.1016/j.ceramint.2013.09.055

Lu, X., Balk, T., Spolenak, R., & Arzt, E. (2007). Dealloying of Au–Ag thin films with a composition gradient: Influence on morphology of nanoporous Au. *Thin solid films*, *515*(18), 7122-7126.

Luo, F., Zhang, Y., Wei, C., Zhang, C., Wang, J., & Zhang, Z. (2020). On the dealloying mechanisms of a rapidly solidified $Al_{80}Ag_{20}$ alloy using in-situ X-ray diffraction. *Intermetallics*, *125*, 106913. https://doi.org/https://doi.org/10.1016/j.intermet.2020.106913

Ma, C., Trujillo, M. J., & Camden, J. P. (2016). Nanoporous silver film fabricated by oxygen plasma: A facile approach for SERS substrates. *ACS applied materials & interfaces*, *8*(36), 23978-23984.

Maaroof, A. I., Cortie, M. B., Gentle, A., & Smith, G. B. (2007). Mesoporous gold sponge as a prototype 'metamaterial'. *Phys. B-Condens. Matter*, *394*(2), 167-170. https://doi.org/https://doi.org/10.1016/j.physb.2006.12.014

Maaroof, A. I., Cortie, M. B., & Smith, G. B. (2005). Optical properties of mesoporous gold films. *J. Opt. A: Pure Appl. Opt.*, *7*, 303-309. https://doi.org/https://ui.adsabs.harvard.edu/link_gateway/2005JOptA...7..303M/doi:10.1088/1464-4258/7/7/007

Maaroof, A. I., Gentle, A., Smith, G. B., & Cortie, M. B. (2007). Bulk and surface plasmons in highly nanoporous gold films. *Journal of Physics D: Applied Physics*, *40*(18), 5675.

Mao, F., Taher, M., Kryshtal, O., Kruk, A., Czyrska-Filemonowicz, A., Ottosson, M., Andersson, A. M., Wiklund, U., & Jansson, U. (2016). Combinatorial study of gradient Ag–Al thin films: microstructure, phase formation, mechanical and electrical properties. *ACS applied materials & interfaces*, *8*(44), 30635-30643. https://doi.org/https://doi.org/10.1021/acsami.6b10659

Marambio-Jones, C., & Hoek, E. M. V. (2010). A review of the antibacterial effects of silver nanomaterials and potential implications for human health and the environment. *Journal of nanoparticle research : an interdisciplinary forum for nanoscale science and technology*, *12*(5), 1531-1551. https://doi.org/10.1007/s11051-010-9900-y

Mathias de Souza, B. L., Escada, A. L. d. A., Costa Fernandes, C. J. d., de Almeida, G. S., Zambuzzi, W. F., Capellato, P., Sachs, D., & Rosifini Alves, A. P. (2024). Obtaining of Antibacterial Nanoporous Layer on Ti7.5Mo Alloy Surface Combining Alkaline Treatment and Silver: In Vitro Studies. *Coatings (Basel)*, *14*(1), 52. https://doi.org/10.3390/coatings14010052

Mattox, D. M. (2010). *Handbook of physical vapor deposition (PVD) processing*. William Andrew.

McAlister, A. (1987). The Ag− Al (silver-aluminum) system. *Bulletin of Alloy Phase Diagrams*, *8*(6), 526-533.

McCue, I., Benn, E., Gaskey, B., & Erlebacher, J. (2016). Dealloying and dealloyed materials. *Annual review of materials research*, *46*(1), 263-286.

McCue, I., Gaskey, B., Geslin, P.-A., Karma, A., & Erlebacher, J. (2016). Kinetics and morphological evolution of liquid metal dealloying. *Acta Materialia*, *115*.

Měřička, P., Janoušek, L., Benda, A., Lainková, R., Sabó, J., Dalecká, M., Prokšová, P., Salmay, M., Špunda, R., Pecha, O., Jandová, M., Gregor, J., Štěrba, L., Špaček, M., & Lindner, J. (2021). Cell Viability Assessment Using Fluorescence Vital Dyes and Confocal Microscopy in Evaluating Freezing and Thawing Protocols Used in Cryopreservation of Allogeneic Venous Grafts. *International journal of molecular sciences*, *22*(19), 10653. https://doi.org/10.3390/ijms221910653

Michael, B. C., Abbas, M., Geoffrey, B. S., & Phuti, N. (2006). Nanoscale coatings of AuAlx and PtAlx and their mesoporous elemental derivatives. *Current applied physics*, 440-443.

Mint, U. S. B. o. t. (1964). *Annual Report of the Director of the Mint*. Department of the Treasury, Bureau of the Mint. https://books.google.com.au/books?id=bpLV5iz8zvQC

Miyaji, T., & Nitta, N. (2017). Nanoporous Structure Formation on the Surface of InSb by Ion Beam Irradiation. *Nanomaterials*, *7*(8), 204.

Miyazawa, N., Hakamada, M., & Mabuchi, M. (2018). Antimicrobial mechanisms due to hyperpolarisation induced by nanoporous Au. *Scientific Reports*, *8*(1), 3870-3878. https://doi.org/10.1038/s41598-018-22261-5

Mohammed, A., & Abdullah, A. (2018). Scanning electron microscopy (SEM): A review. Proceedings of the 2018 International Conference on Hydraulics and Pneumatics—HERVEX, Băile Govora, Romania,

Mokhtari, M., Le Bourlot, C., Adrien, J., Bonnin, A., Wada, T., Duchet-Rumeau, J., Kato, H., & Maire, E. (2018). Microstructure characterization by X-ray tomography and EBSD of porous FeCr produced by liquid metal dealloying. *Materials Characterization*, *144*, 166-172.

Monteiro, D. R., Gorup, L. F., Takamiya, A. S., de Camargo, E. R., Filho, A. C. R., & Barbosa, D. B. (2012). Silver Distribution and Release from an Antimicrobial Denture Base Resin Containing Silver Colloidal Nanoparticles. *Journal of prosthodontics*, *21*(1), 7-15. https://doi.org/10.1111/j.1532-849X.2011.00772.x

Moore, K., Johnson, W., Howe, J., Aaronson, H., & Veblen, D. (2002). On the interaction between Ag-depleted zones surrounding γ plates and spinodal decomposition in an Al-22 at.% Ag alloy. *Acta Materialia*, *50*(5), 943-956.

Morrish, R., & Muscat, A. J. (2009). Nanoporous Silver with Controllable Optical Properties Formed by Chemical Dealloying in Supercritical CO2. *Chemistry of Materials*, *21*(16), 3865-3870. https://doi.org/10.1021/cm9015386

Moskovits, M., & Jeong, D. H. (2004). Engineering nanostructures for giant optical fields. *Chemical Physics Letters*, *397*(1-3), 91-95.

Muehlethaler, C., Ng, K., Gueissaz, L., Leona, M., & Lombardi, J. R. (2017). Raman and SERS characterization of solvent dyes: An example of shoe polish analysis. *Dyes and Pigments*, *137*, 539-552. https://doi.org/https://doi.org/10.1016/j.dyepig.2016.10.049

Muhammed Shafi, P., & Chandra Bose, A. (2015). Impact of crystalline defects and size on X-ray line broadening: A phenomenological approach for tetragonal SnO2 nanocrystals. *AIP Advances*, *5*(5).

Murray, J. L. (2016). *Alloy Phase Diagrams* (Vol. 3). ASM Materials International.

Mwema, F. M., Jen, T.-C., & Zhu, L. (2022). *Thin Film Coatings: Properties, Deposition, and Applications*. CRC Press.

Newman, R., Corcoran, S., Erlebacher, J., Aziz, M., & Sieradzki, K. (1999). Alloy corrosion. *MRS bulletin*, *24*(7), 24-28.

Nomier, Y., Meiβner, J., & Kietzmann, M. (2023). Novel Study Antimicrobial and Biocompatibility Effect of Magnesium Silver Alloys 1% on Bovine Bacterial Species. *Veterinary Medicine International*, *2023*. https://doi.org/https://doi.org/10.1155/2023/8627515

Nowak, M., Trojanowska, A., Marciniak, L., Binczyk, M., Runka, T., Tylkowski, B., & Jastrzab, R. (2019). Preparation and characterization of long-term stable SERS active materials as potential supports for medical diagnostic. *Applied Surface Science*, *472*, 93-98. https://doi.org/https://doi.org/10.1016/j.apsusc.2018.04.055

Ohke, S., Satomura, Y., Umeda, T., & Cho, Y. (1995). A new integral expression for the effective refractive index of optical waveguides and its application for a fast numerical solution finder for the effective refractive index. *Optics communications*, *118*(3), 227-234. https://doi.org/10.1016/0030-4018(95)00275-D

Ohring, M., Zarrabian, S., & Grogan, A. (1992). The materials science of thin films. *Appl. Opt*, *31*(34), 7162.

Okon, E., Shehu, H., & Gobina, E. (2018). Evaluation of the performance of α-alumina nano-porous ceramic composite membrane for esterification applications in petroleum refinery. *Catalysis today*, *310*, 146-156.

Pandian, S. R. K., Deepak, V., Kalishwaralal, K., Viswanathan, P., & Gurunathan, S. (2010). Mechanism of bactericidal activity of Silver Nitrate-a concentration dependent bi-functional molecule. *Brazilian Journal of Microbiology*, *41*, 805-809. https://doi.org/https://doi.org/10.1590/s1517-83822010000300033

Pawley, C. J., Perez-Gavilan, A., Foley, K. S., Lentink, S., Welsh, H. N., Tuijthof, G., Steen Redeker, E., Diliën, H., Eersels, K., & Van Grinsven, B. (2017). Studying the drug delivery Kinetics of a Nanoporous matrix using a MIP-based thermal sensing platform. *Polymers*, *9*(11), 560.

Peiponen, K. E., Vartiainen, E. M., & Asakura, T. (1998). *Dispersion, Complex Analysis and Optical Spectroscopy: Classical Theory*. Springer Berlin Heidelberg. https://books.google.com.au/books?id=pERPzx6VYFcC

Peter, Y., & Cardona, M. (2010). *Fundamentals of semiconductors: physics and materials properties*. Springer Science & Business Media.

Pham, T. T. T., Bessho, T., Mathews, N., Zakeeruddin, S. M., Lam, Y. M., Mhaisalkar, S., & Grätzel, M. (2012). Light scattering enhancement from sub-micrometer cavities in the photoanode for dye-sensitized solar cells. *Journal of Materials Chemistry*, *22*(32), 16201-16204.

Pickering, H., & Swann, P. (1963). Electron metallography of chemical attack upon some alloys susceptible to stress corrosion cracking. *Corrosion*, *19*(11), 373t-389t.

Piegari, A., & Masetti, E. (1985). Thin film thickness measurement: a comparison of various techniques. *Thin solid films*, *124*(3-4), 249-257. https://doi.org/https://doi.org/10.1016/0040-6090(85)90273-1

Pilot, R., Signorini, R., Durante, C., Orian, L., Bhamidipati, M., & Fabris, L. (2019). A Review on Surface-Enhanced Raman Scattering. *Biosensors (Basel)*, *9*(2), 57. https://doi.org/10.3390/bios9020057

Plötze, M., & Niemz, P. (2011). Porosity and pore size distribution of different wood types as determined by mercury intrusion porosimetry. *European journal of wood and wood products*, *69*(4), 649-657.

Politano, G. G., & Versace, C. (2023). Spectroscopic Ellipsometry: Advancements, Applications and Future Prospects in Optical Characterization. *Spectroscopy Journal*, *1*(3), 163-181.

Poole, R. K. (2019). *Advances in Microbial Physiology* (1 ed.). Elsevier Science & Technology.

Porter, D. A., & Easterling, K. E. (2009). *Phase transformations in metals and alloys (revised reprint)*. CRC press.

Portilla, L. (2017). *Functionalization of Metal Oxide Nanostructures via Self-Assembly. Implications and Applications*

Prochaska, M., Jin, J., Rochefort, D., Zhuang, L., DiSalvo, F. J., Abruña, H. D., & Van Dover, R. (2006). High throughput screening of electrocatalysts for fuel cell applications. *Review of scientific instruments*, *77*(5).

Qian, L., Yan, X., Fujita, T., Inoue, A., & Chen, M. (2007). Surface enhanced Raman scattering of nanoporous gold: Smaller pore sizes stronger enhancements. *Applied Physics Letters*, *90*(15).

Qian, L. H., & Chen, M. W. (2007). Ultrafine nanoporous gold by low-temperature dealloying and kinetics of nanopore formation. *Applied Physics Letters*, *91*(8). https://doi.org/10.1063/1.2773757

Qian, Y., Xiao, Y., Qin, T., Zhang, F., Tang, H., Liu, Y., & Lin, B. L. (2020). Investigating the formation mechanism of a nanoporous silver film electrode with enhanced catalytic activity for CO2 electroreduction. *ChemElectroChem*, *7*(21), 4354-4360.

Qing, Y., Li, K., Li, D., & Qin, Y. (2020). Antibacterial effects of silver incorporated zeolite coatings on 3D printed porous stainless steels. *Materials Science and Engineering: C*, *108*, 110430. https://doi.org/https://doi.org/10.1016/j.msec.2019.110430

Qing, Y. a., Cheng, L., Li, R., Liu, G., Zhang, Y., Tang, X., Wang, J., Liu, H., & Qin, Y. (2018). Potential antibacterial mechanism of silver nanoparticles and the optimization of orthopedic implants by advanced modification technologies. *International journal of nanomedicine*, *13*, 3311-3327. https://doi.org/10.2147/ijn.s165125

Qiu, H., Zhang, Z., Huang, X., & Qu, Y. (2011a). Dealloying Ag–Al Alloy to Prepare Nanoporous Silver as a Substrate for Surface-Enhanced Raman Scattering: Effects of Structural Evolution and Surface Modification. *ChemPhysChem*, *12*, 2118 - 2123.

Qiu, H., Zhang, Z., Huang, X., & Qu, Y. (2011b). Dealloying Ag–Al alloy to prepare nanoporous silver as a substrate for surface-enhanced raman scattering: effects of structural evolution and surface modification. *ChemPhysChem*, *12*(11), 2118-2123. https://doi.org/https://doi.org/10.1002/cphc.201100205

Qiu, H. J., Kang, J. L., Liu, P., Hirata, A., Fujita, T., & Chen, M. W. (2014). Fabrication of large-scale nanoporous nickel with a tunable pore size for energy storage. *Journal of power sources*, *247*, 896-905. https://doi.org/10.1016/j.jpowsour.2013.08.070

Qiu, H. J., Xu, H.-T., Liu, L., & Wang, Y. (2015). Correlation of the structure and applications of dealloyed nanoporous metals in catalysis and energy conversion/storage. *Nanoscale*, *7*(2), 386-384. https://doi.org/10.1039/c4nr05778c

Quinn, G. P., & Keough, M. J. (2002). *Experimental design and data analysis for biologists*. Cambridge university press.

Rai, M. K., Deshmukh, S. D., Ingle, A. P., & Gade, A. K. (2012). Silver nanoparticles: the powerful nanoweapon against multidrug-resistant bacteria. *Journal of applied microbiology*, *112*(5), 841-852. https://doi.org/10.1111/j.1365-2672.2012.05253.x

Raney, M. (1940). Catalysts from alloys. *Industrial & Engineering Chemistry*, *32*(9), 1199-1203.

Raza, M. A., Kanwal, Z., Rauf, A., Sabri, A. N., Riaz, S., & Naseem, S. (2016). Size-and shape-dependent antibacterial studies of silver nanoparticles synthesized by wet chemical routes. *Nanomaterials*, *6*(4), 74. https://doi.org/https://doi.org/10.3390%2Fnano6040074

Rebbecchi Jr, T. A., & Chen, Y. (2018). Template-based fabrication of nanoporous metals. *Journal of materials research*, *33*(1), 2-15.

Rijesh, M., Sreekanth, M., Deepak, A., Dev, K., & Surendranathan, A. (2018). Effect of milling time on production of aluminium nanoparticle by high energy ball milling. *Int. J. Mech. Eng. Technol*, *9*(8), 646-652.

Ron, R., Haleva, E., & Salomon, A. (2018). Nanoporous Metallic Networks: Fabrication, Optical Properties, and Applications. *Adv. Mater.*, *30*, 1706755. https://doi.org/https://doi.org/10.1002/adma.201706755

Ron, R., Zielinski, M. S., & Salomon, A. (2020). Cathodoluminescence Nanoscopy of 3D Plasmonic Networks. *Nano letters*, *20*(11), 8205-8211. https://doi.org/10.1021/acs.nanolett.0c03317

Ruffato, G., Romanato, F., Garoli, D., & Cattarin, S. (2011). Nanoporous gold plasmonic structures for sensing applications. *Optics express*, *19*(14), 13164-13170.

Ryser, E. T., & Marth, E. H. (2007). *Listeria, Listeriosis, and Food Safety*. CRC Press. https://books.google.com.au/books?id=NZsS6tbSAFYC

Šachl, R., & Amaro, M. (2023). *Fluorescence spectroscopy and microscopy in biology* (1st 2023. ed.). Springer Nature Switzerland AG. https://doi.org/10.1007/978-3-031-30362-3

Salas-Orozco, M., Niño-Martínez, N., Martínez-Castañón, G.-A., Méndez, F. T., Jasso, M. E. C., & Ruiz, F. (2019). Mechanisms of Resistance to Silver Nanoparticles in Endodontic Bacteria: A Literature Review. *Journal of Nanomaterials*, *2019*, 1-11. https://doi.org/10.1155/2019/7630316

Samanta, A. K. (2022). *Colorimetry*. BoD–Books on Demand.

Sanders, E. R. (2012). Aseptic laboratory techniques: plating methods. *JoVE (Journal of Visualized Experiments)*(63), e3064.

Sanders, W. C. (2019). *Atomic Force Microscopy: Fundamental Concepts and Laboratory Investigations*. CRC Press.

Sang, Q., Hao, S., Han, J., & Ding, Y. (2022). Dealloyed nanoporous materials for electrochemical energy conversion and storage. *EnergyChem*, *4*(1), 100069. https://doi.org/https://doi.org/10.1016/j.enchem.2022.100069

Sardana, N., Birr, T., Schlenker, S., Reinhardt, C., & Schilling, J. (2014). Surface plasmons on ordered and bi-continuous spongy nanoporous gold. *New Journal of Physics*, *16*(6), 063053. https://doi.org/http://dx.doi.org/10.1088/1367-2630/16/6/063053

Scandura, G., Kumari, P., Palmisano, G., Karanikolos, G. N., Orwa, J., & Dumée, L. F. (2023). Nanoporous Dealloyed Metal Materials Processing and Applications– A Review. *Industrial & Engineering Chemistry Research*, *62*(4), 1736-1763.

Schwartz, M. (2016). *Encyclopedia and Handbook of Materials, Parts and Finishes*. CRC Press. https://books.google.com.au/books?id=CFazDAAAQBAJ

Schwarz, J. A., Contescu, C. I., & Putyera, K. (2004). *Dekker Encyclopedia of Nanoscience and Nanotechnology*. M. Dekker. https://books.google.com.au/books?id=3PBv7pTesJQC

Seehra, M. S. (2018). Introductory Chapter: Overview of the Properties and Applications of Noble and Precious Metals. In. IntechOpen. https://doi.org/10.5772/intechopen.75503

Seok, J. Y., Lee, J., & Yang, M. (2018). Self-Generated Nanoporous Silver Framework for High-Performance Iron Oxide Pseudocapacitor Anodes. *ACS applied materials & interfaces*, *10*(20), 17223-17231. https://doi.org/10.1021/acsami.8b03725

Sharma, R., Bisen, D., Shukla, U., & Sharma, B. (2012). X-ray diffraction: a powerful method of characterizing nanomaterials. *Recent Res Sci Technol*, *4*(8), 77-79.

Shen, Z., & O'Carroll, D. M. (2015). Nanoporous Silver Thin Films: Multifunctional Platforms for Influencing Chain Morphology and Optical Properties of Conjugated Polymers. *Advanced functional materials*, *25*(22), 3302-3313. https://doi.org/10.1002/adfm.201500456

Sherbrooke, U. d. (n.d.). *CASINO: Monte Carlo Simulation of Electron Trajectory in Solids*. Retrieved July 20, 2020 from http://www.gel.usherbrooke.ca/casino/What.html

Shi, K., Santiso, E. E., & Gubbins, K. E. (2021). Current advances in characterization of nano-porous materials: Pore size distribution and surface area. *Porous Materials: Theory and Its Application for Environmental Remediation*, 315-340.

Shi, L., Zhang, Y., Han, X., Niu, D., Sun, J., Yang, J. Y., Hu, S., & Zhang, X. (2019). SDS-modified Nanoporous Silver as an Efficient Electrocatalyst for Selectively Converting CO2 to CO in Aqueous Solution. *Chinese Journal of Chemistry*, *37*(4), 337-341.

Shpigel, N., Sigalov, S., Malchik, F., Levi, M. D., Girshevitz, O., Khalfin, R. L., & Aurbach, D. (2019). Quantification of porosity in extensively nanoporous thin films in contact with gases and liquids. *Nature communications*, *10*(1), 4394.

Sihvola, A. H. (1999). *Electromagnetic mixing formulas and applications*. Iet.

Sing, K. S. (1985). Reporting physisorption data for gas/solid systems with special reference to the determination of surface area and porosity (Recommendations 1984). *Pure and applied chemistry*, *57*(4), 603-619. https://doi.org/https://doi.org/10.1351/pac198557040603

Sinha, P., Datar, A., Jeong, C., Deng, X., Chung, Y. G., & Lin, L.-C. (2019). Surface area determination of porous materials using the Brunauer–Emmett–Teller (BET) method: limitations and improvements. *The Journal of Physical Chemistry C*, *123*(33), 20195-20209.

Smith, G., & Earp, A. (2009). Metal-in-metal localized surface plasmon resonance. *Nanotechnology*, *21*(1), 015203.

Solé, J., Bausa, L., & Jaque, D. (2005). *An introduction to the optical spectroscopy of inorganic solids*. John Wiley & Sons.

Sondhi, P., Lingden, D., Bhattarai, J. K., Demchenko, A. V., & Stine, K. J. (2023). Applications of Nanoporous Gold in Therapy, Drug Delivery, and Diagnostics. *Metals (Basel)*, *13*(1), 78. https://doi.org/10.3390/met13010078

Song, T., Gao, Y., Zhang, Z., & Zhai, Q. (2011). Dealloying behavior of rapidly solidified Al–Ag alloys to prepare nanoporous Ag in inorganic and organic acidic media. *CrystEngComm*, *13*(23), 7058-7067. https://doi.org/https://doi.org/10.1039/C1CE05538K

Song, T., Gao, Y., Zhang, Z., & Zhaib, Q. (2011). Dealloying behavior of rapidly solidified Al–Ag alloys to prepare nanoporous Ag in inorganic and organic acidic media. *CrystEngComm*, *13*, 7058-7067.

Soonmin, H. (2022). Investigation of Optical Properties of Thin Films by Means of UV-visible Spectrophotometer: A Review.

Sparavigna, A. C. (2016). Depletion gilding: An ancient method for surface enrichment of gold alloys. *arXiv preprint arXiv:1601.00845*.

Speets, P. N., & Kalkman, J. (2024). Experiment and theory of the complex refractive index of dense colloidal media. *JOSA A*, *41*(2), 214-228.

Srinivasan, R., Ramesh, T., Umesh, G., & Sundar, C. (2023). *Experimental Techniques In Physics And Materials Sciences: Principles And Methodologies*. World Scientific.

Srivastava, S. (2013). *Understanding Bacteria*. Springer Netherlands. https://books.google.com.au/books?id=ZKzzCAAAQBAJ

Stewart, I. E., Kim, M. J., & Wiley, B. J. (2017). Effect of morphology on the electrical resistivity of silver nanostructure films. *ACS applied materials & interfaces*, *9*(2), 1870-1876. https://doi.org/https://doi.org/10.1021/acsami.6b12289

Stiefel, P., Schmidt-Emrich, S., Maniura-Weber, K., & Ren, Q. (2015). Critical aspects of using bacterial cell viability assays with the fluorophores SYTO9 and propidium iodide. *BMC microbiology*, *15*(1), 36-36. https://doi.org/10.1186/s12866-015-0376-x

Stuckner, J., Frei, K., Corcoran, S. G., Reynolds Jr, W. T., & Murayama, M. (2020). Assessing the influence of processing parameters and external loading on the nanoporous structure and morphology of nanoporous gold toward catalytic applications. *Journal of Physics and Chemistry of Solids*, *136*, 109139.

Suhag, D., Kaushik, S., & Taxak, V. B. (2024). *Handbook of Biomaterials for Medical Applications, Volume 1: Fundamentals*. Springer Nature Singapore. https://books.google.com.au/books?id=97QVEQAAQBAJ

Sun, Y., & Balk, T. J. (2008). Evolution of structure, composition, and stress in nanoporous gold thin films with grain-boundary cracks. *Metallurgical and Materials Transactions A*, *39*, 2656-2665.

Sun, Y., Liu, E., Li, Z., Jin, Q., & Sun, D. (2024). Effect of dealloying temperature on ligament morphology and size of hierarchically porous silver and its mechanical behaviour.

Supansomboon, S., Porkovich, A., Dowd, A., Arnold, M. D., & Cortie, M. B. (2014). Effect of precursor stoichiometry on the morphology of nanoporous platinum sponges. *ACS Appl. Mater. Interfaces*, *6*(12), 9411–9417. https://doi.org/https://doi.org/10.1021/am501794y

Suprapto, W., Irawan, Y. S., Suparman, S., Amrullah, M. R., Auliasyah, P., & Ramdhani, A. R. (2023). The effect of hold-melt time of micro-regime precipitation size and hardness in Al-Cu alloy. *Eureka, Physics and Engineering (Online)*(2), 222-234. https://doi.org/10.21303/2461-4262.2023.002684

Sur, U. K., & Chowdhury, J. (2013). Surface-enhanced Raman scattering: overview of a versatile technique used in electrochemistry and nanoscience. *Current Science*, 923-939.

Tan, X.-l., Li, K., Niu, G., Yi, Z., Luo, J.-s., Liu, Y., Han, S.-j., Wu, W.-d., & Tang, Y.-j. (2012). Effect of heat treatment of Mn-Cu precursors on morphology of dealloyed nanoporous copper. *Journal of Central South University*, *19*(1), 17-21. https://doi.org/10.1007/s11771-012-0966-9

Tan, Y. H., Davis, J. A., Fujikawa, K., Ganesh, N. V., Demchenko, A. V., & Stine, K. J. (2012). Surface area and pore size characteristics of nanoporous gold subjected to thermal, mechanical, or surface modification studied using gas adsorption isotherms, cyclic

voltammetry, thermogravimetric analysis, and scanning electron microscopy. *Journal of materials chemistry*, *22*(14), 6733-6745.

Tang, S., & Zheng, J. (2018). Antibacterial activity of silver nanoparticles: structural effects. *Advanced healthcare materials*, *7*(13), 1701503. https://doi.org/https://doi.org/10.1002/adhm.201701503

Tański, T., Ziębowicz, B., Jarka, P., & Staszuk, M. (2018). Introductory Chapter: Why Atomic Force Microscopy (AFM) is One of the Leading Methods of Surface Morphology Research of all Engineering Material Groups. In *Atomic-force Microscopy and Its Applications*. IntechOpen.

Tastekova, E. A., Polyakov, A. Y., Goldt, A. E., Sidorov, A. V., Oshmyanskaya, A. A., Sukhorukova, I. V., Shtansky, D. V., Grünert, W., & Grigorieva, A. V. (2018). Facile chemical routes to mesoporous silver substrates for SERS analysis. *Beilstein Journal of Nanotechnology*, *9*(1), 880-889.

Tessema, B., Gonfa, G., & Hailegiorgis, S. M. (2024). Synthesis of modified silica gel supported silver nanoparticles for the application of drinking water disinfection: A review. *Results in engineering*, *22*, 102261. https://doi.org/10.1016/j.rineng.2024.102261

Thukkaram, M., Cools, P., Nikiforov, A., Rigole, P., Coenye, T., Van Der Voort, P., Du Laing, G., Vercruysse, C., Declercq, H., Morent, R., De Wilde, L., De Baets, P., Verbeken, K., & De Geyter, N. (2020). Antibacterial activity of a porous silver doped TiO2 coating on titanium substrates synthesized by plasma electrolytic oxidation. *Applied Surface Science*, *500*, 144235. https://doi.org/10.1016/j.apsusc.2019.144235

Tian, Z.-Q., Ren, B., & Wu, D.-Y. (2002). Surface-enhanced Raman scattering: from noble to transition metals and from rough surfaces to ordered nanostructures. In (Vol. 106, pp. 9463-9483): ACS Publications.

Tisza, M. (2001). *Physical Metallurgy for Engineers*. ASM International. https://books.google.com.au/books?id=y1eTDQRdI2wC

Tjaden, B., Brett, D. J. L., & Shearing, P. R. (2018). Tortuosity in electrochemical devices: a review of calculation approaches. *International materials reviews*, *63*(2), 47-67. https://doi.org/10.1080/09506608.2016.1249995

Tyagi, A. K., & Ningthoujam, R. S. (2021). *Handbook on synthesis strategies for advanced materials. Volume-I, Techniques and fundamentals* (1st 2021. ed.). Springer. https://doi.org/10.1007/978-981-16-1807-9

Vajtai, R. (2013). *Springer handbook of nanomaterials*. Springer Science & Business Media.

van Emden, H. (2012). *Statistics for Terrified Biologists*. Wiley. https://books.google.com.au/books?id=VSik3zxvf-kC

Vantasin, S., Ji, W., Tanaka, Y., Kitahama, Y., Wang, M., Wongravee, K., Gatemala, H., Ekgasit, S., & Ozaki, Y. (2016). 3D SERS imaging using chemically synthesized highly symmetric nanoporous silver microparticles. *Angewandte Chemie*, *128*(29), 8531-8535.

Vidakovic-Koch, T. (2020). *Electrolysis Processes*. Mdpi AG. https://books.google.com.au/books?id=Tk4MEAAAQBAJ

Vimbela, G. V., Ngo, S. M., Fraze, C., Yang, L., & Stout, D. A. (2017). Antibacterial properties and toxicity from metallic nanomaterials. *International journal of nanomedicine*, *12*, 3941-3965. https://doi.org/10.2147/IJN.S134526

Wang, C., Yu, J., Hu, M.-y., & Zhang, K.-H. (2018). In-situ reaction precipitation of AgAl alloy powder and oxygen adsorption performance. *Journal of Alloys and Compounds*, *747*, 966-971.

Wang, C., Zhu, S., Liang, Y., Qin, C., Wang, F., Wang, H., Chang, C., & Inoue, A. (2023). Flexible free-standing antibacterial nanoporous Ag ribbon. *Journal of colloid and interface science*, *645*, 287-296. https://doi.org/10.1016/j.jcis.2023.04.153

Wang, L., He, H., Zhang, C., Sun, L., Liu, S., & Yue, R. (2014). Excellent antimicrobial properties of silver-loaded mesoporous silica SBA-15. *Journal of applied microbiology*, *116*(5), 1106-1118. https://doi.org/https://doi.org/10.1111%2Fjam.12443

Wang, X., Bashir, S., & Liu, J. (2022). *Nanochemistry: From Theory to Application for In-Depth Understanding of Nanomaterials*. De Gruyter. https://books.google.com.au/books?id=JGSVEAAAQBAJ

Wang, X., Li, R., Li, Z., Xiao, R., Chen, X.-B., & Zhang, T. (2019). Design and preparation of nanoporous Ag–Cu alloys by dealloying Mg–(Ag, Cu)–Y metallic glasses for antibacterial applications. *Journal of Materials Chemistry B*, *7*(26), 4169-4176. https://doi.org/https://doi.org/10.1039/C9TB00148D

Wang, X., Qi, Z., Zhao, C., Wang, W., & Zhang, Z. (2009a). Influence of Alloy Composition and Dealloying Solution on the Formation and Microstructure of Monolithic Nanoporous Silver through Chemical Dealloying of Al-Ag Alloys. *J. Phys. Chem. C*, *113*, 13139–13150.

Wang, X., Qi, Z., Zhao, C., Wang, W., & Zhang, Z. (2009b). Influence of alloy composition and dealloying solution on the formation and microstructure of monolithic nanoporous silver through chemical dealloying of Al− Ag alloys. *The Journal of Physical Chemistry C*, *113*(30), 13139-13150. https://doi.org/http://dx.doi.org/10.1021/jp902490u

Wessner, D., Dupont, C., Charles, T., & Neufeld, J. (2020). *Microbiology*. Wiley. https://books.google.com.au/books?id=GzcDEAAAQBAJ

West, P. R., Ishii, S., Naik, G. V., Emani, N. K., Shalaev, V. M., & Boltasseva, A. (2010). Searching for better plasmonic materials. *Laser & photonics reviews*, *4*(6), 795-808. https://doi.org/https://doi.org/10.1002/lpor.200900055

Wiederrecht, G. (2010). *Handbook of Nanoscale Optics and Electronics*. Elsevier Science. https://books.google.com.au/books?id=p-w1jX9Gqq0C

Woollam, J. (2012). Guide to Using WVASE: Spectroscopic Ellipsometry Data Acquisition and Analysis Software: Lincoln. *NE, USA: JA Woollam Company, Incorporated*.

Wu, C., Chen, E., & Wei, J. (2016). Surface enhanced Raman spectroscopy of Rhodamine 6G on agglomerates of different-sized silver truncated nanotriangles. *Colloids and Surfaces A: Physicochemical and Engineering Aspects*, *506*, 450-456.

Wu, L., Li, Y., Fu, Z., & Su, B.-L. (2020). Hierarchically structured porous materials: synthesis strategies and applications in energy storage. *National science review*, *7*(11), 1667-1701.

Wu, T. Y., Wang, X., Huang, J. C., Tsai, W. Y., Chu, Y. Y., Chen, S. Y., & Du, X. H. (2015a). Characterization and Functional Applications of Nanoporous Ag Foams Prepared by Chemical Dealloying. *Metall. Mater. Trans. B*, *46*, 2296-2304. https://doi.org/https://doi.org/10.1007/s11663-015-0392-0

Wu, T. Y., Wang, X., Huang, J. C., Tsai, W. Y., Chu, Y. Y., Chen, S. Y., & Du, X. H. (2015b). Characterization and Functional Applications of Nanoporous Ag Foams Prepared by Chemical Dealloying. *Metallurgical and materials transactions. B, Process metallurgy and materials processing science*, *46*(5), 2296-2304. https://doi.org/10.1007/s11663-015-0392-0

Xia, J., Yuan, Y., Wu, H., Huang, Y., & Weitz, D. A. (2020). Decoupling the effects of nanopore size and surface roughness on the attachment, spreading and differentiation of bone

marrow-derived stem cells. *Biomaterials*, *248*, 120014-120014. https://doi.org/10.1016/j.biomaterials.2020.120014

Xiao, X., Liu, E., Shao, J., & Ge, S. (2021). Advances on biodegradable zinc-silver-based alloys for biomedical applications. *Journal of Applied Biomaterials & Functional Materials*, *19*, 22808000211062407-22808000211062407. https://doi.org/10.1177/22808000211062407

Xie, L., Zeng, H., Zhu, J., Zhang, Z., Sun, H.-b., Xia, W., & Du, Y. (2022). State of the art in flexible SERS sensors toward label-free and onsite detection: from design to applications. *Nano Research*, *15*(5), 4374-4394. https://doi.org/https://doi.org/10.1007/s12274-021-4017-4

Xu, C., Li, Y., Tian, F., & Ding, Y. (2010). Dealloying to nanoporous silver and its implementation as a template material for construction of nanotubular mesoporous bimetallic nanostructures. *ChemPhysChem*, *11*(15), 3320-3328.

Yamauchi, I., Mase, T., Kajiwara, T., & Saraoka, M. (2003). Synthesis of skeletal silver from rapidly solidified Al–Ag precursor. *J. Alloys Compounds*, *348*, 270–277. https://doi.org/https://doi.org/10.1016/S0925-8388(02)00798-3

Yamauchi, I., Mase, T., Kajiwara, T., & Saraoka, M. (2003). Synthesis of skeletal silver from rapidly solidified Al–Ag precursor. *Journal of Alloys and Compounds*, *348*(1-2), 270-277.

Yang, G., Fu, X.-J., Sun, J.-B., & Zhou, J. (2013). Optical properties of aluminum silver alloy films deposited by magnetron sputtering. *Journal of Alloys and Compounds*, *547*, 23-28. https://doi.org/https://doi.org/10.1016/j.jallcom.2012.08.007

Yang, L., Meng, F., Qu, X., Xia, L., Huang, F., Qin, S., Zhang, M., Xu, F., Sun, L., & Liu, H. (2019). Multiple-twinned silver nanoparticles supported on mesoporous graphene with enhanced antibacterial activity. *Carbon*, *155*, 397-402. https://doi.org/https://doi.org/10.1016/j.carbon.2019.09.002

Yang, X., Li, Z., Jin, Q., Liu, M., & Xia, C. (2022). Fabrication of a three-level hierarchically porous silver via GASAR and dealloying processes and its catalytic behavior for formaldehyde oxidation. *Materials Letters*, *324*, 132760.

Yang, Y., Dan, Z., Liang, Y., Wang, Y., Qin, F., & Chang, H. (2019). Asynchronous evolution of nanoporous silver on dual-phase Ag–Sn alloys by potentiostatic dealloying in hydrochloric acid solution. *Nanomaterials*, *9*(5), 743. https://doi.org/https://doi.org/10.3390/nano9050743

Yu, J., Ding, Y., Xu, C., Inoue, A., Sakurai, T., & Chen, M. (2008). Nanoporous metals by dealloying multicomponent metallic glasses. *Chemistry of Materials*, *20*(14), 4548-4550.

Yuan, Y., Zhou, Z., Luo, J., Dan, Z., Qin, F., & Chang, H. (2021). (1 1 1)-facet dominant ultrafine nanoporous silver as SERS substrates with high sensitivities and ultrahigh detection limits. *Applied surface science*, *556*, 149820.

Yue, Y., & Liang, H. (2015). Hierarchical micro-architectures of electrodes for energy storage. *Journal of power sources*, *284*, 435-445. https://doi.org/10.1016/j.jpowsour.2015.03.069

Yuliza, E., Murniati, R., Rajak, A., & Abdullah, M. (2015). Effect of particle size on the electrical conductivity of metallic particles. 2014 International Conference on Advances in Education Technology (ICAET-14),

Zeman, E. J., & Schatz, G. C. (1987). An accurate electromagnetic theory study of surface enhancement factors for silver, gold, copper, lithium, sodium, aluminum, gallium, indium, zinc, and cadmium. *Journal of Physical Chemistry*, *91*(3), 634-643.

Zeng, W.-Y., Wang, Z.-F., Lin, D.-Z., & Cheng, I.-C. (2023). Pore evolution and size effect of nanoporous silver on SERS for malachite green detection. *Applied Surface Science*, *640*, 158306.

Zhang, C., Sun, J., Xu, J., Wang, X., Ji, H., Zhao, C., & Zhang, Z. (2012). Formation and microstructure of nanoporous silver by dealloying rapidly solidified Zn–Ag alloys. *Electrochimica Acta*, *63*, 302-311. https://doi.org/10.1016/j.electacta.2011.12.103

Zhang, C., Wang, X., Sun, J., Kou, T., & Zhang, Z. (2013). Synthesis and antibacterial properties of magnetically recyclable nanoporous silver/Fe3O4 nanocomposites through one-step dealloying. *CrystEngComm*, *15*(19), 3965-3973. https://doi.org/10.1039/c3ce00053b

Zhang, H., Hatoko, M., Yin, D., Yang, Y., Zeng, Y., Komasa, S., Kusumoto, T., Nishizaki, H., Shimizu, H., & Zhao, W. (2018). Antibacterial activity and biocompatibility of nanoporous titanium doped with silver nanoparticles and coated with n-acetyl cysteine. *Journal of Hard Tissue Biology*, *27*(4), 351-358. https://doi.org/https://doi.org/10.2485/jhtb.27.351

Zhang, J., & Li, C. M. (2012a). Nanoporous metals: fabrication strategies and advanced electrochemical applications in catalysis, sensing and energy systems. *Chemical Society Reviews*, *41*(21), 7016-7031.

Zhang, J., & Li, C. M. (2012b). Nanoporous metals: fabrication strategies and advanced electrochemical applications in catalysis, sensing and energy systems. *Chem. Soc. Rev.*, *41*, 7016–7031. https://doi.org/https://doi.org/10.1039/C2CS35210A

Zhang, L., Lang, X., Hirata, A., & Chen, M. (2011). Wrinkled nanoporous gold films with ultrahigh surface-enhanced Raman scattering enhancement. *ACS nano*, *5*(6), 4407-4413. https://doi.org/https://doi.org/10.1021/nn201443p

Zhang, M., Junior, A. J., Pang, S., Zhang, T., & Yavari, A. (2015). Fabrication of nanoporous silver with open pores. *Scripta Materialia*, *100*, 21-23. https://doi.org/https://doi.org/10.1016/j.scriptamat.2014.11.040

Zhang, Q., & Zhang, Z. (2010). On the electrochemical dealloying of Al-based alloys in a NaCl aqueous solution. *Phys. Chem. Chem. Phys.*, *12*, 1453–1472. https://doi.org/https://doi.org/10.1039/B919313H

Zhang, R., Wang, X., Huang, J. C., Li, F., Zhang, Z., & Wu, M. (2019). Formation mechanism of nanoporous silver during dealloying with ultrasonic irradiation. *RSC advances*, *9*(18), 9937-9945. https://doi.org/https://doi.org/10.1039/C9RA01742A

Zhang, R., Wang, X., Zhang, Z., Huang, J. C., Shi, F., & Wu, M. (2018). Structure analysis of precursor alloy and diffusion during dealloying of Ag-Al alloy. *RSC advances*, *8*(17), 9462-9470. https://doi.org/10.1039/c7ra12915g

Zhang, W., Tian, Q., Chen, Z., Zhao, C., Chai, H., Wu, Q., Li, W., Chen, X., Deng, Y., & Song, Y. (2020). Arrayed nanopore silver thin films for surface-enhanced Raman scattering. *RSC advances*, *10*(40), 23908-23915.

Zhang, Y., Liu, L., Shi, L., Yang, T., Niu, D., Hu, S., & Zhang, X. (2019). Enhancing CO2 electroreduction on nanoporous silver electrode in the presence of halides. *Electrochimica Acta*, *313*, 561-569.

Zhang, Z., & Ying, W. (2017). Design and Fabrication of Dealloying-driven Nanoporous Metallic Electrocatalyst. *Electrocatalysts for Low Temperature Fuel Cells: Fundamentals and*

Recent Trends, 533-555. https://doi.org/https://doi.org/10.1002/9783527803873.ch19

Zhang, Z. H., Wang, Y., Qi, Z., Zhang, W. H., Qin, J. Y., & Frenzel, J. (2009). Generalized fabrication of nanoporous metals (Au, Pd, Pt, Ag, and Cu) through chemical dealloying [Article]. *J. Phys. Chem. C*, *113*(29), 12629-12636. https://doi.org/http://dx.doi.org/10.1021/jp811445a

Zhao, C., Wada, T., De Andrade, V., Gürsoy, D., Kato, H., & Chen-Wiegart, Y.-c. K. (2018). Imaging of 3D morphological evolution of nanoporous silicon anode in lithium ion battery by X-ray nano-tomography. *Nano energy*, *52*, 381-390.

Zhao, J., Jensen, L., Sung, J., Zou, S., Schatz, G. C., & Van Duyne, R. P. (2007). Interaction of plasmon and molecular resonances for rhodamine 6G adsorbed on silver nanoparticles. *Journal of the American Chemical Society*, *129*(24), 7647-7656.

Zhao, J., Xue, S., Ji, R., Li, B., & Li, J. (2021). Localized surface plasmon resonance for enhanced electrocatalysis. *Chemical Society Reviews*, *50*(21), 12070-12097.

Zhao, Y., Wang, X., Li, F., Zhang, R., Huang, J., & Wu, M. (2017). Effect of Ag Content on Phase Evolution during the De-Alloying of Ag-Al Alloy: Combining the Electrochemical Noise with the Wavelet and Analysis. *International Journal of Electrochemical Science*, *12*(12), 11150-11162. https://doi.org/https://doi.org/10.20964/2017.12.05

Zhao, Y. H., Bingert, J. F., Topping, T. D., Sun, P. L., Liao, X. Z., Zhu, Y. T., & Lavernia, E. J. (2020). Mechanical behavior, deformation mechanism and microstructure evolutions of ultrafine-grained Al during recovery via annealing. *Materials science & engineering. A, Structural materials : properties, microstructure and processing*, *772*, 138706. https://doi.org/10.1016/j.msea.2019.138706

Zhao, Z. J., Li, W. P., Chen, Y. H., Liu, X. Y., Chou, T. H., Wang, X., Huang, J. C., & Wu, M. (2022). Effect of high temperature oxidation on dealloying mechanism of Ag-Cu alloy. *Journal of Alloys and Compounds*, *896*, 163007. https://doi.org/10.1016/j.jallcom.2021.163007

Zheng, K., Balasubramanian, P., Paterson, T. E., Stein, R., MacNeil, S., Fiorilli, S., Vitale-Brovarone, C., Shepherd, J., & Boccaccini, A. R. (2019). Ag modified mesoporous bioactive glass nanoparticles for enhanced antibacterial activity in 3D infected skin model. *Materials Science and Engineering: C*, *103*, 109764. https://doi.org/https://doi.org/10.1016/j.msec.2019.109764

Zheng, S., Bawazir, M., Dhall, A., Kim, H.-E., He, L., Heo, J., & Hwang, G. (2021). Implication of Surface Properties, Bacterial Motility, and Hydrodynamic Conditions on Bacterial Surface Sensing and Their Initial Adhesion. *Frontiers in bioengineering and biotechnology*, *9*, 643722-643722. https://doi.org/10.3389/fbioe.2021.643722

ZhiLi, D. (2022). *Fundamentals of Crystallography, Powder X-ray Diffraction, and Transmission Electron Microscopy for Materials Scientists*. CRC Press.

Zhou, M., Wei, Z., Qiao, H., Zhu, L., Yang, H., & Xia, T. (2009). Particle size and pore structure characterization of silver nanoparticles prepared by confined arc plasma. *Journal of Nanomaterials*, *2009*.

Zhou, W., Yang, Q., Sun, S., & Liang, S. (2018). Effect of thermal oxidation on microstructures and mechanical properties of nanoporous coppers. *Science China Technological Sciences*, *61*, 1839-1844. https://doi.org/https://doi.org/10.1007/s11431-018-9304-8

Zhou, X. C., Lin, W. Y., Yang, F. B., Zhou, X. D., Shen, J., & Huang, J. P. (2023). Effective medium theory with hybrid impacts of phase symmetry and asymmetry for analyzing phase

transition behavior. *Europhysics letters*, *141*(1), 16001. https://doi.org/10.1209/0295-5075/acabe1

Zhou, Y., Kong, Y., Kundu, S., Cirillo, J. D., & Liang, H. (2012). Antibacterial activities of gold and silver nanoparticles against Escherichia coli and bacillus Calmette-Guérin. *Journal of Nanobiotechnology*, *10*(1), 19-19. https://doi.org/10.1186/1477-3155-10-19

Zhu, C., Du, D., Eychmüller, A., & Lin, Y. (2015). Engineering ordered and nonordered porous noble metal nanostructures: synthesis, assembly, and their applications in electrochemistry. *Chemical reviews*, *115*(16), 8896-8943.

Zhu, H., Hu, C., Zhang, F., Feng, X., Li, J., Liu, T., Chen, J., & Zhang, J. (2014). Preparation and antibacterial property of silver-containing mesoporous 58S bioactive glass. *Materials Science and Engineering: C*, *42*, 22-30. https://doi.org/https://doi.org/10.1016/j.msec.2014.05.004

Zou, X., He, Y., Sun, P., Zhao, J., & Cui, G. (2018). A novel dealloying strategy for fabricating nanoporous silver as an electrocatalyst for hydrogen peroxide detection. *Applied Surface Science*, *447*, 542-547. https://doi.org/https://doi.org/10.1016/j.apsusc.2018.04.018

Zuruzi, A. S., & Siow, K. S. (2015). Electrical conductivity of porous silver made from sintered nanoparticles. *Electronic Materials Letters*, *11*, 308-314. https://doi.org/https://doi.org/10.1007/s13391-014-4357-2